SCALE EFFECTS IN BUCKLING, POSTBUCKLING AND CRIPPLING OF GRAPHITE-EPOXY Z-SECTION STIFFENERS

by

Todd M. Wieland
Department of Engineering Science and Mechanics
Virginia Polytechnic Institute and State University
in partial fulfillment of the requirements for the degree of

DOCTOR OF PHILOSOPHY

in

Engineering Mechanics

APPROVED:

J. Morton, Chairman

O. H. Griffin, Jr.

E. R. Johnson

D. T. Mook

M. P. Singh

December, 1991
Blacksburg, Virginia

SCALE EFFECTS IN BUCKLING, POSTBUCKLING AND CRIPPLING OF GRAPHITE-EPOXY Z-SECTION STIFFENERS

by

Todd M. Wieland
Professor John Morton, Chairman
Department of Engineering Science and Mechanics
(ABSTRACT)

Scale model testing can improve the cost-effectiveness of composite structures by reducing the reliance on full size component testing. Use of scale models requires the relationship be known between the responses of the small scale model and full size component. This relationship may be predicted by dimensional analysis or through mechanics formulations. The presence of physical constraints may prevent the complete reproduction of all responses in small scale models. Scaling relationships may not be available at the level necessary to predict all scaled responses. Investigations of the scalability of composite structures are needed in order to evaluate the reliability of small scale model predictions of the responses of full size components.

The scaling of the responses of graphite-epoxy laminated composite Z-section stiffeners subjected to uniaxial, compressive loading has been evaluated. The response regimes investigated are prebuckling, initial local buckling, postbuckling and crippling. A mechanistic approach to scaling has been used, in which the scalability of the responses has been judged relative to governing mechanics models. A linked-plate analytical model has been obtained which predicts the buckling loads, and from which two nondimensional load parameters have been obtained. The finite element method has been used for prediction of the buckling and postbuckling responses. The analytical and numerical analyses were used to define an experimental program involving fifty-two specimens of seventeen basic geometrical configurations and three stacking sequences.

The buckling, postbuckling and crippling responses were largely determined by the flange-to-web width ratio and both the absolute and relative values of the bending stiffnesses. Buckling loads increased with decreasing flange width and the laminate

orthotropy ratio, and increasing flange-to-web corner radii and laminate thickness. The postbuckling load range was the greatest for specimens having wider flanges, but the failure stresses were greatest among the narrower specimens. The crippling mechanisms included flange free edge delamination at both nodal and anti-nodal axial positions, material crushing in the flange-to-web corner at nodal axial positions, and ply splitting in the flange-to-web corner at anti-nodal axial locations.

The constraint of the potted end supports of the experimental specimens was not scaled. The effect of displacements within the end supports was manifested by lower prebuckling axial stiffnesses than predicted based on the gage length properties alone. This phenomenon required a post-test adjustment to the data in order to permit comparisons of the experimental and finite element predictions of the response of the gage length on an equivalent basis. Once corrected, the prebuckling stiffnesses were generally observed to have scaled.

One of the nondimensional load parameters normalized the buckling loads for specimens of various web widths only. The second parameter normalized the buckling loads for all of the geometric and material variables contained in the model. This parameter also normalized the postbuckling loads, and is, therefore, a general nondimensional parameter for the buckling and postbuckling responses of the Z-section stiffeners. No scale effects were observed in the buckling response. The quality of the postbuckling load predictions degraded with the width of the postbuckling load range. It was not determined whether genuine scale effects were present in the postbuckling response or whether the observed error was a result of inadequate modelling of structural and material nonlinearities or other effects such as damage development in the specimens.

Good correlation between experimental and finite element predictions of the out-of-plane displacements and load-axis strains has been demonstrated. Predicted local material strain development has been related to the structural deformation characteristics. Consideration of individual strain values, however, could not predict which of several competing failure modes would determine the actual crippling response. Neither could the strain data provide any quantitative prediction of the crippling loads. Thus, the determination of strength scale effects is hindered by the complex structural-material interaction and the lack of a mechanics-based interactive failure model.

ACKNOWLEDGEMENTS

I wish to express my appreciation to Professor John Morton for providing me with the benefits of his technical insight and experience, and for the provision of a most enjoyable working relationship and environment. I am grateful to Dr. James H. Starnes, Jr. of NASA Langley Research Center for his support and collaboration in conjunction with this research. I wish to thank the other members of my graduate committee, Dr. O.H. Griffin, Jr., Dr. E.R. Johnson, Dr. D.T. Mook and Dr. M.P. Singh, for their participation in this research and my academic progress. I would also like to thank the individuals of NASA Langley Research Center who provided excellent technical support of the experimental program. Notable among these are Alan Waters, Ann Cole, Jim Kiss, Tammy Hopkins and Cherie Wood. The sponsorship of NASA Langley Research Center under grant NAG-1-343 is very much appreciated. In addition to the above noted, this work was made possible by:

— the One who provided the mind with which to study and learn.

— my wife, Tina, who was selflessly supportive of this goal.

— my parents, who instilled the motivation for learning and hard work.

— the members of our research group, Dr. S. Kellas, Dr. M.Y. Tsai, Dr. H. Ho, K.T. Teh, H. Budiman, E. Zhang, D. Johnson and C. Traffanstedt.

TABLE OF CONTENTS

CHAPTER 1. INTRODUCTION

1.1 Introduction

The implementation of composite materials in structural applications has involved the production of costly prototypes and large scale experimental verification of certain design concepts. Scale model testing can streamline the development process and help improve the cost-effectiveness of composite structures. Scale model testing requires that the relationship between the responses of the small scale model and full size component be known so that the behavior of the model can be used to predict the response of the full size component. The relationship between the responses can be predicted using dimensional analysis to obtain a scaling law or mechanics models to obtain the functional relationship between the response characteristic and the properties of the structure. However, the presence of physical constraints or conflicts can prevent the complete reproduction of certain responses in small scale models. Furthermore, the mechanics formulations are still evolving for advanced material systems and may not provide the scaling relationships at the local material level necessary to relate all aspects of the response throughout the size range. Therefore, investigations of the scalability of composite structures are needed in order to evaluate the reliability of small scale model predictions of the responses of full size components, sources of non-scaled behavior or "scale effects", and the level of scaling of the structural and material characteristics necessary to achieve scaled behavior.

In the present study, a representative structural element has been selected which exhibits several response regimes of increasing complexity. The configuration is a laminated composite Z-section stiffener subjected to uniaxial, compressive loading. Investigated are the prebuckling, initial local buckling and postbuckling responses and failure by crippling. The configuration and response modes are relevant to a common aerospace design concept, in which a thin outer skin is reinforced by thin-walled stiffeners. Under compressive loads the skin and stiffeners may undergo local buckling. The structure may be required to carry additional load in the buckled configuration, necessitating the understanding of the structural behavior in the postbuckled response mode.

1.2 Objectives

The objectives of this work are: 1) to perform an investigation of the scalability of a representative composite material structural element; 2) to illustrate a mechanistic approach to scaling, as opposed to the traditional method of dimensional analysis; 3) to identify the scaling relationships which govern the responses; 4) to identify the responses which are either subject to scaling conflicts or inadequately modelled by the available mechanics formulations; and 5) to illustrate the parametric sensitivities of the responses of the specific structural component under investigation.

1.3 Approach

At least two approaches to a study in scaling are available. The first involves the use of dimensional analysis and similitude principles to define those nondimensional groups of geometric and material variables which govern the responses of scale models. From these parameters an experimental program can be defined using a number of scaled specimens to permit validation of the scaling parameters and to identify any "scale effects" or non-scaled behavior. A second approach is more mechanistic in nature and will be used in the current work. Here, a scale effect is identified as a departure of the response from a known mechanics model, which occurs systematically with specimen size. In contrast to the similitude approach, the mechanistic approach permits "selective scaling" or the evaluation of the response as a subset of the material and/or geometric parameters is varied. This approach facilitates the evaluation of the parametric dependence of the response of structures which are defined by many geometrical and material properties, in addition to the determination of the scalability of the responses.

A three-fold analytical, numerical and experimental approach has been used in this work. An analytical model for initial local buckling is obtained which predicts buckling loads and also provides nondimensional scaling parameters. The finite element method is used to also predict buckling loads and to extend the analysis into the postbuckling response regime. Both of these phases of work were used to define an experimental program, which contained 52 specimens of various geometrical and material properties. The experiments have been performed at NASA Langley Research Center.

1.4 Outline of Dissertation

Chapter 2 provides a foundation of background information related to the stability of plates and shells under compressive loading, and general scaling concepts. Also presented is a review of previous work related to the stability of composite stiffeners and scaling investigations of composite materials and structures. Chapter 3 presents the formulation of the analytical and numerical models for the buckling and postbuckling responses. Chapter 4 provides the details of the experimental program. The experimental buckling, postbuckling and crippling responses are presented in Chapter 5. The discussion of the experimental results is contained in Chapter 6. The correlation between the predicted and observed responses is included in the discussion. Chapter 7 provides a summary of the accomplishments and results, and recommendations for further work.

CHAPTER 2. BACKGROUND

2.1 Stability of Plates and Shells

A conventional approach to the design of a structure requiring a high stiffness-to-weight ratio employs a thin, stressed skin, which is reinforced by an underlying gridwork of beam-column-like stiffeners. A cylindrical fuselage, for example, might be constructed using a thin, cylindrical skin, stiffened by circumferential rings and longitudinal stringers. Many stiffener geometries are comprised of several plate-like strips, and are formed by folding or extruding operations. Common configurations include cross-sections of angle, channel, hat, I, J, T or Z shape, as shown in Figure 2-1. An unreinforced thin plate or shell would be susceptible to buckling under relatively low compressive loadings. The stiffeners reduce the susceptibility to buckling by essentially partitioning the skin into a series of smaller panels, the boundaries of which are defined by the gridwork of stiffeners. Under compressive loading, the skin may still buckle locally between stiffeners, but this will occur at much higher loads than in the unstiffened case. The in-plane stiffness of the skin is greatly reduced as a result of buckling, so that additional load will tend to concentrate into the stiffeners. At still higher loads, the stiffeners themselves may also undergo buckling. The in-plane stiffnesses of the various plate elements comprising the stiffener are similarly reduced as a result of local buckling in the stiffeners. Additional load will tend to concentrate into the nominally, straight, unbuckled portions of the stiffeners corresponding to the junctions between the various elements. The final failure or crippling process in a metallic stiffened panel typically is associated with material yielding in the corners of the stiffeners. This local collapse of the stiffener may then determine the strength of the entire stiffened panel. The buckling and crippling behavior of individual metallic stiffeners has been extensively characterized, due to the role of these responses in determining overall panel strength.

Composite materials offer higher specific strength and stiffness than the commonly used metal alloys. One approach to fabricating high stiffness-to-weight ratio structures using composite materials is to use the same stiffened skin approach that is being used for metallic structures. Investigations of the buckling of composites reported in the literature

have largely concentrated on the subcomponents of a stiffened panel, i.e. the stiffeners themselves and the unstiffened plate alone. Analyses of the subcomponents tend to be more tractable and less expensive than studies of the entire stiffened panel. In addition, the understanding of the individual responses might be used in formulating design methodologies, as has been done for the metallic stiffened panels. The presence of the same progression of buckling and postbuckling responses in the composite structure has necessitated the study of the buckling and crippling behavior of individual composite stiffeners. Much of the earliest experimental work was performed by Spier [1] using channel, hat, I and Z-section stiffeners. The laminates were $[\pm 45/0_3/90]_s$ A-S/3501-6 graphite/epoxy. Both the semi-static and cyclic buckling responses were investigated. A significant finding of Spier's work was that channel and Z-sections of the same cross-sectional dimensions had different crippling strengths. Spier indicated that the lower crippling strength of the channel sections was associated with a shift of the neutral axis in those sections after buckling, which increased the maximum compressive strain locally. The neutral axis shifted away from the plate elements which were critical with respect to buckling. For example, specimens with large flanges underwent buckling in the flanges first, so that the reduction in axial stiffness in the flanges caused a shift in the neutral axis toward the web. Little or no shift was observed in the Z-sections due to the point symmetry about the center of the web. Some of the stiffeners were cycled above and below the buckling load for up to 100,000 cycles at two cycles per second. Those which failed during this cyclic loading typically exhibited a change in the number of half waves in the buckled shape over the load range. The stiffeners which survived the cyclic loading did not exhibit a mode number change over the load range.

A second extensive experimental program consisting of 13 channel and 11 Z-sections is reported in Reference 2. Three stacking sequences of AS4/3502 graphite/epoxy were tested: $[\pm 45/0/90]_s$, $[\pm 45/0/90]_{2s}$ and $[45/-45_2/45/90/0_3]_s$. Flange-to-web corner radii were 0.125 and 0.25 in. The ends of the specimens were potted in an aluminum-filled epoxy compound to a depth of 1 inch, to aid in the uniform introduction of load, prevent separation of the plies in contact with the platens of the load frame and simulate clamped boundary conditions. Both global and local buckling responses were observed, in addition to short column material crushing, and one instance of unstable column buckling with local buckling interaction. Buckling loads were predicted using the PASCO and VIPASA computer codes. Agreement between the predicted and observed buckling loads was

improved by using the observed prebuckling stiffness of each specimen to estimate the corresponding ply stiffness in the fiber direction to be used in the analyses. This work also identified that several crippling mechanisms may be present in composite stiffeners, including failure in the corner and delamination at the flange free edge.

An experimental program based on I-sections fabricated from C3000/5225 graphite/epoxy woven cloth is reported in References 3 and 4. Reference 3 discusses the results for I-sections with the same stacking sequences ($[+45/0/-45]_S$, $[0/90]_{2S}$, $[+45/0/90/-45]_S$, $[0/\pm45/90]_S$ and $[0/90/0]_S$) in the flanges and web. The stacking sequences in the work of Reference 4 were $[0]_{4S}$, $[45/0_2/45]_S$, $[0/45_2/0]_S$, $[0]_{3S}$ and $[45/0/45]_S$. The stacking sequences in the flanges were defined by continuing the web plies divided at the midsurface with half going to each flange, and capping the result with 0° fibers to produce the same thickness as in the web. High-speed (300 frames per second) photography of the failure process revealed that crippling did initiate at the free edge of the flange followed by web failure in an ultimate strength mode [4]. An analytical and experimental program [5] was performed using AS4/PEEK graphite/thermoplastic (APC-2) angle and channel section stiffeners to evaluate whether the increased toughness of the thermoplastic matrix material improved the crippling strength relative to available data for similar stiffeners fabricated from T300/5208 graphite/epoxy . The ends of these specimens were potted in an aluminum-filled epoxy compound to a depth of 1/2 inch. The predominant crippling mechanism observed involved delamination of the outer plies of the laminate. There were no discernable differences in the crippling stresses between the graphite/thermoplastic and graphite/thermoset material systems. Reference 5 also reports results from an analytical Ritz-type model for predicting buckling loads. In this analysis, the stiffener is modelled as being comprised of individual plate elements which are simply-supported at the plate junctions, neglecting the actual rotational restraint present between adjacent plate elements. The estimated buckling loads in Reference 5 for channel sections were below the experimental values by 19% and 7.5% on average for the assumptions of simply-supported and clamped boundary conditions on the loaded edges, respectively. The underestimation of the buckling loads was attributed to the assumption of simply-supported conditions at the flange-to-web junctions.

Experimental and finite element analyses of the buckling of square tube and channel sections are reported in Reference 6. Stacking sequences for the channel sections were

$[\pm 15/0]_{S2}$ and $[\pm 15/0]_S$ AS4/3501-6 graphite/epoxy. The sections were formed over a square section elastomeric core, which was removed prior to loading of the stiffeners. The finite element analysis was based on an hybrid-stress SemiLoof element [7]. Crippling was caused by delamination, with delamination present in the corner regions.

A continuation of the stiffener crippling work of Reference 2 is reported in Reference 8. The stiffener configurations evaluated were I, J, channel and Z-sections. The same material system and stacking sequences of Reference 2 were used. Flange-to-web corner radii were 0.125 and 0.25 in. The buckling and crippling stresses of specimens of the I and J configurations with the larger corner radius were 75-100% and 50% greater, respectively, than equivalent specimens with the smaller corner radius. These significant increases in stresses as a function of corner radius were not observed in the channel and Z-sections. Additional volume was associated with the larger corner radius in the I and J-sections, since flanges exist on both sides of the web in these geometries. This additional volume was filled by "rolls" of 0° fibers, which accounts for the significant increases in stresses observed. No additional volume is associated with the larger corner radius in the channel and Z-sections (in fact a slight reduction occurs), since at each end of the web a flange exists on only one side of the web. The experimental crippling results, particularly for the I-sections, indicated a dependence of the crippling mode on the flange width-to-thickness (b_f/t) ratio. For values of this ratio greater than 20, the wide, thin flanges could tolerate significant postbuckling displacements, with the load being concentrated in the corners. The crippling mode was then crushing in the corner regions. The crippling mode for b_f/t ratios between 10 and 20 was delamination at the flange free edge. For values of this ratio less than 10, the relatively thick flanges were more resistant to buckling. The failure mode was essentially material failure coincident with buckling. The initial buckling loads and postbuckling responses were calculated using the finite element code STAGS (STructural Analysis of General Shells). Agreement between the predicted and observed load-end shortening responses was excellent through buckling, but degraded with increasing load in the postbuckling region. Linear (eigenvalue) buckling load predictions for the Z-sections, for example, were 12.1 to 13.7% higher than the experimental values. Buckling loads calculated from the nonlinear analyses (compression of the stiffener with an imperfection added) were in error from only -1.2% to 6.8%. The load predicted at the end shortening value corresponding to crippling of an I-section stiffener with a significant postbuckling response ($P_{crippling}/P_{buckling} = 3.5$) was 13.6% high relative to the

experimental maximum load. The excess stiffness of the finite element model was attributed in part to the lack of shear deformability in the elements used. The development of damage in the specimens was also cited as a cause for the discrepancy between the numerical and experimental results [8].

Several analytical and numerical models for predicting the buckling and postbuckling responses of stiffeners have been published, in addition to those methods discussed above. Since the common stiffener geometries can be represented as a set of connected plate-strips, many of the analytical models have been based on classical analyses of plate buckling with appropriate (or at least conservative) boundary conditions imposed at the junctions between plate elements. The fundamentals of the stability analyses of isotropic and anisotropic plates can be found in References 9 and 10, respectively. An overview of recent work addressing the buckling of composite plates is given in Reference 11. Reference 9 also includes discussion of the buckling responses of isotropic, linked-plate structures in the torsional, torsional-flexural and local buckling response modes. The analysis method of Reference 9 for local buckling was extended by Lee [12] to apply to the case of linked-plate structures fabricated from orthotropic materials. In these models, the actual elastic restraint between the flange and web is modelled, in contrast to the Ritz analysis discussed above and in Reference 5. Lee's model has been extended in the current work and will be discussed in detail in Chapter 3. More recently, Rehfield and Atilgan [13] have presented a model for buckling of thin-walled, laminated composite, open section beams, which includes transverse shear effects. Rehfield and Atilgan note that buckling load predictions using this model are in good agreement with the experimental data of Reference 6 for channel sections. The finite strip [14,15] and Raleigh-Ritz methods [16,17] are also available for the buckling and nonlinear postbuckling analyses of laminated composite, linked-plate structures, including the elastic restraint at the plate junctions.

Due to the complex, multi-mode nature of the crippling process in composite materials, satisfactory models for the prediction of crippling loads are lacking. Early efforts [18,19] were based on modifications of the same semi-empirical, power law relationships that have been used with metallic structures . Recently, Rehfield and Parnas [20] pointed out that the fundamental differences between the crippling responses of metallic and composite structures may require several, new models for predicting crippling in composites. In Reference 20, a model is described which addresses the corner crushing

type of crippling failure. The model consists of an analytical nonlinear, postbuckling analysis of a simply-supported plate, which is intended to represent the web. A maximum strain criterion is applied to predict the crippling load. The result is that a linear relationship between the buckling and crippling stresses is predicted. Rehfield and Parnas state that comparisons with the limited experimental data of References 3 and 4 are encouraging.

2.2 Scaling Concepts and Previous Work

One method of structural design evaluation has been based on the production of costly prototypes and large scale experimental verification. In many instances, the costs associated with this process may be prohibitive. In some cases, the size and nature of the structure may allow limited testing of nothing but the final, as-built configuration, or may preclude testing of the full size component completely. The size limitation might be manifested in the case of large bridges or dams. The size and flexibility of large space structures which are intended to be assembled in space may also preclude full size testing on earth [21]. For example, testing the full size component on earth may be precluded by the presence of response modes such as buckling by self-weight, which might not be encountered in space. Scale model testing has been used in the design process as an economical alternative to full size component testing. Scale models have also been employed to evaluate structural response when the available analysis tools are inadequate with respect to the modelling of the geometry and/or response. The cost of full size testing of composite structures may be even more prohibitive due to the significantly higher material costs. The tailorability of laminate properties introduces the possibility of more design iterations being desirable. In addition, measuring structural response with new material systems may be desirable, but might not be possible using a full size component due to the small quantity of the new material which would likely be initially available. The cost and feasibility motivations for performing scale model tests are, therefore, further intensified when composite materials are being used.

Scale model testing requires that the relationships between the responses of the small scale model and full size component be known so that the behavior of the model can be used to predict the responses of the full size component. The relationships between the responses can be obtained through applied mechanics techniques. However, the presence of physical constraints or conflicts can prevent the complete reproduction of certain

responses in small scale models. Responses subject to such physical constraints or scaling conflicts include rate-dependent and notch-sensitive behaviors [22]. Furthermore, the mechanics techniques are still evolving for advanced material systems and may not provide the "scaling" relationships at the local material level necessary to relate all aspects of the response throughout the size range. Therefore, work is needed to 1) obtain the scaling relationships which define how the response of composite structures should scale and 2) experimentally validate those relationships and identify the presence of any non-scaled behavior.

Some experimental and analytical scaling studies involving composite materials are available in the literature. In Reference 23, Kellas and Morton investigated the stiffness and strength scaling of various AS4/3502 graphite/epoxy laminates, including cross-ply, angle-ply and quasi-isotropic stacking sequences. A significant strength scale effect was observed, in which the smaller size specimens exhibited higher strengths. The strength scale effect was most pronounced in the matrix-dominated laminates. Also observed was the dependence of the failure mode on specimen size. This dependence was greatest in the fiber-dominated laminates. The laminates were scaled on a ply-level basis, in which plies of like orientation were stacked together to produce the larger sizes. This method is in contrast to the sub-laminate scaling method in which a group of plies are repeated as a group in order to obtain the larger sizes. A consequence of the ply-level method of scaling employed in Reference 23 was significant cure-induced matrix cracking present in the larger sizes, even before first loading. This matrix cracking effectively decoupled groups of plies and is expected to be an underlying factor relative to the size dependences observed. A significant implication of this work is that "size effects" may be associated with both methods of laminate scaling. The size effect associated with the ply-level method has already been discussed. In the case of the sub-laminate scaling method, bending stiffnesses do not scale exactly with the cube of the thickness. If a set of specimens are scaled in this manner and the mechanics governing the response are not known, then the non-scaled bending stiffnesses may result in an apparent size effect in the observed response. Naturally, if a known, complete mechanics model is being used to judge the degree to which the response is scaled, then the actual bending stiffnesses could be used and would not be cause for a scale effect in the response.

A scaling study of the transverse impact response of AS4/3502 graphite/epoxy composite beams was reported by Morton in Reference 22. Stacking sequences evaluated were unidirectional, cross-ply, angle-ply and quasi-isotropic. The impact force magnitude and duration responses scaled to within ±10% in the elastic range. While the degree of scaling achieved is good, the bulk of the error is attributed to the fact that the as-cured thicknesses did not scale exactly. Scaling degraded once damage developed in the specimens. A strength scale effect was also observed in this work, with the smaller specimens exhibiting greater strength.

References 24 and 25 discuss a scaling study of the semi-static and dynamic responses of eccentrically loaded AS4/3502 graphite/epoxy laminated composite beam-columns. Eight different scale models were evaluated, with the largest being 30 in. by 3.0 in. by 48 plies thick. Stacking sequences evaluated were unidirectional, cross-ply, angle-ply and quasi-isotropic. The static load-displacement responses scaled in the small deflection regime, but departures from scaled behavior occurred in the nonlinear response. The departures in the scaled behavior were most pronounced in the angle-ply laminates. The smaller specimens failed at much higher normalized loads and end shortenings, again indicating the presence of a strength scale effect. Damage modes were observed to be consistent within a laminate family and did not exhibit a scale effect, in contrast to the tensile strength work discussed above and in Reference 23. Scaling of the dynamic load-time and strain-time responses was excellent only in the case of the unidirectional laminates, with the angle-ply laminates exhibiting the poorest degree of scaled behavior.

A scaling study of the transverse impact of square laminated composite plates is discussed in Reference 26. The laminates were $[(\pm 72)_\lambda/0_{2\lambda}]_S$ AS4/3501-6 graphite/epoxy, with the scale factor λ ranging from 1 to 5. The load-time and strain-time responses scaled well for low energy impacts, which were believed to be below the threshold for laminate damage. A scale effect was observed in the development of damage under higher energy impacts, with greater delamination occurring in the larger sizes.

A consistent theme emerges from the above studies. The first point is that the degree of scaled response is greatest in the linear or small deflection response regime, which is also most pronounced in fiber-dominated laminates. The second observation is that laminate damage and failure processes do not yet appear to scale, at least based on the

dimensional analyses performed to date using only the more macroscopic structural and material parameters.

Analytical derivations of scaling laws for the responses of orthotropic cylinders are provided in References 27 and 28. Reference 27 contains a detailed derivation of nondimensional parameters using the principles of dimensional analysis. In Reference 28, nondimensional parameters for the magnitude and location of the maximum transverse displacement are obtained for the case of long cylinders by taking a limit of the governing analytical equation. A derivation of scaling parameters for the buckling and postbuckling of orthotropic plates was reported in Reference 29. The scaling parameters were obtained by nondimensionalization of the stability equation for buckling (see Chapter 3) and the nonlinear, large-deflection equations of von Karman for postbuckling. Normalized buckling loads were presented in terms of an aspect ratio parameter and a twisting stiffness parameter, which are respectively,

$$\frac{a}{b}\sqrt[4]{\frac{D_{22}}{D_{11}}} \text{ and } \frac{D_{12} + 2\,D_{66}}{\sqrt{D_{11}\,D_{22}}} \tag{2.1}$$

where a and b are the longitudinal and transverse dimensions of the plate, and the D_{ij} (i,j = 1,2,6) are the bending stiffnesses. Additional parameters for postbuckling are,

$$\frac{A_{22}\,D_{11}}{A_{11}\,D_{22}} \text{ and } \frac{A_{11}\,A_{22} - A_{12}^2 - 2\,A_{12}\,A_{66}}{2\,A_{66}\sqrt{A_{11}\,A_{22}}} \tag{2.2}$$

where the A_{ij} (i,j = 1,2,6) are the extensional stiffnesses. Nondimensional buckling and postbuckling responses can be presented for all material systems, stacking sequences and plate dimensions through use of these parameters.

2.3 Approaches to Scaling Studies

The approach to scaling used in all of the studies discussed above, with the exception of References 28 and 29, is the traditional method of dimensional analysis or similitude [30]. The initial step in a dimensional analysis is to identify a complete set of variables which influence the specific response under consideration. The physical

dimensions of these variables are then catalogued. The variables are then combined such that the resulting groups are nondimensional. The number of these nondimensional groups required is generally equal to the number of variables in the set minus the number of characteristic dimensions (force, length, time etc.) present in the variables. The normalized response of a small scale model and a full size component are then expected to be the same provided the model is constructed such that the values of these nondimensional groups remain the same as for the full size structure. It should be noted that the functional form of the relationship between the variables is neither obtained nor needed in this approach. It is sufficient to say that such a relationship does exist (even if it hasn't been found) and to recognize that it could be transformed into an expression involving the nondimensional groups. Clearly, there is no requirement that this latter expression be of any specific type (i.e. linear load-deflection response). The advantage of this method is that even complex behavior of a full size structure can be predicted through the use of (complete) small scale models, prediction of which might be presently intractable by analytical means. The review of previous scaling studies involving composite materials indicated that some responses did not scale. Apparent nonscaled behavior may result from two sources. The first is that a genuine scale effect may exist. A scale effect may either be readily predicted from the governing mechanics (as in the case of notch-sensitive behavior [22]) or may result from contradictory physical constraints which dictate that the model should be scaled in different ways simultaneously (as in the case of rate-sensitive behavior [22]). Apparent nonscaled behavior may also result from use of an incomplete set of parameters in the dimensional analysis. It is not yet known which micromechanical features of composite materials must be included in a dimensional analysis to form a sufficiently complete set.

A second approach to scaling is possible if a mechanics model governing the response is available. One possibility then is to nondimensionalize the governing equations. Dimensionless coefficients appear preceding the various terms in the equations as a result. This is the approach that was used in the work of Reference 29. A second possibility is to use the governing mechanics model as a criterion for evaluating the degree to which the behavior is scaled. Then, a scale effect is identified as a departure of the response from the known mechanics model, which occurs systematically with specimen size. In contrast to the similitude approach, the mechanistic approach permits "selective scaling" or the evaluation of the response as a subset of the material and/or geometric parameters is varied. This approach may be preferred when there are many variables

involved in characterizing the response, and when it is desired to determine the sensitivity of the response to the change in individual variables. Two possibilities arise when an apparent scale effect is observed in a study using this method. The first is that the observed phenomena is a genuine manifestation of the influence of specimen size on structural response, such as might occur in the case of a scaling conflict as noted above. The second possibility is that the available mechanics model is incomplete with respect to at least some of the processes active in determining the response. An obvious difficulty with this mechanistic approach to scaling is the need to be able to separate genuine scale effects from any inadequacies in the mechanics model being used. Nevertheless, the mechanistic approach to scaling has been used in the present work, because of the many geometric and material variables involved in characterizing a stiffener and the desire to maximize the amount of fundamental understanding of stiffener buckling and crippling responses through evaluation of a wide range of these parameters.

CHAPTER 3. THEORETICAL INVESTIGATION

3.1 Initial Local Buckling

3.1.1 Analytical Model

The geometric parameters pertinent to a Z-section stiffener are the web (b_w) and flange (b_f) widths, the flange-to-web corner radius (r), the thickness (t) and the length (L). The conventions used for these dimensions are identified on a schematic cross-section of a Z-section stiffener in Figure 3-1. Bulson developed an analytical model for the initial local buckling of an isotropic Z-section stiffener with right angle flange-to-web corners [9]. This model is based on a classical linked-plate analysis, in which equilibrium of the bending moments and equivalence of the slopes of the out-of-plane deflections are enforced at the flange-to-web junctions. The model was extended by Lee [12] to apply to sections comprised of single-layered orthotropic plates. A further generalization to the case of symmetric laminates has been achieved in the current work, albeit with the limitation that bending-twisting coupling is neglected.

The mathematical derivation is provided below in outline form, while more complete details are given in the Appendix. The domain of the model consists of one flange and one-half of the web (from the flange-to-web corner to the web centerline), as shown in Figure 3-2. The symmetry of the web about the web center is used to permit modelling of only half of this member. Coordinate systems with origins at the flange-to-web corner are defined for the web and flange plate elements. Governing differential equations for each of the two plate elements may be written as:

$$D_{11}\frac{\partial^4 w}{\partial x^4} + 2(D_{12} + 2D_{66})\frac{\partial^4 w}{\partial x^2 \partial y^2} + D_{22}\frac{\partial^4 w}{\partial y^4} + N_x\frac{\partial^2 w}{\partial x^2} = 0 \qquad (3.1)$$

where D_{ij} (i, j = 1, 2, 6) are the orthotropic plate bending stiffnesses, w is the out-of-plane deflection, x and y are longitudinal and transverse in-plane coordinates respectively, and

N_x is the axial load per unit width. Separate displacement functions w(x,y) are assumed in the web and flange of the form:

$$w(x,y) = f(y) \sin \frac{m\pi x}{L} \tag{3.2}$$

where L is the plate length and m is the number of half-waves in the buckled shape. The functions f(y) describe the variation of the displacement in the transverse direction and are as of yet undetermined. Use of these displacement functions transforms the two partial differential equations in terms of w(x,y) into two ordinary differential equations in terms of f(y). A general solution of these ordinary differential equations is of the form:

$$f(y) = A_1 \cosh \lambda y + A_2 \sinh \lambda y + A_3 \cos \omega y + A_4 \sin \omega y \tag{3.3}$$

where the A_i (i=1 to 4) are undetermined coefficients (which remain undetermined, since they physically represent the amplitude of the buckling displacements) and λ and ω are combinations of the plate dimensions and bending stiffnesses:

$$\lambda, \omega = \frac{m\pi}{L} \sqrt{\sqrt{\left(\frac{D_{33}}{D_{22}}\right)^2 - \frac{D_{11}}{D_{22}} + \frac{N_x}{D_{22}}\left(\frac{L}{m\pi}\right)^2} \pm \frac{D_{33}}{D_{22}}} \tag{3.4}$$

where $D_{33} = D_{12} + 2D_{66}$. A total of eight boundary and/or transition conditions are needed for a specific solution of the two ordinary differential equations. Equilibrium of the bending moments and equivalence of rotations are enforced at the web-to-flange joints and provides two transition conditions. The corner is assumed to remain straight. Therefore, zero transverse displacement at the flange-to-web joint provides two boundary conditions. For the web, the two remaining boundary conditions are zero transverse slope and shear force due to the state of symmetry which exists along the web centerline. For the flange, the two remaining boundary conditions are zero shear force and bending moment along the free edge. The mathematical statement of these boundary conditions produces a system of eight equations involving the unknown constants $(A_1 - A_4)_{web}$ and $(A_1 - A_4)_{flange}$. The final governing or characteristic equation is obtained by setting the determinant of the coefficients of these unknown constants to zero. The resulting equation can be expressed in the form:

$$\left[\frac{\text{F(SS-symmetric)}}{\text{F(clamped-symmetric)}}\right]_{\text{web}} + \frac{b_w}{b_f}\left[\frac{\text{F(SS-free)}}{\text{F(clamped-free)}}\right]_{\text{flange}} = 0 \tag{3.5}$$

where each function F( ) is the characteristic equation of a plate under the indicated boundary conditions on the unloaded edges; SS refers to a simply-supported boundary, symmetric refers to the plate edge being in a plane of symmetry, and b_f and b_w refer to the flange and web widths, respectively. Each characteristic equation represents the expanded determinant of the coefficient matrix formed by application of the indicated boundary conditions. The governing equation is solved iteratively for the buckling load.

Several nondimensional terms appear in the analysis. Two such terms that will prove valuable in what follows are defined as:

$$\alpha = \frac{N_x b_w^2}{\sqrt{D_{11} D_{22}}} \tag{3.6}$$

and

$$\beta = \frac{m\pi b_w}{L}\sqrt{\sqrt{\left(\frac{D_{33}}{D_{22}}\right)^2} - \frac{D_{11}}{D_{22}} + \frac{N_x}{D_{22}}\left(\frac{L}{m\pi}\right)^2} - \frac{D_{33}}{D_{22}} \tag{3.7}$$

3.1.2 Finite Element Model

The finite element method permitted correction of the two limitations of the analytical model identified above; those being the assumption that the flange and web meet at right angles and the omission of the bending-twisting coupling. The actual flange-to-web corner consists of a quarter of a right, circular cylinder, which is defined by the forming tool used to fabricate the stiffener. The bending-twisting coupling is represented by the D_{i6} (i=1,2) bending stiffnesses and is a result of non-zero rotated material stiffnesses Q_{i6} (i=1,2) associated with the off-axis plies present in generally laminated composites. The ABAQUS finite element code was used for the analyses, which were conducted on an Apollo DN4000 work station. Eight and nine-node shear deformable shell

elements with five or six degrees of freedom (dof) per node were used. Transverse shear force resultants were available for the case of the six dof/node elements only. The six degrees of freedom consisted of three displacements and three global rotations. The degrees of freedom for the five dof/node elements were three displacements and two in-surface rotations. The shell elements are formulated based on a degenerated three-dimensional theory. Integration is performed through the thickness of the shell, which permitted definition of a laminated composite directly in terms of the properties of the individual laminae. A typical finite element mesh is shown in Figure 3-3, which consists of 3 elements in each of the flange, web and corner regions, and 16 elements along the length. The number of elements used ranged from 160 to 544. The overall load-end shortening response was determined to have converged for the 160-element models. The more refined meshes were used to evaluate the local strain states in more detail. The ABAQUS user's manual identifies Reference 31 as a useful reference for the shell element formulation.

The eigenvalue buckling problem is described in the following. Consider that the structure is first loaded with fixed or "dead" loads, F^D_n (n=1 to the number of degrees of freedom in the model), and that the elastic tangent stiffness matrix in this configuration is $[K_D]$. Now consider that additional "live" loading F^L_n is applied, which results in the elastic tangent stiffness matrix under the combined loads becoming $[K_L] = [K_D] + [\Delta K_{DL}]$. Assume that the change in stiffness $[\Delta K_{DL}]$ is proportional to the change in the loads F^L_n. This implies that the stiffness under the load state $F^D_n + \lambda F^L_n$ is $[K_L] = [K_D] + \lambda[\Delta K_{DL}]$. The incremental load - displacement relationship is, therefore, $[[K_D] + \lambda[\Delta K_{DL}]]\{du\} = \{dF\}$, where $\{du\}$ and $\{dF\}$ are the vectors of incremental displacements and forces, respectively. Precisely at the buckling load, both the original and the buckled configurations may exist. There can then be a shift from the original configuration to the buckled state, with no change in load. Mathematically, this is stated as the eigenvalue problem $[[K_D] + \lambda[\Delta K_{DL}]]\{du\} = \{0\}$. The objective now is to extract the desired number of eigenvalues, λ_i, which determine the buckling loads as $F^D_n + \lambda_i F^L_n$. ABAQUS performs the eigenvalue extraction using the subspace iteration technique [32], with the Householder Method and the QR method of Francis [33].

3.2 Postbuckling

The ABAQUS finite element code was also used to perform geometrically nonlinear postbuckling analyses based on the Newton -Raphson method with and without a modified Riks procedure [34]. The Newton-Raphson technique is used to obtain the solution at a specific point on the load-deflection curve, while the modified Riks procedure manages the load incrementation to be used to trace the load-deflection curve. Let the basic finite element equation be stated as: $[K(u)]\{u\} = \{F\}$, where $\{u\}$ is the column vector of generalized displacements, $[K(u)]$ is the nonlinear direct stiffness matrix (which is nonlinear because it is a function of the solution $\{u\}$) and $\{F\}$ is the generalized force vector. In the Newton-Raphson method, a residual vector $\{R\}$ is defined as $\{R\} = [K]\{u_r\} - \{F\}$, where $\{u_r\}$ is the approximate solution after the r^{th} iteration. The residual vector can be expanded in a Taylor series in the form:

$$\{R\} = \{R(u_r)\} + \frac{\partial\{R(u_r)\}}{\partial\{u_r\}}\{\delta u_r\} + O(\{\delta u_r\})^2 \tag{3.8}$$

which becomes zero when the solution has converged. The derivative of the residual vector with respect to the solution vector is defined as the tangent stiffness matrix, $[K^{tan}]$. The equation $\{R\} = [K]\{u_r\} - \{F\}$ can then be rewritten to provide an iterative scheme for solving the nonlinear equations as follows:

$$[K^{tan}(u_r)]\{\delta u\} = -\{R(u_r)\} = \{F\} - [K(u_r)]\{u_r\} \tag{3.9}$$

The solution is updated after each iteration using the relation $\{u_{r+1}\} = \{u_r\} + \{\delta u\}$. This process is continued until the solution of the $r+1^{th}$ iteration is sufficiently close to the solution of the r^{th} iteration. While not a factor in the current work, the Riks procedure is particularly advantageous for the case of unstable equilibrium paths, such as that of a cylindrical shell. The load increment is obtained as part of the solution, and is chosen in such a way that singular points in the load-deflection curve are avoided. In this procedure, the vector formed by the load and displacement degrees of freedom from the i^{th} load increment is extrapolated by an amount defined by a pathlength parameter. The $i+1^{th}$ solution is then found by searching for equilibrium on the surface of a sphere normal to this vector. The modification of the Riks procedure used in ABAQUS essentially consists of using the surface of a sphere for the equilibrium search, as opposed to the surface of a

plane. Typically, the analyses were first performed using the Riks procedure to characterize the overall response, and then repeated using only the Newton-Raphson method to explicitly control (i.e. increase) the number of load steps taken near the buckling load.

The postbuckling analyses required that the surface of the "perfect" or unbuckled stiffeners be perturbed slightly to ensure that the secondary (postbuckled) load path would be selected by ABAQUS, as opposed to continuing along the primary path which is physically unstable beyond buckling. The eigenvalue buckling analyses provided the eigenvectors or mode shapes for each buckling load, normalized to a unit maximum out-of-plane displacement. A computer routine was written which added the buckling displacements corresponding to the first two buckling modes, normalized the resulting amplitude to a desired fraction of the laminate thickness, and added the result to the nodal coordinates. These "perturbed" models were then used in the nonlinear postbuckling analyses. Initial imperfection magnitudes of 1, 5 and 10% of the thickness of a nominal 8-ply laminate (0.04 in.) were used.

The analytical and numerical studies were used to define an experimental program. The objectives of the experimental program were to investigate the parametric sensitivity of the buckling, postbuckling and crippling responses to various geometric and material variables and to determine to what extend these responses scaled according to the mechanics models. Since local buckling was of primary interest, the analyses aided in the sizing of the specimens to avoid competing, dominant modes, such as torsional and flexural buckling.

CHAPTER 4. EXPERIMENTAL PROGRAM

4.1 Specimen Geometries and Stacking Sequences

The geometric parameters pertinent to a Z-section stiffener are the web (b_w) and flange (b_f) widths, the flange-to-web corner radius (r), the thickness (t) and the length (L). The experimental program was composed of three phases. The first phase was directed toward evaluating the effects of the corner radius, using section stock available from previous work [2,8]. Determining the effect of the web width was the objective of the second phase. The effects of stacking sequence and laminate thickness were investigated in the third phase. Various flange widths were considered in all three phases. Values of the geometric parameters and stacking sequences for the test specimens are contained in Table 4-1.

Available section stock of the quasi-isotropic stacking sequence $[\pm 45/0/90]_s$ had previously been fabricated from Hercules Inc. AS4/3502 graphite/epoxy preimpregnated tape by the Lockheed-Georgia Company using an open die and autoclave curing under vacuum. Corner radii of 0.125 and 0.25 in., and a web width of 1.25 in. were available. Web widths of 1.75 and 0.75 in. were selected for phase two to complement the web width of 1.25 in. of the first phase. The corner radius for the specimens in phase two was also 0.125 in. In the third phase, the effect of laminate thickness was investigated using a 16-ply quasi-isotropic laminate $[\pm 45/0/90]_{2s}$. Note that this laminate is scaled on a sub-laminate basis, so that the 4-ply groups +45/-45/0/90 and 90/0/-45/+45 are repeated twice in order to double the thickness. This method is in contrast to the ply-thickness scaling method in which the individual plies of like orientation are blocked together, in effect increasing the effective ply thickness. The rationale for selecting the sub-laminate scaling method was to avoid the cure-induced matrix cracking which has been observed in the "thick" plies when using the ply-thickness scaling method [23]. A consequence of using the sub-laminate scaling method is that the bending stiffnesses do not scale exactly with t^3, as they do with the ply-thickness scaling method. This is of little concern in the present work, since the degree to which the behavior is scaled is judge relative to mechanics models and the "actual" stiffnesses for each specimen may used as inputs to these models.

The method in which the stiffnesses scale will more strongly influence an experimental program in which the specimens are being scaled according to similitude principles. An unorthodox $[+30/0_2/-30]_S$ laminate was also selected for phase three in order to evaluate the generality of the scaling parameters developed for a greater degree of bending-twisting coupling and orthotropy than exist in the $[\pm 45/0/90]_S$ laminate. Recall that the bending-twisting coupling is neglected from the analytical model discussed in Chapter 3. The specimens in phases two and three were fabricated at NASA Langley Research Center, also using an open die and autoclave curing. The AS4/3502 graphite/epoxy material system was also used in the later phases, for consistency with the first.

The flange widths were selected to maximize the range of the flange-to-web width ratio and also to avoid competing modes such as torsional buckling and material crushing without buckling. Accordingly, the flange widths for specimens having the 8-ply laminates were 0.5, 0.75, 1.0 and 1.25 in. (with a maximum flange-to-web width ratio of 1). For specimens of the 16-ply laminates, flange widths of 0.75, 1.0 and 1.25 in. were selected.

Specimen lengths were selected such that the buckled mode shapes would include several half waves and yet avoid competing modes such as column buckling. Therefore, all specimens with flange sizes of 1.0 and 1.25 in. have a gage length of 10 in. Specimens having the smaller flange widths have a gage length of 6 in. The total length of each specimen was 2 in. longer than the gage length in order to accommodate the 1 in. deep potted end supports at each end of the specimen. The ends of the specimens were encapsulated in 4-5 in. diameter steel or aluminum rings using an aluminum-filled epoxy compound. These potted end supports promote uniform introduction of the axial load, prevent end-brooming or delamination at the contact point and simulate clamped boundary conditions.

Table 4-1 also contains a description of the specimen designations which will be used when referring to the results of specific specimens. Individual specimens will be identified using a name of the form ABCD-#, where A, B and C are digits referring to the web, flange and corner radii dimensions, D identifies the stacking sequence and "#" the individual specimen replicate number. Accordingly, a specimen type, i.e. a specific geometry and stacking sequence, will be referred to using the name ABCD, with no replicate number needed. For example, A=1, 2, 3 corresponds to web widths of 1.75,

1.25 and 0.75 in., respectively. Similarly, B=1, 2, 3, 4 corresponds to flange widths of 1.25, 1.0, 0.75 and 0.5 in., respectively. Also, C=1, 2 corresponds to corner radii of 0.125 and 0.25 in., respectively. Finally, D = 's', '-2s', and 'orth' will designate the $[\pm 45/0/90]_S$, $[\pm 45/0/90]_{2S}$ and $[+30/0_2/-30]_S$ laminates, respectively.

4.2 Material Properties

Nominal material properties for unidirectional AS4/3502 reported by the manufacturer and quoted in References [2,8] are: E_1 = 18.5 Msi, E_2 = 1.64 Msi, G_{12} = 0.87 Msi and ν_{12} = 0.30. These properties were used in the bulk of the analytical and numerical studies. Classical Lamination Theory predicts equivalent longitudinal moduli E_x of 7.423 and 13.33 Msi for the $[\pm 45/0/90]_S$ and $[+30/0_2/-30]_S$ laminates, respectively. The as-cured equivalent longitudinal moduli of these laminates in compression were measured using coupons 1.5 in. long by 0.75 in. wide cut from the Z-section stock used to fabricate the test stiffeners. A compression fixture designed by Professor Gurdal (ESM Dept., VPI&SU) was used for this testing. The stress-strain curves for the $[\pm 45/0/90]_S$ and $[+30/0_2/-30]_S$ laminates are contained in Figure 4-1. The initial moduli in compression were 7.0 and 12.9 Msi for the $[\pm 45/0/90]_S$ and $[+30/0_2/-30]_S$ laminates, respectively, which are within 6% of the predicted values. The tensile modulus for the $[\pm 45/0/90]_S$ laminate was also measured to be 8.4 Msi, which indicates a significant directional sensitivity of the response. The linear finite element eigenvalue predictions of the buckling stresses for the compression coupons were in excess of 70 ksi. The results in Figure 4-1 indicate that divergence occurred in the front and back strain gage readings at significantly lower stresses, which is indicative of the presence of initial imperfections in the compression coupons and/or misalignment of the specimens in the fixture.

The stress-strain properties of the aluminum-filled epoxy potting compound were also measured in compression and shear, using coupons cut from an actual specimen end pot. These properties were needed in support of analyses of the constraint of the end support on the test stiffeners. The compression behavior was obtained using coupons 1.5 in. long, 0.75 in. wide and 0.2 in. thick and the Gurdal compression fixture. The shear behavior was measured using Iosipescu specimens in a Wyoming Test Fixtures Inc. shear test fixture. The compression and shear stress-strain curves for the potting material are contained in Figure 4-2. The initial moduli in compression and shear were found to be

1.15 and 0.36 Msi, respectively. Yielding in compression occurred at approximately 2000 psi. Significant nonlinearity is evident in the figure in the subsequent plastic deformation in compression and in the entire shear stress-strain response.

4.3 Specimen Characterization

The section stock used in this work was of two vintages. The first consisted of the eight-ply quasi-isotropic stacking sequence and a web size of 1.25 in. This section stock was fabricated by Lockheed-Georgia in the early 1980s for the work of References 2 and 8. The second group of section stock was fabricated at NASA Langley in the early 1990s.

The earlier section stock exhibited significant imperfections in the corner regions. Representative photomicrographs of the cross-sections of the earlier material are illustrated in Figures 4-3 and 4-4, for corner radii of 0.125 and 0.25 in., respectively. In the case of the smaller corner radius, the source of the nonuniformity was generally excess resin on the outside diameter of the corners. It is presumed that corners exhibiting the thin uniform coating of resin were in contact with the forming tool during curing (Figure 4-3a, bottom). A localized ridge or bead of resin typically was present along the other corner (Figure 4-3a, top) and may be associated with a wrinkle or fold in the bleeder cloth. A corner of one specimen, 211s-1, exhibited a less innocuous source of thickness nonuniformity (Figure 4-3b, top). There, the inner +45° ply is thinned locally at the flange-to-corner junction. Specimens having the larger corner radius suffered from a local change in the shape of one corner due to kinking of one or more plies, in addition to the presence of a resin bead along the corner (Figure 4-4, top). A surface +45° ply in specimen 232s-2 is seen in Figure 4-4a to have migrated away from the outer surface of the corner. Figure 4-4b illustrates the distortion of the corner in specimen 222s-1. There, a ridge on the outside diameter of the corner is due to both a bead of excess resin and the outward migration of the ±45/0/90/90 ply group. The result of this ply migration is a pure resin pocket in the interior of the laminate. The corners opposite to which the ply migration occurred typically underwent a gradual thickness variation, with minimum thickness occurring at the center of the arc of the corner.

Thickness uniformity was greatly improved in the later section stock. Figure 4-5 contains the photomicrographs for specimens 111-2s-1 and 121orth-1. The thickness

control in the 16-ply quasi-isotropic specimen (111-2s-1) is generally good, with a slight nonuniformity occurring in one corner, as shown in Figure 4-5a. Specimen 121orth-1 (Figure 4-5b) exhibited slight thickness variations in the corners and some bowing of the web. Representative photomicrographs are shown in Figure 4-6 for 8-ply quasi-isotropic specimens 111s-1 and 212s-2, which have corner radii of 0.125 and 0.25 in., respectively. The thickness uniformity is very good in these specimens. The saw-tooth pattern visible along some of the corners is evidence of the surface texture formed by the resin and bleeder cloth. One corner of specimen 212s-2 (Figure 4-6b, top) exhibits the thin resin coating observed in all of the earlier sections.

4.4 Instrumentation

Back-to-back strain gage pairs were located along the stiffener cross-section at two axial locations corresponding to the numerically predicted positions of antinodes of the first two buckled mode shapes. Strain gage pairs were oriented both longitudinally and transversely to the load direction. The strain gage patterns used are indicated in Figure 4-7. The number of gages used ranged from 28 to 36 per specimen. The gage lengths of the strain gages used were 0.031, 0.062, 0.070 and 0.187 in. The smaller gages were used at the flange free edge and in the flange-to-web corners. Typical strain gage designations included Micro-Measurements CEA-06-062UW-350 and CEA-06-187UW-350. The strain gages aided in the determination of the buckling load and also the resulting redistribution of load in the postbuckled regime. The strain gages also provided insight into the severity of the in-plane stress state when crippling occurred. The back-to-back combination of the gages permitted examination of the membrane and bending components of the strains.

Direct Current Displacement Transducers (DCDTs) were used to measure the end shortening and the out-of-plane displacements, typically of the flanges. DCDTs were placed at 3 or 4 axial locations near the free ends of both flanges. The DCDTs aided in the determination of the initial buckled mode shape as well as the changes in mode shape in the postbuckling regime. Use of the DCDTs at the ends of both flanges at the same axial position also permitted the identification of any twisting of the stiffener due to the bending-twisting coupling inherent in the laminates used.

The face of one flange was also monitored using the shadow moire optical technique. A lined grating (50 lines/inch) on glass was placed in front of the flange, which was painted white. Illumination of the specimen and grating with a bright light source projected a shadow of the grating onto the white flange. Fringe patterns were produced as a result of optical interference between the actual grating and its shadow on the specimen when out-of-plane displacements occurred. The shadow moire provided a distinct, visual indication of when buckling occurred and also the resulting mode shape. Distortion of this fringe pattern also indicated the presence of twisting of the stiffener.

Photographs of the experimental set-up illustrating the various types of instrumentation are contained in Figure 4-8. The specimen is labelled by "1". Side and front views of the moire grating (labelled as "2") are shown in Figures 4-8a and 4-8b, respectively. The front view indicates a buckled mode shape consisting of three half-waves, with the locations of maximum amplitude (antinodes) occurring at the centers of the concentric arcs formed by the fringes. An appreciation for the magnitude of the out-of-plane displacements can be obtained from the side view of a flange in Figure 4-8a. The DCDTs measuring out-of-plane displacements and end shortening are denoted by the points labelled "3" and "5", respectively. The upper platen of the loading machine is labelled as "4". The top and bottom potted end supports are denoted by "6". The tests were recorded using a video recorder and still photography. Photographs of the failed specimens under residual load were also taken.

4.5 Loading and Data Acquisition

The specimens were loaded between the platens of a 120,000-lb-capacity Baldwin testing machine at NASA Langley Research Center. Loading rate was manually controlled at a nominal rate of approximately 25% of the predicted buckling load per minute. Loading rate was reduced approximately by one-half after buckling occurred. All data channels were recorded at the rate of once every two seconds using a MODCOMP Model 80211/NEFF Sytem 620 data acquisition system. The data were downloaded from the data acquisition system onto personal computers for evaluation.

CHAPTER 5. EXPERIMENTAL RESULTS

5.1 Initial Local Buckling Response

5.1.1 Buckling Load Determination

The strain gages and Direct Current Displacement Transducers produced quantitative information which was used to determine the buckling loads. The methodologies used in determining the buckling loads are discussed in this section.

As discussed in Chapter 4, strain gages were placed in back-to-back pairs at many locations on each specimen. An axial cross-sectional view of a typical strain gage pair is shown schematically in Figure 5-1. The state of strain at a gage pair location can be separated into membrane and bending components as shown in the figure. The membrane strain is defined as the average of the two strain readings of the pair, while the bending strain is defined as the difference of either strain gage reading from the membrane strain level. The strain at a gage location is then equivalent to the membrane strain plus or minus the bending strain. A perfectly flat plate loaded in uniform compression along one pair of edges would exhibit a nearly uniform state of membrane strain prior to buckling. The occurrence of out-of-plane deflections as a result of buckling is accompanied by bending strains. The appearance of bending strain could then be used to determine the onset of buckling. A real plate, however, will exhibit a certain degree of lack of flatness largely due to the fabrication processes. These initial imperfections introduce local eccentricities in the load path which must be accompanied by bending moments for equilibrium. The result is the presence of some degree of bending strain as soon as the plate is loaded. Once buckling occurs, the bending strains will develop at a faster rate. Thus, the change in the shape of the load-bending strain response curves can be used to obtain the buckling load of a real plate. The load-bending strain behavior for perfect and imperfect plates is shown schematically in Figure 5-2. The buckling load of a perfect plate is clearly defined by the sudden appearance of bending strain. Some ambiguity in the precise determination of the buckling load of the imperfect plate results from the smooth transition of the pre- and postbuckling portions of the load-strain behavior.

Use of the bending strains to determine the buckling loads of the Z-section stiffeners in this work will be illustrated using the data from specimens 111-2s-1, 111s-1 and 111orth-1. The geometry consists of b_w = 1.75 in., b_f = 1.25 in., r = 0.125 in. and L = 10 in. The stacking sequences are $[\pm 45/0/90]_{2s}$, $[\pm 45/0/90]_s$ and $[+30/0_2/-30]_s$, respectively. These specimens are chosen for illustration because the load-strain behavior covers the range of imperfection sensitivities observed. The maximum longitudinal and transverse bending strains recorded for these specimens as a function of load are contained in Figure 5-3. All of the specimens exhibit nonzero bending strains immediately upon loading. Tangent lines have been constructed along the prebuckling and initial postbuckling portions of the curves. The intersection of these lines is taken to be the buckling load, as determined from the strain gage data.

The relative magnitudes of the longitudinal and transverse bending strains are significantly different between the specimens. For the $[\pm 45/0/90]_{2s}$ laminate, the transverse bending strain is less than the longitudinal bending strain prior to buckling. After buckling, the magnitudes are the same (Figure 5-3a). The transverse bending strain in the $[+30/0_2/-30]_s$ laminate develops at a much faster rate than the longitudinal strain (Figure 5-3c). The behavior of specimen 111s-1 is between these two extremes (Figure 5-3b). A more convenient comparison of the load-bending strain responses of these specimens can be made using Figure 5-4, which consists of separate plots for the longitudinal and transverse strains as functions of the load normalized by the buckling loads (calculated from the longitudinal bending strains as discussed below). The transverse bending strain is seen to increase more rapidly in the case of the $[+30/0_2/-30]_s$ laminate (Figure 5-4b), whereas the development of longitudinal strain prior to buckling is quite similar between the three specimens (Figure 5-4a). The direction of the load path and the relative magnitudes of the bending stiffnesses in the two directions will be used to explain the observed behavior. While the load path is predominantly longitudinal in nature prior to buckling, bending strains due to the initial imperfections will develop in both the longitudinal and transverse directions. The longitudinal bending strain naturally results from the moment produced by the local eccentricity of the load. The transverse bending strain results from the elastic restraint imposed by the material to either side of the location of load eccentricity. This restraint prevents the bending from occurring in a purely cylindrical fashion about an axis parallel to the transverse direction (which would result in

no transverse bending). Which of these two bending strains is larger is dependent on the relative bending stiffnesses in the two directions. The ratios of the transverse to longitudinal bending stiffnesses (D_{22}/D_{11}) are 0.85, 0.79 and 0.17 for the $[\pm 45/0/90]_{2s}$, $[\pm 45/0/90]_s$ and $[+30/0_2/-30]_s$ laminates, respectively. In the case of the first two laminates, the relative transverse bending stiffnesses are high enough such that less curvature (and, therefore, bending) occurs in the transverse direction compared to the longitudinal direction. The very low transverse bending stiffness of the $[+30/0_2/-30]_s$ laminate results in significantly higher transverse bending strains. This laminate is much stiffer in the longitudinal direction, with the result that less curvature develops in this direction. The load-transverse bending strain behavior for the $[+30/0_2/-30]_s$ laminate did not exhibit as clear a transition corresponding to buckling, as did the longitudinal strains, as shown in Figure 5-3. In addition, the strain gage data from several of the $[+30/0_2/-30]_s$ specimens indicated the presence of bending prior to buckling due to a lack of parallelism between the two surfaces of the specimens in contact with the load frame. This will be further discussed in Section 6.2. These bending strains would be particularly noticeable in the transverse direction where the bending stiffness is much lower. The figure also illustrates that a significantly lower buckling load would be calculated from the transverse strains, which will be shown later to be inconsistent with other measures of the buckling load. For these reasons, the longitudinal bending strains were used to determine the buckling loads calculated from the strain gage data. Finally, it should be noted that the above observations concerning the responses of the specimens 111-2s-1, 111s-1 and 111orth-1 are typical of the other specimens of the respective stacking sequences.

The Direct Current Displacement Transducers (DCDTs) provided measurements of the end shortening and the out-of-plane displacements, both of which can be used to determine buckling loads. Use of the end shortening will be discussed first. The axial stiffness of a plate is reduced by approximately 50% as a result of buckling. This change in the slope of the load, P - end shortening, u behavior can then be used to determine the onset of buckling. The change in slope can be more easily seen using a stiffness plotting technique following the work of Reference 3, in which P/u is plotted against the load. The uniaxial stress-strain law $\sigma = E^*\varepsilon$ can be rewritten for stiffener compression prior to buckling as:

$$\frac{P}{A} = E * \frac{u}{L} \text{ or } \frac{P}{u} = \frac{AE}{L}, \tag{5.1}$$

where A, E and L are the cross-sectional area, longitudinal modulus of elasticity and length, respectively. The latter expression in equation 5.1 indicates that P/u is constant for linear elastic behavior. The reduction in axial stiffness that accompanies buckling can be viewed as a reduction in the effective modulus of elasticity. Therefore, P/u should be nearly constant prior to buckling, but will decrease sharply as a result of buckling. The superiority of the stiffness plotting technique versus a simple load-end shortening plot for buckling load determination is illustrated in Figure 5-5. Both P/u and u alone are plotted against the load for specimen 111-2s-1. The bifurcation is much more clearly defined using the stiffness plotting technique. The data for specimens 111-2s-1, 111s-1 and 111orth-1 are plotted in Figure 5-6 using this technique. The ordinate has been changed to PL/AEu, which should have unit value (per equation 5.1) prior to buckling. The fact that non-unit values were observed will be discussed in Section 6.2. The load axis has been scaled by factors of 8 and 12 for specimens 111s-1 and 111orth-1, respectively, to permit presentation of the data on a single plot. The buckling load of specimen 111-2s-1 is easily defined by the sharp "knee" in the curve. Tangent lines constructed along the prebuckling and initial postbuckling portions of the responses are necessary for the other two specimens due to the oscillations of the P/u values and the less sharply defined transition between the response regimes. The stiffness plotting technique provides a reliable and repeatable method of buckling load determination. The method has been observed in this work to be less affected by local imperfections in the structure, since global response quantities are used.

The out-of-plane deflection,w, as measured by the DCDTs was also used to determine the buckling loads. The methodology for load determination and the role of initial imperfections when using the deflections are analogous to those discussed above in conjunction with the use of the bending strains. In Reference 3, the square of the out-of-plane deflection,w^2, was used for buckling load determination, as opposed to w itself. Use of w^2 is consistent with the quadratic dependence of the out-of-plane deflection on the load predicted from models of the initial postbuckling response of plates (e.g. Ref. 35, p. 241). A plot of the load versus both w/t and $(w/t)^2$ is contained in Figure 5-7 for specimens 111-2s-1 and 111orth-1. The data for specimen 111-2s-1 show that little

difference in the estimated buckling load results from using w or w^2. Use of w^2 essentially idealizes the response by minimizing the relative magnitude of the out-of-plane deflection which occurs prior to buckling. Specimen 111orth-1 did not exhibit a sharp change in the P-w response upon the initiation of buckling, in contrast to specimen 111-2s-1. The P-w^2 behavior does exhibit a more clearly defined buckling load. Furthermore, the buckling load of specimen 111orth-1 estimated from the P-w response is 24% below that determined from the stiffness plotting technique, which has proven to be the more consistent and reliable method. For these reasons, the buckling load estimations based on the out-of-plane deflections were made using the P-w^2 response. The results for specimens 111-2s-1, 111s-1 and 111orth-1 are contained in Figure 5-8. The load axis has been scaled by factors of 6 and 12 for specimens 111s-1 and 111orth-1, respectively, to permit presentation of the data on a single plot. The results indicate that the bifurcation is more clearly defined as the buckling load is increased, as was observed when using the stiffness plotting technique.

The buckling loads for all of the specimens in the experimental program have been calculated using the three methods discussed above. The results are summarized in Table 5-1. The table also contains the average value from the three methods and an estimate of the variation between the loads calculated using the three methods. This variation is defined as the range of the values for a given specimen predicted using the three methods, normalized by the average value. The variances range from 0.7 to 14.3%, with an overall average of 4.7%. The highest variations occurred among the specimens of the $[+30/0_2/-30]_S$ stacking sequence. While the number of experiments performed is insufficient for any rigorous statistical treatment, the trend observed is that the variance among the buckling load predictions is decreased for the specimens having higher buckling loads. This trend is consistent with the observation noted above that the distinction between the pre- and postbuckling responses became more well defined as the buckling load increased.

5.1.2 Effects of the Parameters on the Buckling Loads

The buckling data for all of the experiments are summarized in Figure 5-9, in which the buckling stress (P/A) is plotted against the nominal flange-to-web width ratio (b_f/b_w). The stresses are based on the average buckling loads of Table 5-1. Within a specimen family (i.e. a specific web size, corner radius and stacking sequence), the buckling stress is seen to increase as the flange size is reduced. This observation indicates that the specimens

having at least the three largest flange sizes were flange critical. The flanges in these specimens were too wide to stiffen the web without themselves limiting the buckling resistance of the stiffener. The figure indicates that stiffeners with flanges only half the width of the web are still flange critical. This occurs because the flange is elastically restrained along only one longitudinal edge, while the web is restrained along both edges.

The data in Figure 5-9 also indicate that the highest buckling stresses are associated with the thickest laminate (family 1_1-2s) and the most narrow web (family 3_1s). The specimens of the thicker laminate naturally have the highest intrinsic bending stiffnesses (i.e. D_{ij} i,j = 1,2,6), while the narrower web results in greater geometric stiffness due to a lower span (b_w) -to- thickness (t) ratio.

Specimens having the larger corner radius (family 2_2s) buckle at loads up to 18% higher than equivalent sections having the smaller radius (family 2_1s). This dependence can be rationalized in terms of the effect of curvature on bending stiffness and the relative area of the corner regions. The curvature in the corners increases the resistance to bending, particularly in the longitudinal direction, due to the geometric coupling of membrane action to the bending response. The relative fraction of this corner material which is more resistant to buckling increases as the corner radius is increased. Increasing the corner radius also decreases the effective widths of the flanges and web, with the result that these elements are more resistant to buckling as well. It is recognized that the effectiveness of the curvature in increasing the bending stiffness varies inversely with the corner radius. However, the results indicate that the area and width effects discussed above were dominant, at least over the range of corner radii considered in this work.

Finally, the effect of the stacking sequence on the buckling stresses of the 8-ply specimens can be considered through comparisons of the responses between families 1_1s and 1_1orth. The families consist of specimens of identical geometry, with the only difference being the stacking sequence. The data of Figure 5-9 indicate that the buckling stresses of the specimens of family 1_1orth were below those of family 1_1s by approximately 30%. The significance of the relative bending stiffnesses on the development of bending strains in the longitudinal and transverse directions was introduced in Section 5.1.1. Consideration of the differences in the bending stiffnesses between the

two laminates can be used to explain the observed behavior. The ratios of the bending stiffnesses are:

$$\frac{D_{11}\ (1\_1s)}{D_{11}\ (1\_1orth)} = 0.52, \qquad \frac{D_{22}\ (1\_1s)}{D_{22}\ (1\_1orth)} = 2.4 \tag{5.2}$$

The bending stiffnesses have been calculated using Classical Lamination Theory and the ply properties identified in Section 4.2. It is apparent from relation 5.2 that while the longitudinal bending stiffness of the $[+30/0_2/-30]_S$ laminate (family 1_1orth) is almost twice that of the $[\pm 45/0/90]_S$ laminate (family 1_1s), this is overshadowed by the reduced transverse bending stiffness, which is approximately one-quarter of that of the $[\pm 45/0/90]_S$ laminate. The observed behavior simply reflects the fact that the local buckling response is not one-dimensional, in spite of the uniaxial loading.

5.2 Postbuckling Response

5.2.1 Load-End Shortening

The load-end shortening responses of all the specimens throughout the load range are contained in Figures 5-10 through 5-15. The loads are normalized with respect to the cross-sectional area, A, and the equivalent longitudinal modulus, E. The end shortenings are normalized with respect to the gage length, L. Each plot contains the results for a specific specimen family, i.e. for specimens of a certain web width, corner radius and stacking sequence. The results for specimen family 1_1s (Figure 5-10a) illustrate the dependence of the response on the flange size. For the largest flange width (specimen type 111s), buckling occurs at the lowest average strain (and load), but is followed by the most extensive postbuckling load range. Conversely, for the case of the smallest flange (specimen type 141s), the higher bucking strain is accompanied by the smallest postbuckling response regime. In general, the end shortening at failure decreases with the flange width. The overall shape of the nonlinear load-displacement behavior is generally consistent between replicate specimens. However, significant differences in the maximum end shortening attained prior to failure do exist between replicate specimens; compare for example the solid and dashed curves for specimen types 111s or 121s in Figure 5-10a.

The effect of laminate thickness is illustrated by the responses of specimen family 1_1-2s (Figure 5-10b). The stacking sequences of families 1_1s and 1_1-2s are 8- and 16-ply quasi-isotropic, respectively. Apart from the thickness difference, the geometries are the same. The average strain at buckling (u/L or P/AE) for specimens having the largest flanges were approximately 0.1% and 0.3% for the 8- and 16-ply cases, respectively. For the smallest flange width common to both families (0.75 in.), the average buckling strains were approximately 0.2% and 0.7% for the 8- and 16-ply cases, respectively. The same inverse relationship between the buckling load and the range of the postbuckling response is observed with differences in laminate thickness, as was discussed above for varying flange widths. In fact, the combined effects of narrow flange width and increased laminate thickness in specimen type 131-2s results in failure occurring immediately after buckling. Note also from Figure 5-10b the markedly reduced normalized prebuckling stiffness of specimen type 131-2s, compared to the other specimens of the family.

The effect of stacking sequence can be illustrated through comparisons of the results contained in Figures 5-10a and 5-11, which contain the results for specimen families 1_1s and 1_1orth, respectively. The stacking sequences for these families are $[\pm 45/0/90]_S$ and $[+30/0_2/-30]_S$, respectively. The geometries are identical. It is immediately apparent that the average strains at buckling are much lower for the latter case. Buckling strains range from 0.03% to 0.09% among specimens of the $[+30/0_2/-30]_S$ stacking sequence, compared to 0.08% to 0.2% for the quasi-isotropic laminate. The end shortening at failure increases as the flange width is reduced in family 1_1orth, in contrast to the opposite relationship observed for family 1_1s. The differing responses for specimens of the three laminates are summarized in Figure 5-12. Selected specimens representing each geometrical configuration and stacking sequence are contained in the figure. The responses are seen to be grouped by stacking sequence. Prebuckling strains decrease as a function of stacking sequence in the following order: $[\pm 45/0/90]_{2S}$, $[\pm 45/0/90]_S$, $[+30/0_2/-30]_S$.

The responses of the specimen families having the corner radius as the only distinguishing feature between them are contained in Figure 5-13a for specimens 2_1s and Figure 5-13b for specimens 2_2s. The same dependence of the response on flange width is observed within each specimen group. As discussed in Section 5.1.2, the effect of the larger corner radius is to increase the buckling load. This increase in load for the case of

the larger corner radius is maintained throughout the postbuckling regime as well. This is more readily apparent from Figure 5-14, which contains the responses for selected specimens representing each geometry. The responses for specimens having the larger and smaller corner radii are identified by the solid and dashed curves, respectively. The numbers on the curves identify the four different nominal flange sizes. It is apparent from the figure that the responses of specimens 212s-2 and 221s-2 are nearly the same. The former specimen is comprised of both a larger flange size (1.25 in. versus 1.00 in.) and corner radius (0.25 in versus 0.125 in.) compared to the latter. The significance of the result is that these flange and corner radius dimensions exactly offset the effect of each other on the load-end shortening response; the larger flange size tends to decrease the load, while the larger corner radius increases the load.

Finally, the load-end shortening responses for the specimens having the smallest web width are provided in Figure 5-15. The buckling and crippling events essentially coincide for specimens 341s, as they did for specimens 131-2s, even though the former specimens are based on the 8-ply quasi-isotropic stacking sequence. The latter specimens were fabricated form the 16-ply quasi-isotropic laminate and also had much greater in-plane dimensions (b_w = 1.75 in. versus 0.75 in., b_f = 0.75 in. versus 0.50 in.). The results for the two specimen types simply illustrates that it is the width-to-thickness ratio (b/t) that determines where buckling occurs in the load carrying range of the stiffener relative to a material limit or crippling load. The ranking of the load-end shortening responses as a function of the width-to-thickness ratio is illustrated in Figure 5-16. Since a stiffener may have different b/t ratios in the flange and web, a more general width parameter is desirable. Accordingly, the results in the figure are ranked according to the developed width-to-thickness ratio (s/t). The developed width is the summation of the mid-plane arc-lengths of the flanges, corners and web. The developed width-to-thickness ratio is equivalent to A/t^2. The results in the figure are from quasi-isotropic specimens which represent the various web, flange and thickness dimensions. Stiffeners which are thin and/or comprised of wide elements undergo buckling at low strains, but enjoy an extensive postbuckling response regime (curve 1 of Figure 5-16). The partitioning between the pre- and postbuckling response regimes shifts systematically with s/t, such that for a sufficiently thick and/or narrow specimen, buckling is delayed at the expense of nearly all of the postbuckling capability (curve 12 of Figure 5-16).

5.2.2 Strain Redistribution

Local buckling results in a redistribution of load over the width of the stiffener due to the effect of the bucking displacements on axial stiffness. The mechanics of this load redistribution can be reviewed using the example of a plate under uniaxial compressive loading and simply-supported on the edges. The bending displacements are greatest in the center of the plate. The onset of bending reduces the axial stiffness, compared to the prebuckling membrane loading configuration. The out-of-plane displacements are prevented at the edges of the plate by the boundary conditions. Therefore, the axial stiffness is not reduced at the edges. The result is that additional load beyond buckling will tend to concentrate into the edge regions. The center of the plate does not carry much additional load, and hence the "effective" width of the plate is reduced. The same scenario applies to a Z-section stiffener, with the modification that several plate elements are involved. The central web is analogous to the plate discussed above, except that a condition of elastic restraint exists along the edges. The flanges are analogous to one-edge-free plates. In the case of the flanges, buckling displacements will be greatest at the free edges, with the greatest loss of axial stiffness occurring there.

The redistribution of load across the width of the stiffener is reflected by the strain variations across the width. The experimental strain distributions across the stiffener width as a function of load are illustrated in Figure 5-17 for specimen 131s-1. The geometry consists of $b_w = 1.75$, $b_f = 0.75$ and $r = 0.125$ in. The stacking sequence is $[\pm 45/0/90]_S$. The membrane and bending strain distributions are contained in Figures 5-17a and 5-17b, respectively. The axial location of the strain gages which supplied the data corresponds to a peak in the buckled mode shape. The strain data indicate that an approximately uniform, membrane loading condition existed for loads up to 1500 lb. This is evidenced by the lack of any bending strain or variation in the membrane strain levels across the specimen width. Both bending strain and width-wise variations in the membrane strain are discernable at the next load step of 1850 lb. Note from Table 5-1 that the average buckling load for this specimen is 1794 lb. Once buckling occurs, it is apparent from Figure 5-17a that no additional in-plane load is carried at the free ends of the flanges nor at the center of the web. The strain values at these locations remain at or fall slightly below the values present at the onset of buckling. The membrane strain clearly concentrates into the corner regions.

Bending strain develops upon the initiation of buckling, as indicated in Figure 5-17b. The locations of maximum bending are at the free ends of the flanges and the center of the web.

The parametric dependence of the strain redistribution will be illustrated using Figure 5-18. The ordinate is the membrane strain minus the value measured when buckling first began. Thus, the ordinate is a measure of the additional strain at a point since buckling initiated. It is desired to investigate the rate of strain redistribution as a function of the geometric parameters. Since the buckling loads vary enormously between the various geometries, the loads at which the comparisons are made correspond to 0.3% average strain, u/L, beyond the value at buckling. Therefore, the comparisons are made at a constant normalized "distance" down the postbuckling path. The nature of the strain redistribution depends on the flange-to-web width ratio (b_f/b_w) and the laminate thickness, as discussed in the following. Experimental data are provided for specimen types 211s, 111s, 111-2s and 131s. The stacking sequences are either 8- or 16-ply quasi-isotropic. The b_f/b_w ratio for specimen type 211s is unity. The results indicate that the ends of the flanges do not carry any additional load after buckling; in fact the strain is reduced by 0.001 to 0.002 (solid curve, Figure 5-18). The normalized strain level at the corners is 0.003; that is, the local, axial membrane strain has increased by 0.003 since buckling, which is the same increase as in the average axial strain, u/L. This means that the corners have remained approximately straight and are continuing to carry load in the membrane mode. The specimen type 211s is very flange critical, since the flange (with one side supported) is the same width as the web (with both sides supported). The result is that the out-of-plane displacements, and hence the loss of axial stiffness, are much greater at the flange ends than in the center of the web. The data indicate that the web center continues to carry additional load after buckling. The strain increase at the web center is 2/3 of the overall strain increase since buckling began. At the other extreme of the b_f/b_w ratio is specimen type 131s ($b_f/b_w = 0.43$). The data indicate that the flange ends of this specimen have also been unloaded by 0.001 strain, compared to the strain value at buckling. The strain concentration into the corners is slightly more pronounced, compared to the previous case where $b_f/b_w = 1$. The most striking difference, however, is in the response of the web. This specimen type is much less flange critical. As a result of the additional bending at the web center, unloading occurs there to the same extent as at the flange ends. In between these two extremes of the b_f/b_w ratio are two specimen types with a b_f/b_w ratio of 0.71. These specimen types are 111s (8-ply) and 111-2s (16-ply). The ends of the flanges of

both specimens unload after buckling by a strain magnitude of 0.001, as in the other cases discussed above. The amount of additional load carried at the center of the web is intermediate to that observed for the specimens of the two extreme b_f/b_w values. In the 8-ply quasi-isotropic case, the strain at the center of the web remains at the bucking strain level. The greater bending stiffness of the 16-ply quasi-isotropic laminate resists the out-of-plane deflections of the web more effectively, with the result that the stiffness reduction is less, compared to the 8-ply laminate. The strain at the center of the thicker web increases by 0.001 with the 0.003 average strain increase since buckling, compared to the unchanged value measured for the 8-ply case.

5.2.3 Postbuckled Mode Shape

Photographs of the shadow moire fringe patterns provide a means for examining the development of the mode shape during the postbuckling response regime. A series of fringe patterns is provided for specimens 111-2s-2, 111s-2 and 111orth-1 in Figures 5-19, 5-20 and 5-21, respectively. These specimens have a web width of 1.75 in., flange width of 1.25 in. and corner radius of 0.125 in. The onset of initial buckling of the 16-ply quasi-isotropic specimen is indicated by the development of the contour lines shown in Figure 5-19a. As the load increased into the postbuckling range (Figures 5-19b to 5-19f), the density of the contour lines increased, indicating increasing displacement magnitudes, but no changes in the overall mode shape (i.e. the number of half-waves) were observed. Failure of the specimen occurred at a nodal position, as indicated by Figures 5-19f and 5-19g. Discussion of the failure locations and modes will be given in Section 5.3.2. Each set of contour lines in the figure is composed of nearly concentric arcs, which are symmetrical with respect to a horizontal reference line placed at the location of maximum out-of-plane displacement. This symmetry is indicative of the absence of twisting deformation.

Fringe patterns for the 8-ply quasi-isotropic specimen are shown in Figure 5-20. The pattern of Figure 5-20a corresponds to a load of 1090 lb, and shows that the specimen has begun to buckle. This specimen exhibited a very extensive postbuckling load carrying capability, failing at 3944 lb. While not all of the front flange was covered by the moire grating, the initial buckled configuration appears to have been composed of three half-waves. At 3010 lb (Figure 5-20d), the mode number has increased to at least four, with

the presence of twisting of the section indicated at the bottom. With still higher loads, out-of-plane deflection becomes concentrated in the half-wave located at the middle of the section. By 3940 lb (Figure 5-20d), the specimen becomes severely distorted, with failure occurring shortly after at a nodal position (Figure 5-20g). Note for this specimen that the sets of fringe patterns near the middle of the gage length tend to be fairly symmetrical, while those near the base indicate the presence of twisting.

Fringe patterns for the $[+30/0_2/-30]_s$ specimen are shown in Figure 5-21. The photograph taken at 760 lb (Figure 5-21a) indicates that the specimen has already buckled. It is readily apparent from the figure that the wavelength of the mode shape is much longer for this specimen, with only two half-waves appearing along the gage length. This results from the much higher longitudinal bending stiffness of this laminate (D_{11} = 76.6 in. lb) compared to the 8-ply quasi-isotropic case (D_{11} = 39.9 in. lb). It is also immediately apparent at the next load step (Figure 5-21b) that significant twisting of the section is indicated by the loss of symmetry in the contour lines. Large bending curvatures develop at the flange-to-corner junction at the mid-height location, as shown in Figure 5-21e for a load of 2490 lb. Failure of the specimen develops at this axial location, as indicated in Figure 5-21f.

5.3 Crippling Response

5.3.1 Crippling Loads

The crippling load, stress and maximum end shortening data are summarized in Table 5-2 for all of the experimental specimens. Failure stresses range from 16 to 56 ksi. The range of average axial strains, u/L, at failure is 0.4% to 1.1%. The crippling (and buckling) stress data are plotted in Figure 5-22 as a function of a normalized width of the specimens. This normalized width, s/t, is defined as the sum of the width dimensions of the various flange, web and corner portions of the stiffener, normalized by the laminate thickness. The response of wide and thin specimens (high s/t) is characterized by buckling at a relatively low stress, followed by an extensive postbuckling load range. As the width of the stiffener decreases and/or the thickness increases (i.e. s/t decreases), the buckling stress increases. The crippling stress also increases, but the postbuckling load range decreases. That is, the partition between the pre- and postbuckling responses moves up the

stress scale. As the ratio s/t decreases, bending stiffnesses increase in either the absolute or relative sense. The absolute or intrinsic bending stiffnesses increase with the thickness cubed, and are laminate properties which are independent of the in-plane configuration. The relative or geometrical bending stiffness is related to the "unsupported span" associated with the in-plane dimensions in a structural sense. The data indicate that the buckling stresses increase for both types of stiffness increases. Finally, the buckling and crippling curves converge with decreasing s/t to a data point from Reference 2 in which the buckling and crippling events occurred simultaneously. The geometrical configuration was such that buckling was delayed until the load at which a competing mode (short-column compression failure) became active.

5.3.2 Post-Failure Examination

Photographs of the failed specimens under residual load were taken to aid in the determination of the failure mechanisms. It should be noted at the outset of this discussion, that post-failure appearances must be interpreted with caution since features related to secondary failure mechanisms will likely be present, in addition to those introduced by the primary cause of failure. Representative post-failure photographs are provided in Figures 5-23 to 5-29. Detailed discussion of the failure mechanisms will be deferred to Section 6.7, where use will be made of the results of the numerical analyses.

The most prevalent post-failure feature of the 16-ply quasi-isotropic specimens is delamination at the free ends of the flanges. For some specimens, this delamination was the only visible damage after failure. The failure location in specimen 111-2s-2 corresponded to a nodal position, as indicated in Figures 5-19f and 5-19g. The post-failure appearance of this specimen is contained in Figure 5-23a, in which significant delamination at the free end of the flange is indicated. This delamination occurred at the 0/90 ply interfaces and propagated a distance of approximately one-third of the gage length. Flange free-edge delamination with relatively little other laminate damage was typically observed in the 16-ply quasi-isotropic specimens with the larger flange widths. The post-failure appearance of specimen 121-2s-1 is shown in Figures 5-23b and 5-23c. The flange width of this specimen is 1.0 in. The failure location in this specimen corresponded to an anti-nodal position. The free end of one flange exhibits the delamination mode (Figure 5-23c), while a more localized material crushing mode is demonstrated in the other (Figure 5-23b).

The horizontal cracking of the web on the more compressive side of the wave (Figure 5-23c) likely resulted from the overloading caused by the failure of the flanges. Post-failure appearances of a replicate specimen (121-2s-3) are contained in Figures 5-24 and 5-25. This specimen underwent failure at two axial positions, both corresponding to anti-nodes in the buckled mode shape, as indicated in Figures 5-24a and 5-25a. The flange on side "2" of the specimen in Figure 5-24b failed on the more tensile side of the wave crests, with the outer plies debonding and breaking away. The opposite flange (side "2" in Figure 5-25b) exhibits the familiar delamination at the upper location and an unusual unidirectional laminate splitting at the lower location. This splitting is characterized by a horizontal crack through half of the laminate on the more tensile side of the wave crest, which turns at the mid-plane and runs down along the mid-plane. Horizontal splitting of the web due to the overload caused by flange failure is again observed (near the upper failure location in Figure 5-24b and at the lower failure location in Figure 5-25b). A final specimen of the 16-ply quasi-isotropic stacking sequence (131-2s-2) is illustrated in Figure 5-26. The flange width is 0.75 in. The failure location corresponds to a nodal position in the buckled mode shape. This specimen exhibits both flange-free-edge delamination (side "2" of Figure 5-26a,b) and crushing in the flange-to-web corner (side "1" of Figure 5-26a,b). The average stress level at crippling was seen in Section 5.3.1 to increase with decreasing flange width. Therefore, the strain energy at failure is greater in the specimens of smaller flanges, as evidenced by the more pervasive laminate damage observed.

The post-failure appearance of the 8-ply quasi-isotropic specimens is characterized by the presence of both flange free edge delamination and crushing in the flange-to-web corners. Typical post-failure appearances of the 8-ply quasi-isotropic specimens are contained in Figures 5-27 and 5-28. The failure location of specimen 111s-2 (Figure 5-27) corresponded to a nodal location, as indicated in Figures 5-20f,g. The flange width is 1.25 in. The specimen underwent delamination at the free ends of the flanges, extending over a third of the gage length (e.g. side "2", Figure 5-27a,b). Crushing of the flange-to-web corner is also apparent near side "1" of Figure 5-27b. The appearance of specimen 121s-1, with a flange width of 1 in., is contained in Figure 5-28. The failure location was near a nodal position in the mode shape. The classical free edge delamination at the 0/90 interfaces is clearly shown along side "2" of Figure 5-27a. Significant crushing of the corner opposite to this flange is apparent near side "1" of Figure 5-27b.

Post-failure features of the $[+30/0_2/-30]_S$ specimens are illustrated in Figure 5-28. The most prevalent feature in specimens of this stacking sequence is non-crushing type damage in the flange-to-web corners. This corner damage is characterized by surface splitting and cracking. Notably absent in the specimens with the larger flange widths is any flange free edge delamination. The flanges and web of these specimens are characterized by "creasing" near the corners along a line perpendicular to the surface ply fiber orientation, as shown in Figures 5-28a,b. This creasing is associated with corner damage of the type shown in Figures 5-28c,d. The surface ply splitting at the corner shown in Figures 5-28b,c is associated with the high bending curvatures seen in the moire fringe patterns at the corners (see Figure 5-21e,f). The vertical cracking at the flange-to-corner junction is a reflection of the weak transverse strength of this laminate due to the absence of any 90° plies. Flange free edge delamination was only seen in the specimens of the smaller flange widths (0.75, 0.5 in.).

CHAPTER 6. DISCUSSION OF RESULTS

6.1 Initial Local Buckling

6.1.1 Analytical and Finite Element Buckling Load Predictions

The analytical model used for the buckling predictions was discussed in Section 3.1.1, with a complete derivation given in the Appendix. Recall that the model does not include the actual curved flange-to-web corner, nor the effect of the bending-twisting coupling stiffnesses D_{i6} (i=1,2). These limitations were removed in the finite element analyses. The buckling loads were predicted numerically using both the linear eigenvalue finite element analysis method discussed in Section 3.1.2 and the nonlinear analyses of the imperfect structure discussed in Section 3.2.

6.1.2 Effect of the Assumed Initial Imperfection

The initial imperfection in the finite element models of the stiffeners had the same effect of smoothing the transition between the pre- and postbuckling responses as was observed experimentally. Accordingly, the methods discussed in Section 5.1.1 for determining the experimental buckling loads were again used to find the buckling loads predicted from the nonlinear analyses. Recall from Section 5.1.1 that the bending strain, end shortening and out-of-plane deflection were used to estimate the experimental buckling loads. In the displacement-based finite element formulation used in this work, the solution vector consists of generalized displacements, both translations and rotations. The strain components are then derived from the gradients of the solution vector. As a result, the strains predicted from the finite element analyses are clearly not an independent response quantity which could be used to obtain an independent measure of the buckling load. Accordingly, only the out-of-plane deflections and the end shortening were used to predict the buckling loads from the numerical analyses.

The response of the finite element models was strongly influenced by the magnitude of the assumed initial imperfection. A comparison of the responses for initial imperfections

of 1%, 5% and 10% of the 8-ply laminate thickness of 0.04 in. is provided in Figure 6-1. The out-of-plane deflection (normalized by the thickness) and the stiffness (P/u) responses are given in Figure 6-1a as functions of load for stiffener type 131s, which consists of b_w = 1.75 in., b_f = 0.75 in., r = 0.125 in., L = 6 in. and the $[\pm 45/0/90]_S$ stacking sequence. Note that the prebuckling stiffnesses have been normalized to unit value prior to buckling. The actual differences in prebuckling stiffnesses will be discussed in Section 6.2. The responses of the finite element models are compared to the experimental results for specimen 131s-1. The finite element results shown in the figure illustrate that the transition between the pre- and postbuckling responses becomes less distinct as the magnitude of the imperfection increases. Naturally, different buckling loads would be calculated from these results for the different cases as well. The highest buckling load would be predicted in the case of the lowest value of the initial imperfection, as expected. The experimental data lie in between the predicted responses for the 1% and 5% imperfection cases and, therefore, suggest that the magnitude of the imperfection actually in the specimen is between 1 and 5% of the laminate thickness. This conclusion is supported by the results from the other 8-ply specimens as well. A second example is provided in Figure 6-1b for stiffener type 331s, which consists of b_w = 0.75 in., b_f = 0.75 in., r = 0.125 in., L = 6 in. and the $[\pm 45/0/90]_S$ stacking sequence. The same magnitudes of the initial imperfection of 1%, 5% and 10% of the laminate thickness were assumed. Experimental results for specimens 331s-1 and 331s-2 are also contained in the figure. Again, the experimental behavior falls in between the predicted responses based on initial imperfections of 1% and 5%. Based on these observations, an imperfection magnitude of 5% was selected for the finite element prediction of buckling of all 8-ply specimens in order to provide a conservative (lower bound) estimate.

At least two possibilities exist for the case of the 16-ply laminate: either the imperfections scale directly with laminate thickness or the absolute magnitudes remain constant, as might occur if the imperfections are determined by the machining tolerances of the forming tool surface. Accordingly, finite element analyses were conducted based on imperfection magnitudes of 2.5% and 5% of the laminate thickness of 0.08 in., which correspond to the constant and scaled magnitude cases, respectively. Results are contained in Figure 6-2 for stiffener type 111-2s, which consists of b_w = 1.75 in., b_f = 1.25 in., r = 0.125 in., L = 10 in. and the stacking sequence $[\pm 45/0/90]_{2S}$. Experimental results for specimen 111-2s-3 are also contained in the figure. The predicted response based on the

larger imperfection clearly indicates earlier buckling and a more gradual transition between pre- and postbuckling responses than observed experimentally. The experimental response for this and all other 16-ply specimens suggests that the as-fabricated initial imperfection is on the order of 2.5% of the laminate thickness. This conclusion indicates that the magnitude of the initial imperfection remained constant and did not scale with laminate thickness. Therefore, a magnitude of 2.5% was used in the finite element analyses to determine the buckling loads of the 16-ply stiffeners.

6.1.3 Experimental and Predicted Buckling Loads

A comparison of the experimental and numerical axial stiffness (P/u) and out-of-plane deflection (w/t) responses for stiffener types 111-2s, 111s and 111orth is given in Figure 6-3. These specimen types are the same as those used in Chapter 5 to illustrate the range of responses observed. As discussed in Section 5.1.1, the P/u ordinate has been changed to PL/AEu, which should have unit value during the approximately uniaxial response prior to buckling . The out-of-plane deflection has been normalized with respect to the laminate thickness. An immediate observation from the results of specimen types 111-2s and 111s is that the experimental prebuckling stiffness is lower than predicted. The prebuckling stiffness of one specimen of type 111orth is higher than predicted. Resolution of this issue will be deferred to Section 6.2. The prebuckling, buckling and initial postbuckling responses of specimens 111-2s are seen in Figure 6-3a to be extremely consistent between replicate specimens. Variations between the responses of replicate specimens are much greater for specimen types 111s and 111orth, as illustrated in Figures 6-3b and 6-3c, respectively. This observation may in part be a reflection of increased sensitivity of the response to local variations in dimensions (such as thickness) as the magnitudes are reduced. With the exception of the prebuckling stiffnesses, the agreement between the experimental and numerical results is good.

The finite element predictions of the buckling loads based on the axial stiffness and out-of-plane deflection responses are contained in Table 6-1. Also included in the table are the analytical and linear finite element eigenvalue predictions of the buckling loads, together with the errors associated with all of the predictions with respect to the average experimental buckling loads from Table 5-1. The errors associated with the finite element predictions of the buckling loads range from -4.5 to 4.5% and 3.3 to 19.4% for the

nonlinear and linear analyses, respectively. The errors associated with the analytical predictions of the buckling loads range from -3.7 to 29.4%. The overall average errors are 1.4, 10.2 and 13.3% for the nonlinear FEM, linear FEM and analytical predictions, respectively.

In the case of the nonlinear FEM predictions, the magnitudes of the errors are small, and no clear trend was observed between the error magnitudes and any of the geometric or material variables. The linear FEM and analytical predictions tended to overestimate the buckling loads. In both cases, error is introduced by neglecting the effect of the imperfections in the structure. In the analytical model, additional sources of error are the omission of the bending-twisting coupling present in all of the laminates to varying degrees, the neglecting of the actual curved flange-to-web corner and the *a priori* assumption of a sinusoidal displacement function for the buckled shape. The effect of the corner radius on the error of the analytical load prediction is apparent from a comparison of the results between specimen families 2_1s and 2_2s. The only difference between these families is the corner radius. The analytical model overestimates the buckling loads of the specimens having the smaller corner radius (2_1s) by 16.5 to 21.4%. The error is reduced to -3.7 to 1.5% for the specimens having the larger corner radius (2_2s), since the experimental buckling loads increase significantly with the corner radius. The largest errors in the linear FEM predictions (19.4%) and in the analytical predictions (29.4%) were for the specimens having the smallest flange and web widths (341s-1,-2). The error of the nonlinear FEM buckling load predictions for these same specimens, however, was only 1%. Therefore, the large errors in the linear FEM and analytical predictions would seem to be related to differences between those models and the nonlinear analyses, as opposed to some fundamental disagreement between the predicted and observed responses. The additional features included in the nonlinear analyses which may account for the improved prediction of the buckling response are the interacting effects of the initial imperfections and secondary mode interaction. Secondary mode interaction of varying degrees was predicted and observed for many of the specimens and will be discussed in Section 6.5.

The best prediction of the buckling loads clearly came from the nonlinear finite element analyses. Since the error in the predictions did not exhibit any systematic variation with the geometric parameters, it is concluded that no significant scale effects were present in the initiation of the local buckling response. The initial local buckling response is

sometimes treated in a linearized manner, as was done in the cases of the FEM eigenvalue and analytical analyses. This means that the initial equilibrium configuration contains no out-of-plane deflection, and the buckling load is defined as that load at which an adjacent configuration (infinitesimally disturbed from the initial state) can achieve equilibrium. If the local buckling of the stiffeners is viewed as linear in this way and recognizing that the loads were below that at which any permanent material deformation would be expected, then the buckling response can be initially described as "elastic". That this elastic response was observed to scale in the current work is consistent with observations for the scaling of other elastic response types. For example, the impact force magnitudes and durations were observed to scale in the elastic range for transversely impacted beams as reported in Reference 22. Scaled behavior in the elastic or small deflection regime has also been observed for tensile stiffness (23) and eccentrically loaded beam-columns (24,25). In real structures, however, nonlinear effects are present prior to buckling, i.e. the interaction between the axial load and the initial imperfections produces out-of-plane deflections. In fact, these nonlinear effects were used to determine the buckling loads of the stiffeners in this work. Therefore, when the buckling of the stiffeners is viewed as the nonlinear response phenomenon that it really is, it can be further concluded that scaling of the response was also achieved in the (initial) nonlinear response regime as well.

6.1.4 Normalized Buckling Loads

The nondimensional buckling load parameters obtained from the analytical model discussed in Section 3.1.1 are:

$$\alpha = \frac{N_x\, b_w^2}{\sqrt{D_{11}\, D_{22}}} \tag{6.1}$$

and

$$\beta = \frac{m\pi b_w}{L}\sqrt{\sqrt{\left(\frac{D_{33}}{D_{22}}\right)^2} - \frac{D_{11}}{D_{22}} + \frac{N_x}{D_{22}}\left(\frac{L}{m\pi}\right)^2} - \frac{D_{33}}{D_{22}} \tag{6.2}$$

The range of buckling stresses will be illustrated first to provide a means for judging the effectiveness of the normalization of the buckling response. The buckling stresses for all

of the experimental specimens are again plotted versus the flange-to-web width ratio (b_f/b_w) in Figure 6-4. The buckling stresses predicted by the analytical model are also contained in the figure as continuous functions of b_f/b_w. Clearly each of the stiffener families (i.e. a specific web size and stacking sequence) exhibit a different relationship between the buckling stress and b_f/b_w. The agreement between the observed and predicted buckling stresses is generally improved over the load predictions, since the lower observed loads are offset by the smaller cross-sectional areas of the test specimens based on the actual corner radii. The model predicts the same dependence of the buckling response on the various geometric and material variables (excluding the corner radius) as was observed experimentally and discussed in Section 5.1.2. Both the experimental data and the analytical predictions are re-plotted in terms of the normalized load parameter, α, in Figure 6-5. The analytical curves for the various web sizes having the 8-ply quasi-isotropic stacking sequence are condensed onto single curve using the parameter α. Separate curves are still required for the other two stacking sequences. Thus, the load parameter α only normalizes the response for various web sizes. Finally, the data are plotted a third time in terms of the load parameter, β, in Figure 6-6. Here, the normalized buckling loads are plotted in terms of the effective b_f/b_w ratio, which is based on partitioning the arc length of one-half of each flange-to-web corner equally between those elements (see Figure 3-1). It is apparent that the analytical curves are very nearly condensed onto a single curve. The individual curves are nearly indistinguishable outside of a b_f/b_w range of 0.3 to 0.6. The experimental data points from the various stiffener families are likewise grouped along this single curve. The normalization is thus seen to be effective for two different quasi-isotropic stacking sequences, as well as the unorthodox $[+30/0_2/-30]_s$ laminate. This latter result is significant in view of the high degree of bending-twisting coupling present in this laminate, which is not included in the analytical model. Indeed, this fact was the underlying reason for selecting this laminate for this study. The linear and nonlinear finite element predictions of the buckling loads are presented in Figure 6-7 in terms of the load parameter β. The linear predictions often lie very nearly on the analytical curve. Again, the results from all of the stiffener types are grouped along the single analytical curve.

The generality of the buckling load parameter β can be further supported by examination of the buckling data available in the literature for both Z- and channel sections. These data are available in References 1, 2, 5, 6 and 8, and encompass a number of quasi-isotropic and $[0/\pm\theta]$-type stacking sequences and several material systems. The predicted

buckling loads for the various geometries and laminates in terms of the parameter β are plotted against the nominal b_f/b_w ratio in Figure 6-8. The specific stacking sequences and material systems are indicated on the figure. An estimate of the variation in the β values between the various specimen types is also included in the figure. This variation is defined as the range of the β values for a given b_f/b_w ratio normalized by the mean value. The results indicate that this variation is at or below 2% outside of the b_f/b_w range 0.25 to 0.65, and peaks at a value of 4% within this range. The corresponding experimental data are contained in Figure 6-9. The agreement between the data and the (mean) analytical curve is considered good, particularly in view of the variability in buckling load determination methods and specimen preparation which likely exists. Therefore, the load parameter β is seen to be quite general with respect to the available data.

6.2 Prebuckling Response

6.2.1 Prebuckling Stiffness

As identified in Section 6.1, the observed prebuckling stiffnesses of the test specimens were generally lower than predicted by a uniaxial model, the use of which is justified by the nonlinear finite element analyses of the gage length alone. The numerical results indicate that any constraint on the Poisson expansion due either to the non-planar geometry of the cross-section or the clamping of the ends is insufficient to cause an appreciable deviation from overall, uniaxial behavior prior to buckling. This is apparent from the predicted unit values of PL/AEu seen previously in Figure 6-3 prior to buckling. The normalized prebuckling stiffnesses (PL/AEu) for all of the test specimens prior to buckling are summarized in Table 6-2. The observed values range from 0.84 to 1.05; the former representing a prebuckling stiffness 16% lower than initially predicted. The lowest stiffnesses occurred in the specimens having the shorter gage length. Only four specimens, all having the $[+30/0_2/-30]_S$ stacking sequence, exhibited stiffnesses greater than or equal to unity.

Potential sources of error in the prebuckling stiffnesses calculated are naturally the values of P, A, E, u, and L used to define the stiffness. The accuracy of the load, P, and end shortening, u, measurements is considered satisfactory. The cross-sectional area, A, was calculated based on the actual stiffener dimensions. The value of the thickness used in

the area calculations was based on an average of values measured primarily along the flanges. The thickness variations in the corners discussed in Section 4.3 were not included in the area calculations. The equivalent longitudinal moduli in compression, E, were measured using coupons cut from the Z-section stock as discussed in Section 4.2, and were found to be 4 to 6% lower than predicted from lamination theory using nominal ply properties of E_1 = 18.5 Msi, E_2 = 1.64 Msi, G_{12} = 0.87 Msi and ν_{12} = 0.3. Therefore, the actual values of the equivalent longitudinal moduli might account for a portion of the observed discrepancy in some cases. However, error in both the cross-sectional area and the assumed moduli would more likely cause a consistent bias in the response, as opposed to the more systematic variation observed and discussed below.

Strain gage data generally indicated that local strain values were the same as the load-based global, uniaxial strain measure, P/AE, prior to buckling. For example, membrane strain data (the average of front and back strain gage pairs) for specimen 131-2s-3 are provided in Figure 6-10. Note that this specimen had the second largest prebuckling load range and the second lowest value of normalized prebuckling stiffness (0.85). Membrane strain data from various positions along the cross-section, along with the length-normalized end shortening, u/L, are plotted against the load-based strain, P/AE, in the figure. The data clearly indicate that the local strains (strain gage data) are consistent with P/AE. This means that the local strains are basically the same as an overall, average strain value based on the load. The local strain measures are not affected by any assumed properties or dimensions. Significant errors in the assumed values of A and/or E would certainly result in disagreement between the local and global load-based prebuckling strains. The displacement-based average strain, u/L, is shown in the figure to be clearly inconsistent with the other strain measures. Therefore, the error in prebuckling stiffness is attributed primarily to the quantity u/L. While it was noted above that the measurement of the end shortening was considered satisfactory, it remains to be determined to what extent this displacement represents the response of the gage length alone. Alternatively, error in the quantity u/L can be viewed in terms of the active length of the stiffener. That is, the effective length may be between the total length and the gage length due to the fact that some displacement can occur within the potted end supports. Note from Table 4-1 that the total depth of the end supports is either 20% or 33% of the gage length.

6.2.2 Qualitative Model for Prebuckling Stiffness

The constraint offered by the potted end supports varied as a function of specimen geometry and stacking sequence. A qualitative prediction of the behavior can be obtained from the following model. The total end shortening between the platens of the test machine can be expressed as $u_t = u_g + u_p$, where u_g and u_p are the net shortening of the specimen which occurs in the gage length and potted end supports, respectively. The uniaxial response of the stiffener prior to buckling is represented by the equation $P / AE = u_g / L_g$, where L_g is the gage length . The shortening in the potted end supports may be represented as $u_p = k L_p P / s$, where L_p is the sum of the depths of the potted end supports, s is the total width of the developed cross-section of the stiffener and k is a proportionality factor. The mechanics of the loading configuration and the dimensions of factor k (length/force) suggest that k would be inversely proportional to an effective material modulus and a characteristic length of the potting-to-laminate interface (e.g. the thickness of a boundary layer over which the constraint of the potting is imposed). Since the boundary layer thickness may be influenced by the other material and geometric parameters, the treatment of k as a constant in this discussion is an approximation. Combining the above functional dependencies yields:

$$\frac{P}{AE} = \frac{u_g}{L_g} = \frac{u_t - u_p}{L_g} = \frac{1}{\left[1 + \frac{kEtL_p}{L_g}\right]} \frac{u_t}{L_g} = n \frac{u_t}{L_g} \tag{6.3}$$

where

$$n = \frac{1}{\left[1 + \frac{kEtL_p}{L_g}\right]} \tag{6.4}$$

and the cross-sectional area A is equal to (s*t), for laminate thickness t. The model predicts that the effect of the potted end supports on axial stiffness of the complete potted specimen should increase with increasing laminate thickness and decreasing gage length, and be independent of flange or web widths.

The above model suggests that a plot of $1/n = (u_t/L_g) / (P/AE)$ versus (EtL_p/L_g) would produce a line of slope k and an intercept of 1. Such a plot is contained in Figure 6-

11 using the experimentally observed "n" values. The dependence of the data on the parameters E, t and L_g is generally consistent with the trends predicted by the model. However, the model does not predict the exact functional dependence of the behavior, nor the large differences among replicate specimens. The correlation with the observed response of the specimens of the $[+30/0_2/-30]_s$ laminate is particularly poor. Some variation in the response between replicate specimens of the $[+30/0_2/-30]_s$ stacking sequence is attributed to varying degrees of lack of parallelism between the two surfaces of the potted end supports in contact with the platens of the test machine, as indicated by the strain gage data shown in Figure 6-12. Longitudinal membrane strain data for specimen 121orth-2 are provided in the figure from various locations over the cross-section. Note from Table 6-2 that this specimen had a significantly lower normalized prebuckling stiffness (0.84) compared to the two replicate specimen values of 1.02 and 0.92. The data exhibit a systematic variation in the strain along the cross-section from the end of one flange to the other. This behavior indicates that contact between the specimen and the loading machine began at the end of one flange and progressed along the cross-section until contact was made at the end of the opposite flange. In fact, the data suggest that the cross-section initially rotated about the mid-point of the web upon application of the compressive load, with tensile strains first developing in the flange opposite to the first contact point. As a result, the membrane strain in the last-contacted flange lagged behind that of the other. Note also from the figure that the end shortening response reflects an increasing specimen stiffness upon initial loading while the specimen is being fully seated. A calculation of the difference in the lengths of the specimen at diametrically opposed locations necessary for the observed difference in membrane strains between the two flange ends is provided in Figure 6-13. The result is that only 0.004 in. difference in axial length across the 5 in. diameter of the potted end support would be necessary to cause the observed behavior. The lack of parallelism would reduce axial stiffness first by reducing the amount of the cross-section undergoing compression, and then due to the bending which develops in the process of the specimen becoming fully seated. The specimens of the $[+30/0_2/-30]_s$ stacking sequence would be particularly sensitive to this phenomenon due to the small prebuckling load range associated with these specimens. For example, the average longitudinal strains at buckling (P/AE) for specimens 111-2s, 111s and 111orth were 0.32, 0.08 and 0.03%, respectively. The greater prebuckling load range available for the quasi-isotropic specimens permitted the estimation of initial stiffness at loads above those where these effects are particularly noticeable.

The reason for the unit values of normalized initial stiffness for some of the specimens of the $[+30/0_2/-30]_S$ stacking sequence is not apparent. The equivalent longitudinal moduli measured using coupons removed from the Z-section stock were approximately 4% below the predicted values, as discussed in Section 4.2. Further verification of the laminate properties (particularly bending stiffnesses) was provided by deplying coupons cut from all of the $[+30/0_2/-30]_S$ section stock used to fabricate the stiffeners. This was accomplished by heating the coupons at 450 °C for 30 minutes. The correct stacking sequence was verified, and all fiber angles were measured to be within 0.5°. As these stiffeners were of the later vintage, thickness uniformity was generally excellent, even in the corner regions.

6.2.3 Quantitative Analysis of End Supports

Finite element analyses of the potting-to-stiffener constraint were performed to provide a more quantitative correction to the experimental end shortening behavior. This was done to permit comparisons of the experimental and predicted responses on an equivalent basis throughout the entire load range. Two-dimensional plane strain and generalized plane strain analyses were performed for this purpose. These two analysis types are expected to bound the actual behavior of the three-dimensional geometry. The plane strain assumption prevents the Poisson expansion in the transverse direction of the laminate, which yields a more stiff response than expected in the real case. The generalized plane strain analyses permit a uniform strain to develop in the transverse direction of the laminate, thus maintaining the between-ply constraints induced by the mismatch in stiffness properties between plies of different orientations. The transverse strain which develops in the generalized plane strain analyses, however, is not limited by the constraint imposed by the adjacent elements of the stiffener within the endpot, as would occur in the real case. For example, the transverse tensile strain in the web present due to the longitudinal compression would be opposed by the adjacent flanges which are backed on both sides by potting material. Therefore, the generalized plane strain analyses are expected to yield a softer response than in the actual case. The finite element mesh used contained 3398 elements to provide a reasonable degree of mesh refinement near the top portion of the potting-to-stiffener interface where strain gradients will be large, as shown in Figure 6-14. The potting material properties of Figure 4-2 indicate significant nonlinearity in both the

compression and shear stress-strain responses. Therefore, linear and nonlinear (constitutive and kinematic) analyses were performed. The Ramberg-Osgood deformation plasticity approach was used to model the nonlinear response of the potting material. Here, the uniaxial stress-strain response is fit to a relation of the form:

$$E\,\varepsilon = \sigma\left[1 + \alpha\left(\frac{|\sigma|}{\sigma_o}\right)^n\right] \tag{6.5}$$

where E is the initial (linear) elastic modulus, σ_o is an offset yield stress, α is the yield offset parameter and n is the hardening exponent. Since the effectiveness of the constraint of the potting material is likely influenced by both its shear and compression properties, it was desired to perform analyses using both of these measured properties, although ABAQUS would only permit modelling of the extensional moduli as in Equation 6.5. Therefore, use of the measured shear stress-strain response in the analyses was accomplished by fitting Equation 6.5 to the shear test data converted to a stress intensity-strain intensity basis, using the relations below:

$$\sigma_i = \left[(\sigma_x-\sigma_y)^2 + (\sigma_y-\sigma_z)^2 + (\sigma_z-\sigma_x)^2 + 3(\tau_{xy}^2 + \tau_{yz}^2 + \tau_{zx}^2)\right]^{1/2}$$

$$\varepsilon_i = \frac{1}{2^{1/2}\,(1+\nu)}\left[(\varepsilon_x-\varepsilon_y)^2 + (\varepsilon_y-\varepsilon_z)^2 + (\varepsilon_z-\varepsilon_x)^2 + \frac{3}{2}(\gamma_{xy}^2 + \gamma_{yz}^2 + \gamma_{zx}^2)\right]^{1/2}$$

$$\sigma_i = E\varepsilon_i \tag{6.6}$$

where σ_i and ε_i are the stress and strain intensities, respectively. The compression and shear stress-strain intensity data measured using samples of the potting material, together with the respective fits to Equation 6.5 are provided in Figure 6-15. The data clearly indicate that the shear stress-strain response is the more compliant. The fit of the data to Equation 6.5 is very good.

Results from the linear, generalized plane strain finite element analyses will be used to illustrate the difference in the constraint offered by the potted end supports as a function of the geometric and material parameters. The distribution of longitudinal compressive strain and shear strain along the potting-to-stiffener interface is provided in Figure 6-16 for

all three stacking sequences. In the case of the 8-ply quasi-isotropic laminate $[\pm 45/0/90]_S$, the compressive strain decreases to 50% of the far-field value (in the unpotted portion of the laminate) within the top 20% of the pot depth, as shown in Figure 6-16a. The same 50% reduction in compressive strain in the $[+30/0_2/-30]_S$ and $[\pm 45/0/90]_{2S}$ laminates does not occur until the mid-depth location in the end support. The compressive strain in the laminate at the bottom surface of the end support in contact with the loading platen is predicted to be a function of the laminate modulus and thickness. In the 8-ply quasi-isotropic case, the compressive strain at the bottom is 25% of the value in the laminate away from the end support, as seen in the figure. The strain reduction at the base is a reflection of the load transfer into the potting material under the action of the shear stress present at the laminate-to-potting material interface. The compressive strain at the base of the 16-ply quasi-isotropic and orthotropic laminates is approximately 40% of the far-field values. The results for the three stacking sequences indicate that the load in the end supports is carried by both uniaxial compression and shear mechanisms, and that the relative participation of the mechanisms is a function of the axial stiffness (E*A) of the laminate. The latter observation underscores the fact that the proportionality factor k discussed in the qualitative model of Section 6.2.2 is not a constant, but instead represents the functional dependence of the compression and shear mechanisms on the geometrical and material variables. The rate of shear strain decay with distance from the top of the endpot depends on the stacking sequences in the same way, as shown in Figure 6-16b. Thus, the strain decay rates are seen to vary inversely with the axial laminate stiffness, E*A. This simply means that the relative effect of the additional axial stiffness offered by the endpot decreases as the intrinsic stiffness of the laminate (E*A) increases. Note that the magnitude of the shear strain decreases to the value of the longitudinal strain in the laminate away from the endpot within the top 10% of the endpot depth. Therefore, the amount of the potting material significantly affected by the nonlinear material response will likely be small.

The generalized plane strain finite element predictions of the additional end shortening which occurs in the potted end supports as a function of the average applied stress (P/A) are shown in Figure 6-17. The results indicate that the effect of the geometric and material nonlinearities (solid curves) is relatively minor as suggested by the rate of strain decay. The largest displacements within the endpots occur with the 16-ply quasi-isotropic laminate, consistent with the slowest rate of longitudinal strain decay with depth

into the potting material for this case. The least displacement in the end supports is associated with the $[+30/0_2/-30]_S$ laminate. This occurs because the longitudinal strains are so much smaller by virtue of the high longitudinal modulus of the laminate, even though the rate of strain decay in the endpot is predicted to be slow, as seen in Figure 6-16.

6.2.4 Adjustment to End Shortening Data

The relationships between the additional displacement in the end supports and the applied stress were used to "adjust" the experimental end shortening data, i.e. the predicted displacements in the endpots were subtracted from the experimental data. This was done to permit comparisons of the experimental and numerically predicted responses on an equivalent basis. In addition, the adjustment was applied to the experimental behavior (as opposed to adding the displacement within the end supports to the numerically predicted response of the gage length) to facilitate subsequent investigation of the relationships between the overall structural responses of the gage length and the development of local strains which are instrumental in determining ultimate strength. Application of the results from the two-dimensional finite element analyses to the three-dimensional stiffeners was accomplished on an average stress (P/A) basis. It is recognized that after buckling, the stress distribution along the stiffener cross-section in the endpot will reflect the load redistribution that occurs within the gage length, and will, therefore, deviate from the average stress. In addition, the potting material in the interior portion of the flange-to-web corners will likely be more highly stressed due to the locally reduced volume of potting material in relation to interface area. Both of these effects will tend to increase the displacements within the endpots due to an increase in the nonlinearity of the material response at higher stresses. Nevertheless, the two-dimensional analyses will be used as an approximation of the behavior, due to the expense of a three-dimensional analysis of sufficient refinement. The normalized stiffness values (PL/AEu) for all of the specimens adjusted in this manner are listed in Table 6-2, in addition to the unadjusted values. The average unadjusted prebuckling stiffnesses for the various specimen families (i.e. 1_1orth etc.) range from 0.88 to 0.93. The range of individual values is greater as noted above. The average adjusted stiffnesses for these families range from 0.94 to 1.00 and 0.98 to 1.04 for the generalized plane strain and plane strain analyses, respectively. Overall, the two analysis types result in adjusted stiffnesses very close to unity. The generalized plane strain analyses slightly under-corrected the stiffnesses, while the plane strain analyses

slightly over-corrected. The effect of the material nonlinearity was a maximum in stiffener type 131-2s, but increased the normalized stiffness only by 2% (i.e. from an average stiffness of 0.95 to 0.97 for the generalized plane strain case).

The displacement occurring in the end supports will influence the apparent axial stiffness of a specimen throughout the entire load range, and not just prior to buckling. The significance of the above discussion is that an experimental artifact such as these potted end supports might result in an apparent size dependence of the overall structural response. This might be interpreted falsely as a scale effect if the mechanics governing the constraint of the potted end supports are not included in the analyses. In a rigorously scaled experiment, the boundary conditions must be properly scaled as well. The implications for the specimens of this study can be illustrated by a simple example. Let a 1-in.-deep by 4-in.-diameter potted end support used in this work be designated as size 1. Now consider strictly scaled experiments using scale factors, λ, of up to only 3. Simply scaling all of the potted end support dimensions would result in the volume of the largest potted end support (scaling as λ^3) being an ungainly 1.5 gallons of potting material! Note also that the model discussed above would not require the potted end supports to be scaled in this manner. The model predicts that the specimen and potted end supports should be sized such that the nondimensional group ($k E t L_p/L_g$) remains constant. In effect, the entire volume of the potted end support may not need to be scaled, since the constraint is imposed locally in a relatively thin layer of potting material along the interface with the stiffener. In summary, scaling specimens without consideration of the mechanics governing the behavior can result in unnecessary experimental difficulties and incorrect identification of scale effects.

6.3 Load-End Shortening Response

6.3.1 Experimental and Predicted Responses

The predicted load-end shortening responses exhibited excess stiffness with respect to the experimentally observed behavior. Excess stiffness was typically present even in the prebuckling regime, and increased with increasing load beyond buckling. Typical results are shown in Figures 6-18 and 6-19. Results for specimens 111-2s-2 and 131-2s-2 are contained in Figure 6-18a. These specimens were fabricated from the 16-ply quasi-isotropic laminate and represent flange sizes of 1.25 and 0.75 in. The gross difference

between the predicted and unadjusted experimental prebuckling stiffness is apparent in the figure for specimen 131-2s-2. The adjustment made to compensate for the displacement which occurs in the potted end supports was discussed in the previous section. For specimen 131-2s-2, the extent of the prebuckling load range and the error in the unadjusted prebuckling stiffness practically preclude an effective comparison in the small postbuckled region. The error in prebuckling stiffness is seen to be smaller for specimen 111-2s-2. The overestimation of the load in the postbuckling range of this specimen is relatively modest at 6.3%.

These results can be contrasted with those of specimens 111s-2 and 131s-2 using Figure 6-18b. The difference between the two groups of specimens is the laminate thickness (16-ply quasi-isotropic in Figure 6-18a versus 8-ply quasi-isotropic in Figure 6-18b). The prebuckling stiffness errors are not as obvious in the 8-ply specimens, since the relative size of the prebuckling load range is much smaller. The maximum errors associated with the predicted loads in the postbuckling range are much greater, however, reaching a magnitude of 23.3% for specimen 111s-2. The size of the postbuckling range is much greater for this specimen as well. In fact, the ratio of the maximum value of end shortening at failure to the value at buckling is greater than 11 for specimen 111s-2. Finally, the results for equivalent geometries of specimens having the $[+30/0_2/-30]_s$ laminate are presented in Figure 6-19. Significant damage develops in specimens of this laminate prior to final catastrophic failure, which limits the maximum postbuckling load at which comparisons between the experimental and predicted loads can be made. With this in mind, the maximum overprediction of the load is only 8% for these specimens. It is worth noting that the ratio of maximum end shortening-to-end shortening at buckling is nearly 12 for specimen 111orth-2. Therefore, the relative sizes of the postbuckling ranges are comparable between specimens 111s-2 and 111orth-2, while the maximum errors in estimated loads differ by a factor of 3.

A summary of the errors associated with the numerical load predictions is presented in Table 6-3. Both the experimental and numerically predicted loads are reported for each specimen at the minimum value of end shortening attained experimentally which coincides with partial or complete failure of the specimen. Partial damage of the specimen was indicated by a discontinuity in the load-end shortening response. Thus, the indicated errors are the maximum errors reached, until some localized failure effectively changed the

character of the material, obviating meaningful comparisons at any higher load. The errors range from -2.3% to 23.3%. The greatest errors occurred with specimens of the 8-ply quasi-isotropic laminate having the larger flanges (e.g., specimen 111s-2). These specimens also exhibited the largest postbuckling load range. The bulk of the stiffness disparity in the prebuckling regime is attributed to the displacements which occur in the potted end supports of the experimental specimens, as discussed above in Section 6.2. The discrepancies between the predicted and observed load values can be correlated with the absolute size of the postbuckling load range as illustrated in Figure 6-20, in which the overestimation of load (expressed as a percentage of the experimental load value) for all of the specimens is plotted against the difference between the maximum end shortening attained prior to damage and the value at buckling. The trend of the data indicates that the error in the load prediction increases with this difference in end shortening values. The difference in the end shortening values between damage initiation and buckling is a measure of the size of the nonlinear response regime. Therefore, the data trend indicates that the actual geometric and/or material nonlinearities are not being modelled completely. Nonlinearity in the stress-strain response of the material is not included in the finite element formulation and would become increasingly important as strains increase with distance into the postbuckling range. Geometric nonlinearity is modelled in ABAQUS based on the small strain, large rotation assumption. The finite deformation (i.e. large strain) strain-displacement relations due to Green are:

$$\varepsilon_{xx} = \frac{\partial u}{\partial x} + \frac{1}{2}\left[\left(\frac{\partial u}{\partial x}\right)^2 + \left(\frac{\partial v}{\partial x}\right)^2 + \left(\frac{\partial w}{\partial x}\right)^2\right]$$

$$\varepsilon_{yy} = \frac{\partial v}{\partial y} + \frac{1}{2}\left[\left(\frac{\partial u}{\partial y}\right)^2 + \left(\frac{\partial v}{\partial y}\right)^2 + \left(\frac{\partial w}{\partial y}\right)^2\right]$$

$$\gamma_{xy} = \frac{\partial u}{\partial y} + \frac{\partial v}{\partial x} + \frac{\partial^2 u}{\partial x \partial y} + \frac{\partial^2 v}{\partial x \partial y} + \frac{\partial^2 w}{\partial x \partial y} \qquad (6.7)$$

where x,y and u,v are the in-plane coordinate directions and displacements, respectively. The out-of-plane deflection is w. The small strain, large rotation assumption is invoked by including only the nonlinear terms in the out-of-plane deflection as shown below:

$$\varepsilon_{xx} = \frac{\partial u}{\partial x} + \frac{1}{2}\left(\frac{\partial w}{\partial x}\right)^2, \quad \varepsilon_{yy} = \frac{\partial v}{\partial y} + \frac{1}{2}\left(\frac{\partial w}{\partial y}\right)^2, \quad \gamma_{xy} = \frac{\partial v}{\partial x} + \frac{\partial u}{\partial y} + \frac{\partial^2 w}{\partial x \partial y} \tag{6.8}$$

Therefore, the omission of the higher order terms in the in-plane displacements will lead to reduced accuracy as the in-plane strains become large. Detailed discussion of the predicted strain magnitudes will be deferred to Section 6.6. For the present purpose, however, it is sufficient to note that some strain magnitudes are predicted to exceed 3%. There are two implications of such a magnitude with respect to the agreement between the predicted and observed load-end shortening behavior. Firstly, as noted above, in-plane strains of this magnitude may begin to violate the small strain assumption upon which the finite element formulation is based. Secondly, such magnitudes certainly indicate that some local material failures are to be expected for the material system used at load values below that of final, catastrophic failure. The consequence of this is that the constitutive relationship for the material is no longer constant, and could be significantly reduced locally.

6.3.2 Sensitivity of Predicted Response to Material Properties.

Limited analyses were performed in an attempt to identify sources of the excess stiffness observed in the numerical models. Material properties naturally had to be assumed in order to perform the finite element analyses. In general, estimates of material properties may be wrong right from the beginning of an analysis in the worst case, or may become inadequate as the analysis penetrates the nonlinear response regime. Various test analyses were performed to evaluate the two considerations: sensitivity to the initial values and the effects of degraded properties. Since a rigorous sensitivity analysis was not performed, the magnitudes of the material property changes considered can be used as a guide as to which of the above considerations each numerical experiment was directed. The properties assumed in this work were verified experimentally to a limited extent using test coupons removed from the Z-section stock, as discussed in Section 4.2. The actual or effective material properties *in-situ* could change as strains became large and as damage developed in the laminates. For example, shear moduli of graphite/epoxy unidirectional material typically exhibit a highly nonlinear stress-strain behavior. The result is that the effective or instantaneous shear modulus at high strain may be considerably lower than the

initial value, which will cause a "softening" of the true response compared to the response predicted using the initial (higher) value. The strength of unidirectional composites in the direction transverse to the fibers is typically very low. The transverse strength may be exceeded locally and manifested by matrix cracking, without necessarily causing immediate catastrophic failure of the entire specimen. Therefore, the discontinuity across any matrix cracks in one or more plies prior to failure effectively decreases the material stiffness near those cracks.

The sensitivity of the load-end shortening response to the assumed value of the fiber modulus is illustrated in Figure 6-21. Experimental results from specimen 211s-1 and the results from the baseline finite element case (E_{11} = 18.5 Msi) are contrasted with those of an analysis in which the fiber modulus E_{11} was reduced by 5%, compared to the baseline case. The stacking sequence is $[\pm 45/0/90]_S$. The flange and web widths are 1.25 in. The 5% reduction in E_{11} translates into a near 5% reduction in the equivalent longitudinal and transverse extensional and bending stiffnesses of the laminate. Accordingly, the computed loads for this case are reduced by 5% throughout the load range, as indicated in Figure 6-21a. The prebuckling and initial postbuckling portions of the response are contained in Figure 6-21b. The experimental data for specimen 211s-1 is provided in both the unadjusted and adjusted (for the displacement predicted to occur within the potted end supports) forms. The reality of the experimental configuration is that some displacement will occur within these end supports. The results in Figure 6-21b indicate that the overall axial stiffnesses of the baseline FEM and the adjusted experimental cases are nearly the same. In addition, the results for the reduced E_{11} FEM case and the unadjusted experimental case are also virtually identical, but equal to a lower value. Clearly, both the displacement within the end supports and the fiber modulus play significant roles in determining prebuckling stiffness. It is apparent in Figure 6-21a, however, that the two factors have significantly different impact on the postbuckling portion of the response. In Figure 6-21a, the reduced modulus results in similarly reduced predicted loads as has been noted, while the displacement within the end supports becomes insignificant compared to the large deformations in the extensive postbuckling load range. The point of this discussion is that inference of material properties from the experimental response (i.e. assuming the true fiber modulus to be that of the 5% reduced case based on its agreement with the unadjusted experimental results), without consideration of the effect

of the end conditions, would result in an artificially improved prediction of the postbuckling response.

An upper bound numerical prediction of the effect of transverse matrix cracking on the load-end shortening response was performed by reducing the transverse modulus E_{22} by a factor of 1.0E6 throughout those plies assumed to have cracked. It is recognized that in reality such a reduction would occur only in local regions of tensile stress. Therefore, effects such as the asymmetry of the material properties with respect to the mid-plane of the laminate which would occur in reality, and the details of the resulting load redistribution are not considered. These effects would certainly be important in determining the strength of the stiffener. However, this approach has been used here only to estimate the effect of cracking on overall stiffness. Results from the baseline FEM analysis (E_{22} = 1.64 Msi) and experimental specimen 211s-1 are contrasted with two cases of reduced E_{22} in Figure 6-22a. The configuration is the same as used in the discussion in the preceding paragraph. In one analysis, the reduced E_{22} is imposed on the ±45° surface plies. In a second, extreme case, the reduced E_{22} is imposed on all plies in the laminate. The results indicate a load decrease of 4% for the former case of surface ply cracking. The load reduction increases to 7% for the assumption of reduced E_{22} in all plies. The point of the analyses of the effect of E_{22} is primarily to provide a qualitative indication of the effect of matrix cracking on stiffness late in the postbuckling region. The results suggest that not more than about 5%, out of a total 17% "error" in predicted loads at failure, could likely be attributed to matrix cracking.

The sensitivity of the load-end shortening behavior to shear moduli was also considered. Results from an analysis based on a reduced in-plane shear modulus G_{12} are contained in Figure 6-22b. The shear modulus was reduced 20% from the baseline FEM case to a value of 0.7 Msi. This value is well within the range of secant moduli typical of graphite-epoxy material at the strains encountered in the stiffeners. The maximum load reduction is only 2%, compared to the baseline finite element analysis. This result is a simple reflection of the fiber-dominant nature of the stacking sequences used. The sensitivity of the response to in-plane shear moduli would naturally increase with more matrix dominated stacking sequences and material systems.

Finite element results for an analysis based on reduced transverse shear moduli are also contained in Figure 6-22b. The ABAQUS finite element formulation is based on a first-order shear deformation theory, in which the normal to the laminate mid-surface remains straight throughout the thickness, but is allowed to rotate in response to transverse forces. A limitation of this theory is that the transverse shear strain is forced to be constant throughout the laminate thickness at a point, instead of distributed parabolically. A correction factor is employed in the theory such that the constant transverse shear strain is the same as the thickness-averaged value computed from a three-dimensional elasticity solution of some simple geometries and load cases. This was verified in the current work using the problem of cylindrical bending of a laminated composite plate under distributed load. Excess stiffness naturally will be predicted due to the inexact modelling of the kinematics of the transverse shearing action, in any geometry and loading configurations where the correction factor used is not appropriate. In addition, the higher maximum strain in the true distribution will induce more material nonlinearity than indicated from the first order theory.

As an extreme case, an analysis was performed in which the transverse shear moduli were reduced by a factor of ten compared to the baseline FEM case (G_{13} = 0.87 Msi, G_{23} = 0.5 Msi). This order-of-magnitude change was selected to encompass the combined effects of the kinematical constraint on transverse shearing inherent in the model and the reduced material property associated with higher strain levels present in the experimental specimens. The predicted load at the maximum value of experimental end shortening is just 3% above the experimental load, compared to the 17% overestimation of the load in the baseline FEM analysis. This reduction in predicted loads in the postbuckling response regime is not accompanied by the contra-indication of reduced prebuckling stiffness, as was the case when the fiber modulus was reduced. The dependence of the load reduction due to reduced transverse shear stiffness on the stacking sequence is illustrated in Figure 6-23. Results are presented for the three stacking sequences, using specimens having web and flange widths of 1.75 and 1.25 in., respectively. The errors of the numerical load predictions at the maximum experimental end shortenings (upon initiation of stiffness-reducing damage) expressed as a percentage of the experimental loads are +9%, -2% and -5% for the $[\pm 45/0/90]_S$, $[+30/0_2/-30]_S$ and $[\pm 45/0/90]_{2S}$ stacking sequences, respectively. In the latter two cases, the numerical load-end shortening curves fall below those of the experimental specimens. The reductions in the predicted loads as a

percentage of the baseline FEM loads are 12%, 6% and 11% for the $[\pm 45/0/90]_S$, $[+30/0_2/-30]_S$ and $[\pm 45/0/90]_{2S}$ stacking sequences, respectively. Therefore, the quasi-isotropic laminates are more sensitive to the transverse shear stiffness reduction.

A final sensitivity to be discussed is that of the magnitude of the assumed initial imperfection. This was discussed in Section 6.1.2 in connection with the determination of buckling loads. The greatest sensitivity to this magnitude was observed to occur with specimen type 131-2s, which consists of the smallest flange (0.75 in.) among the 16-ply quasi-isotropic laminates. Numerical load-end shortening curves for assumed initial imperfection magnitudes of 2.5%, 5% and 10% of the 0.08 in. laminate thickness are provided in Figure 6-24. The experimental results for specimen 131-2s-2 (adjusted for the displacement occurring in the potted end supports) are also contained in the figure. The predicted load for the 10% imperfection case at the maximum adjusted experimental end shortening value is 5% below the experimental load. The predicted prebuckling response for this model is also significantly different from the experimental response for loads above one-half the buckling load, and indicates the onset of buckling at substantially lower loads than observed experimentally. The experimentally observed prebuckling response provided a guide as to the actual value of the imperfection magnitude for those specimens that exhibited any sensitivity of the postbuckling load-end shortening response to that magnitude. The relatively larger out-of-plane postbuckling displacements among the thinner and/or wider specimens made their response insensitive to the assumed magnitude. Therefore, the value of the assumed initial imperfections actually used is not considered to be a source of significant error in the postbuckled stiffness, since either the response was insensitive to the magnitude or the prebuckling response effectively determined what the consistent assumed magnitude was.

In summary, the predicted load-end shortening responses exhibited relatively minor dependencies on physically plausible and experimentally non-inconsistent variations in the initial, constant material properties. The response was most sensitive to the fiber modulus E_{11}. This conclusion is consistent with the analyses of the postbuckling response of laminated composite plates reported in Reference 36. However, in the current work it was determined that while a slight reduction in the fiber modulus was consistent with the unreduced experimental data, such a modulus reduction was inconsistent with the experimental response once corrected for the displacement which was predicted to occur

due to the potted end supports. Therefore, it is concluded that error in the assumed initial value of fiber modulus is not a dominant source of excess stiffness in the numerical models. The effect of reducing the ply stiffness in the direction transverse to the fibers to essentially zero, such as would accompany matrix cracking, was small relative to the magnitudes of the errors in predicted loads. Similarly, a reduction in the in-plane shear modulus well within the range of secant moduli possible for the material system produced a minor load reduction. A large reduction in the transverse shear stiffness did produce a significant reduction in the predicted loads, even to the point of them being underestimated. This observation is not consistent with the conclusion of Reference 36 for laminated plates, in which it was stated that the responses were "insensitive" to transverse shear moduli. Candidate sources of excess stiffness in the numerical models which were not evaluated are the kinematical small strain assumption and the assumption of constant material properties.

6.3.3 Normalized Load-End Shortening Response

Normalized buckling load parameters were discussed in Section 6.1.4. The parameter β also normalizes the postbuckling load-end shortening responses of specimens fabricated from the various stacking sequences for a given flange-to-web width ratio. Normalized experimental load-end shortening results are provided in Figure 6-25. The load is presented as β raised to the fourth power. The parameter β appears in the form 6.2 from the solution of the characteristic polynomial of the fourth-order differential equation governing the initial buckling response, (see Section 3.1.1 and the Appendix). The load appears raised to the one-fourth power in this parameter, which tends to compress the load results. The presence of the ratios of the bending stiffnesses under the radical in this parameter tends to dampen this compression, however. In any case, the postbuckling curves based on the load normalized in terms of the parameter β become virtually horizontal deep in the postbuckling response regime. Therefore, the postbuckled loads are normalized in terms of β^4 to accurately reflect the positive postbuckled stiffness that all of these specimens exhibit and to remove any ambiguity in the effectiveness of the parameter in normalizing the postbuckled response. The end shortening is normalized with respect to the value at buckling, based on the average buckling loads of Table 5-1. The symbols denote the specific stacking sequence and are located at the ultimate failure load. The top three sets of curves illustrate that the results for the various stacking sequences are effectively normalized for a given flange-to-web width ratio. The web size for these three

cases is the same at 1.75 in. The bottom set of curves illustrates that the normalization depends only on the flange-to-web width ratio, and not on the absolute value of either element. The results in this bottom set of curves correspond to a flange-to-web width ratio of unity, but represent web widths of 0.75 in. and 1.25. It is concluded, therefore, that the parameter β effectively normalizes the buckling and postbuckling load values for the various material properties and absolute dimensions for a given flange-to-web width ratio.

6.4 Out-of-Plane Deflection

6.4.1 Displacement Magnitudes

The Direct Current Displacement Transducers (DCDTs) provided experimental measurements of the out-of-plane deflections at 3 (gage length = 6.0 in.) or 4 (gage length = 10 in.) axial locations on each specimen. These measurements were generally obtained near the flange free edges. Comparisons of the experimentally observed and numerically predicted displacement amplitudes are provided in Figures 6-26 to 6-28. The comparisons which follow should be prefaced by noting that the displacements were only sampled experimentally at a relatively few points, while the finite element solution is more "whole-field" in nature. Photographs of the flanges monitored using shadow moire indicate that a DCDT was generally located at or near an anti-node of the flange, (see for example Figure 4-8b). Still, there is no guarantee that the maximum displacement at every load occurred at a point being monitored by a DCDT. Therefore, interpretation of the significance of any experimental values which are less than the predicted amplitudes should be made with caution, since the actual maximum displacement occurring in the specimen may not have been measured.

The responses of all the 16-ply quasi-isotropic specimens are contained in Figure 6-26. The finite element predictions are based on an initial imperfection magnitude of 2.5% of the laminate thickness. The results indicate that the actual imperfection magnitudes may have been less than this, since the experimental specimens consistently exhibited a more sharply defined transition between the pre- and postbuckling load-deflection responses. The agreement in the postbuckling load range is generally good. The monotonic increase of the deflection with load is a consequence of the fact that these specimens did not undergo any mode number changes in the postbuckling regime. The maximum out-of-plane

deflection of 2.5 laminate thicknesses occurred in a specimen with the greatest flange width.

The responses of the 8-ply quasi-isotropic specimens are provided in Figure 6-27. The changes in the shapes of the load-deflection curves of specimen types 111s and 121s correspond to changes in the number of half-waves in the mode shape which occurred during postbuckling. Discussion of the specific mode shapes and changes will be provided in the next section. In general, the agreement between the observed and predicted deflections is good. Note in particular the agreement obtained for specimen type 111s. Recall that the predicted loads for these specimens were up to 23% high with respect to the experimental loads at the maximum value of end shortening. This excess stiffness of the numerical model is not observed in the out-of-plane deflection response of this specimen type, as indicated in Figure 6-27a. This observation is also true of nearly all other specimen types as well. Therefore, the results indicate that the geometric nonlinearity is modelled quite successfully with respect to the out-of-plane response.

Finally, the load-deflection responses of the $[+30/0_2/-30]_S$ specimens are provided in Figure 6-28. Again, mode shape changes (both predicted and observed) are signified by the local changes in the shapes of the curves. Overall agreement between the predicted and observed amplitudes is good prior to the development of damage in the specimens.

6.4.2 Changes in Local Buckling Mode Shape

A more definitive illustration of the ability of the numerical analyses to predict the postbuckled configuration can be obtained by contrasting the predicted and observed out-of-plane displacements at selected points along the gage length. For example, the mid-height flange-end displacements for specimen 111s-1 are contained in Figure 6-29a. The experimental results (solid lines) and numerically predicted responses (broken lines) indicate that two mode changes are observed and predicted reasonably well. The mid-height, flange-end responses for specimen 111-2s-1 are contained in Figure 6-29b. No mode changes are encountered in this case. After buckling, the agreement between the experiments and analysis is nearly perfect. The responses for two specimens of the $[+30/0_2/-30]_S$ stacking sequence are provided in Figure 6-30. The first mode change in specimen 111orth-1 (Figure 6-30a) is predicted well. Note that the numerical model

predicts a second mode change at 2000 lb, which the experimental specimen does not experience. The load at which this second mode change is encountered coincides with the predicted maximum transverse tensile strain reaching a nominal strength value of 0.46% (based on Y_t = 7.5 ksi, and E_{22} = 1.64 Msi). Therefore, the departure of the predicted and observed mode shapes may be partly due to the development of damage in the specimen. The results for a second specimen of the $[+30/0_2/-30]_s$ stacking sequence (111orth-2) are provided in Figure 6-30b. In this case, the two mode changes are both predicted and observed.

6.4.3 Scaling of the Response

The results of the preceding section demonstrate the ability of the numerical analyses to predict the out-of-plane deflection responses of the largest specimens. The purpose of the present section is to identify the presence of any "scale effects" in the response of the smaller specimens. Recall that the working definition of a "scale effect" in the mechanistic approach to scaling being used here is the departure from the mechanics model of the observed response, which occurs systematically with the specimen size. The experimental and finite element predictions of the out-of-plane deflections for specimens 231s-1 and 331s-2 are contained in Figures 6-31a and 6-31b, respectively. The web widths of these specimens are 1.25 and 0.75 in., respectively, in contrast to the 1.75 in. web width of the specimens discussed in Section 6.4.2. The flange width is 0.75 in., as opposed to the 1.25 in. flange width of the specimens discussed above. Direct Current Displacement Transducer (DCDT) data and finite element nodal displacement values at the ends of the flanges at the mid-height axial location are presented.

The correlation between the experimental and numerical responses of specimen 231s-1 is nearly perfect throughout the entire load range (Figure 6-31a). The correlation is less good for specimen 331s-2 (Figure 6-31b). The observed difference in the prebuckling response is no greater than that observed in the larger specimens, however. The prebuckling response at a given point is naturally very sensitive to the nature of the actual local imperfection. Therefore, some difference in the predicted and observed prebuckling responses at a specific point is anticipated. The agreement between the postbuckling responses of one flange of specimen 331s-2 is good. The correlation between the experimental and numerical responses is less good for the other flange. Here, the

agreement is good while the specimen begins to buckle. Immediately thereafter, however, a discontinuity develops in the experimental response, with the result that less out-of-plane deflection was observed experimentally than predicted. Still, the overall correlation between the experimental and finite element responses is considered good for the smaller specimen sizes. No systematic degradation in the ability of the mechanics model (FEM) to predict the response was observed to occur as a function of specimen size. Therefore, the presence of scale effects was not indicated.

6.4.4 Axial Distribution of Out-of-Plane Displacement

Results of the numerical analyses will now be used to further characterize the postbuckling mode shapes. The predicted development of the mode shapes in the postbuckling response regime can be illustrated by the distribution of the out-of-plane displacement along the gage length at the end of the flange as a function of load. Displacement distributions of this type are contained in Figures 6-32a, 6-32b and 6-33 for specimen types 111-2s, 111s and 111orth, respectively. The evolution of the mode shape with increasing load for the 16-ply quasi-isotropic specimen type 111-2s is characterized only by increasing displacement amplitudes, with no change in the number of half-waves (Figure 6-32a). The 8-ply quasi-isotropic specimen type 111s undergoes increasing displacement amplitudes, but also a change in the number of half-waves from 3 to 4 at approximately 2500 lb (Figure 6-32b). The higher longitudinal bending stiffness of the $[+30/0_2/-30]_S$ laminate results in fewer half-waves in the buckled mode shape for a given geometrical configuration. At a load of 1200 lb, for example, specimen 111s of the $[\pm 45/0/90]_S$ stacking sequence exhibits three half-waves, while specimen 111orth exhibits only two (see Figures 6-32b and 6-33).

6.5 Secondary Mode Interaction

A second characteristic of the postbuckled mode shapes is the distortion which takes place as a result of coupling between bending and twisting actions. This coupling results from the D_{i6} (i=1,2) material bending stiffnesses. The twisting of the section is manifested by a shift in the axial locations of wave crests from the end of one flange compared to the other. The presence of twisting is further indicated by oppositely signed in-plane displacements at the ends of the flanges. These phenomena are illustrated by the

finite element results presented in Figures 6-34 through 6-36, for specimen types 111-2s, 111s and 111orth, respectively. The relative magnitudes of the bending-twisting coupling stiffnesses (D_{16}/D_{11}) for these three cases are 0.06, 0.16 and 0.21, respectively. There is little difference from one side of the section to the other in the locations of the nodal and anti-nodal positions for specimen 111-2s (Figure 6-34a). This is a reflection of the relatively low coupling that is present in the 16-ply quasi-isotropic laminate. The in-plane displacements indicate that some twisting is occurring, but the displacement magnitudes are on the order of only two ply thicknesses (Figure 6-34b). The relative coupling term is much greater in the 8-ply quasi-isotropic laminate, with the result that much more twisting of the section occurs. From Figure 6-35a, it can be seen that there is an approximately one inch difference in axial location of wave crests between one flange and the other. In addition, the magnitude of the in-plane displacements are on the order of 6 ply thicknesses (Figure 6-35b). Finally, the magnitude of the bending-twisting coupling is still greater in the $[+30/0_2/-30]_s$ laminate. Differences in the axial location of wave crests from one flange to the other are approximately two inches for this case (Figure 6-36a). The equal magnitude, but oppositely signed in-plane displacements further indicate the presence of twisting of the section (Figure 6-36b).

There is ample experimental evidence that the predicted twisting actually occurred. The shadow moire fringe patterns (Figures 5-19 to 5-21) indicate the presence of twisting by the distortion of the contour patterns which increases in proportion to the relative magnitude of the bending-twisting coupling (D_{16}/D_{11}). The displacement transducer data also indicate twisting by the difference in magnitudes from one flange to the other at a given axial location. This is illustrated in Figure 6-37, using data from specimens 111-2s-2 ($D_{16}/D_{11} = 0.06$) and 111orth-1 ($D_{16}/D_{11} = 0.21$). The data shown were obtained from displacement transducers located near two adjacent anti-nodes of the buckled configuration. The data for specimen 111-2s-2 indicate that the flanges were "in-phase" with each other; that is, the displacements were of the same sign and approximately the same magnitude at a given axial position (Figure 6-37a). The low relative bending-twisting coupling of this laminate produced little distortion of the mode shape. The response of specimen 111orth-1 is significantly different (Figure 6-37b). Here, the magnitudes of the out-of-plane displacements are markedly different between the two flanges. In fact, in the initial postbuckling load range, one flange developed significant bucking displacements, while the other at the same axial location, was practically at a nodal position. The displacements of

"flange 1" at an axial position of 7 in., remained approximately the same as those of "flange 2" at an axial position of 5 in. Thus, the predicted two inch shift in the mode shape discussed above was also observed experimentally.

Twisting of the sections may result from simply the bending-twisting coupling present in these laminates, or a secondary torsional mode interaction, which is possible even in isotropic materials. In an attempt to quantify the material and structural contributions to the twisting, a finite element analysis of specimen type 111orth was performed, in which the bending-twisting coupling terms were set equal to zero. The resulting displacement distributions along the gage length are shown in Figure 6-38. It is apparent from the out-of-plane displacements (Figure 6-38a) that no distortion of the mode shape occurs over the cross-section when the coupling terms are omitted. That is, the axial positions of the nodes and anti-nodes do not vary over the cross-section. The in-plane displacements predicted by both the baseline FEM analysis and the analysis in which the coupling terms are neglected are shown in Figure 6-38b. The results clearly indicate that twisting of the section occurs in both instances. The flange-end in-plane displacements for the zero coupling case are nearly perfectly equal, but oppositely signed, with slightly smaller magnitudes and no width-wise distortion compared to the case in which the coupling terms are included. The results for the two analysis types indicate that the distortion of the mode shape with respect to the shift in the axial locations of nodes and anti-nodes in the width-wise direction of the specimen is due to the material-related bending-twisting coupling present in the laminates. This twisting is naturally present only in local regions where bending occurs. The more global twisting of the sections, as indicated by the equal, but oppositely signed in-plane displacements at the flange ends is caused by a secondary, torsional mode interaction. The occurrence of this mode interaction regardless of whether the coupling terms are included indicates that the interaction is a structural, rather than a material, response phenomenon.

In general, the vast majority of geometrical configurations were predicted to exhibit only twisting interaction. Specimens of the smallest flange-to-web width ratio, however, were predicted to undergo a flexural mode interaction. The transition from a torsional to a flexural mode interaction with decreasing flange size is illustrated in Figure 6-39 for specimens of the 8-ply quasi-isotropic stacking sequence. The maximum in-plane displacements at the flange ends and at the center of the web are plotted as a function of

axial load in the figures. The axial location of the maximum in-plane displacements is at or near the mid-height position. The results for specimen type 111s with the widest flanges (1.25 in.) are shown in Figure 6-39a. The flange-end displacements are nearly equal, but oppositely signed, which is characteristic of the global twisting discussed above. The in-plane displacement at the web center exhibits a slightly positive value (the sign convention is illustrated in the figures). Therefore, the center of twist is migrating along the web toward one of the flanges. The response of the specimen with a flange width of 0.75 in. (131s) is contained in Figure 6-39b. Here, the flange-end displacements are oppositely signed, but the absolute magnitudes differ by a factor of two at the higher loads. The in-plane displacement of the web is virtually zero. Thus, twisting of the section is still occurring, but the center of twist is migrating approximately perpendicular to the web. Finally, the results for the smallest flange width (0.50 in., specimen type 141s) are given in Figure 6-39c. The in-plane displacements at the ends of the two flanges are approximately equal and of the same sign. The in-plane displacement at the web center is negatively signed. This combination of displacements indicates that the specimen is undergoing a flexural mode interaction about the minor axis of the cross-section. The implication of these results for a scaling study based on the mechanistic approach is that a complete mechanics model must be able to account for the differing influence and type of secondary mode interaction that might occur as specimens are "selectively" scaled; that is, as only a subset of the geometric and material parameters are scaled.

6.6 Analysis of Strain Data

6.6.1 Predicted and Experimental Longitudinal Strains

The goal of this section is to establish the credibility of the finite element strain predictions in the postbuckling response regime. This is desirable to permit use of these results to complement the experimental strain gage data in evaluating the crippling mechanisms. Predicted and measured longitudinal membrane and bending strains at various points over the specimen width at a certain axial location are plotted versus the end shortening in Figures 6-40 to 6-42. Strain data are provided at the flange end, corner and mid-web locations. The axial locations correspond to anti-nodes in the buckled shape and are either at L/2 or L/3, for gage length, L. Naturally, the agreement obtained will be very sensitive to the precise axial locations of the anti-nodes. Results for specimen 111-2s-2

(b_w = 1.75, b_f = 1.25, r = 0.125 in., $[\pm 45/0/9]_{2s}$) at the mid-height location are contained in Figure 6-40. The membrane strain data of Figure 6-40a indicate that the corner strain magnitudes are predicted exceptionally well. The strain concentration into the corners and the unloading of the flanges and web after buckling is also apparent. The amount of unloading of the web due to buckling is greater than the predicted amount by 0.001 strain. The amount of unloading at the flange ends is less than the predicted amount by slightly more than 0.001 strain. Some discrepancy at the flange ends is expected since finite element nodal values at the ends of the flanges are being compared to strain gage readings, which represent an average value of some finite width region near the flange end. The bending strain predictions are seen to be excellent in Figure 6-40b, with the maximum bending occurring at the flange ends and essentially none in the corner regions.

The same strain comparisons are provided in Figure 6-41 for specimen 111s-1 (b_w = 1.75, b_f = 1.25, r = 0.125 in., $[\pm 45/0/9]_s$) at the mid-height location. The nature of the agreement between the predicted and measured strains is similar for this specimen, as discussed for the 16-ply quasi-isotropic case above. The predicted corner strain magnitudes become slightly greater than observed late in the postbuckling response. Note that a mode change is observed and predicted at a length-normalized end shortening value of 0.0035. Once again, more unloading of the web center and less unloading of the flange ends occurs experimentally than is predicted.

Finally, the strain comparisons for specimen 111orth-2 (b_w = 1.75, b_f = 1.25, r = 0.125 in., $[+30/0_2/-30]_s$) at the axial location L/3 are provided in Figure 6-42. The prediction of the membrane strain magnitude in one corner is nearly perfect, while a discrepancy between the observed and predicted magnitudes develops in the other corner late in the postbuckling response. This latter corner is adjacent to the flange which did not undergo the second predicted mode change, as discussed above and shown in Figure 6-30a. The same trends in the amount of unloading at the flange ends and the web center are encountered for this stacking sequence, as discussed above. The bending strain predictions in the web and one flange are excellent (Figure 6-42b). Note that the predicted and observed responses of the other flange are qualitatively the same, but with a difference in magnitudes. The various observations for this flange indicate that there is a difference in the predicted and observed response of this specimen, but that this is restricted primarily to the axial position of the anti-node in one flange. The correlation of the responses for the

remainder of the specimen is good. There is essentially no bending in the corners. Note that the magnitude of the bending is not the same in the two flanges, due to the bending-twisting coupling present in this laminate.

6.6.2 Scaling of the Response

The ability of the numerical analyses to predict the development of strain in the largest specimens was demonstrated in the preceding section. The presence of any non-scaled behavior in the response of the smaller specimens will be discussed in this section. Membrane and bending strain distributions of the type used in the previous section are provided in Figures 6-43 and 6-44 for specimens 231s-1 and 331s-2, respectively. The web widths of these specimens are 1.25 and 0.75 in., respectively. The flange width is 0.75 in. The stacking sequence is $[\pm 45/0/90]_S$.

The membrane strain distribution over the cross-section of specimen 231s-1 (Figure 6-43a) is phenomenologically the same as discussed in Section 6.6.1 for the larger specimens. Membrane strain concentrates into the corners, while the flange ends essentially completely unload. Less unloading at the web center occurs, since the specimen is flange critical. The nature of this strain redistribution in the smaller specimen as a result of buckling is predicted at least as well as for the larger specimens. The bending strain distribution in specimen 231s-1 (Figure 6-43b) is likewise predicted well. In fact, the absence of mode number changes in the smaller specimen simplifies the response to the extent that the overall agreement between the experiments and the numerical model is better.

The membrane strain distribution for specimen 331s-2 is shown in Figure 6-44a. The overall response is predicted well. The unit value of the flange-to-web width ratio (b_f/b_w) of this specimen is reflected in the fact that the web center continues to carry additional load in the postbuckling load range, as discussed in Section 5.2.2. The strain level in one flange remains constant after buckling, while the other flange unloads. These responses are directly related to the difference in the out-of-plane deflections indicated for the flanges in Figure 6-31. The variation of the deflection and strain responses from one flange to the other is again caused by the twisting mode interaction present in these specimens. The bending strain distribution for specimen 331s-2 is predicted very well (Figure 6-44b).

In summary, the predictions of the strain distributions in the smaller specimens are at least as good as for the larger specimens. No non-scaled behavior is indicated, since no systematic change in the ability of the mechanics model to predict the response was observed to occur with specimen size.

6.7 Crippling Response

The comparisons discussed above between the observed and predicted out-of-plane deflections, postbuckled mode shapes and strain magnitudes suggest that the numerical model can quite adequately represent at least some of the local features of the postbuckling response. These comparisons inspire confidence in the use of the predicted strain distributions to aid in the evaluation of the crippling modes which follows. The magnitudes of the strains will be discussed first, followed by illustration of the local structural deformation patterns, which are responsible for the maxima in the various strains. Finally, these analyses will be related to the experimentally observed failure modes and locations.

6.7.1 Predicted Maximum Material Strains

The maximum tensile and compressive strains computed in the local material coordinate system as a function of the normalized end shortening, u/L, are summarized in Figures 6-45 to 6-48. All three stacking sequences are represented. The geometries consist of $b_w = 1.75$, $b_f = 1.25$ and 0.75, and $r = 0.125$ in. Both in-plane extensional and shear strains, and the average transverse shear strains are presented. Nominal strength values of the in-plane strains based on Ref. 37 data are also indicated on the figures. The curves are terminated at the value of end shortening at which stiffness-reducing laminate damage developed or crippling of the experimental specimens occurred.

The in-plane maximum tensile fiber strains are presented in Figure 6-45a. Only specimen type 111s (large flange, $[\pm 45/0/90]_s$) exhibits maximum values at crippling near the strength value of 1.1% strain. All but one of the other specimen types exhibit a maximum tensile fiber strain of 0.6%. The fiber strain in the remaining specimen (111orth) is even lower, at just 0.35% strain. In summary, a primary crippling mechanism of fiber

tension would only be plausible in specimen 111s, which exhibited the most extensive postbuckling load range. The maximum in-plane tensile matrix strains, ε_{22}, are shown in Figure 6-45b. It is immediately apparent that all of the specimen types greatly exceed the nominal matrix strength in tension, in contrast to the low "usage" of the fiber strength in tension noted above. The implication is that both the Tsai-Wu (maximum strain) and Tsai-Hill ("interactive" quadratic) strength criteria are inadequate when based on the tensile matrix strains. One physical interpretation is that some matrix cracking must develop in the specimens at loads far below the ultimate failure load. In fact, the characteristic sound of matrix cracking was often audible during the experiments. This matrix cracking will certainly change the character of the material locally (the constitutive relation, at the very least) in some way, which is not included in the numerical model. It was noted in Section 6.3.2 that matrix cracking might not significantly alter the overall specimen stiffness. However, specimen failure is almost certainly related to a local deformation pattern, which could be dramatically affected by the presence of matrix cracking. Therefore, the large tensile matrix strains may invalidate the numerical analyses of the local strain states to some extent, late in the postbuckling response.

The maximum fiber compressive strains are indicated in Figure 6-46a. The nominal strength value is based on assuming equal fiber strengths in tension and compression as a first approximation. Note that specimen 111s exceeds the compression strength by a significant amount, whereas it only matched the strength value in tension. The results suggest that fiber failure in compression might be expected before a tensile failure. The quasi-isotropic specimens (both 8- and 16-ply) having the smaller flange width (0.75 in.) are predicted to meet the fiber compression strength value upon crippling. Once again, the "usage" by the $[+30/0_2/-30]_S$ specimens of the fiber strength in compression is low. Therefore, a primary crippling mode of fiber compression failure is plausible for the quasi-isotropic specimens only. The maximum compressive matrix strains are shown in Figure 6-46b. Only specimen type 111s exceeds a nominal strength value of 1.8% strain. Since the amount by which this strength value is exceeded is less than that associated with the matrix tension and fiber compression criteria, it is anticipated that matrix compression is not a primary crippling mechanism.

The maximum in-plane shear strains are presented in Figure 6-47. Most of the specimens exhibited shear strains at crippling fairly close to the strength value of 1.6%.

Once again, the strain in specimen 111s is nearly double the strength value. The maximum average transverse shear strain, γ_{xz}, is contained in Figure 6-48a. Recall that "x" and "z" are the axial and laminate thickness directions, respectively. Note that the first order shear deformation theory upon which the numerical model is based, assumes a constant strain value over the thickness, as opposed to the quadratic shear strain distribution which likely exists. Thus, the true maximum value (at the mid-plane, for example) will be greater than the values illustrated. Here, the 16-ply quasi-isotropic specimens exhibit the largest values of strain, with the average values reaching 1.2% in the specimen with the smaller flanges. Maximum average values of near 0.8% occur in the specimen with the larger flange, and in the 8-ply quasi-isotropic specimen of the narrower flange. The average value in specimen 111s (which has met or exceeded all previous strength values) at failure is only 0.5%. The results for the $[+30/0_2/-30]_S$ specimens are even lower. Insofar as the transverse shear may be related to the onset of delamination, it is apparent that this crippling mode might be most prevalent among the thicker specimens, and the 8-ply quasi-isotropic specimens with the narrower flanges. The maximum average transverse shear strain, γ_{yz}, is contained in Figure 6-48b. Note that "y" is the width-wise direction, perpendicular to the loading axis. Specimen 111s achieves a maximum of 1.0% strain, while all other specimens fail at values at or below 0.4% strain. Thus, only in specimen 111s would delamination induced by this shear strain be plausible.

6.7.2 Structural Deformation Associated With Maximum Strains

The purpose of this section is to identify the structural response mechanisms which produce the maximum strain states discussed above. This is necessary in support of relating the predicted locations of the most severe strain conditions to the experimentally observed failure locations.

The locations of maximum extensional strains are illustrated on a deformed mesh in Figure 6-49. The local deformation patterns which determine the maximum material strains are related to the overall postbuckled mode shape. The location of maximum fiber compression is generally at a peak in a buckled flange, on the more compressive side, near the flange-to-corner junction (Figure 6-49, upper right). This occurs in the outermost 0° ply of the quasi-isotropic laminates and in the surface +30° ply of the $[+30/0_2/-30]_S$ laminate. Maximum compression there results from a combination of the strain

concentration into the corner and bending of the flange. Maximum fiber and matrix tension in the 16-ply quasi-isotropic specimens are associated with transverse bending of the web at an anti-nodal position (Figure 6-49, middle right). Fiber tension occurs on the tensile side of the wave in the outermost 90° ply, while matrix tension occurs in the adjacent 0° ply. Maximum fiber and matrix tension in the 8-ply laminates occurs in the flange-to-web corner at a nodal position of the buckled mode shape (Figure 6-49, lower right). The corner undergoes twisting about the longitudinal axis due to the change in sign of the out-of-plane displacements from above to below the nodal position. A surface in-plane shear condition in the global (not material) coordinate system results from this twisting, as indicated in the figure. This global shear state can be resolved into a biaxial strain state of equal, but oppositely signed strains in the material coordinate system, also shown in the figure. Thus, maximum fiber tension occurs in the surface +45° ply, and maximum matrix tension occurs in the -45° ply underneath. Both of these maximum strains occur at the inside diameter of the corner. In the case of the $[+30/0_2/-30]_S$ laminate, maximum fiber tension occurs in the inside diameter surface +30° ply, while matrix tension occurs in the opposite +30° ply on the outside diameter. In summary, crippling mechanisms which are dominated by tensile strains are anticipated to occur at anti-nodal axial positions in the 16-ply laminates, and at nodal locations in the 8-ply laminates. Crippling mechanisms dominated by fiber compression are anticipated to occur at anti-nodal axial positions.

The locations of maximum shear strains are illustrated on a deformed mesh in Figure 6-50. The location of maximum transverse shear strain γ_{yz} is at the flange-to-web corner at an anti-nodal position (Figure 6-50, upper left). This shear strain results from the compatibility enforced between the flange and the corner. The transverse shear force applies the constraint of the corner onto the flange (in addition to a bending moment). This transverse shear is greatest at an anti-nodal position, since that is where the greatest difference in the out-of-plane displacements between the free end of the flange and the corner occurs, and hence where the constraint of the corner is greatest. The location corresponding to the maximum of the other transverse shear strain, γ_{xz}, is at a nodal position, typically at the flange free edge (Figure 6-50, lower left). This transverse shear is necessary for overall axial force equilibrium at nodal positions, where the angle between the load axis and the plane of the laminate (and, therefore, the in-plane force resultant) is the greatest. The magnitude of this shear is then a function of the out-of-plane displacement, the wavelength of the mode shape and the amount of the postbuckling load

being carried there. The maximum in-plane shear develops in the flange-to-web corner at an anti-nodal position in the mode shape (Figure 6-50, middle left). This location is subjected to a biaxial strain state in the global coordinate system, caused by longitudinal compression in the corner and transverse tension due to the buckling displacements. This global, biaxial strain state can be resolved into an in-plane shear condition in the local, material coordinate system, as shown in the figure. In summary, primary crippling mechanisms related to transverse shear-induced delamination might be anticipated at both nodal and anti-nodal positions, while mechanisms dominated by in-plane shear are expected to occur at anti-nodal axial positions.

The finite element predictions of the maximum strain locations can be summarized as follows: Strains which are greatest at the nodal positions of the mode shape are fiber and matrix tension in the 8-ply laminates, and transverse shear, γ_{xz}. Strains which are maximized at peaks in the mode shape are fiber and matrix tension in the 16-ply laminates, in-plane shear and fiber compression. What has been neglected in this discussion is the effect of interaction among the strains. The most severe strain state with respect to material failure could easily be associated with a combination of strains, none of which are actually maxima at the particular location. Thus, the above analysis is only intended to guide the evaluation of the responsible crippling mechanisms.

6.7.3 Crippling Mechanisms

The crippling load data of Table 5-2 were discussed in Section 5.3.1. Additional experimental details pertinent to the discussion of the crippling mechanisms are contained in Table 6-4. Included are the number of half-waves in the buckled configuration at failure, the axial location of the visible laminate damage after failure and identification of this location in relation to nodes and peaks in the buckled mode shape.

The failure locations in the 16-ply quasi-isotropic specimens corresponded to both nodal and anti-nodal axial locations, as indicated in Table 6-4. Specimen 111-2s-1 failed at an anti-nodal location. A preliminary failure event was observed at a load 600 lb below the ultimate failure load. The local failure event was characterized by sudden increases in the the flange end displacements and the transverse corner opening strains at the axial location where final failure occurred. It is postulated that the preliminary failure event corresponded

to development of damage in the corners, possibly by in-plane shear. The resulting loss of constraint by the corner on the flanges would be responsible for the sudden increases in flange-end displacements. This corner damage would be a likely initiation site for the extensive flange delamination that was observed. A second specimen which failed at an anti-nodal position was specimen 121-2s-1 (Figure 5-23b,c). The post-test appearance of this specimen is characterized by a bending compression failure of several outer plies of one flange, from which delamination propagated. The other flange and the web appear to have failed in bending due to the overloading caused by the failure in the first flange. Both of the above anti-nodal failure scenarios are consistent with the structural-material interaction predicted numerically and discussed in Section 6.7.2. Significant flange end delamination was observed in both instances. Flange end delamination may be associated with the transverse shear strain, γ_{xz}, which was shown in the previous section to be greatest at nodal positions. The apparent contradiction is resolved by the initiation sites for delamination which could be produced by other damage mechanisms. In the case of specimen 111-2s-1, this mechanism was likely in-plane shear at the corner, as predicted from the numerical analyses. For specimen 121-2s-1, the mechanism may have been compression fiber failure in bending, also consistent with the numerical analyses.

Most of the other 16-ply quasi-isotropic specimens failed at nodal positions. Flange end delamination was the primary failure mode in these cases. Typically, significant delamination was observed in one flange (e.g. Figure 5-23a), with the web failing due to the associated overloading in bending (Figure 5-23c, 5-24b, 5-25b). Failure modes of the other flange consisted of free end delamination, crushing in compression (Figure 5-23b) and compression failure in bending. The total amount of visible post-test laminate damage was generally proportional to the crippling stress, and therefore the strain energy. For example, the post-test appearance of the wide flange specimens (low crippling stress) was characterized mostly by free edge delamination and relatively few visible fiber fractures (e.g. Figure 5-23a). The crippling stresses of the narrow flange specimens were higher. The higher strain energy at failure was reflected in the development of damage over the entire cross-section of the specimens (e.g. Figure 5-26b).

Most of the specimens of the $[+30/0_2/-30]_s$ stacking sequence did not exhibit any flange end delamination, in contrast to the dominance of that mode in the $[\pm 45/0/90]_{2s}$ specimens discussed above. Instead, failure of the "orthotropic" specimens was dominated

by corner damage at axial locations corresponding to anti-nodes in the buckled mode shape. The discussion of Section 6.7.2 indicated that the in-plane shear strain is a maximum at the outside diameter of the corner at an anti-node due to the biaxial loading composed of longitudinal compression and transverse bending tension. All of the orthotropic specimens exhibited a preliminary failure event at loads approximately 400 lb below the maximum load achieved. These local failure events were accompanied by sudden increases in the flange end displacements and transverse corner strains at a particular axial location. Thus, it is believed that these local failure events corresponded to the development of corner damage, most likely due to in-plane shear (e.g. near the painted flange in Figures 5-29c, 5-29d). The loss of some integrity of the corner is believed to be responsible for the vertical splitting at the flange-to-corner junction (Figure 5-29d). This is caused by the reduced ability of the degraded corner to resist the transverse shear resultant Q_{yz}, which is predicted to be a maximum at an anti-nodal position. One specimen of the 0.75 in. flange width and all specimens of the 0.5 in. flange width exhibited flange end delamination, in addition to the corner damage discussed above. The data of Figure 6-48a indicate that the transverse shear strain, γ_{xz}, is predicted to be greater for the smaller flange widths. Thus the appearance of the delamination mode in the specimens with the smaller flange widths might be anticipated based on both the finite element analyses and the increased free edge stresses associated with the smaller width/thickness case. Apart from the delamination appearing in the smaller specimens, the failure characteristics of the orthotropic specimens were remarkably consistent between specimens.

The 8-ply quasi-isotropic specimens typically exhibited both flange end delamination and corner damage. The failure locations generally corresponded to nodal positions in the buckled mode shape. The corner damage mode was crushing in compression (e.g. near point "1" in Figures 5-27b and 5-28b), in contrast to the shear mode discussed above for the $[+30/0_2/-30]_s$ specimens. In general, it could not be positively determined whether flange end delamination or corner crushing was the primary crippling mechanism. Note also that very high tensile matrix strains were predicted for specimens of this laminate, as shown in Figure 6-45b. It is not certain what role these strains have, if real, in the determination of the crippling mechanism. Visible matrix cracking was photographed in one specimen (212s-1) in the corner region at an anti-nodal position at a load 200 lb below the final failure load. Thus, it is clear that tensile matrix

strains sufficient to cause local material failure did occur, but that such failures were not necessarily immediately catastrophic.

In summary, the experimental failure locations did correspond to the locations of maximum strain predicted by the finite element analyses. The observed failure mechanisms could be related to the structural deformations, in the same way that the predicted maximum strains were related to the predicted deformed mode shape. However, the maximum strain-type analyses could not predict which of several plausible failure modes would determine failure and at what load it would occur. It should also be noted that the finite element formulation did not include the interlaminar normal stress. Attempts to correlate an average value of the normal stress with the onset of delamination have been successful using uniaxial test data [38]. The analyses performed in the current work clearly could not predict the variations in the failure modes among replicate specimens. For example, specimen 111-2s-1 failed at a peak location, while replicate specimens 111-2s-2 and 111-2s-3 failed at nodal positions. The numerical analyses, therefore, were useful in guiding the interpretation of the observed crippling phenomena, but could not provide a quantitative prediction of the crippling loads or a precise determination of the responsible failure mechanism. The above discussion of the predicted strain development and the observed crippling responses should be placed in the context of the characteristics of the real material discussed in Section 4.3. Recall that the laminate is modelled as being comprised of uniform, homogeneous, orthotropic layers. The photographs contained in Figures 4-3 and 4-4, indicate that the real material was anything but homogeneous and uniform, at least in the corners of the older material. The significance of this nonuniformity in the corners is aggravated by the fact that the load is concentrated into the corners during additional loading in the postbuckling range. Since damage development and failure are inescapably related to the local deformation and material states, it is anticipated that only with more detailed analyses of the local geometry will a mechanics-based failure prediction capability be realized.

6.7.4 Strength Scale Effects

Overall, average stress values (i.e. load/area) may be expected to scale directly for some responses of a model which has been scaled according to the laws of similitude. A global measure of the existence of strength scale effects is then based on whether the

average failure stress (of the P/A type) is the same between specimens of various size scales. Failure phenomena in composite materials, however, occur on a much more local scale. That is, failure of a laminate might be determined by the local stress state within and/or between individual plies. Therefore, a definitive statement of the presence of strength scale effects cannot be made solely on the basis of some overall, average failure stress data. What must also be considered is to what extent the local stress state responsible for failure and the failure mode itself are reproduced among the specimens of differing scales.

The mechanistic approach to scaling used in the present work relies on the use of mechanics models as the bases on which to determine the scalability of the response. This approach does not require that the models be scaled according to the laws of similitude, provided a suitable mechanics model is available. Indeed the specimens of the current study have not been scaled in the rigorous manner. It is clear from the previous section, that a suitable mechanics model has not been found which governs the crippling response. Therefore, neither directly scaled specimens nor a suitable model is available with which to evaluate the existence of strength scale effects.

The available experimental data can be used, however, to provide a limited indication of the absence of any significant scale effects in the observed crippling responses. Consider the specimen type 111-2s. The web and flange widths are 1.75 and 1.25 in., respectively. The stacking sequence is 16-ply quasi-isotropic. Let this specimen be considered to be of "size 2", that is having been scaled-up from a smaller specimen using a scale factor of 2. The corresponding "size 1" specimen would have dimensions b_w = 0.875 and b_f = 0.625 in. The 8-ply quasi-isotropic laminate would be the scaled down stacking sequence, based on the sub-laminate scaling method. A specimen of the indicated dimensions does not exist in the database of the current work, however. The nearest available dimensions are b_w = 0.75 and 1.25 in., and b_f = 0.5 and 0.75 in. An approximation of the buckling and crippling stresses of this hypothetical "size 1" specimen will be constructed by linearly interpolating between the available experimental data points, contained in Tables 5-1 and 5-2. While the functional dependence of buckling and crippling on the flange and web dimensions is not generally linear, the differences in the magnitudes over which the interpolation is made are not large. In addition, the dimensions of the hypothetical specimen are fairly close to those of one for which experimental data are

available. A similar hypothetical "size 1" specimen can be constructed to correspond to the actual "size 2" specimen type 121-2s. The dimensions of the latter specimen are $b_w = 1.75$ and $b_f = 1.0$ in.. The laminate is again the 16-ply quasi-isotropic stacking sequence. The corresponding "size 1" specimen would have dimensions $b_w = 0.875$ and $b_f = 0.50$ in. Note that this flange size does exist in the experimental database, thereby limiting the necessary interpolation to the web width only.

The buckling and crippling stresses of these hypothetical specimens are contained in Figure 6-51, normalized with respect to the respective buckling and crippling stresses of the corresponding experimental "size 2" specimens. The successful normalization of the buckling responses discussed in Section 6.1.4 indicates that the initial local buckling loads were scalable. The approximately unit values of the normalized buckling stresses of the hypothetical scaled specimens in Figure 6-51 is a reflection of the scaled buckling responses observed, and provides some confirmation of the validity of this interpolation scheme. The normalized crippling stresses of the hypothetical scaled specimens in Figure 6-51 are likewise near unity. This result provides some indication that no significant strength scale effects were experienced, based on an overall, average measure of the response phenomenon. The post-failure appearances of the large and small specimens of a given flange-to-web width ratio exhibited the same basic features of flange end delamination and crushing in the corner. Whether or not the actual failure mechanism was common to both size specimens cannot be stated with certainty. A more definitive determination of strength scale effects in stiffener crippling would require additional experimental data based on a set of rigorously scaled specimens, with some means of determining the precise failure mechanisms in the specimens of the various sizes.

CHAPTER 7. SUMMARY AND CONCLUSIONS

An investigation of the scalability of the responses of a representative laminated composite structure has been performed. The configuration used was the Z-section stiffener loaded in uniaxial compression. The response modes evaluated were prebuckling stiffness, initial local buckling, postbuckling and crippling. An analytical, numerical and experimental approach has been used. The analytical model is a linked plate analysis in which the elastic constraint of the flange-to-web corner is included. First order shear deformable degenerated shell elements in the ABAQUS finite element code were used for the numerical analyses. Testing of fifty-two experimental specimens of seventeen basic geometrical configurations and three stacking sequences was performed at NASA Langley Research Center. A mechanistic approach to scaling has been used, in which the scalability of the responses have been judged relative to governing mechanics models. Use of this approach facilitated the evaluation of both parametric sensitivities and the scalability of the responses.

7.1 Parametric Sensitivities

The buckling, postbuckling and crippling responses were largely determined by the flange-to-web width ratio and both the absolute and relative values of the bending stiffnesses. Specimens with wider flanges buckled at lower average stresses, since the flanges were too wide to efficiently stiffen the web without themselves limiting the buckling resistance. The postbuckling load range was the greatest in the specimens with the wider flanges, since the wide, flexible flange elements were more capable of undergoing large out-of-plane displacements. While the postbuckling load range was greatest in specimens with the wider flanges, the ultimate average failure stresses were greatest among the narrower specimens. Buckling loads were higher in specimens with a larger flange-to-web corner radius. The greater radius of curvature provided additional resistance to bending, and therefore the initiation of buckling. The increase in load at buckling for specimens of the larger corner radius was maintained throughout the postbuckling response. The buckling loads increased with the cube of the laminate thickness among otherwise identical geometries, commensurate with the increase in the

absolute magnitudes of the bending stiffnesses. The buckling loads decreased for specimens of an orthotropic stacking sequence compared to identical specimens of the quasi-isotropic laminate of the same thickness. The large increase in the longitudinal bending stiffnesses of the orthotropic laminate was more than offset by a decrease in the transverse properties.

The crippling mechanisms included flange free edge delamination at both nodal and anti-nodal axial positions, material crushing in the flange-to-web corner at nodal axial positions, and ply splitting in the flange-to-web corner at anti-nodal axial locations. Flange free edge delamination dominated the crippling response of the 16-ply quasi-isotropic specimens, but was entirely absent in the wide-flanged specimens of an orthotropic laminate. Failure of these latter specimens was dominated by damage of the flange-to-web corners in a ply splitting mode. This splitting was likely caused by matrix cracking and/or in-plane shear. The crippling response of the 8-ply quasi-isotropic specimens exhibited both delamination at the flange free edges and material crushing in the flange-to-web corner.

7.2 Scaling Considerations

The constraint of the potted end supports of the experimental specimens was not scaled, and therefore, varied as a function of the geometric and material parameters. The effect of displacements within the end supports was manifested by lower prebuckling axial stiffnesses than predicted based on the gage length properties alone. This phenomenon required a post-test adjustment to the data in order to permit comparisons of the experimental and finite element predictions of the response of the gage length on an equivalent basis. These adjustments were based on finite element analyses of the constraint of the end supports using potting material properties measured from coupons removed from actual end supports.

Two nondimensional parameters were identified from the analytical model. One such parameter normalized the buckling loads for specimens of various web widths, but for a given stacking sequence. The second parameter normalized the buckling loads for all of the geometric and material variables contained in the model. This parameter also normalized the postbuckling loads. Thus, a general nondimensional load has been

determined for the buckling and postbuckling responses of the Z-section stiffeners. The buckling load predictions by the analytical model and the finite element analysis were very good. No systematic degradation in the ability to predict the onset of buckling as a function of specimen size was observed. Thus, no scale effects were observed in the buckling response. The quality of the postbuckling load predictions degraded with the width of the postbuckling load range, reaching a maximum error of 20%. The geometric nonlinearity was modelled only in the small strain, large rotation sense, and the material nonlinearity was not modelled at all. Therefore, it remains to be determined whether genuine scale effects were present in the postbuckling response or whether the observed error was a result of inadequate modelling of the nonlinearities and/or other effects such as the development of damage in the laminates.

Good correlation between experimental and finite element predictions of the out-of-plane displacements and load-axis strains has been demonstrated. The verification of the ability of the numerical analyses to accurately represent at least some of the structural response characteristics was a prerequisite to the use of the analyses in the interpretation of the experimental crippling modes. The predicted development of local material strains has been related to the structural deformation characteristics. This provided guidance for the correlation of the location and nature of the crippling damage with the responsible failure mechanisms. Consideration of individual strain values, however, could not predict which of several competing failure modes would determine the actual crippling response. Neither could the strain data provide any quantitative prediction of the crippling loads. Thus, the determination of strength scale effects is hindered by the complex structural-material interaction and the lack of a mechanics-based interactive failure model.

7.3 Suggested Further Work

Resolution of the apparent excess stiffness of the numerical model late in the postbuckling response must be made before a definitive conclusion can be issued concerning the presence or absence of scale effects in the nonlinear response regime. The issues in need of consideration include the validity of the small strain assumption, the effect of material nonlinearity, the effect of through-the-thickness strains which are excluded from the model, the possibility of progressive stiffness-reducing laminate damage suggested by

the high predicted tensile matrix strains, and changes in the axial and bending constraint provided by the potted end supports.

An interactive mechanics-based failure model is necessary in order to provide a quantitative prediction of the crippling response. A model is needed which can relate a variety of failure mechanisms to the local stress-strain state at a point, and rank the severity of the stress-strain states of various points.

REFERENCES

[1]. Spier, E.E., "Postbuckling Fatigue Behavior of Graphite-Epoxy Stiffeners," AIAA Paper No. 82-0779, *Proceedings of AIAA/ASME/ASCE/AHS 23th Structures, Structural Dynamics and Materials Conference*, May 10-12, 1982, New Orleans, LA, pp. 511-527.

[2]. Tyahla, S.T. and Johnson, E.R., "Failure and Crippling of Graphite-Epoxy Stiffeners Loaded in Compression," Virginia Polytechnic Institute and State University, Blacksburg, VA, CCMS-84-07 and VPI-E-84-19, June 1984.

[3]. Reddy, A.D., Rehfield, L.W., Bruttomesso, R.I. and Krebs, N.E., "Local Buckling and Crippling of Thin-walled Composite Structures Under Axial Compression," AIAA Paper No. 85-0672, *Proceedings of AIAA/ASME/ASCE/AHS 26th Structures, Structural Dynamics and Materials Conference*, April, 1985, Orlando, FL, pp. 804-810.

[4]. Rehfield, L.W. and Reddy, A.D., "Observations on Compressive Local Buckling, Postbuckling and Crippling of Graphite/Epoxy Airframe Structure," AIAA Paper No. 86-0923, *Proceedings of AIAA/ASME/ASCE/AHS 27th Structures, Structural Dynamics and Materials Conference*, May 19-21, 1986, San Antonio, TX, pp. 301-306.

[5]. Causbie, S.M. and Lagace, P.A., "Buckling and Final Failure of Graphite/PEEK Stiffener Sections," AIAA Paper No. 86-0921, *Proceedings of AIAA/ASME/ASCE/AHS 27th Structures, Structural Dynamics and Materials Conference*, May 19-21, 1986, San Antonio, TX, pp. 280-287.

[6]. Wang, C., Pian, T.H.H., Dugundji, J. and Lagace, P.A., "Analytical and Experimental Studies on the Buckling of Laminated Thin-Walled Structures," AIAA Paper No. 87-0727, *Proceedings of AIAA/ASME/ASCE/AHS 28th*

Structures, Structural Dynamics and Materials Conference, April 6-8, 1987, Monterey, CA, pp. 135-140.

[7]. Irons, B.M., "The SemiLoof Shell Element," *Finite Elements for Thin-Shells and Curved Members*, (D.G. Ashwell and R.H. Gallagher, eds.), John Wiley and Sons, Ltd., London, 1976, pp. 197-222.

[8]. Bonanni, D.L., Johnson, E.R. and Starnes, J.H. Jr., "Local Crippling of Thin-Walled Graphite-Epoxy Stiffeners," *AIAA Journal*, Vol. 29, Nov. 1991, pp. 1951-1959.

[9]. Allen, H.G. and Bulson, P.S., *Background to Buckling*, McGraw-Hill Book Company (UK) Ltd., Maidenhead-Berkshire, 1980.

[10]. Lekhnitskii, S.G., *Anisotropic Plates,* translated by S.W. Tsai and T. Cheron, Gordon and Breach Science Publishers, Inc., New York, N.Y., 1968.

[11]. Leissa, A.W., "An overview of Composite Plate Buckling," *Composites 4, Proceedings of the Fourth International Conference on Composite Structures* (I.H. Marshall, ed.), Applied Science Publishers, London, 1987, pp. 1.1-1.29.

[12]. Lee, D.J., "The Local Buckling Coefficient for Orthotropic Structural Sections," *Aeronautical Journal*, July 1978, pp. 313-320.

[13]. Rehfield, L.W. and Atilgan, A.R., "On the Buckling Behavior of Thin Walled Laminated Composite Open Section Beams," AIAA Paper No. 89-1171-CP, *Proceedings of AIAA/ASME/ASCE/AHS 30th Structures, Structural Dynamics and Materials Conference*, April 3-5, 1989, Mobile, AL, pp. 104-112.

[14]. Stoll, F. and Gurdal, Z., "Nonlinear Analysis of Compressively Loaded Linked-Plate Structures," AIAA Paper No. 90-0968-CP, *Proceedings of AIAA/ASME/ASCE/AHS 31th Structures, Structural Dynamics and Materials Conference*, April 2-4, 1990, Long Beach, CA , pp. 903-913.

[15]. Graves Smith, T.R., "The Finite Strip Analysis of Thin-Walled Structures," *Developments in Thin-Walled Structures-3*, (J. Rhodes and A.C. Walker, eds.), Elsevier Applied Science Publishers, London, 1987, pp. 205-235.

[16]. Banks, W.M. and Rhodes, J., "The Buckling Behavior of Reinforced Plastic Box Sections," *Proceedings of the Reinforced Plastics Congress '80*, Brighton, November 1980, pp. 85-88.

[17]. Banks, W.M. and Rhodes, J., "The Postbuckling Behavior of Composite Box Sections," *Composites, Proceedings of the First International Conference on Composite Structures* (I.H. Marshall, ed.), Applied Science Publishers, London, 1981, pp. 402-414.

[18]. Spier, E. E. and Klouman, F.L., "Empirical Crippling Analysis of Graphite/Epoxy Laminated Plates," *Proceedings of the Fourth Composite Materials: Testing and Design Conference*, ASTM STP 617, 1977, pp. 255-271.

[19]. Spier, E. E., "Stability of Graphite/Epoxy Structures with Arbitrary Symmetrical Laminates," *Experimental Mechanics*, Vol. 18, November, 1978, pp. 401-408.

[20]. Rehfield, L.W. and Parnas, K.L., "An Approach for Predicting the Crippling Strength of Thin-Walled Composite Airframe Structures Under Compression," *Proceedings of the American Society for Composites Third Technical Conference*, September 25-29, 1988, Seattle, WA, pp. 615-622.

[21]. Shih, C.-F., "Verification of Large Beam-Type Space Structures," *Journal of Spacecraft*, Vol. 24, Sept.-Oct. 1987, pp. 469-473.

[22]. Morton, J., "Scaling of Impact Loaded Fiber Composites," *AIAA Journal*, Vol. 26, Aug. 1988, pp. 989-994.

[23]. Kellas, S. and Morton, J., "Strength Scaling of Fiber Composites," NASA Contractor Report 4335, Nov. 1990.

[24]. Jackson, K.E. and Fasanella, E.L., "Scaling Effects in the Static Large Deflection Response of Graphite-Epoxy Composite Beams," NASA TM 101619, June 1989.

[25]. Jackson, K.E. and Fasanella, E.L., "Scaling Effects in the Impact Response of Graphite-Epoxy Composite Beams," SAE Technical Paper 891014, *Proceedings of the General Aviation Aircraft Meeting and Exposition*, Wichita, KS, April 11-13, 1989.

[26]. Qian, Y., Swanson, S.R., Nuismer, R.J. and Bucinell, R.B., "An Experimental Study of Scaling Rules for Impact Damage in Fiber Composites," *Journal of Composite Materials*, Vol. 24, May 1990, pp. 559-570.

[27]. Morgan, G.W., "Scaling Techniques for Orthotropic Cylindrical Aerospace Structures," *Proceedings of AIAA 5th Structures and Materials Conference*, April 1-3, 1964, Palm Springs, CA , pp. 333-343.

[28]. Abu-Arija, K.R. and Chaudhuri, R.A., "Influence of Transverse Shear Deformation on the Scaling of Cross-Ply Cylindrical Shells," *Journal of Composite Materials*, Vol. 23, July 1989, pp. 673-694.

[29]. Stein, M., "Postbuckling of Orthotropic Plates Loaded in Compression," *AIAA Journal*, Vol. 21, Dec. 1983, pp. 1729-1735.

[30]. Goodier, J.N., "Dimensional Analysis", *Handbook of Experimental Stress Analysis*, (M. Hetenyi, ed.), John Wiley and Sons, London, 1950, Appendix II, pp. 1035-1045.

[31]. Hughes, T.J.R., and Liu, W.K., "Nonlinear Finite Element Analysis of Shells: Part I. Three-Dimensional Shells," *Computer Methods in Applied Mechanics and Engineering*, Vol. 26, June 1981, pp. 331-362.

[32]. Bathe, K-J and Wilson, E.L., "Large Eigenvalue Problems in Dynamic Analysis," *Proceedings of the ASCE, EM6,* Vol. 98, December 1972, pp. 1471-1485.

[33]. Froberg, C.-E., *Numerical Mathematics,* The Benjamin/Cummings Publishing Company, Inc., Menlo Park, CA, 1985, pp. 200-206.

[34]. Crisfield, M.A., "A Fast Incremental/Iteration Solution Procedure that Handles Snap-Through," *Computers and Structures*, Vol. 13, 1981, pp. 55-62.

[35]. Koiter, W.T., "On the Stability of Elastic Equilibrium," AFFDL, TR 70-25, 1970.

[36]. Noor, A.K., Starnes, J.H. Jr. and Waters, W.A. Jr., "Numerical and Experimental Simulations of the Postbuckling Response of Laminated Anisotropic Panels," AIAA Paper No. 90-0964, *Proceedings of AIAA/ASME/ASCE/AHS 31th Structures, Structural Dynamics and Materials Conference*, April 2-4, 1990, Long Beach, CA, pp. 848-861.

[37]. Tsai, S.W., *Composites Design, Fourth Edition*, Think Composites, Dayton, OH, 1988, p. 11-8.

[38]. Soni, S.R. and Pagano, N.J., "Elastic Response of Composite Laminates," *Mechanics of Composite Materials: Recent Advances,* (Z. Hashin and C.T. Herakovich, eds.), Pergamon Press, New York, 1982, pp. 227-242.

TABLE CAPTIONS

FIGURE CAPTIONS

Figure 6-29. Comparison of DCDT and FEM out-of-plane deflections at mid-height axial location. Stacking sequences: (a) $[\pm 45/0/90]_S$ and (b) $[\pm 45/0/90]_{2S}$. Geometry: $b_w = 1.75$, $b_f = 1.25$, $r = 0.125$ in.

Figure 6-30. Comparison of DCDT and FEM out-of-plane deflections. Stacking sequence $[+30/0_2/-30]_S$. Geometry: $b_w = 1.75$, $b_f = 1.25$, $r = 0.125$ in. Axial location and experimental specimen: (a) 5.0 in., 111orth-1 and (b) 2.5 in., 111orth-2.

Figure 6-31. Comparison of DCDT and FEM out-of-plane deflections at mid-height axial location. Geometry: $b_f = 0.75$, $r = 0.125$, $b_w = 1.25$ (a) and 0.75 (b) in. Stacking sequence is $[\pm 45/0/90]_S$.

Figure 6-32. FEM distribution of out-of-plane deflection along the gage length at the flange free end. Stacking sequences: (a) $[\pm 45/0/90]_{2S}$ and (b) $[\pm 45/0/90]_S$. Geometry: $b_w = 1.75$, $b_f = 1.25$, $r = 0.125$ in.

Figure 6-33. FEM distribution of out-of-plane deflection along the gage length at the flange free end. Stacking sequence: $[+30/0_2/-30]_S$. Geometry: $b_w = 1.75$, $b_f = 1.25$, $r = 0.125$ in.

Figure 6-34. FEM mode shape for specimen type 111-2s and 10,000 lb load. Out-of-plane (a) and in-plane (b) displacements at the ends of both flanges and the center of the web. Stacking sequence: $[\pm 45/0/90]_{2S}$. Geometry: $b_w = 1.75$, $b_f = 1.25$, $r = 0.125$ in.

Figure 6-35. FEM mode shape for specimen type 111s and 3600 lb load. Out-of-plane (a) and in-plane (b) displacements at the ends of both flanges and the center of the web. Stacking sequence: $[\pm 45/0/90]_S$. Geometry: $b_w = 1.75$, $b_f = 1.25$, $r = 0.125$ in.

Figure 6-36. FEM mode shape for specimen type 111orth and 2700 lb load. Out-of-plane (a) and in-plane (b) displacements at the ends of both flanges and the center of the web. Stacking sequence: $[+30/0_2/-30]_S$. Geometry: $b_w = 1.75$, $b_f = 1.25$, $r = 0.125$ in.

Figure 6-37. Symmetry of mode shape between the flanges as indicated by out-of-plane displacements for specimen 111-2s-2 (a) and 111orth-1 (b). Loss of symmetry caused by bending-twisting coupling.

Figure 6-38. Effect of bending-twisting coupling stiffnesses D_{16} and D_{26} on mode shape of specimen type 111orth at 2700 lb load. Out-of-plane (a) and in-plane (b) displacements. Stacking sequence: $[+30/0_2/-30]_S$. Geometry: $b_w = 1.75$, $b_f = 1.25$, $r = 0.125$ in. Material coupling causes mode shape distortion, but structural mode interaction causes overall twisting of section.

Figure 6-39. FEM transition from torsional to flexural mode interaction with decreasing flange width. Stacking sequence: $[\pm 45/0/90]_S$. Geometry: $b_w = 1.75$, $r = 0.125$, (a) $b_f = 1.25$, (b) $b_f = 0.75$ and (c) $b_f = 0.50$ in.

TABLES AND FIGURES

Table 4-1. Summary of experimental details: geometries, stacking sequences, strain gage placement and specimen identification.

Specimen type designation[a]	#	Laminate	Web width[b] b_w, in.	Flange width[b] b_f, in.	Corner radius[b] r, in.	Gage length[c] L, in.	Strain gage pattern and axial location[d]	
111-2s	3	$[\pm 45/0/90]_{2s}$	1.75	1.25	0.125	10	A 5.0	B 3.8
121-2s	3		"	1.00	"	"	A 4.0	B 5.0
131-2s	3		"	0.75	"	6	C 2.0	D 3.0
111s	2	$[\pm 45/0/90]_s$	1.75	1.25	0.125	10	A 5.0	B 3.5
121s	2		"	1.00	"	"	A 5.0	B 3.8
131s	2		"	0.75	"	6	C 4.0	D 3.0
141s	2		"	0.50	"	"	C 3.0	D 4.0
111orth	3	$[30/0_2/-30]_s$	1.75	1.25	0.125	10	A 3.3	B 5.0
121orth	3		"	1.00	"	"	A 6.8	B 5.0
131orth	3		"	0.75	"	6	C 3.0	D 4.0
141orth	3		"	0.50	"	"	C 4.0	D 3.0
211s	2	$[\pm 45/0/90]_s$	1.25	1.25	0.125	10	A 5.0	B 6.2
221s	3		"	1.00	"	"	A 6.2	B 5.0
231s	3		"	0.75	"	6	A 3.0	B 2.1
241s	2		"	0.50	"	"	A 3.0	D 2.2
212s	3	$[\pm 45/0/90]_s$	1.25	1.25	0.250	10	A 4.0	B 5.2
222s	2		"	1.00	"	"	A 3.8	B 5.0
232s	2		"	0.75	"	6	A 2.1	B 3.0
242s	2		"	0.50	"	"	A 1.0	D 2.1
331s	2	$[\pm 45/0/90]_s$	0.75	0.75	0.125	6	A 3.0	B 2.2
341s	2		"	0.50	"	"	A 2.4	B 3.0

[a] Specimen designation: ABCD-#

A => web size: 1 => 1.75 in. 2 => 1.25 in. 3 => 0.75 in.

B => flange size: 1 => 1.25 in. 2 => 1.00 in. 3 => 0.75 in. 4 => 0.50 in.

C => corner radius: 1 => 0.125 in. 2 => 0.250 in.

D => laminate: s => $[\pm 45/0/90]_s$ -2s => $[\pm 45/0/90]_{2s}$ orth => $[+30/0_2/-30]_s$

#=specimen replicate number

[b] Nominal dimensions. See Figure 3-1 for definitions.

[c] The total length of all specimens was two inches longer than the gage length. The ends of each specimen were cast into the center of steel or aluminum rings of 4-5 in. diameter to a depth of one in. using an aluminum-filled epoxy compound.

[d] Strain gage patterns are defined in Figure 4-7. Locations refer to the axial position of the strain gage pattern along the gage length.

Table 5-1. Experimental buckling load summary.

Specimen number	Buckling loads (lb) as determined from: Bending strain	Load/end-shortening	Out-of-plane displacement	Average buckling loads (lb)	% Variance (= range/ave.) of load measurements
111-2s-1	7852	8022	7996	7957	2.1
111-2s-2	7682	8022	7915	7873	4.3
111-2s-3	7750	7908	7937	7865	2.4
121-2s-1	9502	9807	9807	9705	3.1
121-2s-2	10117	10357	10205	10226	2.4
121-2s-3	10444	10524	10380	10449	1.4
131-2s-1	12662	12668	12790	12707	1.0
131-2s-2	13044	13132	13066	13081	0.7
131-2s-3	12806	12812	12693	12770	0.9
111s-1	999	1012	1004	1005	1.3
111s-2	999	1033	1083	1038	8.1
121s-1	1243	1308	1278	1276	5.1
121s-2	1291	1316	1290	1299	2.0
131s-1	1776	1808	1799	1794	1.8
131s-2	1734	1799	1799	1777	3.7
141s-1	1759	1781	1745	1762	2.0
141s-2	1784	1816	1824	1808	2.2
111orth-1	628	726	698	684	14.3
111orth-2	646	705	680	677	8.7
111orth-3	642	670	690	667	7.2
121orth-1	887	939	873	900	7.3
121orth-2	830	842	833	835	1.4
121orth-3	876	889	873	879	1.8
131orth-1	1154	1114	1141	1136	3.5
131orth-2	1332	1268	1272	1291	5.0
131orth-3	1209	1279	1287	1258	6.2
141orth-1	1304	1341	1334	1326	2.8
141orth-2	1162	1227	1227	1200	5.4
141orth-3	1257	1326	1326	1311	7.0

(cont.)

Table 5-1. Experimental buckling load summary (cont.)

Specimen number	Buckling loads (lb) as determined from: Bending strain	Load/end-shortening	Out-of-plane displacement	Average buckling loads (lb)	% Variance (= range/ave.) of load measurements
211s-1	907	900	961	923	6.6
211s-2	866	939	961	922	10.3
221s-1	1137	1181	1211	1176	6.3
221s-2	1162	1204	1235	1200	6.1
221s-3	1143	1219	1196	1186	6.4
231s-1	1579	1736	1656	1657	9.5
231s-2	1716	1839	1892	1816	9.7
231s-3	1699	1801	1839	1780	7.9
241s-1	2437	1526	2439	2467	3.6
241s-2	2532	1515	2506	2518	1.0
212s-1	1066	1103	1067	1079	3.4
212s-2	1050	1169	1134	1118	10.7
212s-3	1012	1042	1022	1025	2.9
222s-1	1372	1449	1479	1433	7.5
222s-2	1393	1403	1441	1412	3.4
232s-1	2159	2166	2210	2178	2.3
232s-2	1997	2067	2130	2065	6.4
242s-1	2820	2961	2953	2911	4.8
242s-2	2831	2881	2881	2864	1.8
331s-1	1520	1556	1686	1587	10.5
331s-2	1494	1551	1557	1534	4.1
341s-1	2329	2386	2246	2320	6.0
341s-2	2296	2341	2322	2320	1.9

Table 5-2. Experimental crippling data.

Specimen number	Crippling Values Load (lb)	Stress (ksi)	u/L
111-2s-1	10099	31.5	0.0053
111-2s-2	11948	37.2	0.0069
111-2s-3	11599	36.0	0.0066
121-2s-1	11350	39.9	0.0065
121-2s-2	11828	42.2	0.0069
121-2s-3	12091	43.5	0.0070
131-2s-1	13271	55.0	0.0089
131-2s-2	13344	56.2	0.0093
131-2s-3	13159	54.6	0.0093
111s-1	3298	20.1	0.0067
111s-2	3943	24.0	0.0108
121s-1	3996	27.9	0.0108
121s-2	3280	22.8	0.0068
131s-1	3090	25.0	0.0058
131s-2	3374	27.2	0.0075
141s-1	3003	28.9	0.0075
141s-2	2957	28.4	0.0070
111orth-1	3752	22.2	0.0035
111orth-2	2723	16.3	0.0036
111orth-3	2803	16.7	0.0038
121orth-1	2779	18.8	0.0038
121orth-2	2842	19.8	0.0041
121orth-3	2700	18.6	0.0038
131orth-1	2957	23.3	0.0046
131orth-2	3000	24.3	0.0044
131orth-3	3143	25.1	0.0045
141orth-1	2827	26.1	0.0045
141orth-2	2753	26.6	0.0044
141orth-3	2954	27.2	0.0046

Specimen number	Crippling Values Load (lb)	Stress (ksi)	u/L
211s-1	3855	26.6	0.0102
211s-2	3927	27.1	0.0107
221s-1	3701	29.8	0.0095
221s-2	3770	30.4	0.0097
221s-3	3659	29.4	0.0100
231s-1	3254	31.1	0.0073
231s-2	3436	33.4	0.0080
231s-3	3543	33.9	0.0086
241s-1	3078	36.3	0.0074
241s-2	3063	36.6	0.0070
212s-1	4226	29.5	0.0094
212s-2	4361	30.1	0.0106
212s-3	4039	28.4	0.0103
222s-1	3953	33.0	0.0094
222s-2	3732	31.5	0.0082
232s-1	3565	35.6	0.0087
232s-2	3369	33.8	0.0076
242s-1	3265	41.1	0.0075
242s-2	3240	40.8	0.0072
331s-1	2637	30.5	0.0061
331s-2	2290	26.2	0.0048
341s-1	2493	38.2	0.0061
341s-2	2457	37.7	0.0060

Table 6-1. Comparison of experimental and predicted buckling loads.

Specimen type	Buckling Loads (lb)				% Error[e]			
	Exp ave[a]	Nonlin FEM[b]	Linear FEM[c]	Analy-tical[d]	Nonlin FEM	Linear FEM	Analy-tical	% crnr area[f]
111-2s	7898	8144	8474	8624	3.1	7.3	9.2	12.6
121-2s	10127	9790	10674	11201	-3.3	5.4	10.6	14.4
131-2s	12853	12844	13709	14454	-0.1	6.7	12.5	16.7
111s	1022	1051	1155	1178	2.9	13.1	15.3	11.0
121s	1288	1344	1482	1544	4.4	15.1	19.9	12.6
131s	1786	1813	1946	2008	1.5	9.0	12.5	14.6
141s	1785	1838	1988	2085	3.0	11.4	16.8	17.4
111orth	690	720	779	814	4.3	12.8	17.9	11.0
121orth	871	896	962	1054	2.8	10.4	21.0	12.6
131orth	1228	1232	1355	1356	0.3	10.3	10.4	14.6
141orth	1279	1221	1321	1429	-4.5	3.3	11.7	17.4
211s	923	950	1064	1090	3.0	15.3	18.2	12.6
221s	1187	1241	1378	1442	4.5	16.1	21.4	14.6
231s	1751	1787	1976	2042	2.1	12.8	16.6	17.4
241s	2493	2492	2692	2904	0.0	8.0	16.5	21.4
212s	1074	1064	1134	1090	-0.9	5.6	1.5	24.1
222s	1423	1419	1511	1442	-0.2	6.2	1.4	28.1
232s	2122	2129	2262	2042	0.4	6.6	-3.7	33.7
242s	2888	3004	3171	2904	4.0	9.8	0.6	42.0
331s	1561	1615	1750	1830	3.5	12.1	17.3	21.4
341s	2320	2344	2771	3001	1.0	19.4	29.4	28.0

[a]Average of experimental values for replicate specimens and different load determination methods. Data from Table 5-1.

[b]Average of buckling loads determined from load-end shortening and out-of-plane deflection responses of finite element models. Magnitude of assumed initial imperfection is 5% of 8-ply laminate thickness.

[c]Buckling load calculated from linear finite element analysis, (see Section 3.1.2).

[d]Buckling loads computed using analytical model of Section 3.1.1. Model neglects actual corner radius and bending-twisting coupling.

[e]% error defined as: (predicted-experiment)/experiment * 100%.

[f]Percentage of cross-sectional area occupied by corner.

Table 6-2. Experimental prebuckling stiffness.

Specimen number	Normalized prebuckling stiffness (PL/AEu) Uncorrected	Gen pln strain[a]	Plane strain[b]
111-2s-1	0.93	1.01	1.03
111-2s-2	0.93	1.01	1.03
111-2s-3	0.92	1.00	1.02
121-2s-1	0.94	1.01	1.03
121-2s-2	0.95	1.02	1.04
121-2s-3	0.97	1.04	1.06
131-2s-1	0.87	0.97	0.99
131-2s-2	0.88	0.99	1.02
131-2s-3	0.85	0.95	0.97
ave.	0.92	1.00	1.02
111s-1	0.97	1.01	1.04
111s-2	0.93	0.98	1.01
121s-1	0.97	1.01	1.04
121s-2	0.94	0.98	1.01
131s-1	0.88	0.93	0.97
131s-2	0.89	0.95	0.99
141s-1	0.91	0.97	1.02
141s-2	0.92	0.98	1.03
ave.	0.93	0.98	1.01
111orth-1	1.00	1.02	1.08
111orth-2	1.05	1.10	1.17
111orth-3	1.00	1.04	1.10
121orth-1	1.02	1.06	1.13
121orth-2	0.84	0.87	0.91
121orth-3	0.92	0.96	1.01
131orth-1	0.89	0.95	1.04
131orth-2	0.88	0.93	1.02
131orth-3	0.90	0.96	1.05
141orth-1	0.88	0.94	1.03
141orth-2	0.86	0.91	0.99
141orth-3	0.86	0.91	0.99
ave.	0.93	0.97	1.04

Specimen number	Normalized prebuckling stiffness (PL/AEu) Uncorrected	Gen pln strain[a]	Plane strain[b]
211s-1	0.93	0.96	0.99
211s-2	0.94	0.98	1.01
221s-1	0.93	0.97	1.00
221s-2	0.97	1.01	1.04
221s-3	0.98	1.02	1.05
231s-1	0.89	0.94	0.98
231s-2	0.92	0.97	1.02
231s-3	0.91	0.97	1.02
241s-1	0.88	0.94	0.98
241s-2	0.93	0.99	1.04
ave.	0.93	0.98	1.01
212s-1	0.97	1.01	1.04
212s-2	0.96	1.00	1.03
212s-3	0.96	0.99	1.02
222s-1	0.96	1.00	1.03
222s-2	0.98	1.02	1.05
232s-1	0.91	0.98	1.03
232s-2	0.91	0.98	1.03
242s-1	0.92	0.99	1.04
242s-2	0.93	1.01	1.06
ave.	0.94	1.00	1.04
331s-1	0.88	0.93	0.97
331s-2	0.90	0.96	1.01
341s-1	0.86	0.92	0.96
341s-2	0.87	0.93	0.97
ave.	0.88	0.94	0.98

[a] Experimental end shortening corrected using generalized plane strain FEM analysis.

[b] Experimental end shortening corrected using plane strain FEM analysis.

Table 6-3. Agreement between experimentally observed and numerically predicted postbuckling loads.

Specimen number	Max u/L[a]	Load (lb)[b] Exp	Load (lb)[b] FEM	% Error[c]
111-2s-1	0.00494	10102	10579	4.7
111-2s-2	0.00649	11953	12710	6.3
111-2s-3	0.00616	11584	12270	5.9
121-2s-1	0.00608	11348	11852	4.4
121-2s-2	0.00639	11824	12208	3.2
121-2s-3	0.00645	12088	12284	1.6
131-2s-1	0.00762	12983	13465	3.7
131-2s-2	0.00820	13342	14028	5.1
131-2s-3	0.00820	13157	14028	6.6
111s-1	0.00636	3288	3737	13.7
111s-2	0.01060	3944	4862	23.3
121s-1	0.01060	3997	4735	18.5
121s-2	0.00631	3265	3621	10.9
131s-1	0.00558	3089	3213	4.0
131s-2	0.00727	3373	3707	9.9
141s-1	0.00723	2993	3320	10.9
141s-2	0.00674	2956	3264	10.4
111orth-1	0.00260	2573	2692	4.6
111orth-2	0.00263	2556	2708	5.9
111orth-3	0.00270	2597	2749	5.8
121orth-1	0.00226	2357	2357	0.0
121orth-2	0.00270	2566	2675	4.2
121orth-3	0.00291	2593	2798	7.9
131orth-1	0.00273	2519	2656	5.4
131orth-2	0.00343	2830	3051	7.8
131orth-3	0.00320	2911	2930	0.6
141orth-1	0.00278	2474	2459	-0.6
141orth-2	0.00319	2601	2670	2.7
141orth-3	0.00322	2746	2683	-2.3

(cont.)

Table 6-3. Agreement between experimentally observed and numerically predicted postbuckling loads (cont.)

Specimen number	Max u/L[a]	Load (lb)[b] Exp	FEM	% Error[c]
211s-1	0.01002	3854	4709	22.2
211s-2	0.00997	3883	4698	22.8
221s-1	0.00932	3702	4399	18.8
221s-2	0.00957	3768	4456	18.3
221s-3	0.00886	3606	4289	18.9
231s-1	0.00701	3255	3685	13.2
231s-2	0.00770	3435	3782	10.1
231s-3	0.00825	3544	3923	10.7
241s-1	0.00703	3078	3363	9.3
241s-2	0.00668	3064	3283	7.2
212s-1	0.09011	4225	4547	7.6
212s-2	0.01044	4359	4836	10.9
212s-3	0.00927	4009	4602	14.8
222s-1	0.00924	3954	4475	13.2
222s-2	0.00802	3732	4183	12.1
232s-1	0.00619	3268	3516	7.6
232s-2	0.00698	3373	3780	12.1
242s-1	0.00706	3266	3536	8.3
242s-2	0.00673	3239	3467	7.0
331s-1	0.00586	2635	2870	8.9
331s-2	0.00454	2291	2397	4.6
341s-1	0.00574	2491	2656	6.6
341s-2	0.00561	2458	2611	6.2

[a] Adjusted experimental end shortening corresponding to the initiation of laminate damage as indicated by discontinuity in specimen stiffness.

b Experimentally observed loads and loads predicted from the nonlinear finite element analyses corresponding to the u/L value.

[c] The % error is defined as:

$$\frac{P_{FEM} - P_{Exp}}{P_{Exp}} * 100\%$$

Table 6-4. Post-test specimen characterization.

Specimen number	Mode number,m, at failure	Axial position of laminate damage (in.) [a]	Failure location at node (N) or peak (P) [b]	Axial extent of flange end delamination (in.)
111-2s-1	3	4.9	P	3.7-7.3
111-2s-2	3	6.1	N	3.7-7.9
111-2s-3	3	3.6	N	0.8-6.7
121-2s-1	3	4.7-5.2	P	2.6-7.4
121-2s-2	4	4.5-4.7	N	3.2-5.6
121-2s-3	4	5.0-6.4	N+P	2.6-5.9
131-2s-1	3	3.6	N	0.7-3.4
131-2s-2	3	2.9-3.7	N	2.4-4.9
131-2s-3	3	2.8	P/N	1.7-3.8
111s-1	5	8.5-8.9	N-base	7.7-10.0
111s-2	5	6.2-6.6	N	5.3-9.0
121s-1	4	4.9-5.1	N	3.4-10.0
121s-2	4	6.9-7.2	N	6.4-8.0
131s-1	2	2.7-3.3	P/N	2.6-4.1
131s-2	3	2.3-2.7	N	1.2-3.4
141s-1	3	4.0-4.3	N	3.2-4.7
141s-2	3	2.0-2.4	N	1.4-2.0
111orth-1	3	3.8-4.5	P	none
111orth-2	3	5.0-5.5	P	none
111orth-3	3	5.3	P	none
121orth-1	3	3.9-5.0	P	none
121orth-2	3	5.0-5.6	P	none
121orth-3	3	4.5-5.0	P	none
131orth-1	2	1.4-2.5	P	none
131orth-2	2	2.0-3.2	P	none
131orth-3	2	3.3-4.5	P	2.1-3.1
141orth-1	2	3.2	P	2.3-3.9
141orth-2	2	2.2-3.0	P	1.9-2.9
141orth-3	2	2.5-3.0	P	2.2-3.4

(cont.)

Table 6-4. Post-test specimen characterization (cont.)

Specimen number	Mode number,m, at failure	Axial position of laminate damage (in.) [a]	Failure location at node (N) or peak (P) [b]	Axial extent of flange end delamination (in.)
211s-1	5	5.0	P/N	3.3-6.1
211s-2	5	3.5-4.5	N	3.5-6.0
221s-1	5	5.0	P/N	3.4-5.3
221s-2	5	5.3	N	4.4-7.0
221s-3	5	3.6	N	3.0-6.0
231s-1	3	2.0	N	1.6-3.0
231s-2	3	3.3	N	2.4-4.3
231s-3	3	4.0	P/N	2.8-4.3
241s-1	3	2.2	P/N	1.7-3.0
241s-2	3	2.8	P/N	1.9-3.1
212s-1	5	3.5	N	2.3-5.0
212s-2	5	3.5-5.3	N+P	3.3-10.0
212s-3	5	6.4	N	2.2-7.6
222s-1	5	5.4	N	4.6-7.1
222s-2	5	0.8	base	0-2.6
232s-1	2	3.8	N	2.8-4.2
232s-2	3	2.2	P/N	1.7-3.2
242s-1	3	3.6	P	3.2-4.1
242s-2	3	2.8	P/N	2.4-3.5
331s-1	3	1.9	N	1.2-2.7
331s-2	3	3.8	P/N	2.8-4.4
341s-1	3	1.5	P/N	0.9-2.0
341s-2	3	2.6	N	2.1-3.1

[a] Band of gage length containing primary laminate damage.

[b] "N+P" denotes laminate damage at both nodal and peak locations.
"P/N" denotes failure between nodal and peak locations.
"N-base" denotes failure at the nodal position nearest the end support.
"base" denotes failure at the end support.

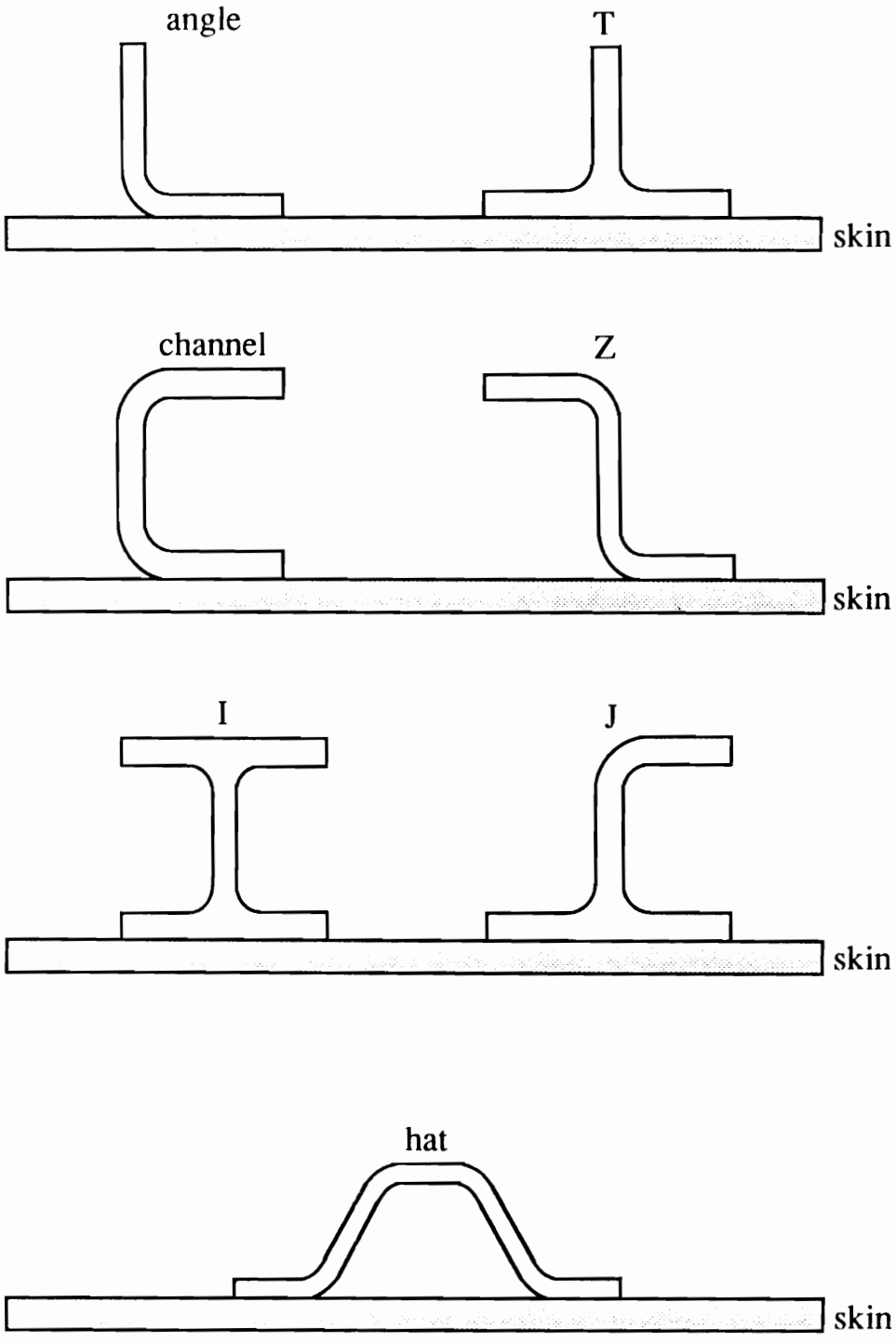

Figure 2-1. Cross-sections of common stiffener configurations.

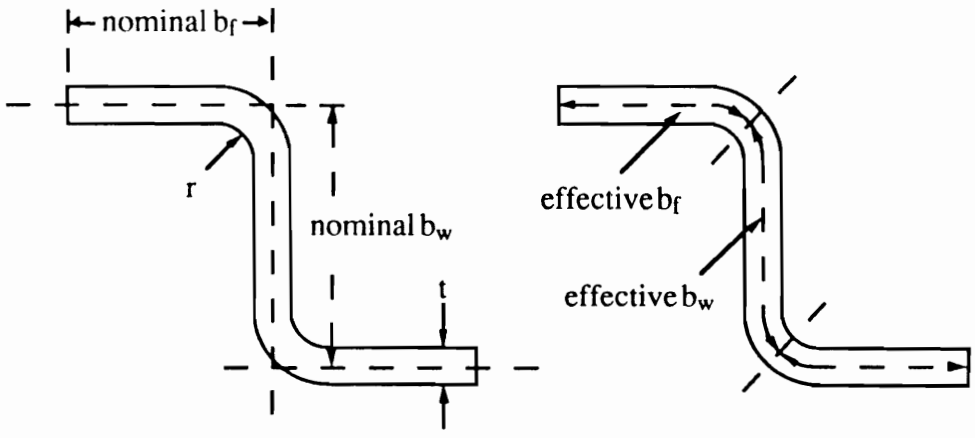

Figure 3-1. Dimension conventions used for the Z-section stiffeners.

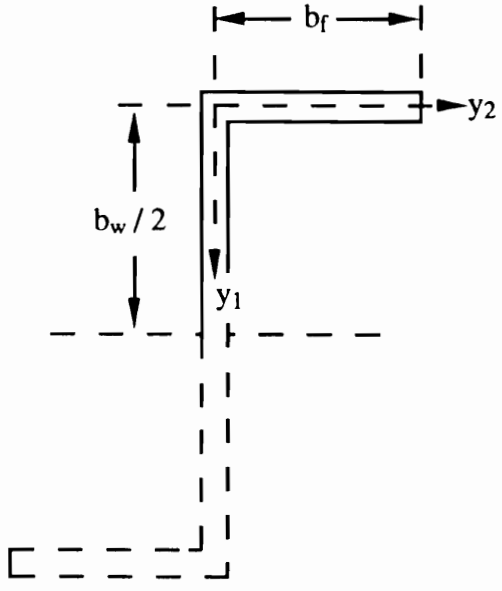

Figure 3-2. Geometry and coordinate system for linked-plate analysis of initial local buckling.

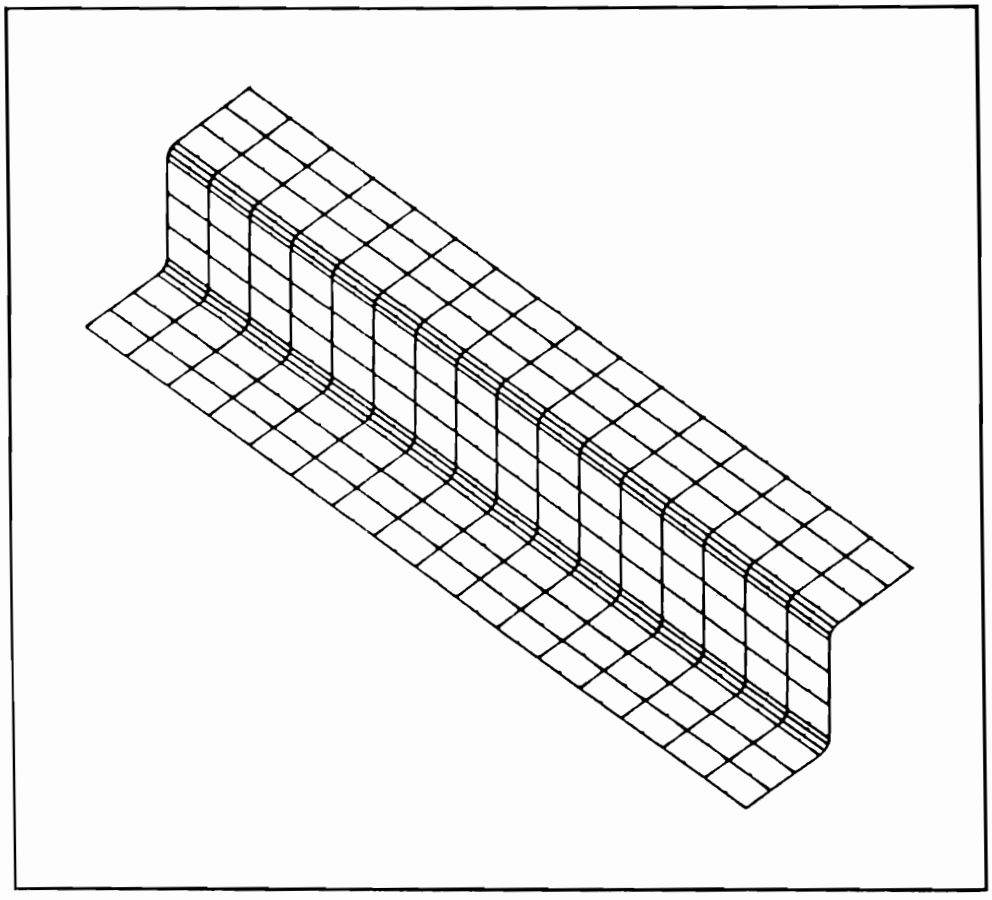

Figure 3-3. Finite element mesh used in buckling and postbuckling analyses.

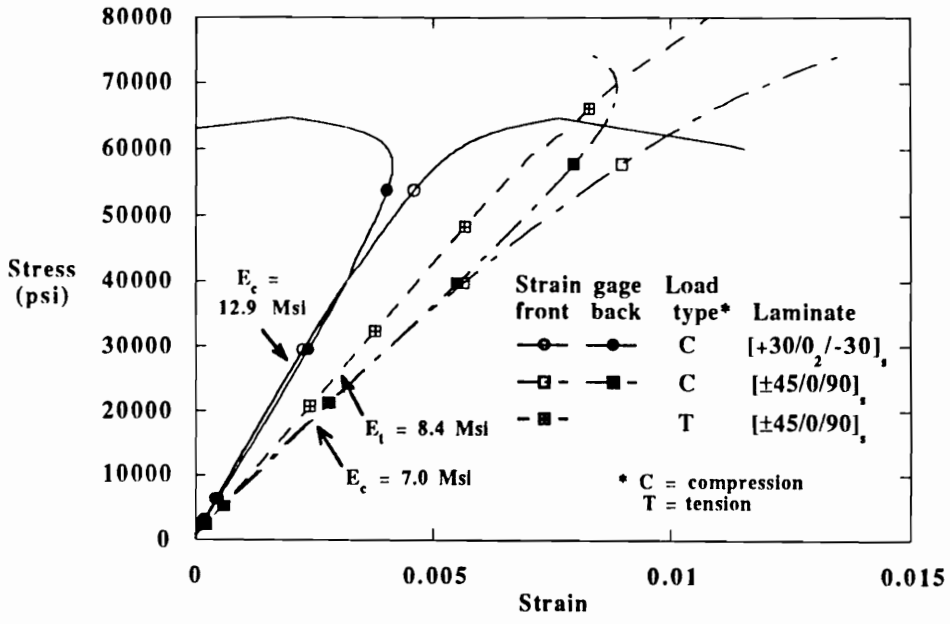

Figure 4-1. Stress-strain curves for $[\pm 45/0/90]_S$ and $[+30/0_2/-30]_S$ laminates. Data obtained using specimens cut from Z-section stock.

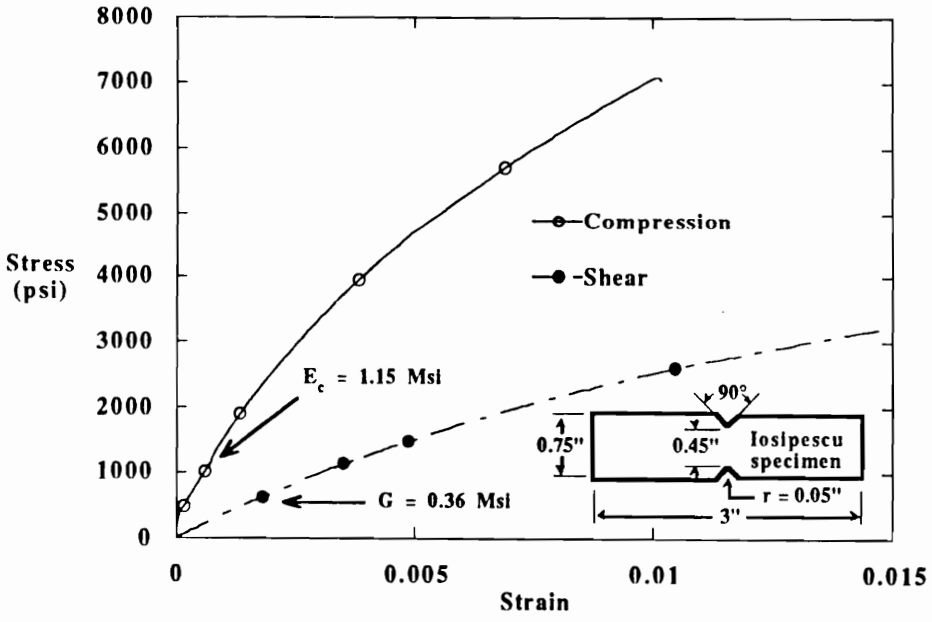

Figure 4-2. Compression and shear stress-strain curves for aluminum-filled epoxy potting compound. Data obtained using specimens fabricated from a potted end support of a Z-section test stiffener.

Figure 4-3. Photomicrographs of the cross-sections of specimens 211s-1 (a) and 231s-1 (b). Corners exhibit either a thin, uniformly distributed resin layer at the surfaces or a localized ridge of resin on the outer diameter.

(b)
(a)

Figure 4-4. Photomicrographs of the cross-sections of specimens 232s-2 (a) and 222s-1 (b). Corners exhibit either nonuniform thickness with a thin resin layer on the surface, or outward ply migration, together with a localized ridge of resin on the outer diameter.

(a)
(b)

Figure 4-5. Photomicrographs of the cross-sections of specimens 111-2s-1 (a) and 121orth-1 (b). Thickness variations are generally minor. Specimen 121orth-1 exhibits some local thickness and shape variations in the corners.

(b)
(a)

Figure 4-6. Photomicrographs of the cross-sections of specimens 111s-1 (a) and 212s-2 (b). Thickness uniformity is good in specimens of both corner radii.

(b)
(a)

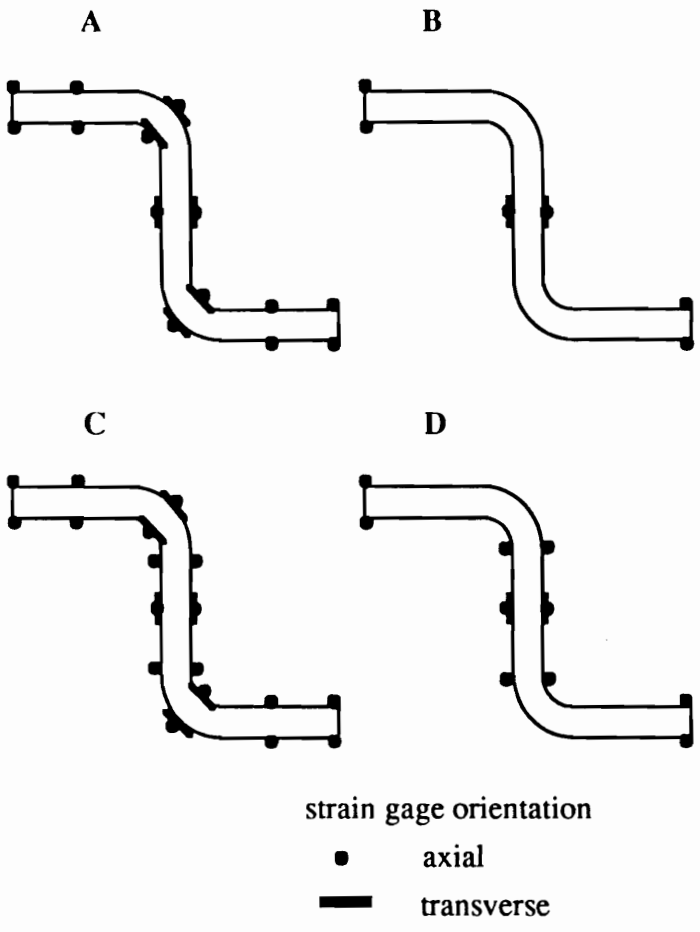

Figure 4-7. Patterns used for placement of back-to-back strain gage pairs. Both longitudinally (load axis) and transversely oriented pairs were used. See Table 4-1 for specific applications.

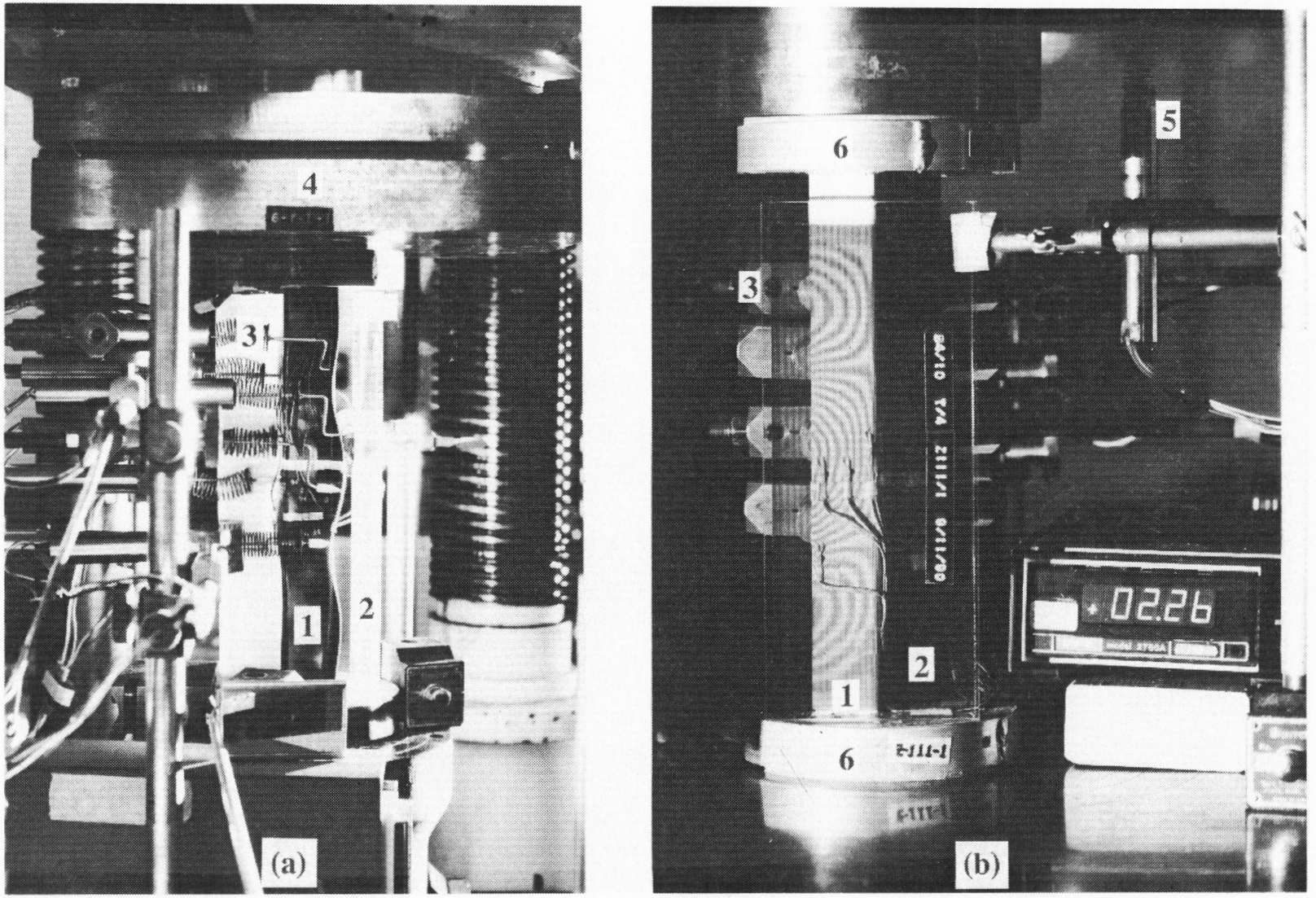

Figure 4-8. Photograph of experimental apparatus illustrating displacement transducers and shadow moire. Side view (a) and front view (b).

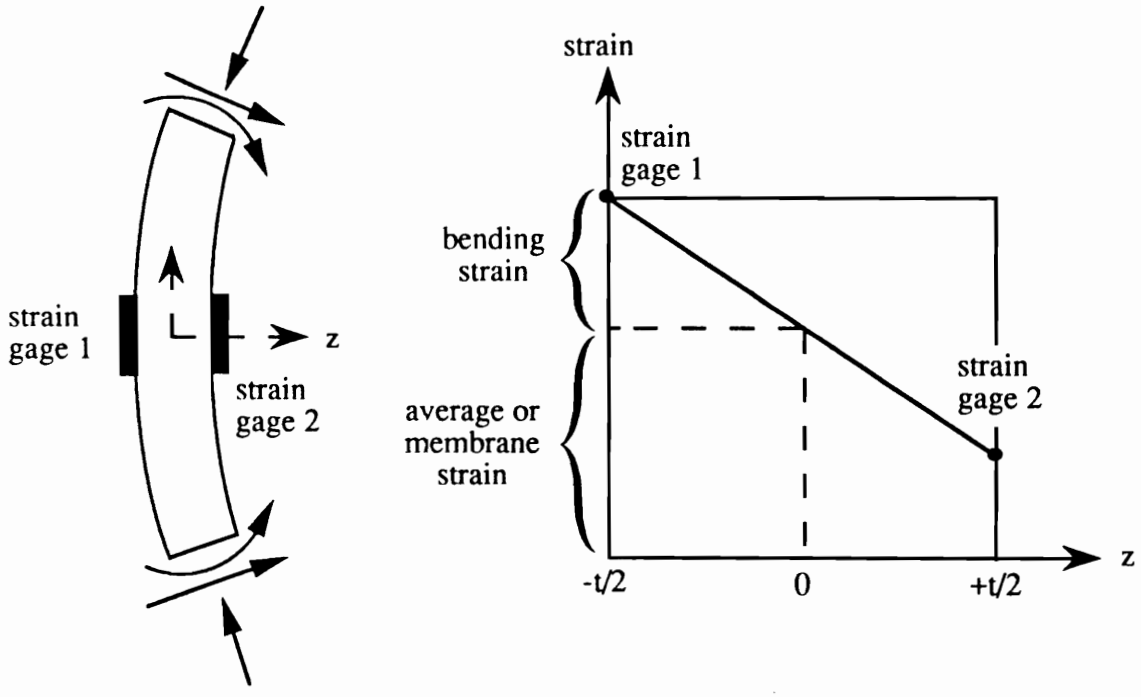

Figure 5-1. Schematic illustration of membrane and bending components of strain.

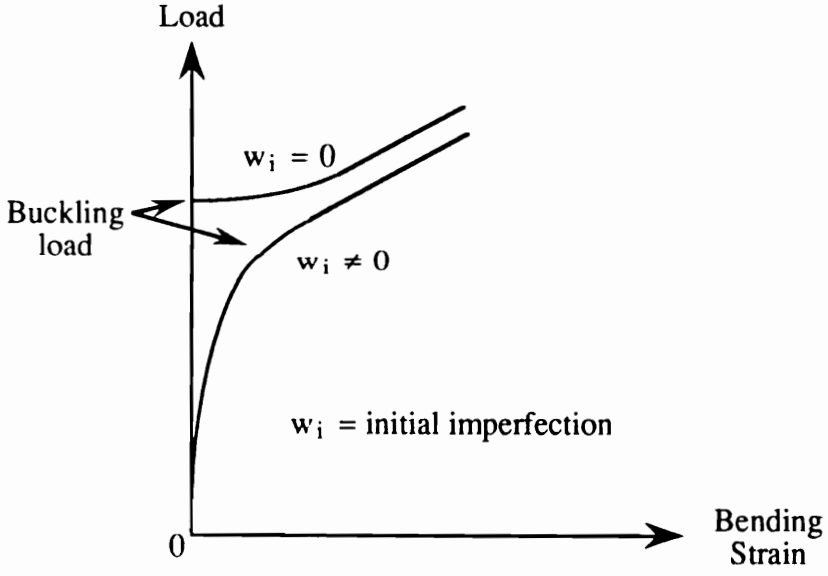

Figure 5-2. Schematic illustration of the effect of initial imperfections on the development of bending strain.

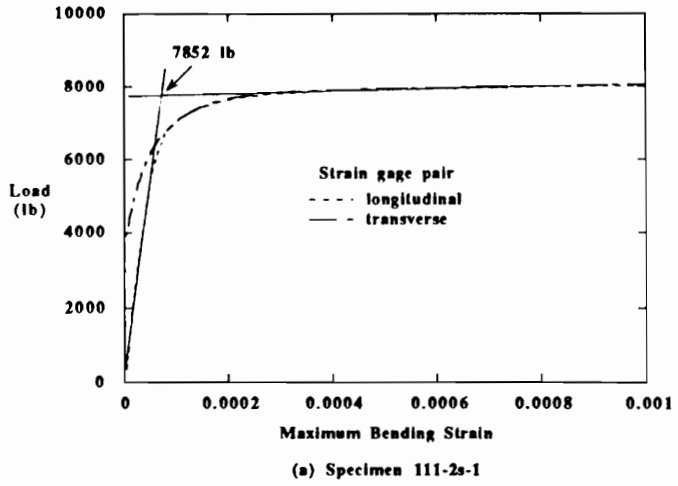

(a) Specimen 111-2s-1

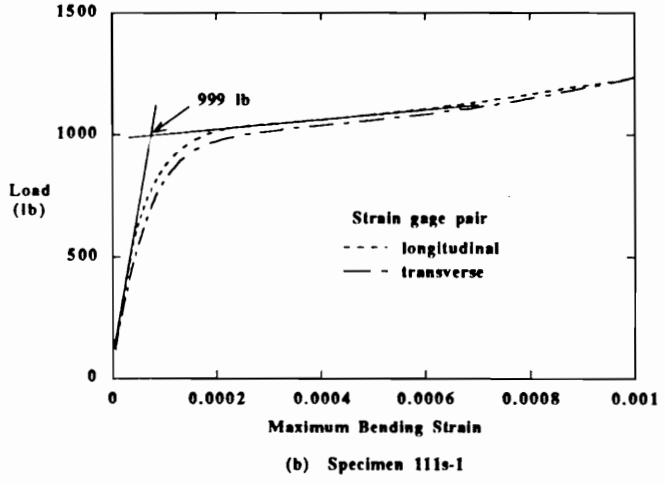

(b) Specimen 111s-1

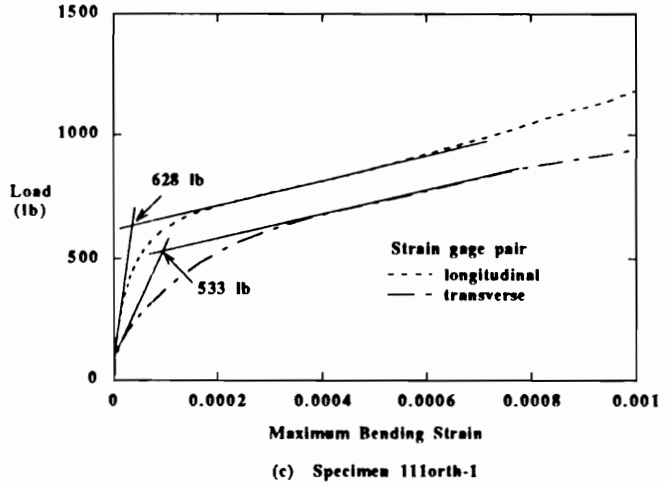

(c) Specimen 111orth-1

Figure 5-3. Buckling load determination for specimen 111-2s-1 (a), 111s-1 (b) and 111orth-1 (c) using load-bending strain response. Relative magnitudes of the longitudinal and transverse components are a function of stacking sequence.

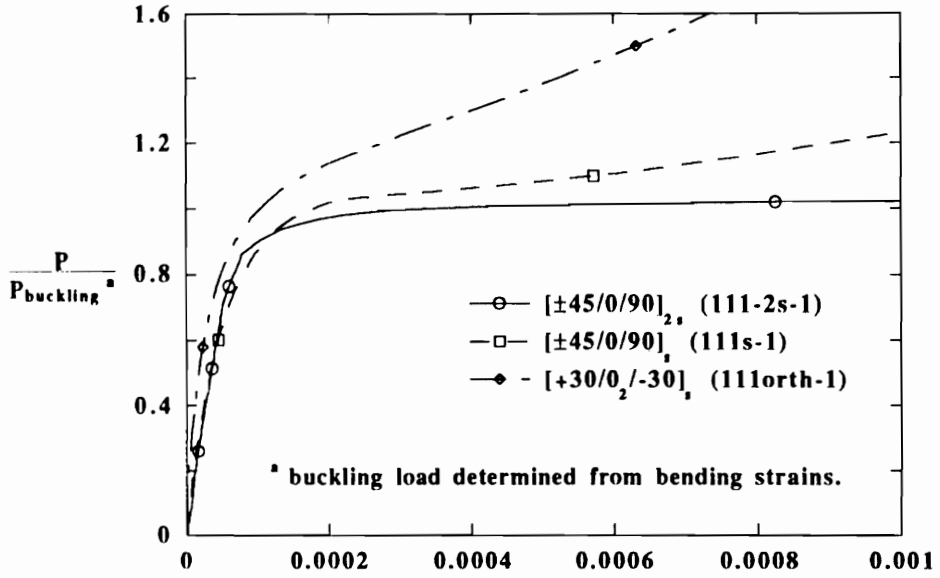

(a) Maximum Longitudinal Bending Strain

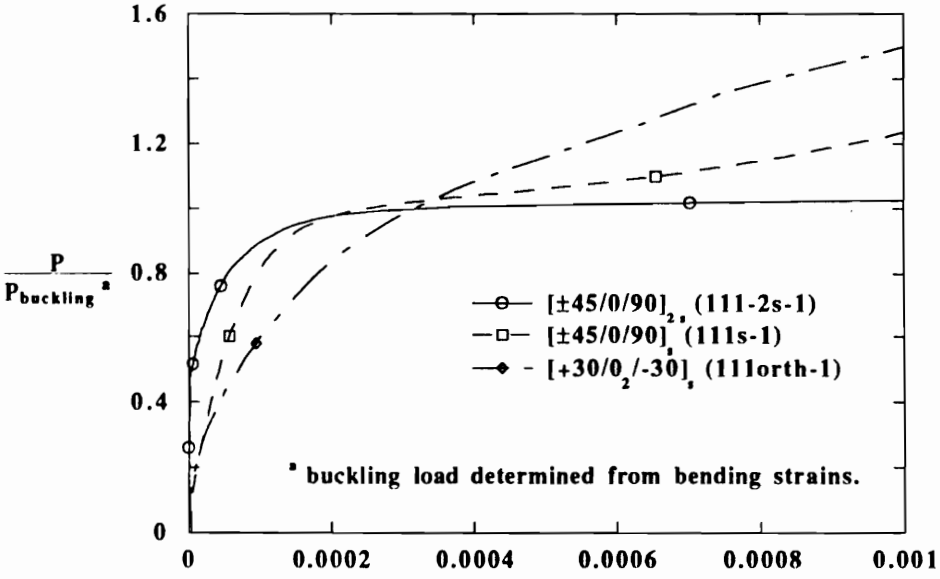

(b) Maximum Transverse Bending Strain

Figure 5-4. Longitudinal (a) and transverse (b) bending strains in specimens 111-2s-1, 111s-1 and 111orth-1.

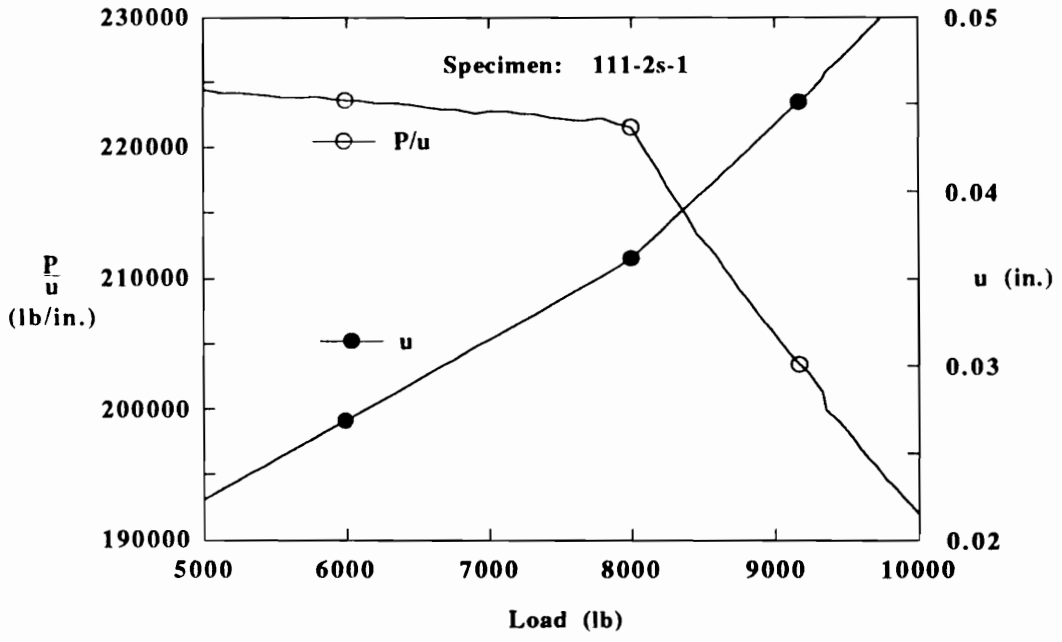

Figure 5-5. Methods of using the load (P) - end shortening (u) response to determine buckling loads. The plot of P/u versus P provides a more distinct indication of the buckling load compared to the P versus u response.

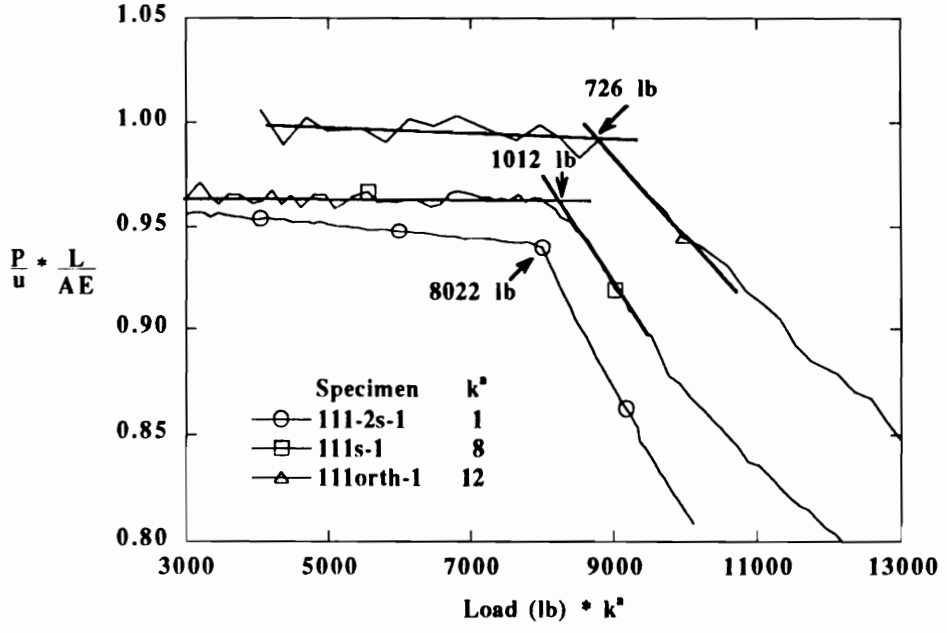

Figure 5-6. Buckling load determination for specimens 111-2s-1, 111s-1 and 111orth-1 using the stiffness plotting technique.

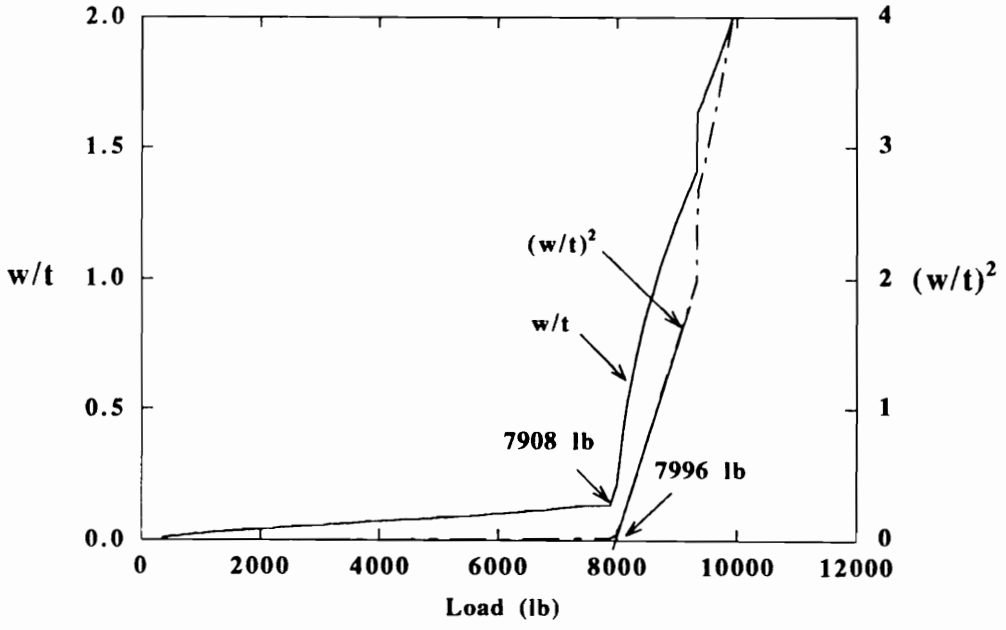

(a) Specimen 111-2s-1

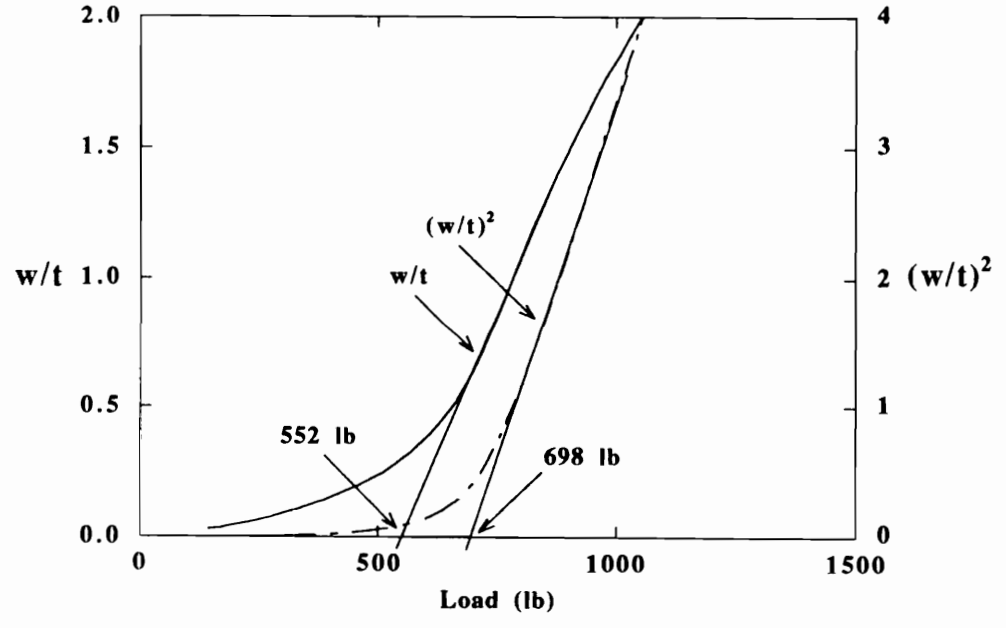

(b) Specimen 111orth-1

Figure 5-7. Use of the out-of-plane deflection, w, response to estimate buckling loads of specimens 111-2s-1 (a) and 111orth-1 (b). Deflections are normalized with respect to laminate thickness. The load versus w^2 response provides a more distinct indication of buckling. The imperfection sensitivity is greater in specimen 111orth-1 with the lower buckling load.

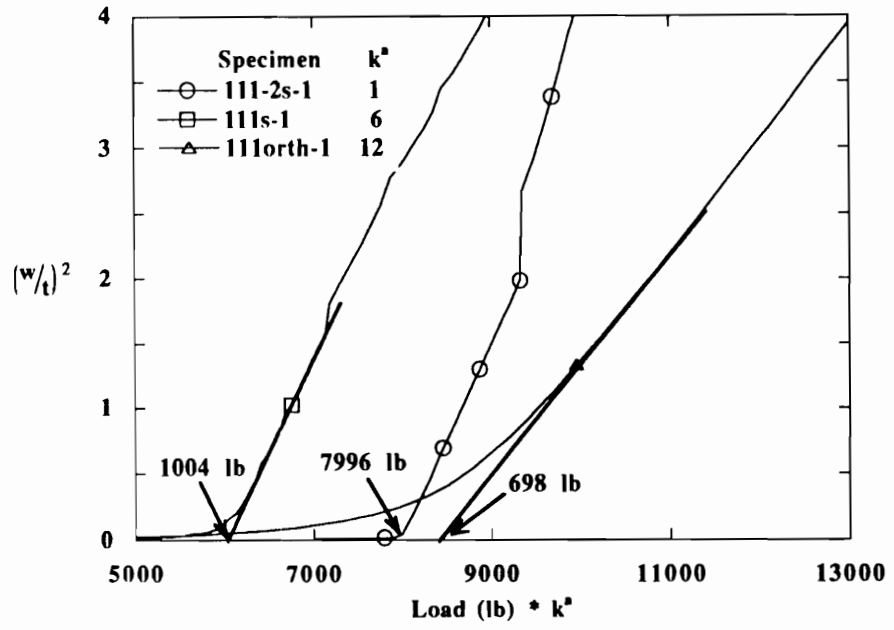

Figure 5-8. Buckling load determination for specimens 111-2s-1, 111s-1 and 111orth-1 using the square of the normalized out-of-plane deflection (w/t). The abscissa has been scaled for specimens 111s-1 and 111orth-1.

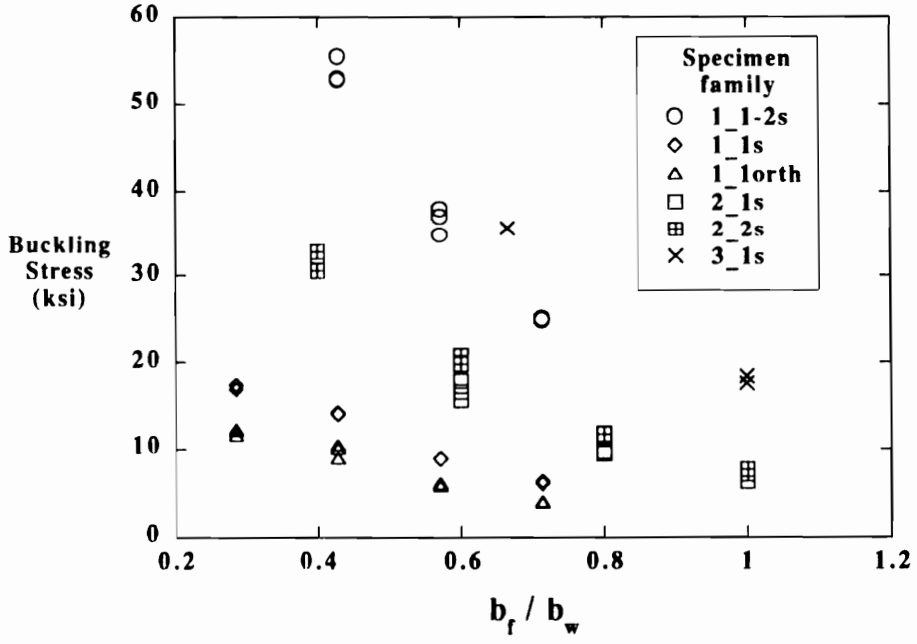

Figure 5-9. Average experimental buckling stresses as a function of the flange-to-web width ratio (b_f/b_w). Buckling stresses increase with decreasing flange and web widths and increasing corner radii and laminate thickness.

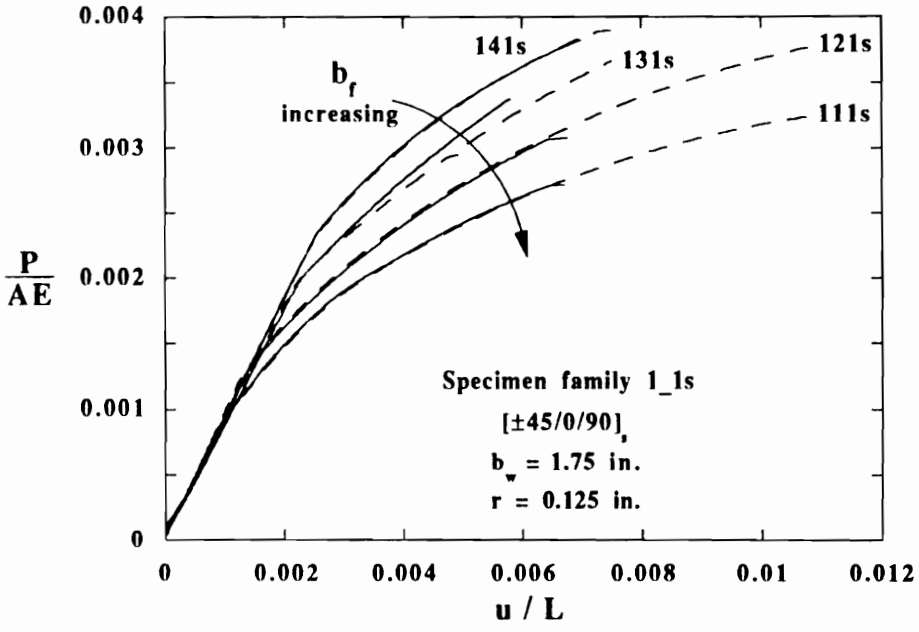

(a)

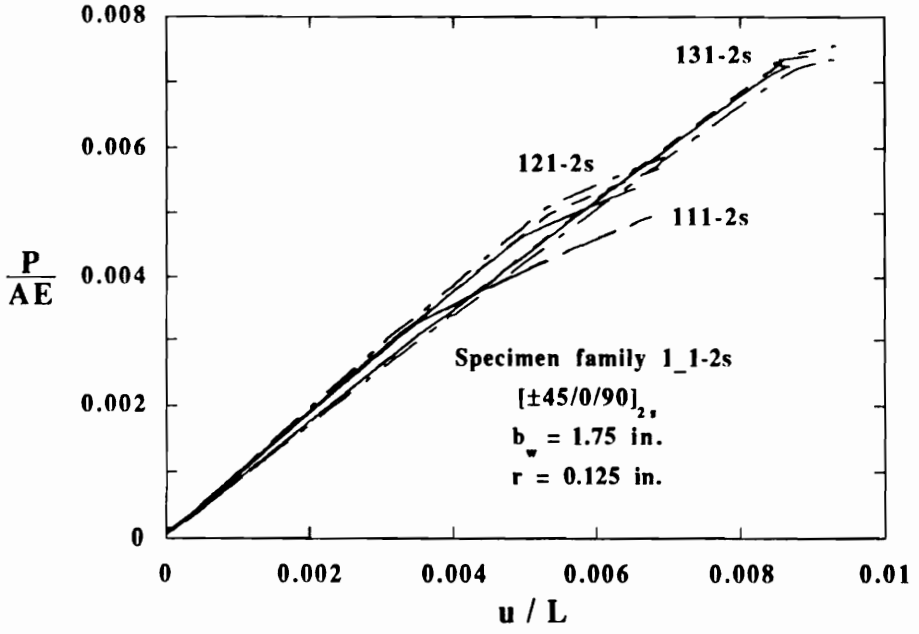

(b)

Figure 5-10. Normalized load-end shortening responses for specimens having a web width of 1.75 in. and stacking sequence: (a) 8-ply quasi-isotropic $[\pm 45/0/90]_S$ and (b) 16-ply quasi-isotropic $[\pm 45/0/90]_{2S}$. Flange sizes range from 0.5 to 1.25 in. Solid and dashed lines indicate replicates of a given specimen type.

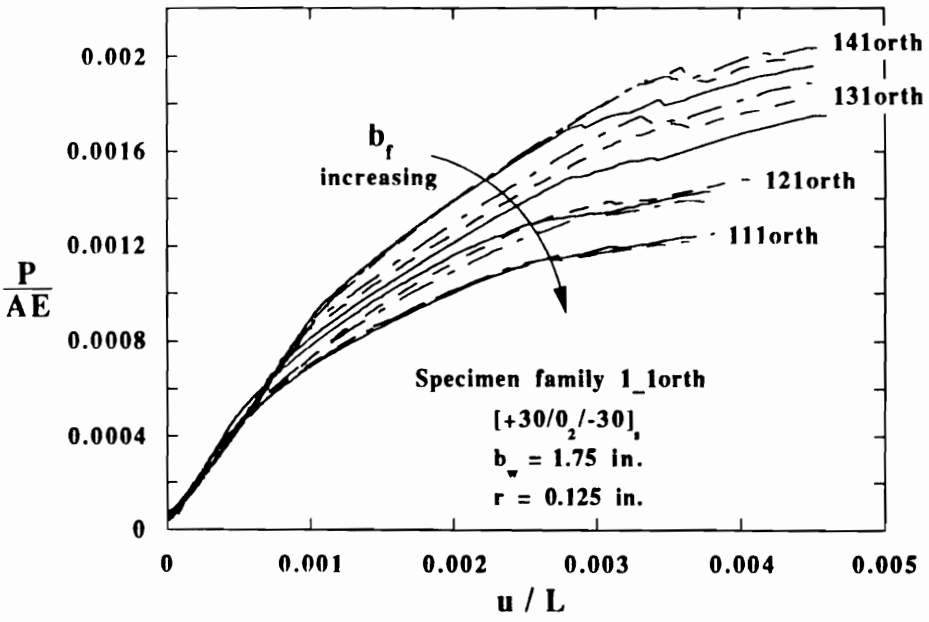

Figure 5-11. Normalized load-end shortening responses for specimens having a web width of 1.75 in. and the $[+30/0_2/-30]_S$ stacking sequence. Solid and dashed lines indicate replicates of a given specimen type.

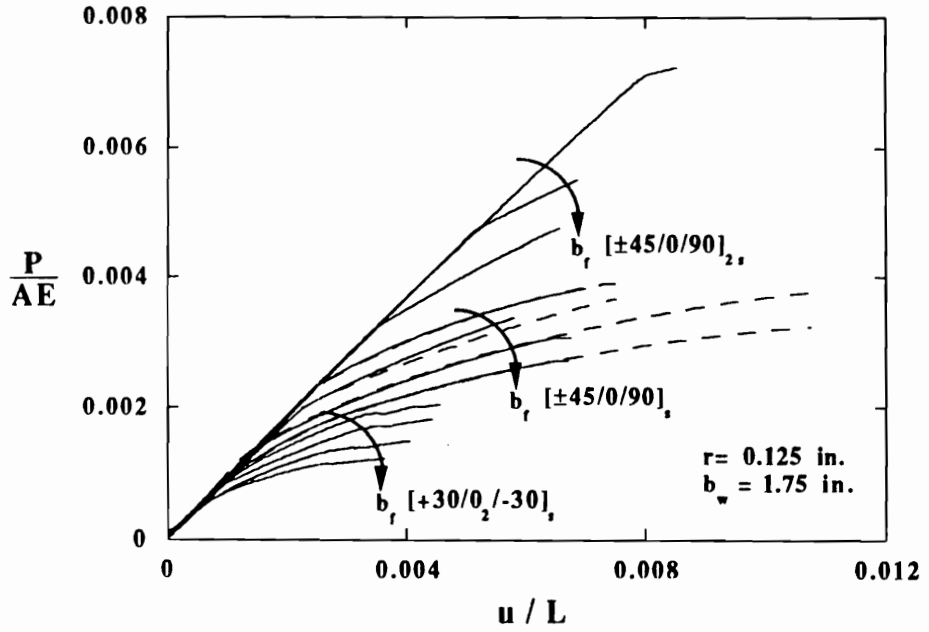

Figure 5-12. Comparison of the normalized load-end shortening responses between specimens of the $[\pm45/0/90]_{2S}$, $[\pm45/0/90]_S$ and $[+30/0_2/-30]_S$ stacking sequences. Web width is 1.75 in. Solid and dashed lines indicate replicates of a given specimen type.

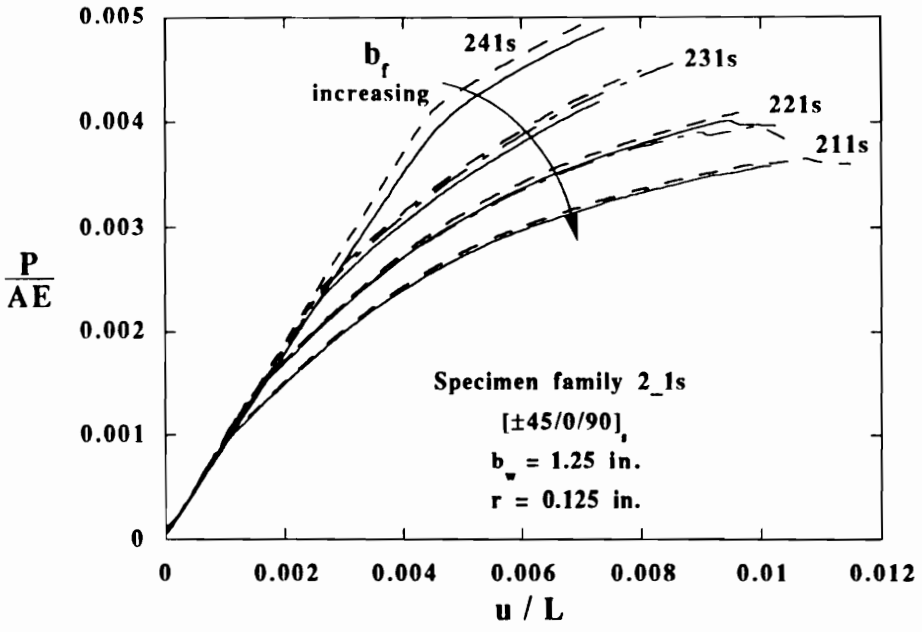

(a)

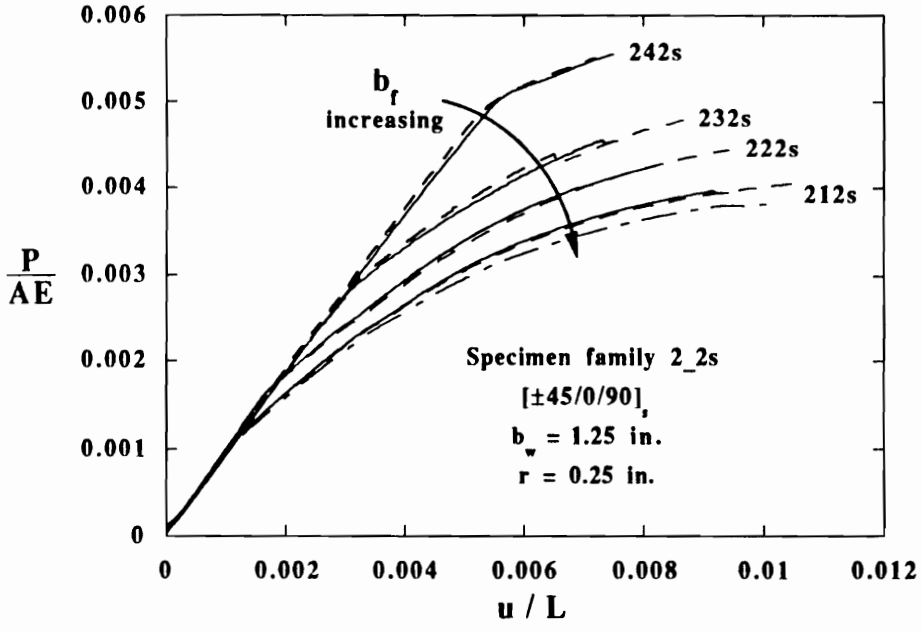

(b)

Figure 5-13. Normalized load-end shortening responses for specimens having a web width of 1.25 in., stacking sequence $[\pm 45/0/90]_S$ and corner radii of (a) 0.125 in. and (b) 0.25 in. Flange sizes range from 0.5 to 1.25 in. Solid and dashed lines indicate replicates of a given specimen type.

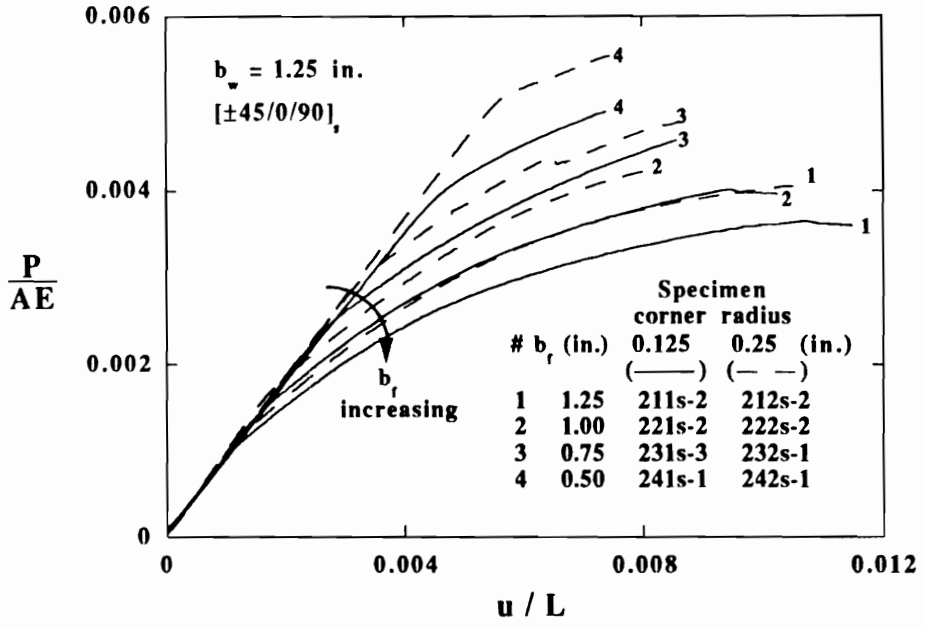

Figure 5-14. Dependence of load-end shortening response on corner radius. Larger corner radius increases buckling and postbuckling stresses. Web width is 1.25 in. The stacking sequence is $[\pm 45/0/90]_S$.

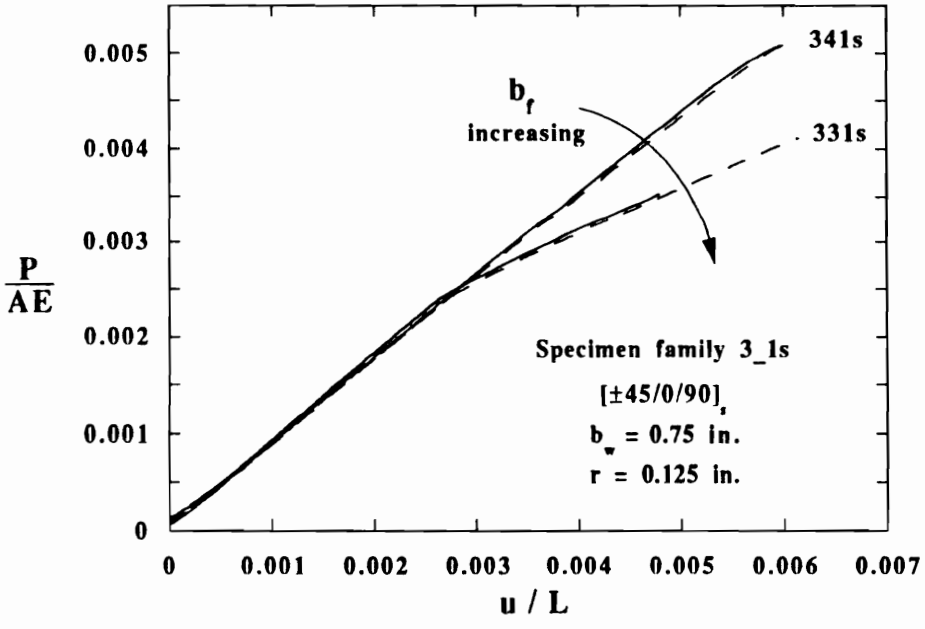

Figure 5-15. Normalized load-end shortening responses for specimens having the smallest web width (0.75 in.). The stacking sequence is $[\pm 45/0/90]_S$. Flange sizes are 0.50 and 0.75 in. Solid and dashed lines indicate replicates of a given specimen type.

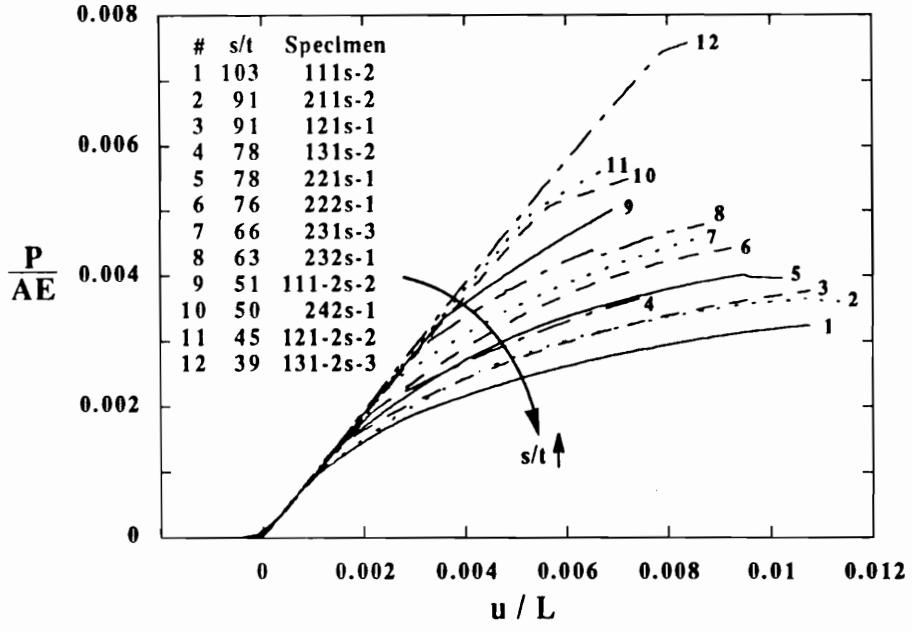

Figure 5-16. Dependence of the load-end shortening response on the normalized section width, s/t. The normalized width is the total width of the developed section, normalized by the laminate thickness.

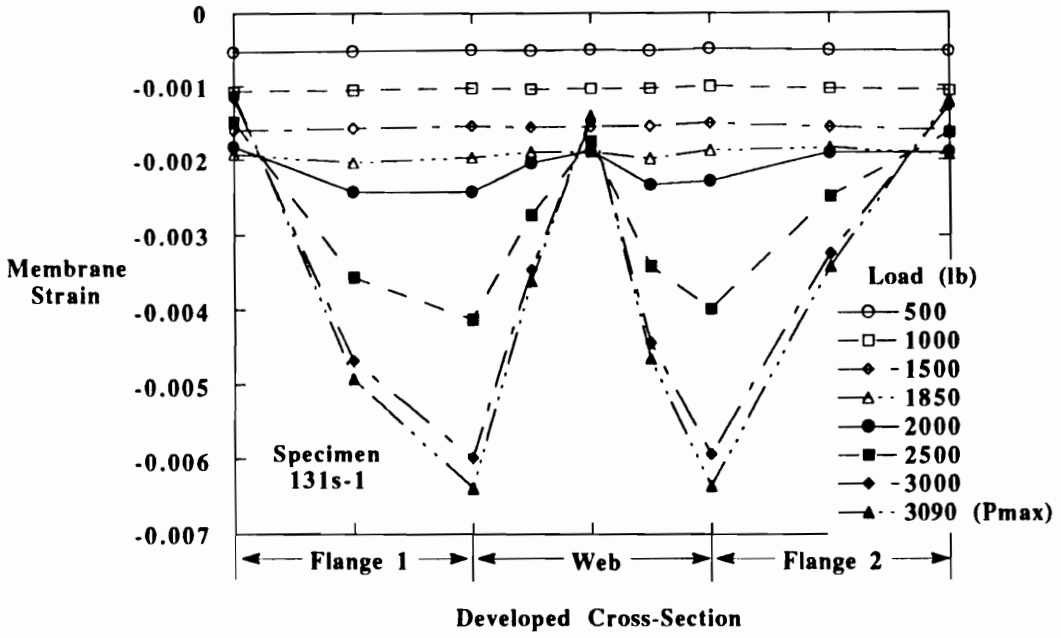

(a)

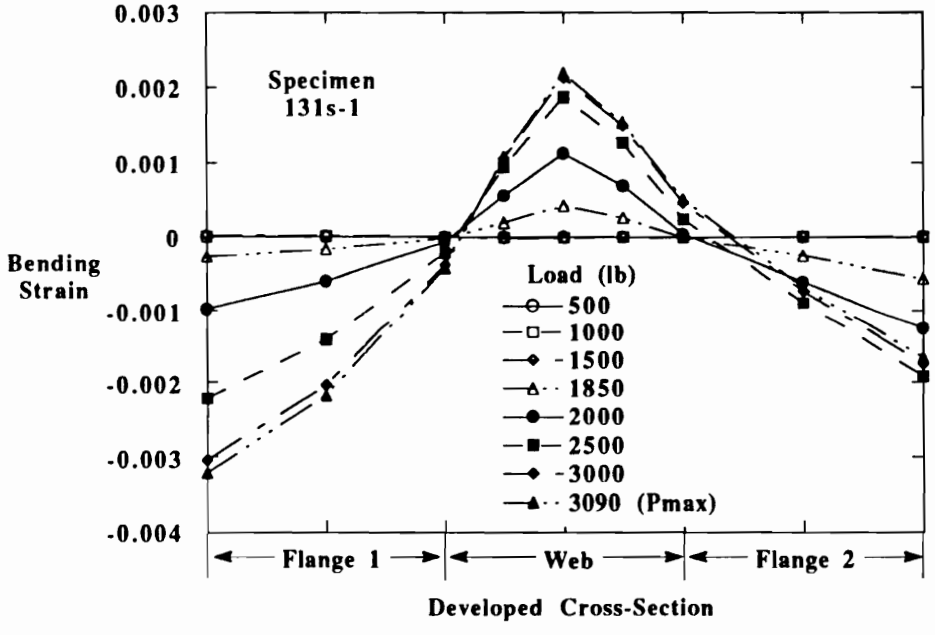

(b)

Figure 5-17. Membrane (a) and bending (b) strain distributions over the width of specimen 131s-1. Geometry: $b_w = 1.75$, $b_f = 0.75$, r = 0.125 in. Stacking sequence is $[\pm 45/0/90]_S$.

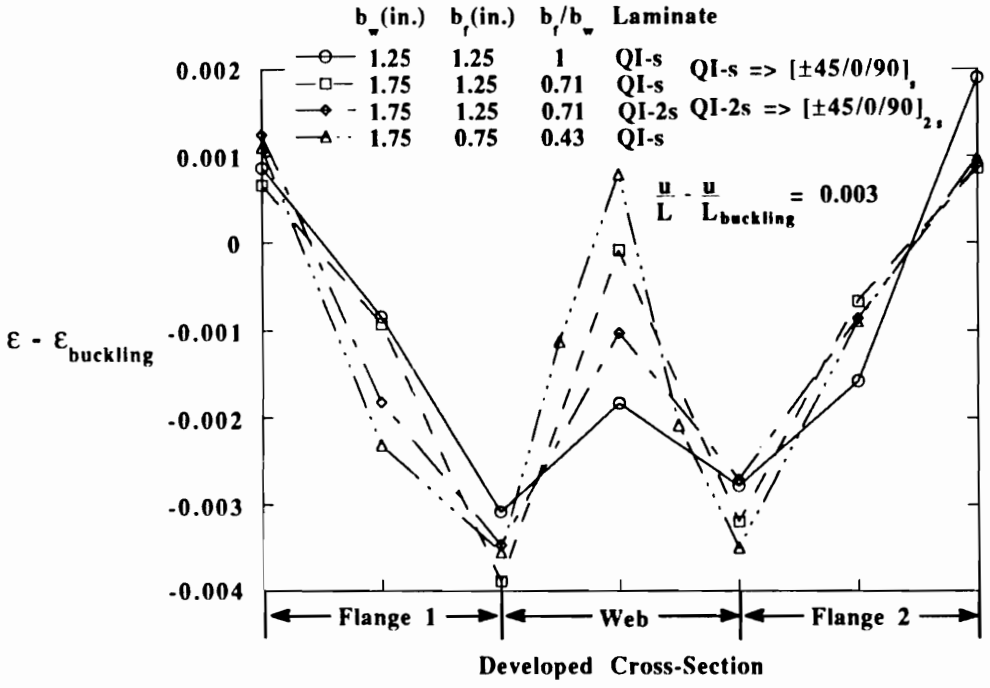

Figure 5-18. Dependence of strain redistribution as a result of buckling on the flange-to-web width ratio and laminate thickness.

Figure 5-19. Photographs of shadow moire fringe patterns for specimen 111-2s-2. Geometry: $b_w = 1.75$, $b_f = 1.25$, $r = 0.125$ in. Stacking sequence: $[\pm 45/0/90]_{2s}$. No visible twisting. Failure at nodal position.

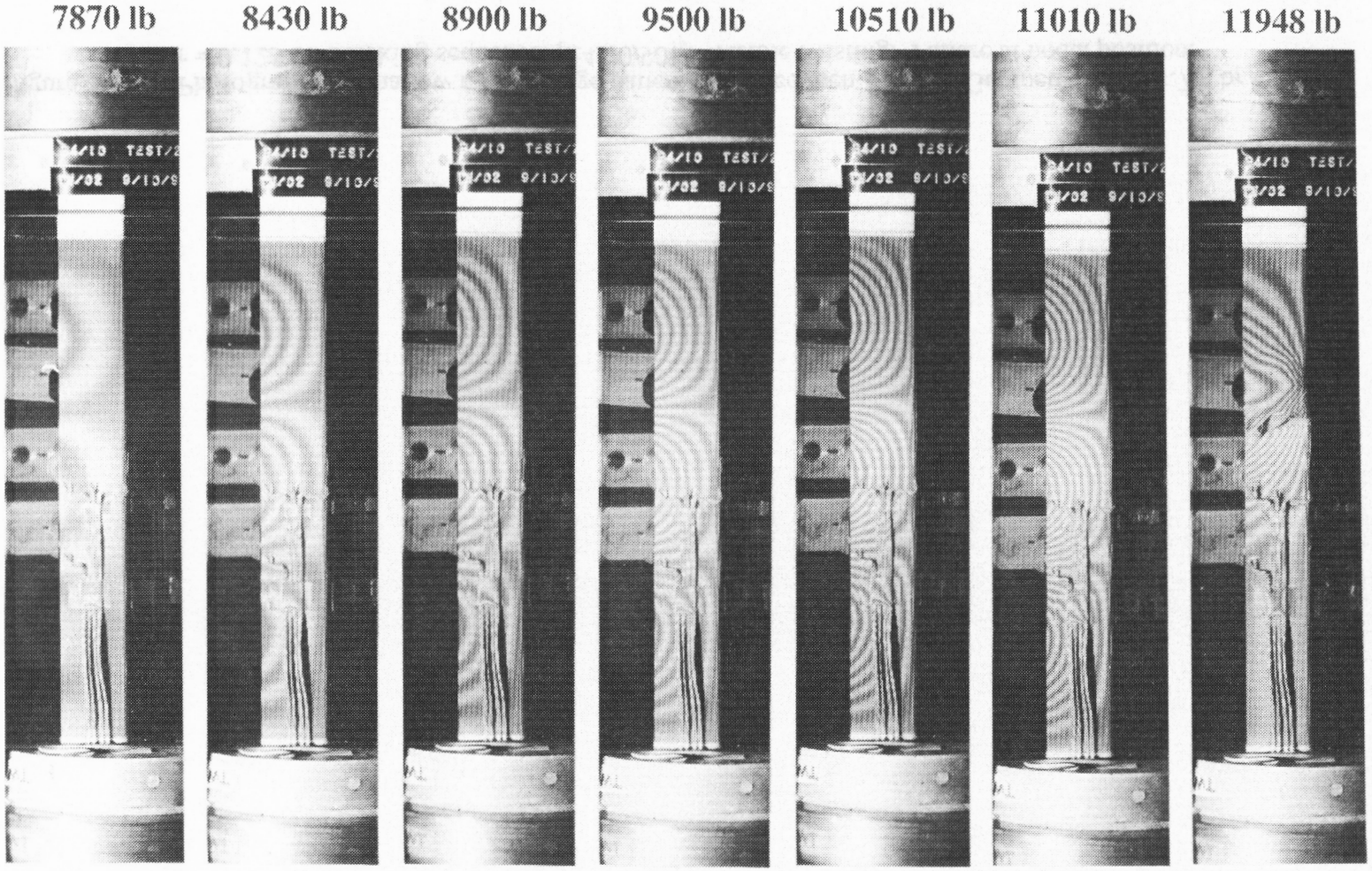
7870 lb
8430 lb
8900 lb
9500 lb
10510 lb
11010 lb
11948 lb
(a)
(b)
(c)
(d)
(e)
(f)
(g)

Figure 5-20. Photographs of shadow moire fringe patterns for specimen 111s-2. Geometry: $b_w = 1.75$, $b_f = 1.25$, $r = 0.125$ in. Stacking sequence: $[\pm 45/0/90]_s$. Visible twisting. Failure at nodal position.

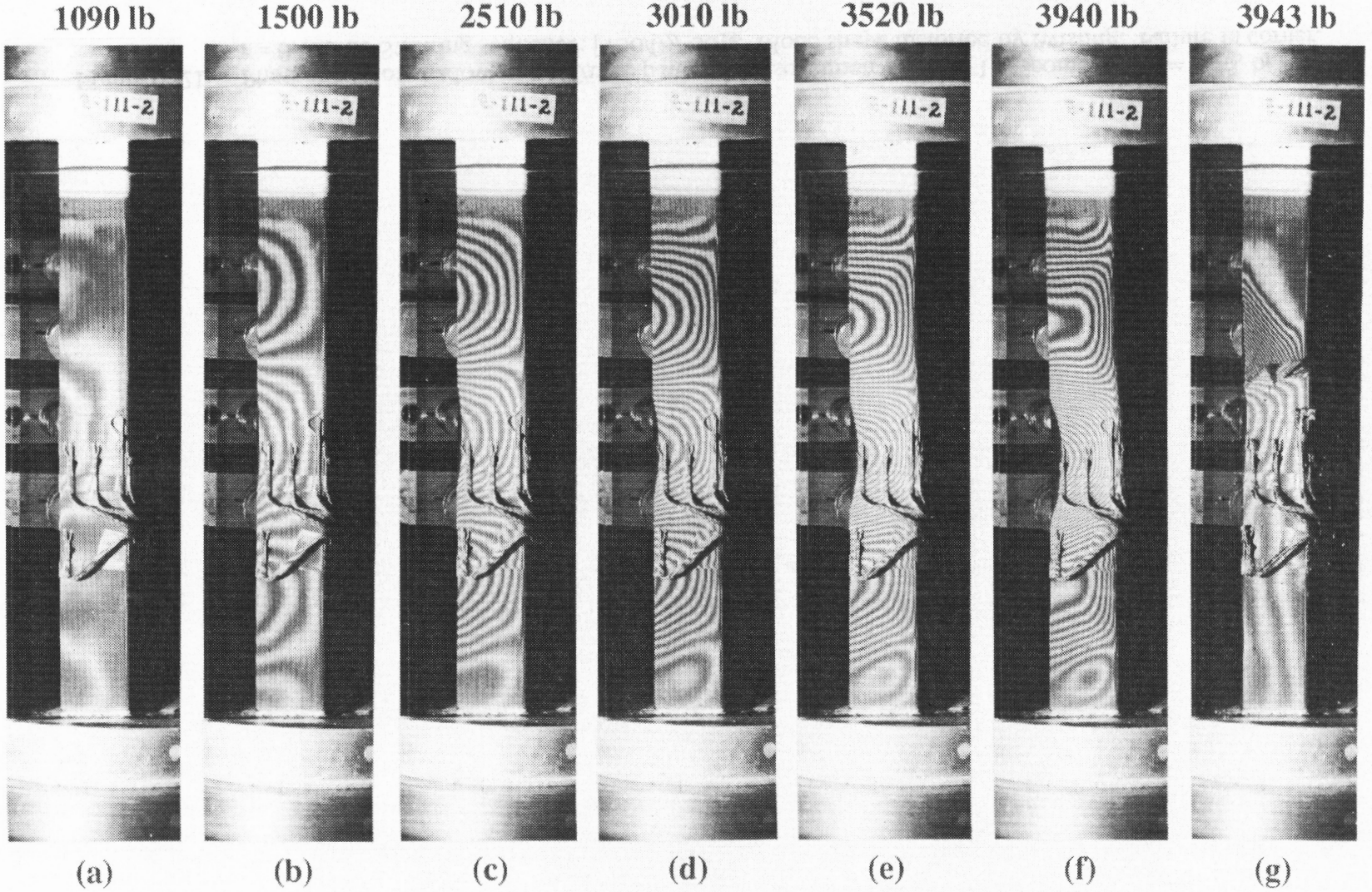
1090 lb
1500 lb
2510 lb
3010 lb
3520 lb
3940 lb
3943 lb
(a)
(b)
(c)
(d)
(e)
(f)
(g)

Figure 5-21. Photographs of shadow moire fringe patterns for specimen 111orth-1. Geometry: $b_w = 1.75$, $b_f = 1.25$, $r = 0.125$ in. Stacking sequence: $[+30/0_2/-30]_s$. Mode shape distorted by twisting. Failure in corner.

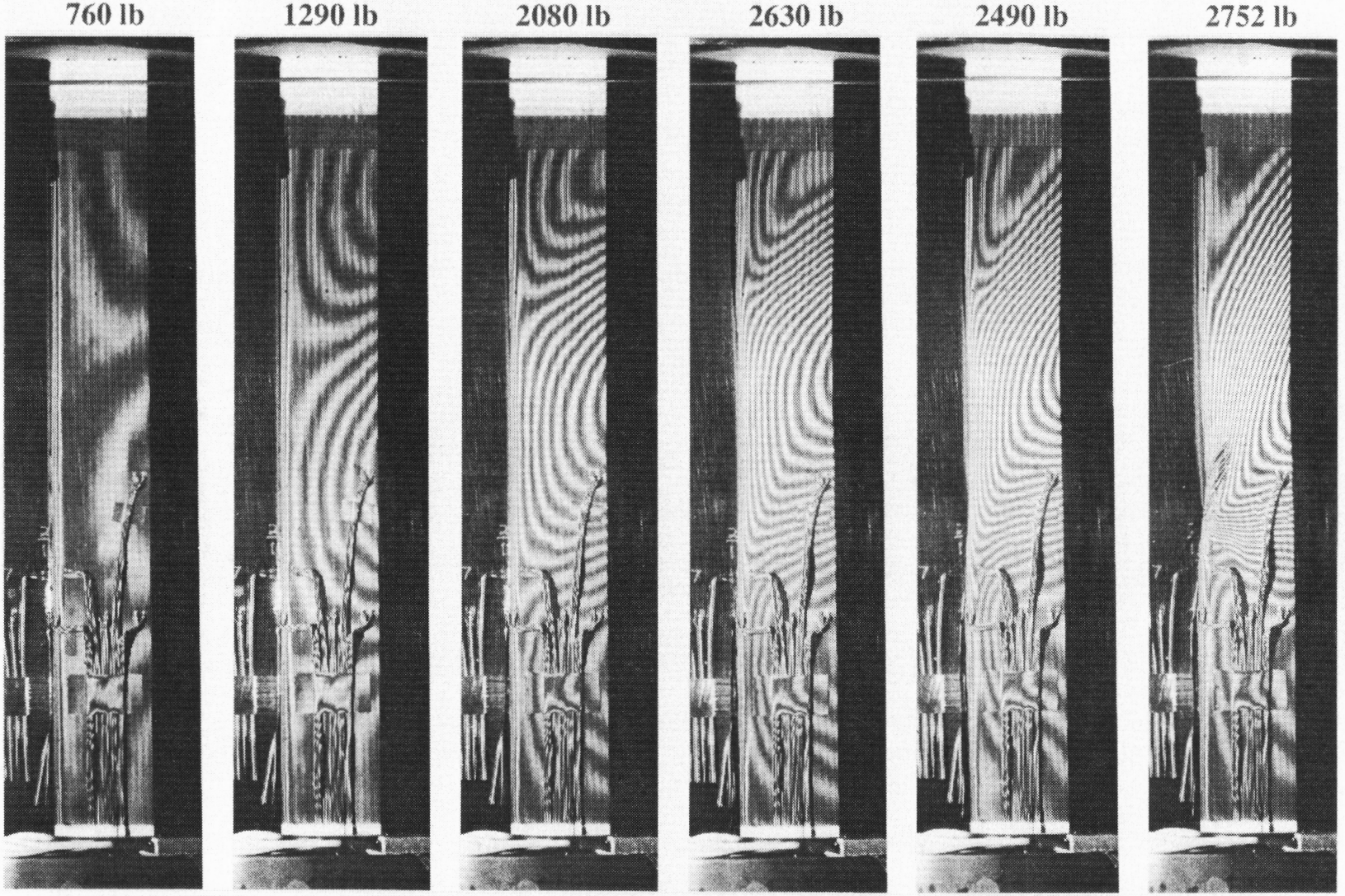
760 lb
1290 lb
2080 lb
2630 lb
2490 lb
2752 lb
(a)
(b)
(c)
(d)
(e)
(f)

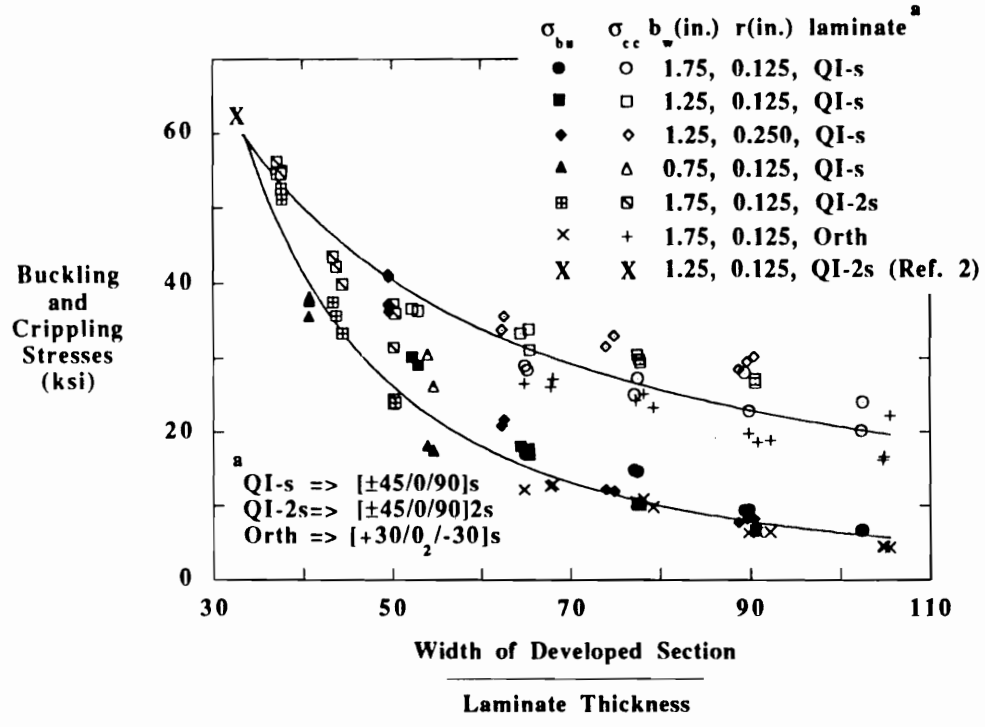

Figure 5-22. Experimental buckling and crippling stress summary. Data plotted versus normalized width = width of developed section/thickness.

Figure 5-23. Post-failure photographs of $[\pm 45/0/90]_{2s}$ specimens (a) 111-2s-2 (nodal failure) and (b,c) 121-2s-1 (anti-nodal failure). Features include flange free edge delamination (a,c), crushing (b), and bending compression failure of web (c).

TW-04
(c)
TW-04
(b)
TW-02
(a)

Figure 5-24. Overall (a) and macro (b) post-failure photographs of $[\pm 45/0/90]_{2s}$ specimen 121-2s-3. Tensile failure of flanges in bending at two axial locations.

2
90M1
(b)
1

2
1
(a)

Figure 5-25. Overall (a) and macro (b) post-failure photographs of $[\pm 45/0/90]_{2s}$ specimen 121-2s-3. Flange free edge delamination and compressive bending failure of web.

2
90MT
(b)
1

2
1
(a)

Figure 5-26. Overall (a) and macro (b) post-failure photographs of $[\pm 45/0/90]_{2s}$ specimen 131-2s-2. Damage throughout laminate, including free edge delamination and corner crushing at nodal position.

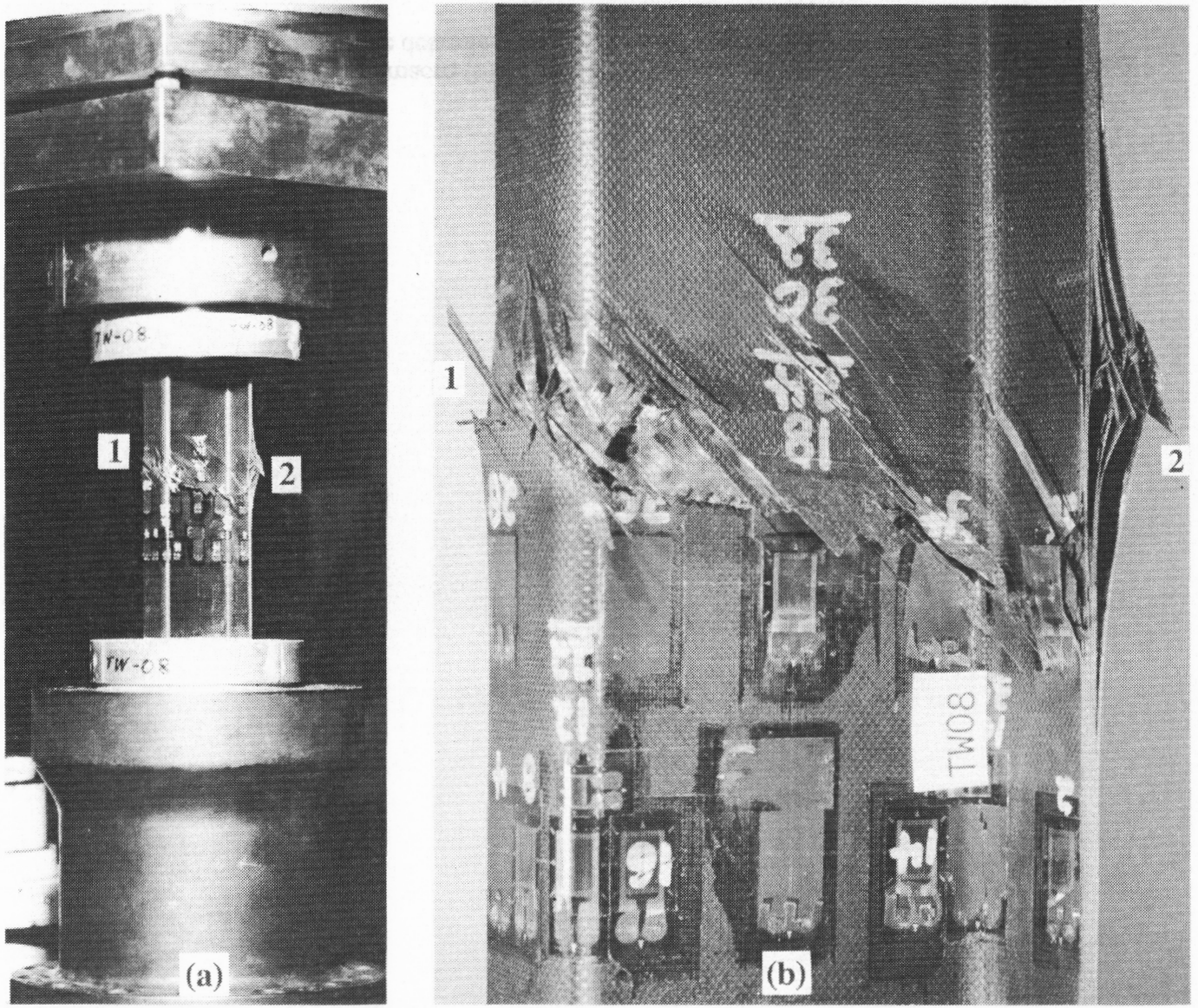
TW-08
1
2
TW-08
(a)
1
2
TW08
(b)

Figure 5-27. Overall (a) and macro (b) post-failure photographs of $[\pm 45/0/90]_s$ specimen 111s-2. Flange free edge delamination and corner crushing at nodal position.

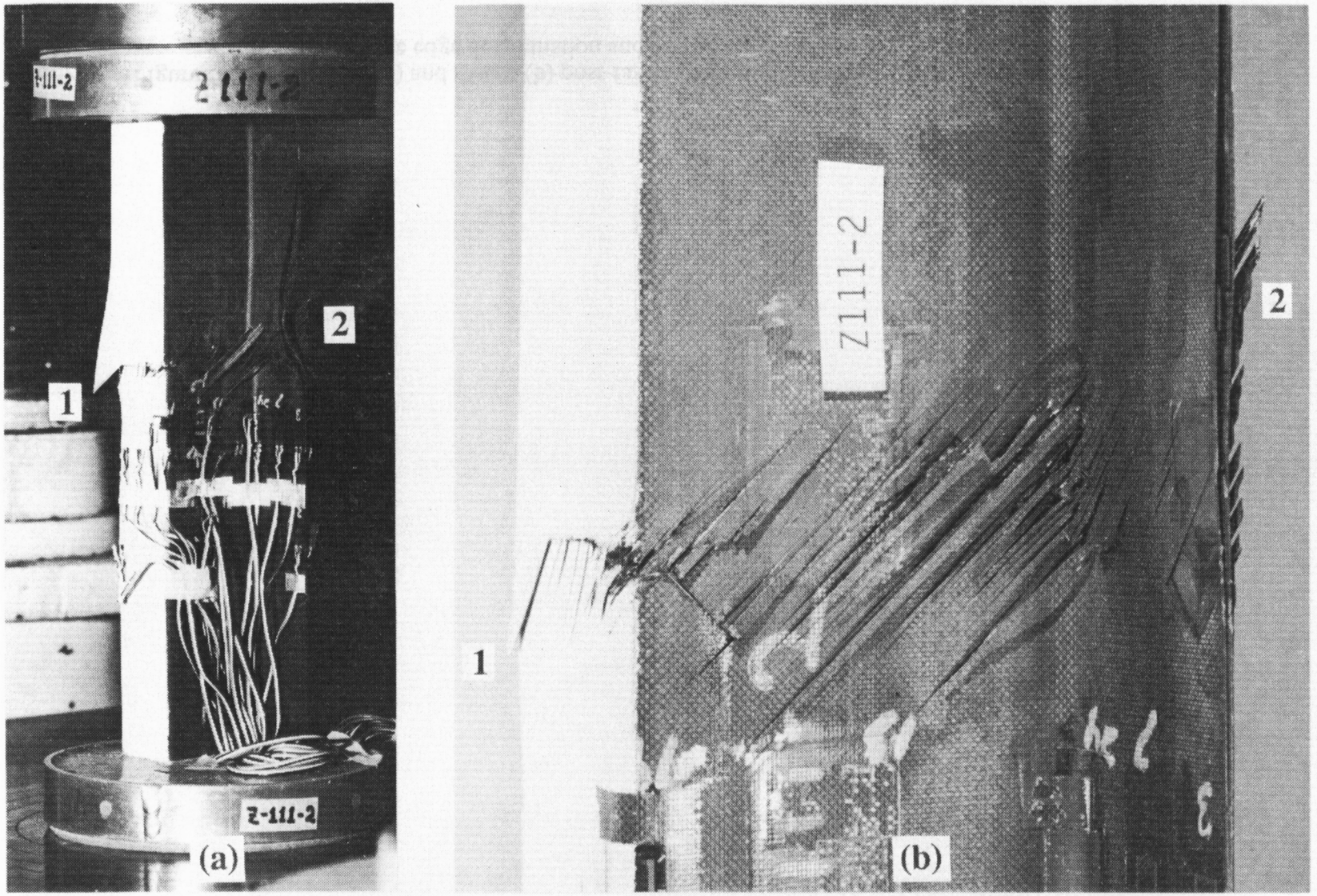
Z111-2
Z-111-2
1
2
(a)
Z111-2
1
2
(b)

Figure 5-28. Overall (a) and macro (b) post-failure photographs of $[\pm 45/0/90]_s$ specimen 121s-1. Flange free edge delamination and corner crushing at nodal position.

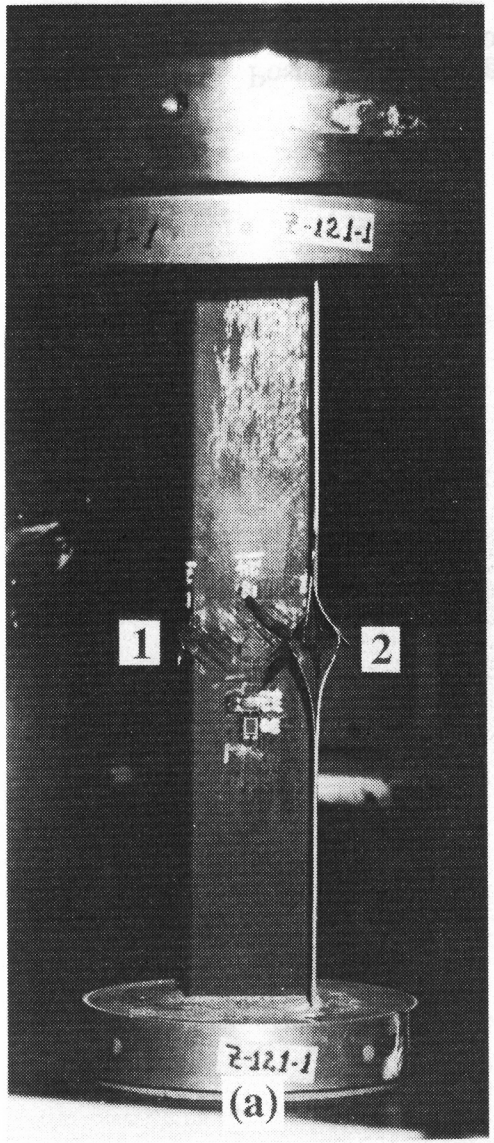
Z-121-1
1
2
Z-121-1
(a)

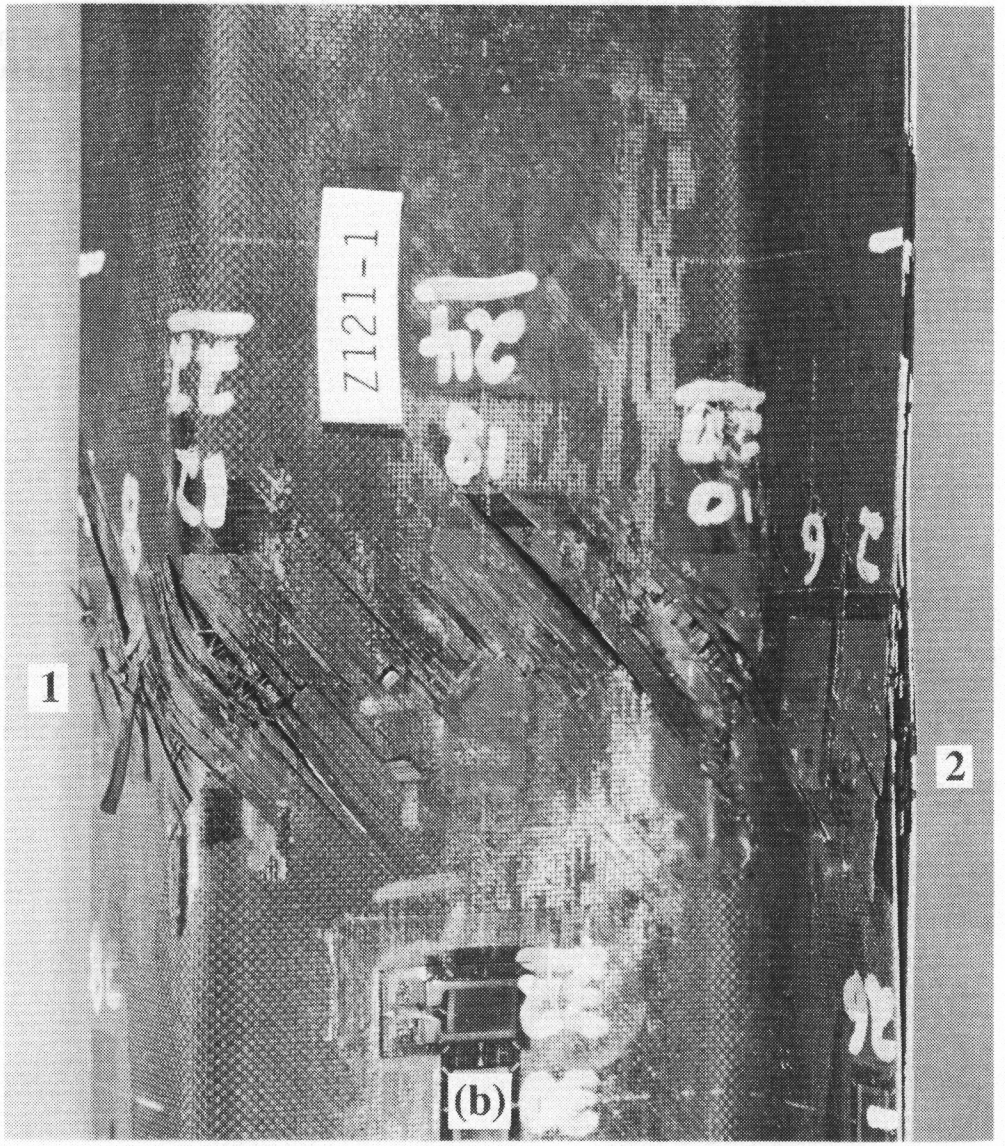
Z121-1
1
2
(b)

Figure 5-29. Post-failure photographs of $[+30/0_2/-30]_S$ specimens (a,b) 111orth-3, (c) 121orth-2 and (d) 121orth-3. Shown is the creasing of the flanges and web, and ply splitting near the corners.

(d)
Z-121-ORTH-2
(c)
(b)
(a)

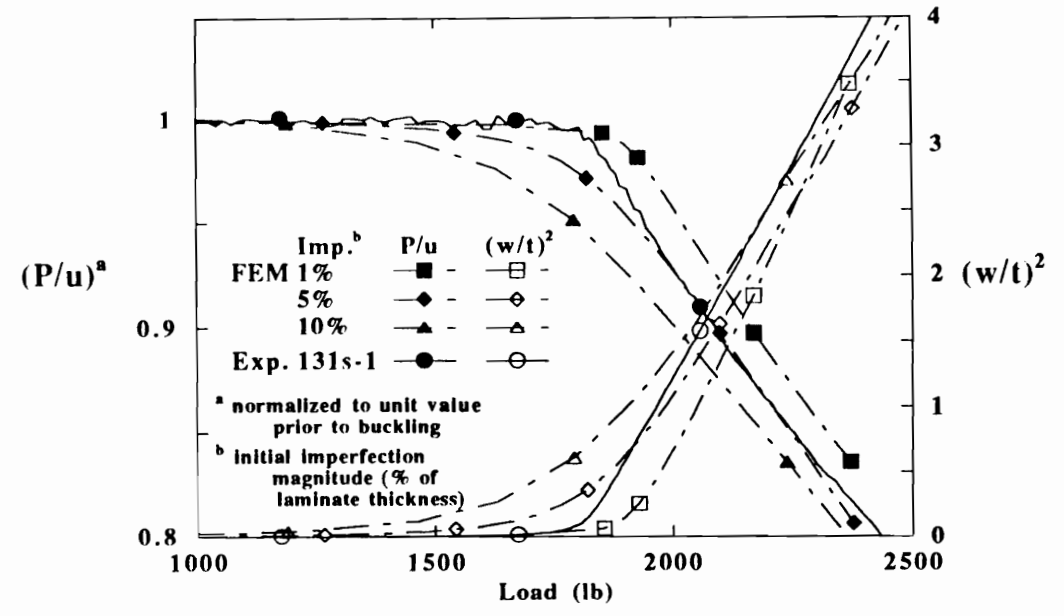

(a)

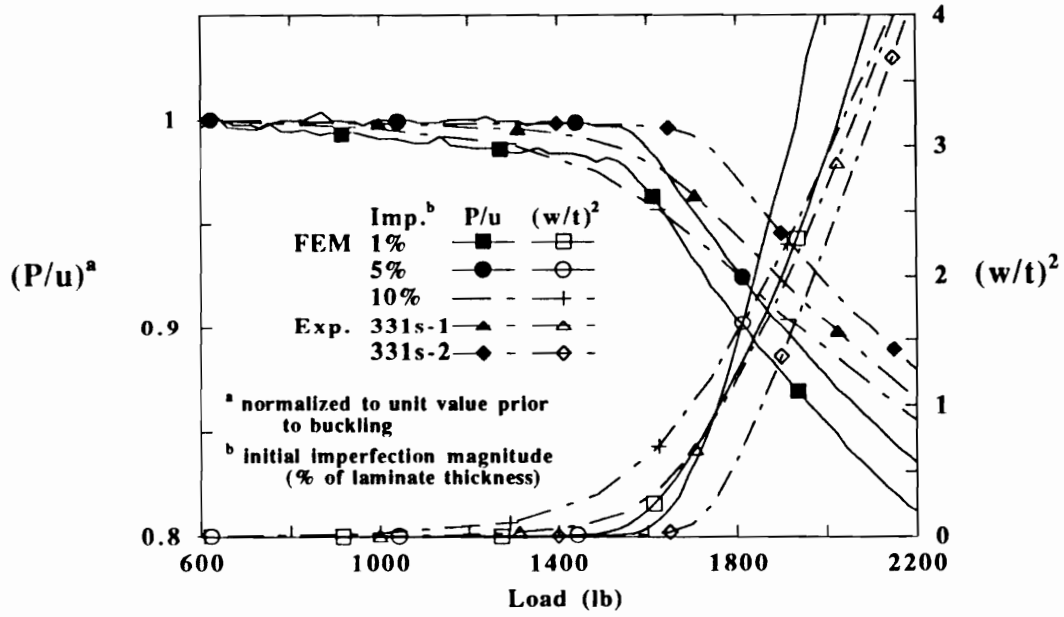

(b)

Figure 6-1. Effect of assumed initial imperfections on the end shortening and out-of-plane displacement responses near buckling. Numerical predictions and experimental results are provided for specimen types 131s (a) and 331s (b). Results indicate the as-fabricated imperfection is between 1 and 5% of the laminate thickness.

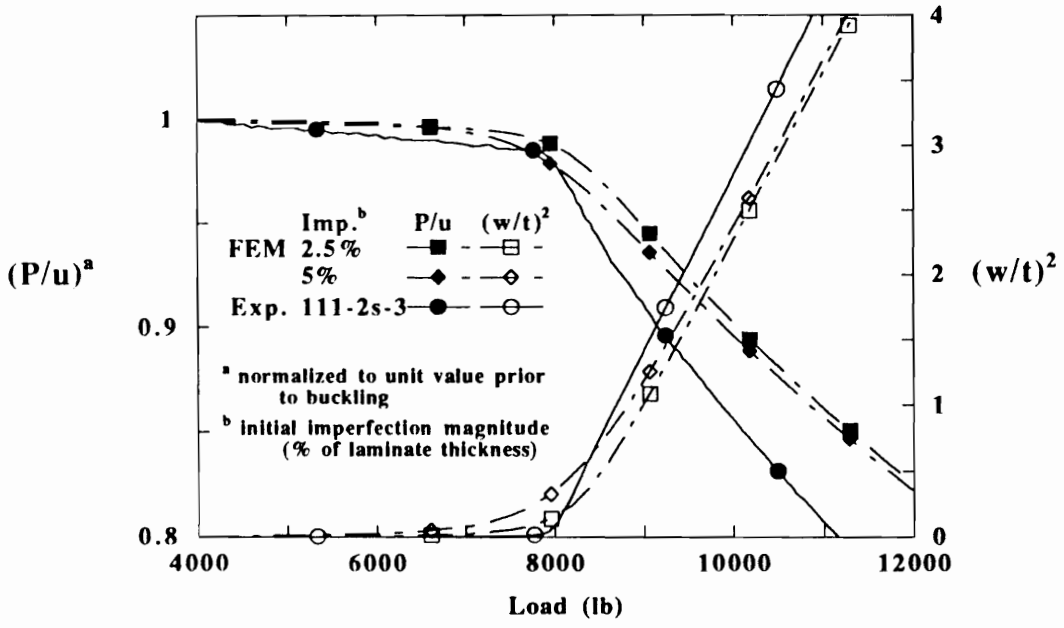

Figure 6-2. Effect of assumed initial imperfections on the end shortening and out-of-plane displacement responses near buckling. Numerical predictions and experimental results are provided for the 16-ply quasi-isotropic specimen type 111-2s. Results indicate the as-fabricated imperfection is approximately 2.5% of the laminate thickness.

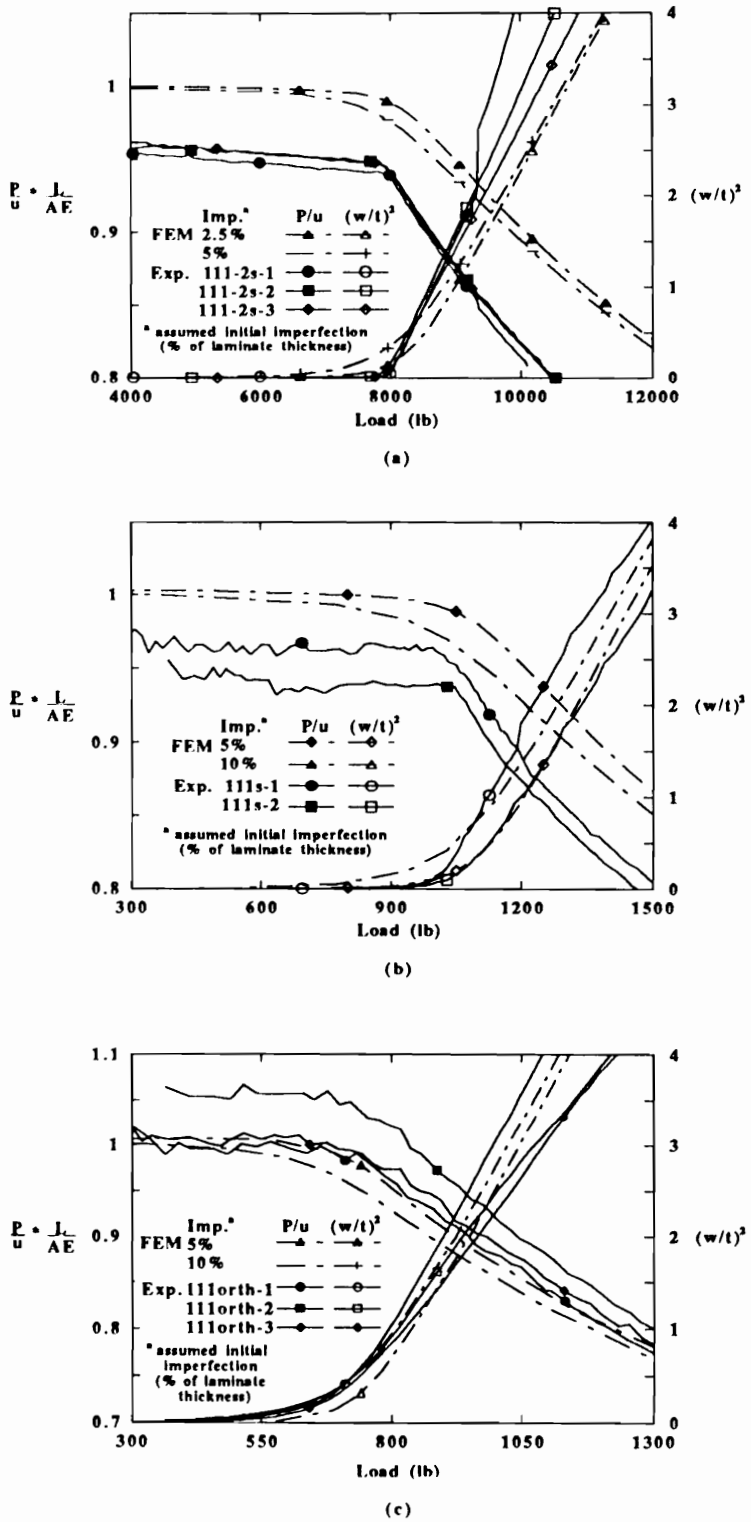

Figure 6-3. Correlation of experimental and predicted end shortening and out-of-plane displacement responses at buckling for specimen types 111s-2s (a), 111s (b) and 111orth (c).

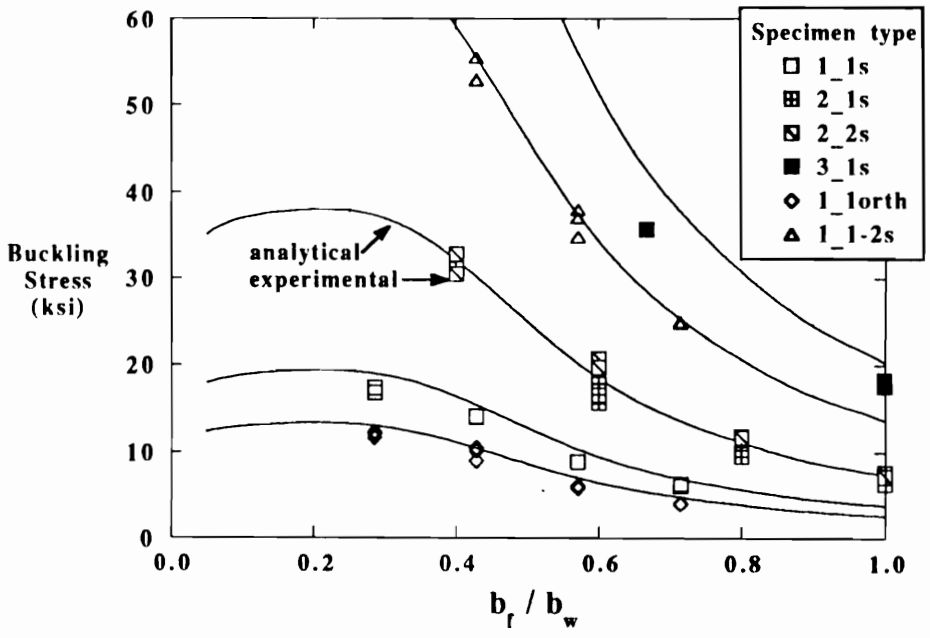

Figure 6-4. Buckling stresses as a function of the flange-to-web width ratio. Experimental data and analytical predictions.

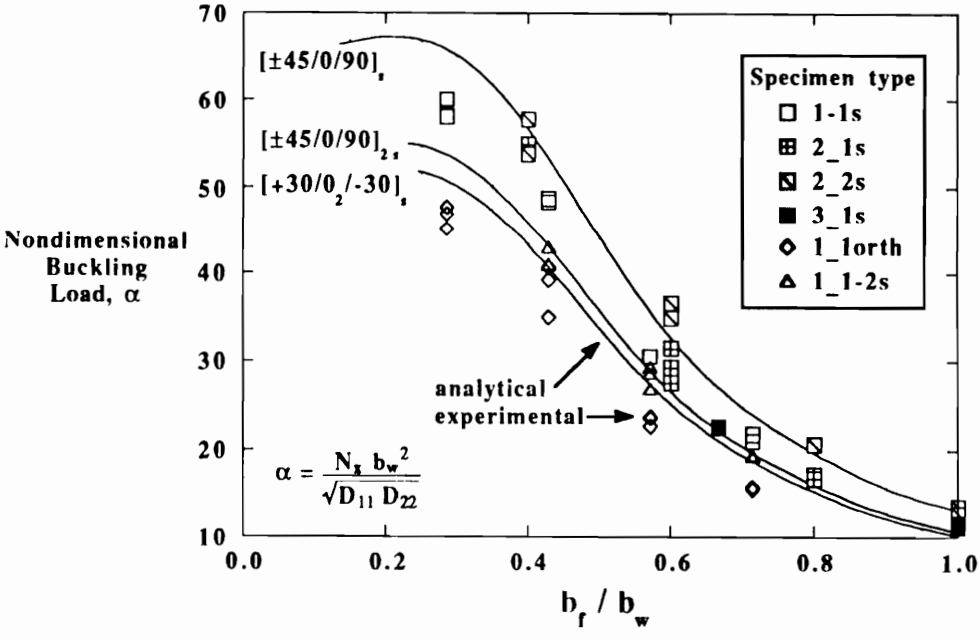

Figure 6-5. Buckling loads normalized in terms of parameter α as a function of the flange-to-web width ratio. Load parameter α normalizes data for various web sizes. Experimental data and analytical predictions.

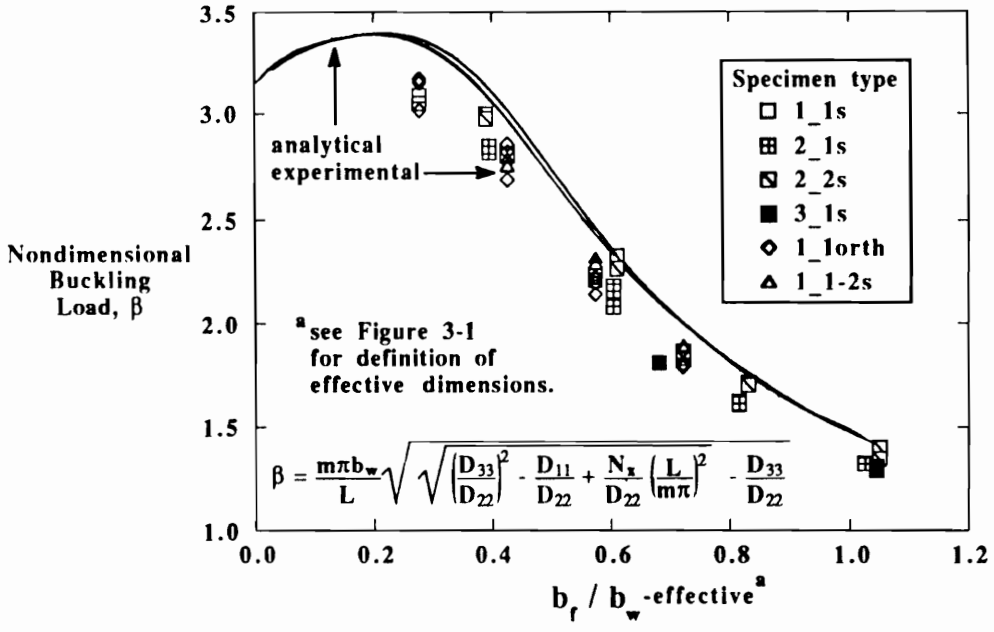

Figure 6-6. Normalized buckling loads in terms of parameter β as a function of the flange-to-web width ratio. Load parameter β normalizes data for all of the material and geometrical variables. Experimental data and analytical predictions.

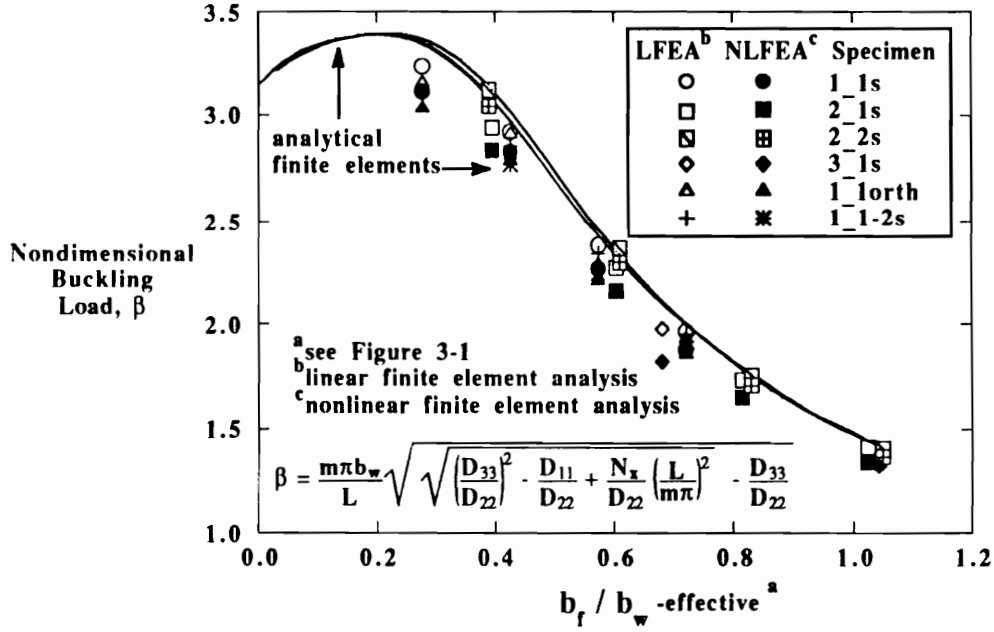

Figure 6-7. Buckling loads normalized in terms of parameter β estimated by linear and nonlinear finite element analyses as a function of the flange-to-web width ratio.

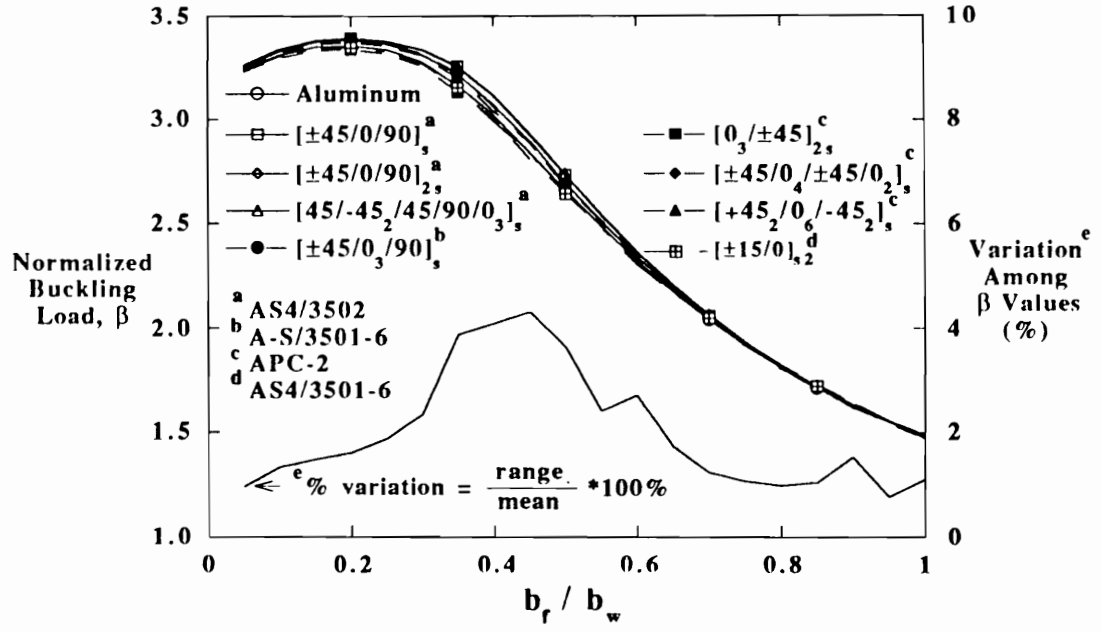

Figure 6-8. Range of predicted β–normalized buckling curves for Z- and channel section stiffeners reported in the literature.

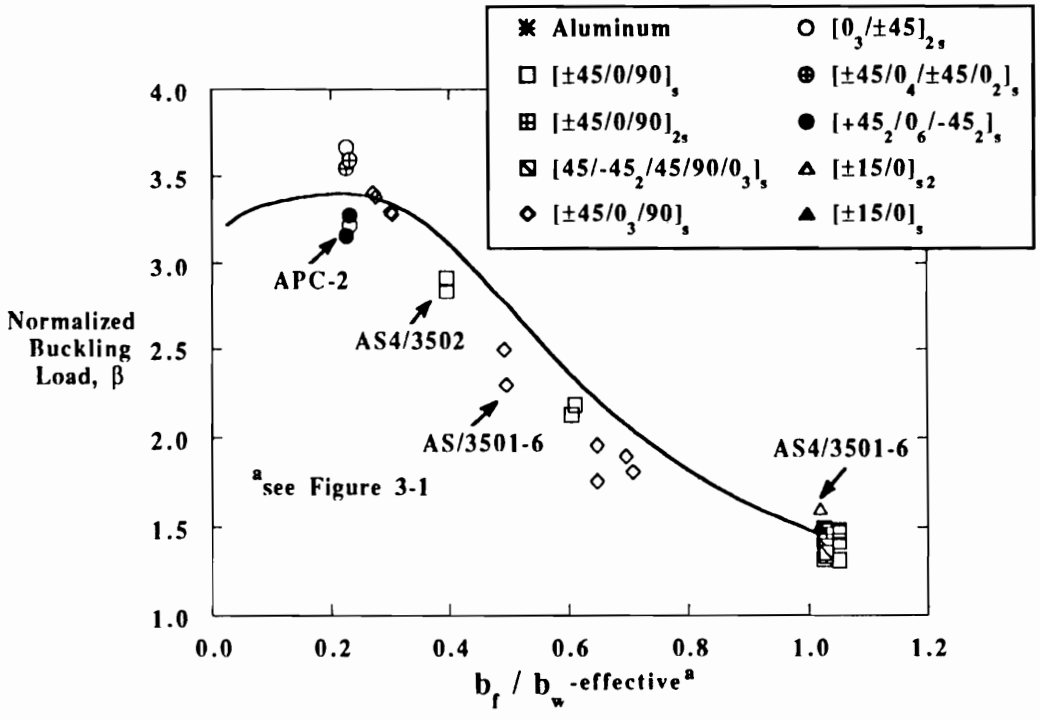

Figure 6-9. Buckling loads normalized in terms of parameter β as a function the flange-to-web width ratio. Experimental data for Z- and channel section stiffeners reported in the literature.

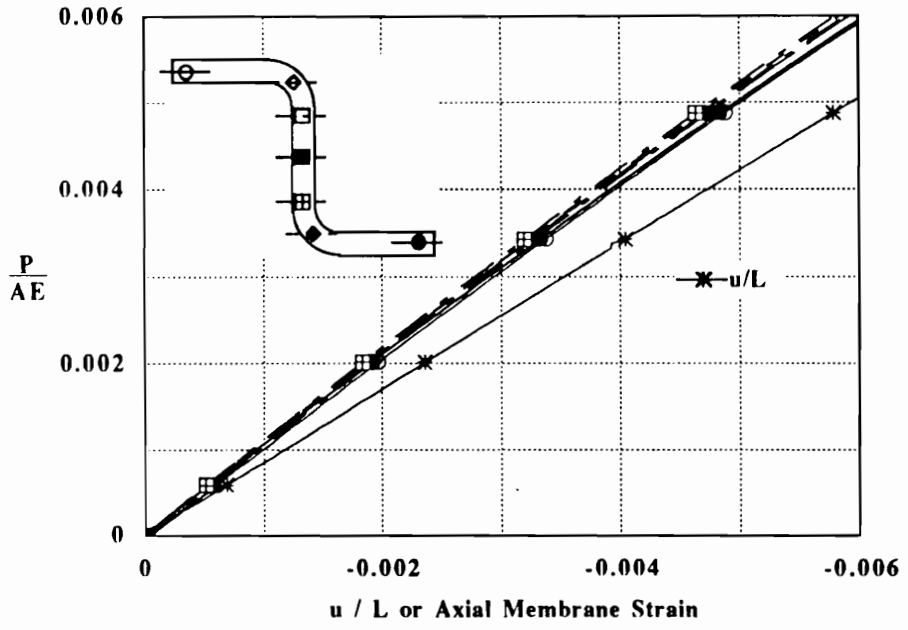

Figure 6-10. Comparison of experimental prebuckling local membrane strains with load- and displacement-based global strain measures for specimen 131-2s-3. The lower displacement-based global strain suggests prebuckling stiffness error is related to the end shortening.

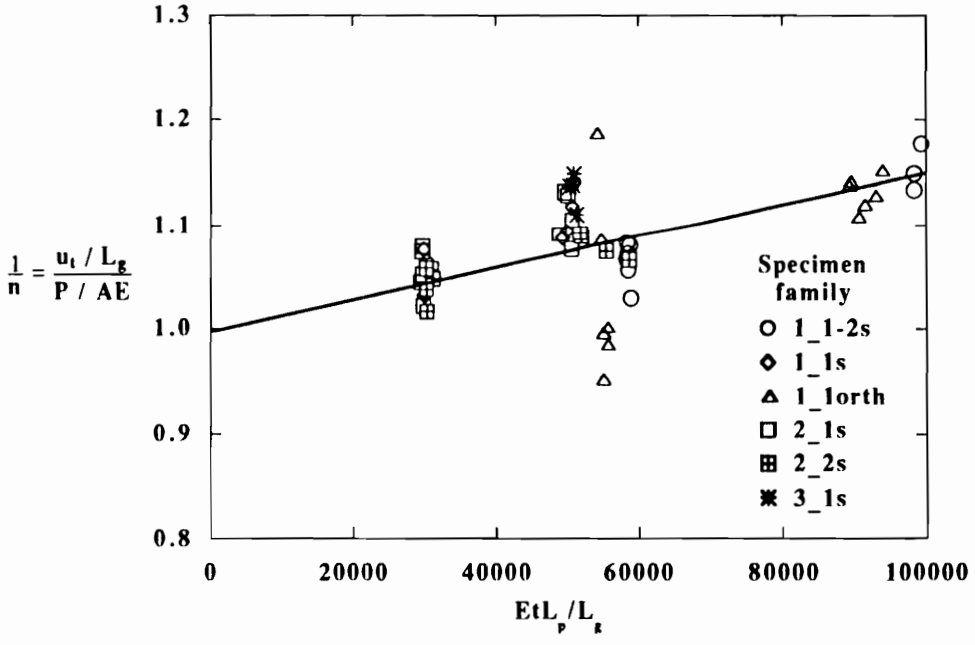

Figure 6-11. Prebuckling stiffness deviation as a function of grouping of geometric and material variables predicted from model.

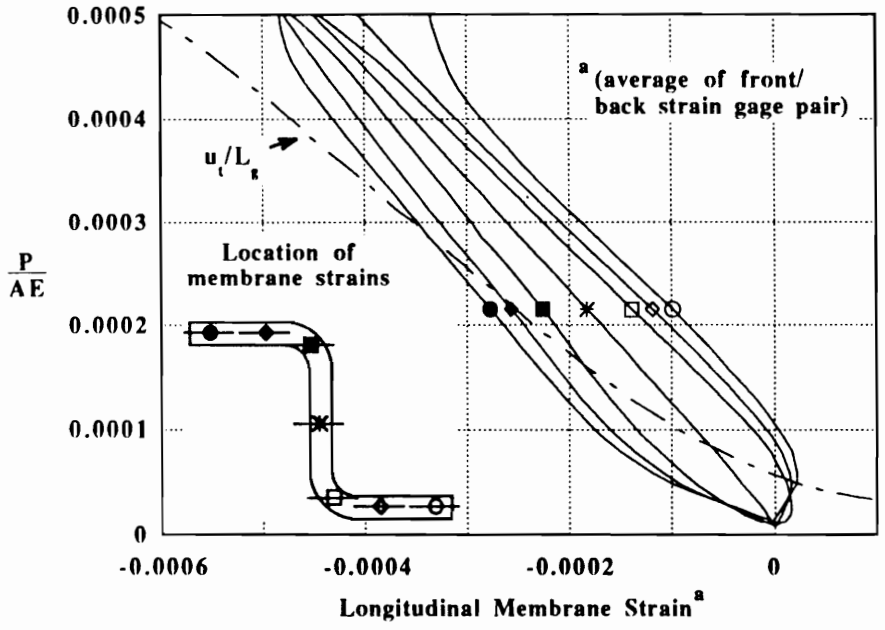

Figure 6-12. Prebuckling membrane strain distribution over cross-section of specimen 121orth-2. Distribution indicates a lack of parallelism between top and bottom surfaces in contact with testing machine.

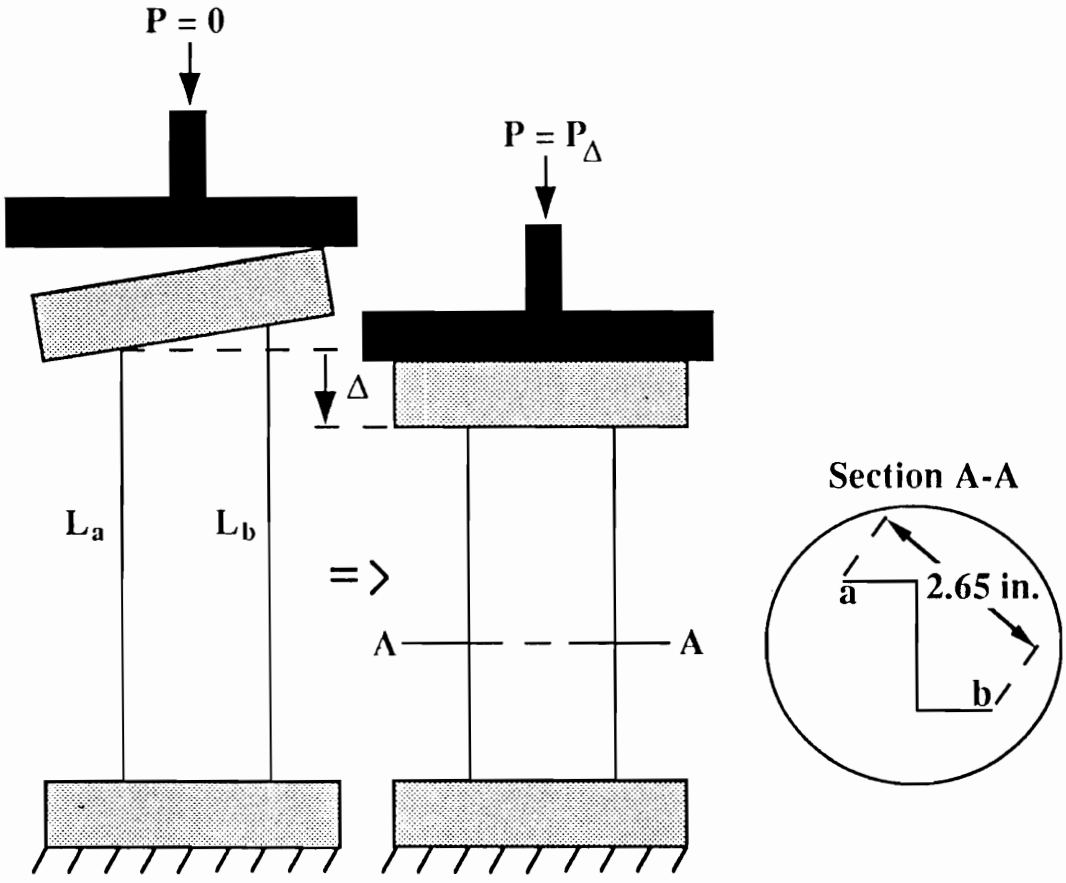

$$\varepsilon_a = \frac{\Delta}{L_a};\quad \varepsilon_b = \frac{\Delta + (L_b - L_a)}{L_b}$$

if $L_a = k * L_b$, then

$$\varepsilon_b - \varepsilon_a = \frac{\Delta + L_b(1-k)}{L_b} - \frac{\Delta}{kL_b} = 1.82*10E\text{-}4$$ for specimen 121orth-2 from strain gage data.

If $\Delta = 0$ and $L_b = 10$ in.,

then $k = 0.9998$ and $L_a = 9.998$ in.

δL across 5 in. diameter endpot is:

$$\delta L = \frac{5}{2.65}(10 - 9.998) = 0.004 \text{ in.}$$

Figure 6-13. Calculation of the difference in the distances between the surfaces of specimen 121orth-2 at diametrically opposed positions in contact with the testing machine necessary for the observed strain distribution.

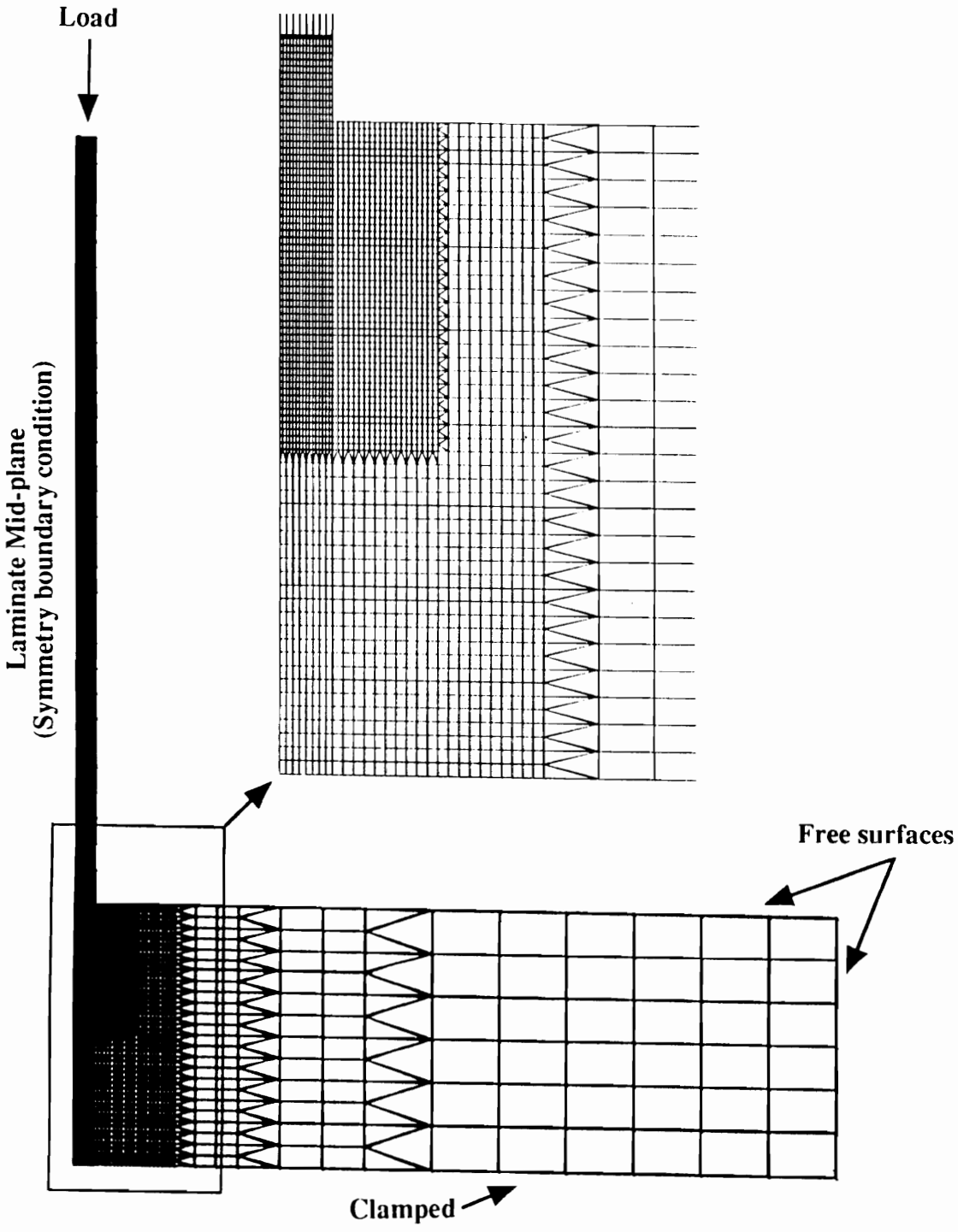

Figure 6-14. Two-dimensional finite element mesh used to investigate potting-to-stiffener constraint.

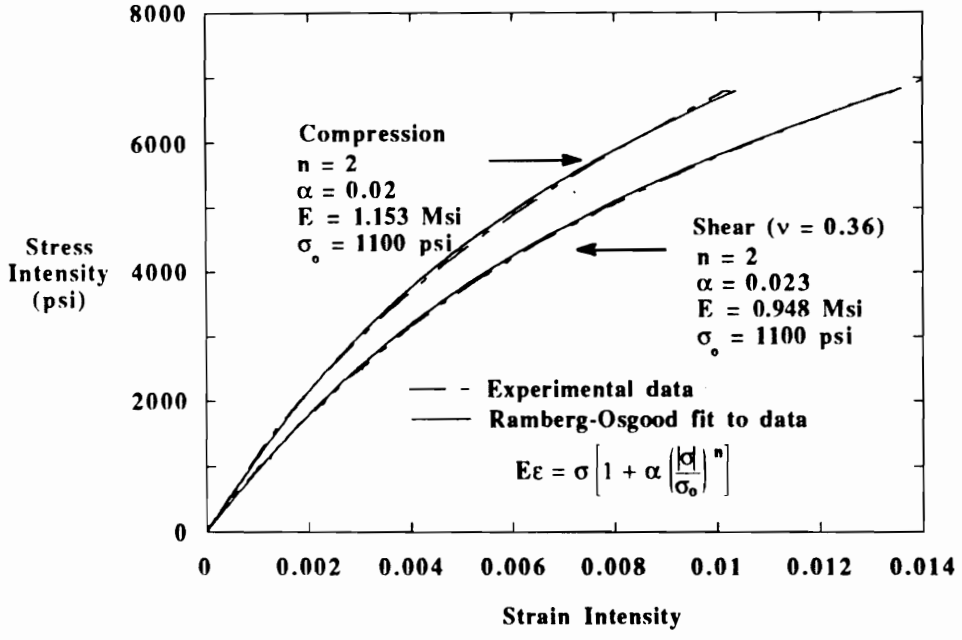

Figure 6-15. Compression and shear stress intensity-strain intensity for potting material. Experimental data and Ramberg-Osgood deformation theory fit to data.

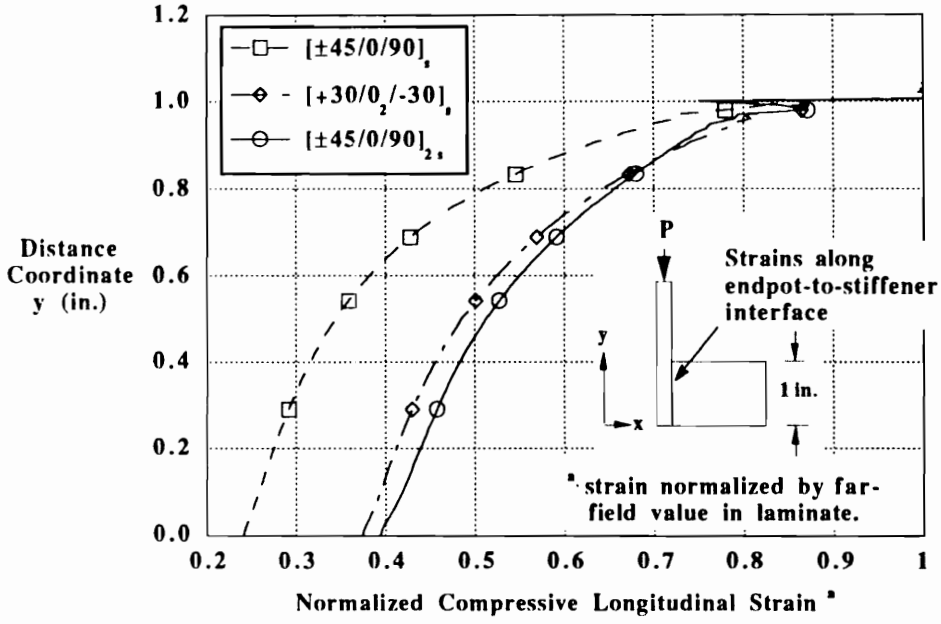

(a)

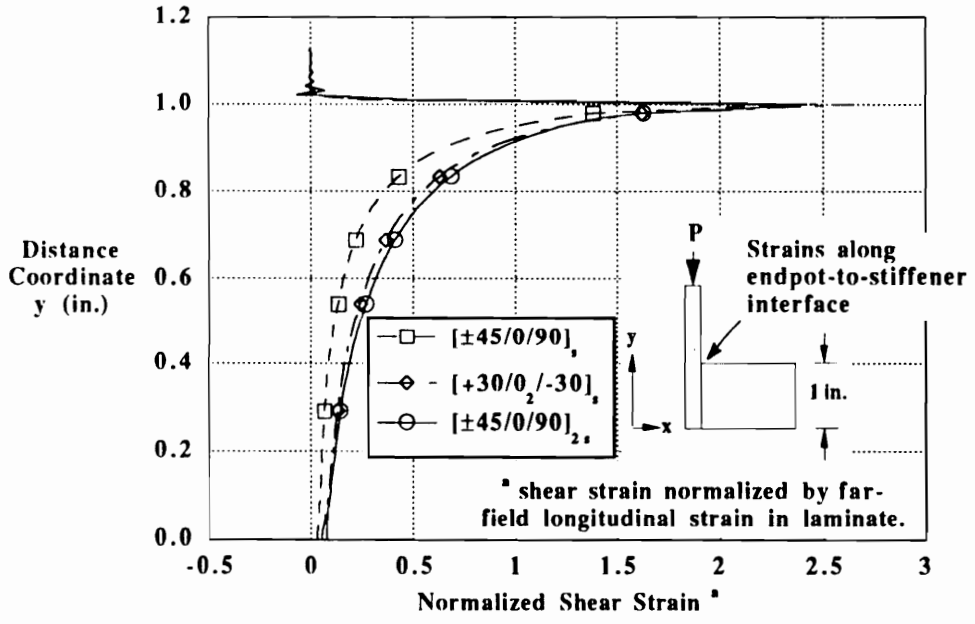

(b)

Figure 6-16. Compression (a) and shear (b) strain distributions within the potted end supports predicted by 2-dimensional finite element analyses. Values are normalized with respect to the far-field value in the unsupported laminate.

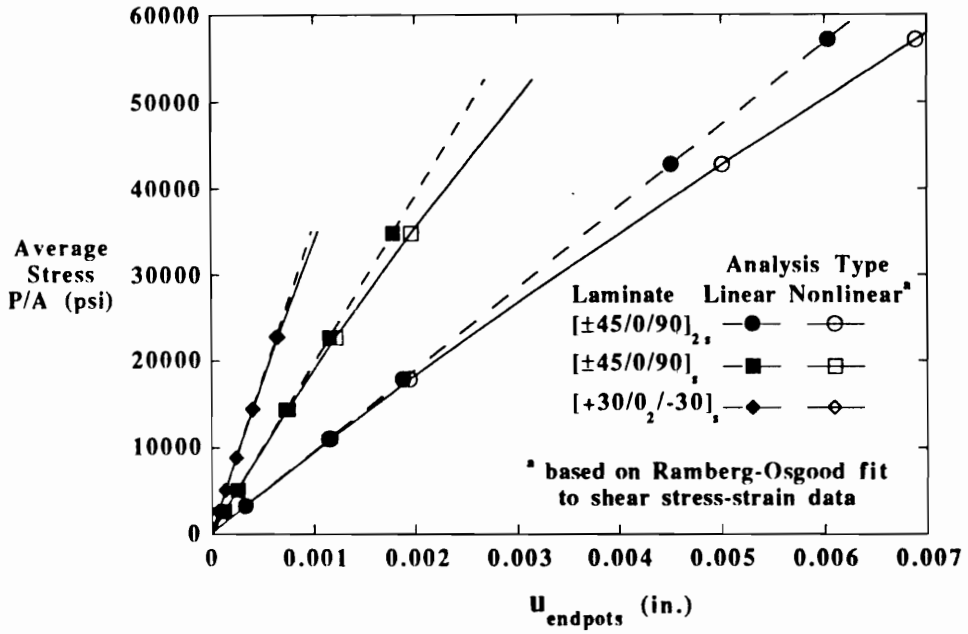

Figure 6-17. Displacement in the potted end supports predicted by the 2-dimensional generalized plane strain finite element analyses. Influence of material nonlinearity is small.

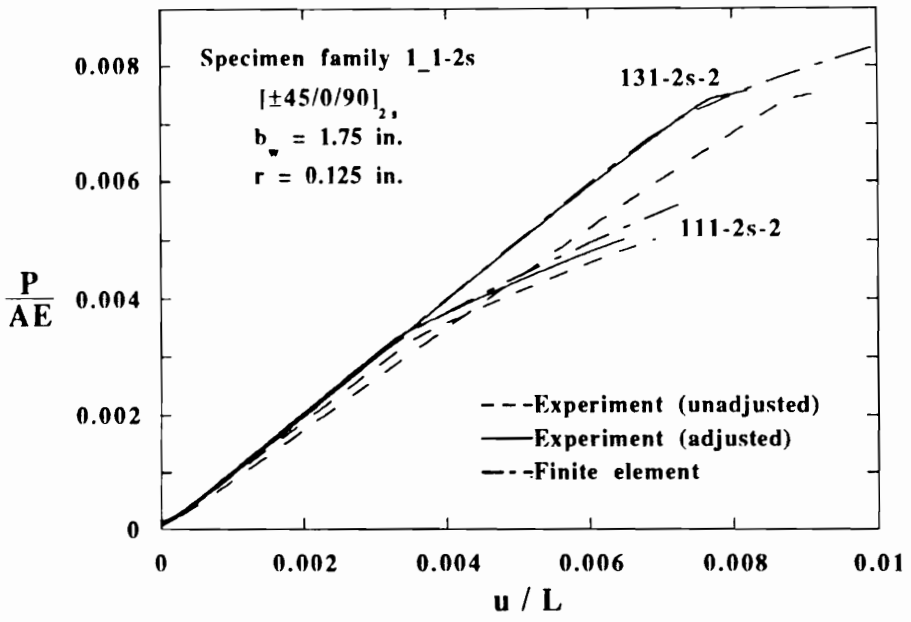

(a)

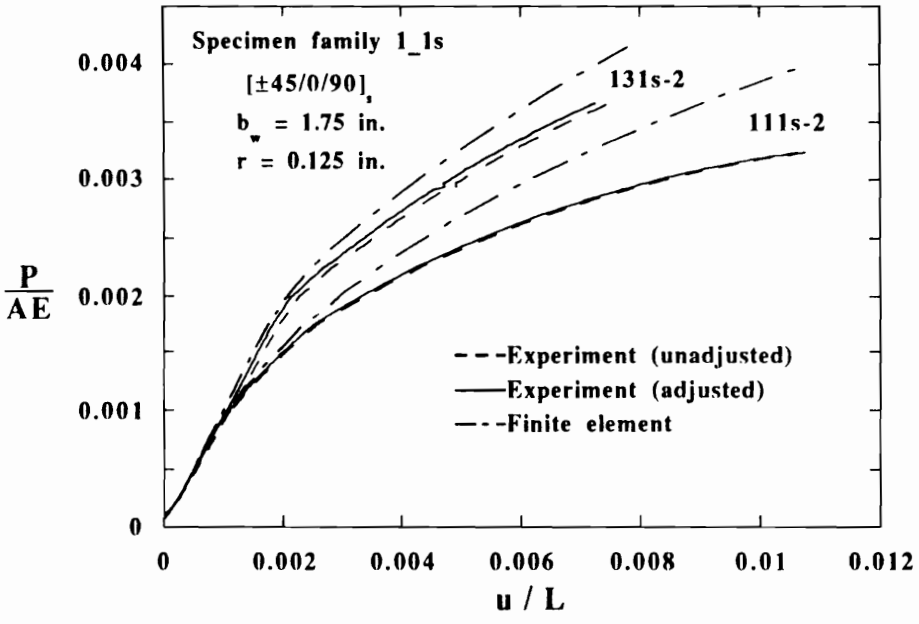

(b)

Figure 6-18. Normalized load-end shortening responses illustrating adjustment for displacement which occurs within the potted end supports. Stacking sequences are: (a) $[\pm 45/0/90]_{2S}$ and (b) $[\pm 45/0/90]_{S}$. Web width is 1.75 in. Flange sizes are 1.25 and 0.75 in.

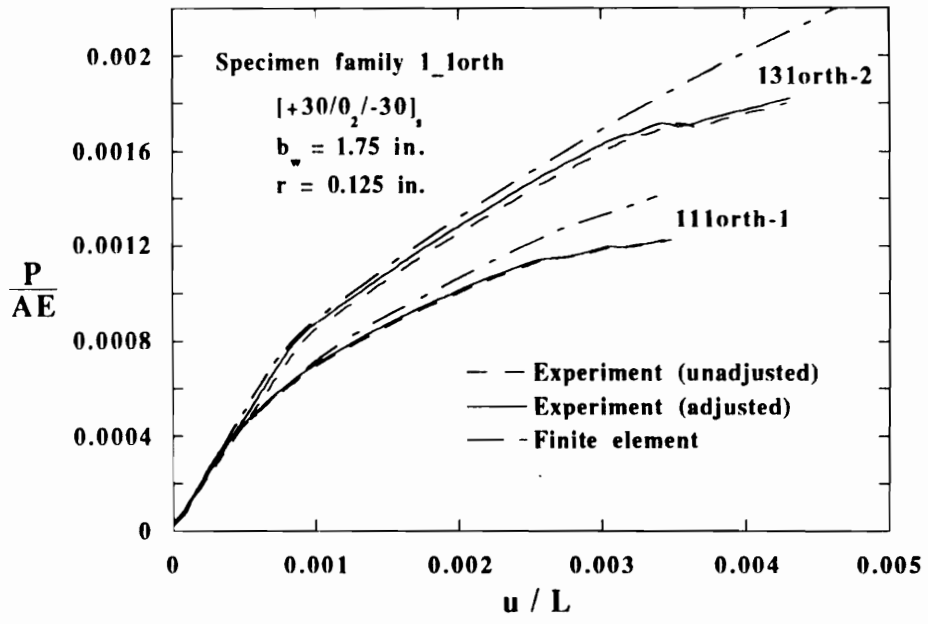

Figure 6-19. Normalized load-end shortening responses illustrating adjustment for displacement which occurs within the potted end supports. Stacking sequence is $[+30/0_2/-30]_S$. Web width is 1.75 in. Flange sizes are 1.25 and 0.75 in.

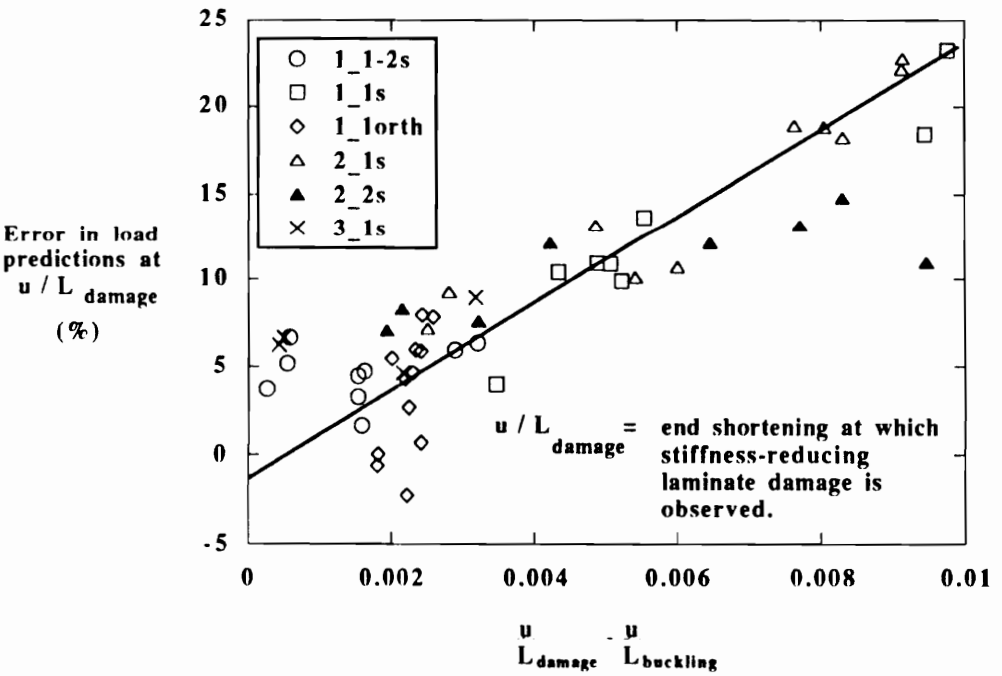

Figure 6-20. Correlation of the numerical overprediction of load with the size of the postbuckling response regime.

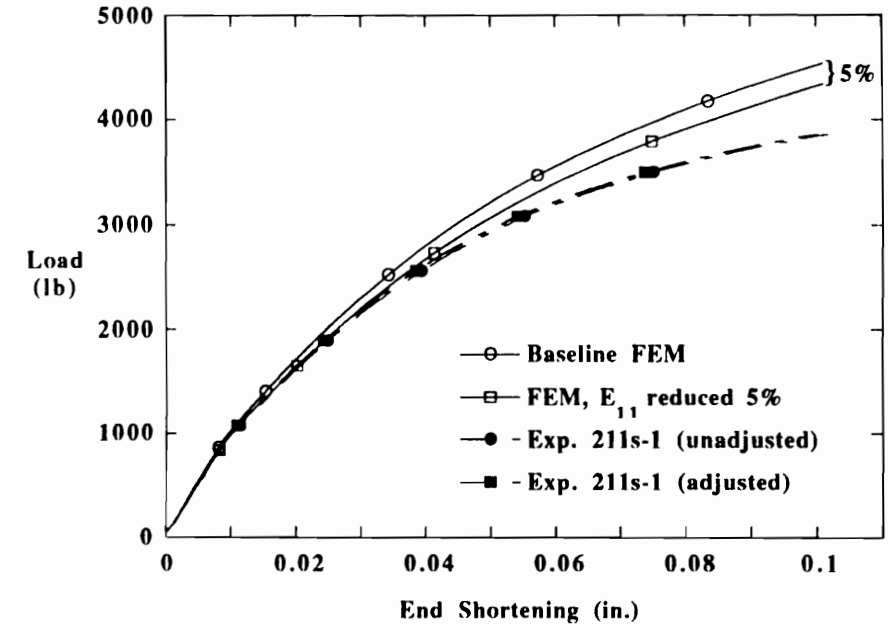

(a)

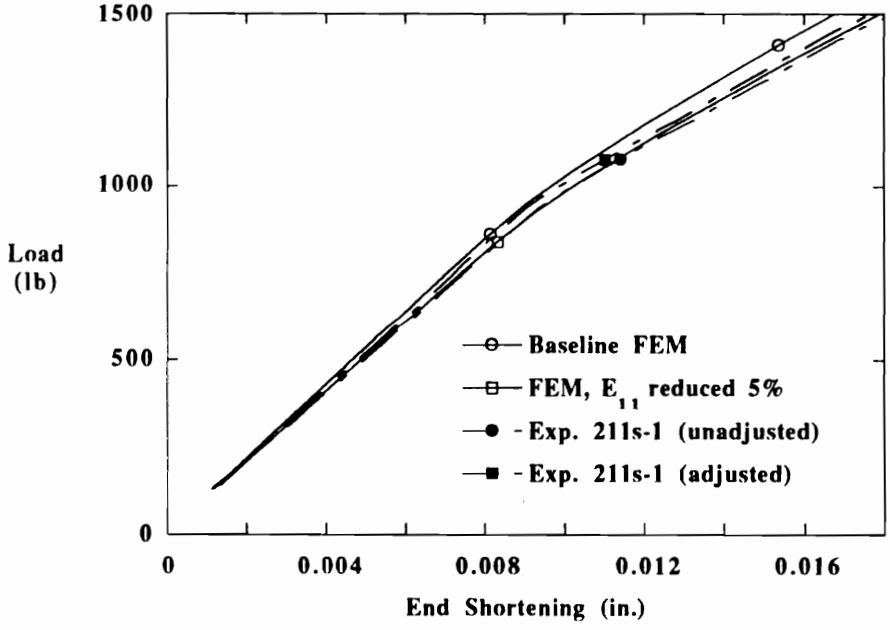

(b)

Figure 6-21. Sensitivity of the predicted load-end shortening response to the fiber modulus E_{11}. Specimen type 211s: $b_w = 1.25$, $b_f = 1.25$, $r = 0.125$ in., $[\pm 45/0/90]_S$. Full load range (a) and prebuckling and initial postbuckling responses (b).

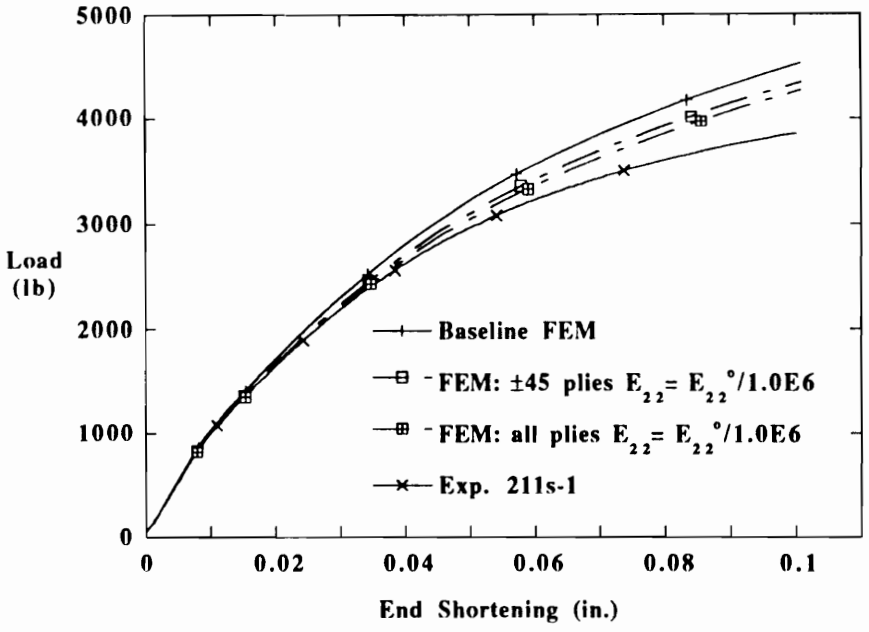

(a)

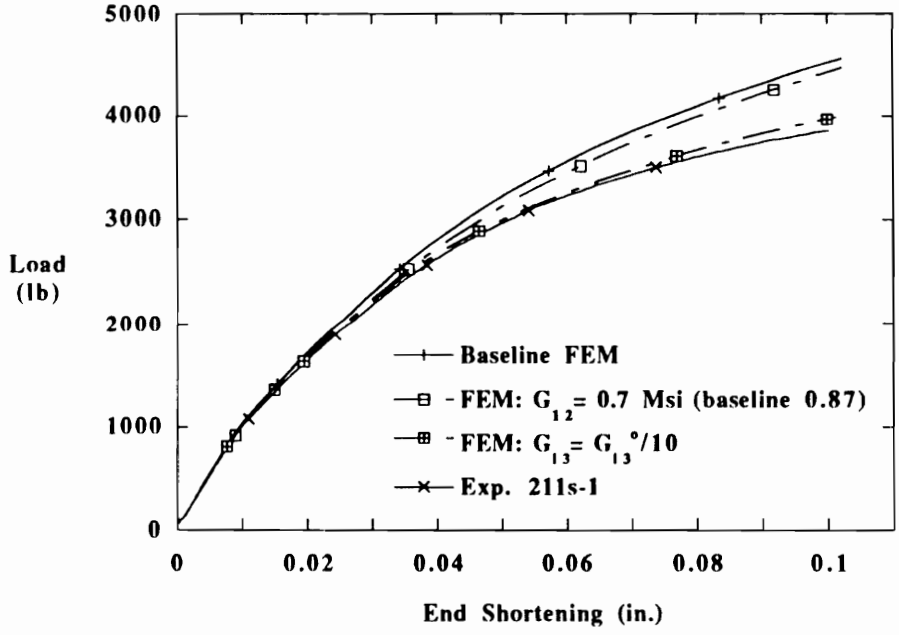

(b)

Figure 6-22. Sensitivity of the predicted load-end shortening response to the matrix modulus E_{22} (a) and shear moduli G_{ij} (b). Specimen type 211s: b_w = 1.25, b_f = 1.25, r = 0.125 in., $[\pm 45/0/90]_s$.

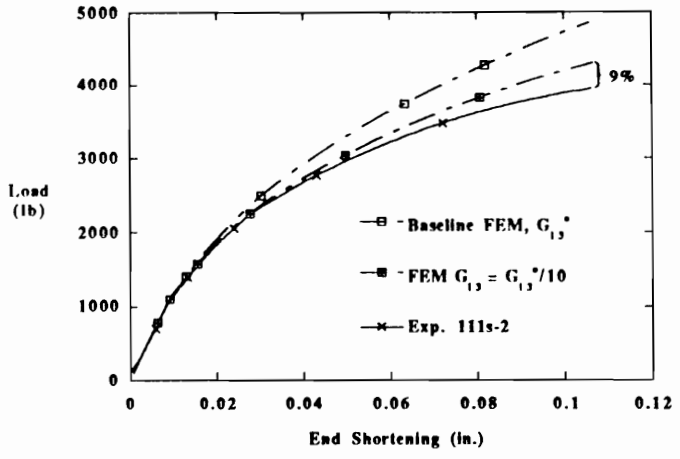

(a)

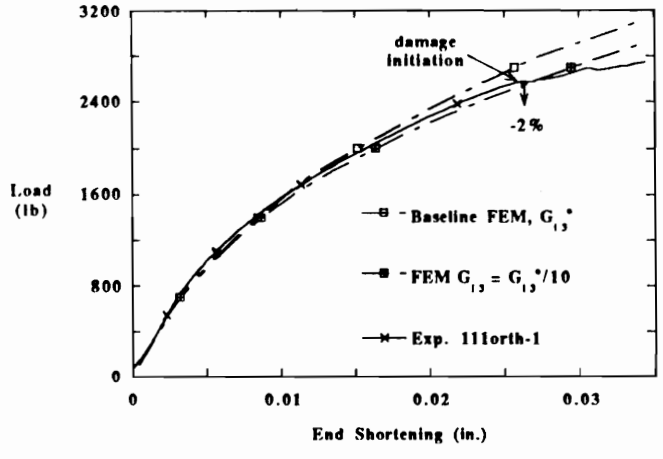

(b)

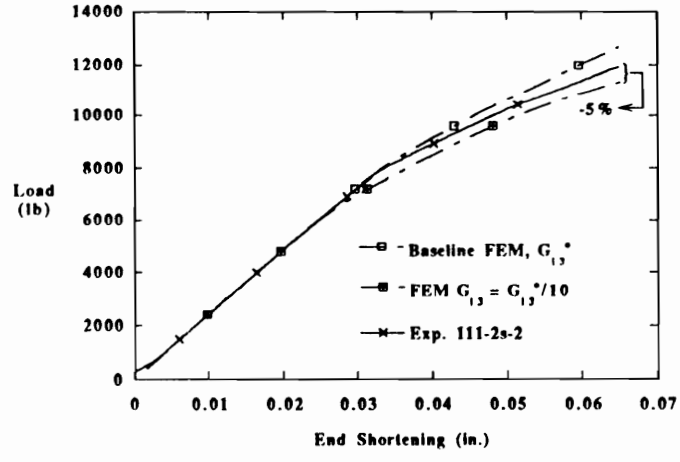

(c)

Figure 6-23. Dependence on stacking sequence of the sensitivity of the predicted load-end shortening response to transverse shear moduli. Geometry: $b_w = 1.75$, $b_f = 1.25$, $r = 0.125$ in. Stacking sequences are: (a) $[\pm 45/0/90]_s$, (b) $[+30/0_2/-30]_s$ and (c) $[\pm 45/0/90]_{2s}$.

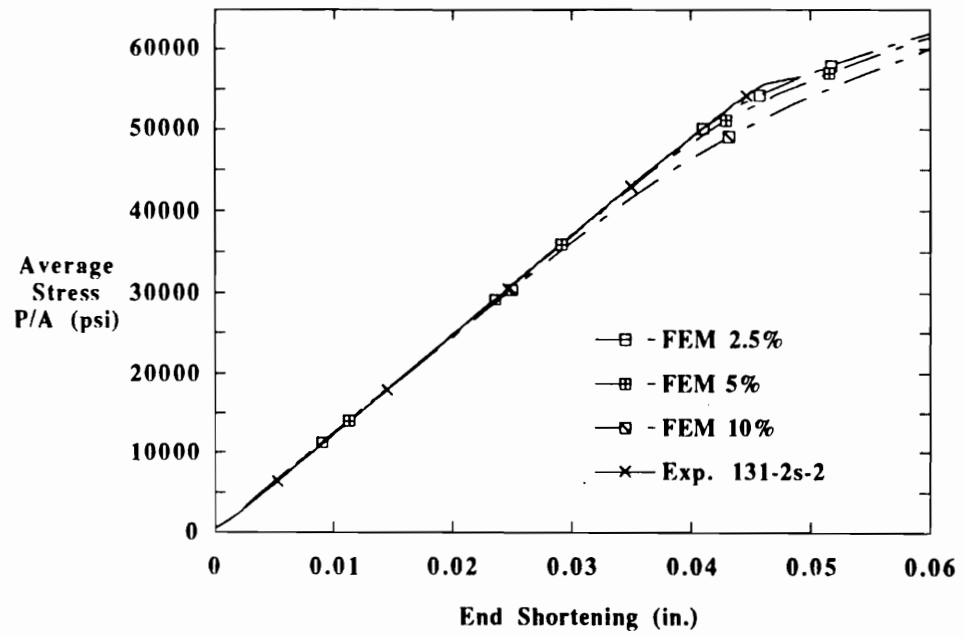

Figure 6-24. Sensitivity of the predicted load-end shortening response to the magnitude of the assumed initial imperfection. Specimen type 131-2s: $b_w = 1.75$, $b_f = 0.75$, r = 0.125 in., $[\pm 45/0/90]_{2s}$.

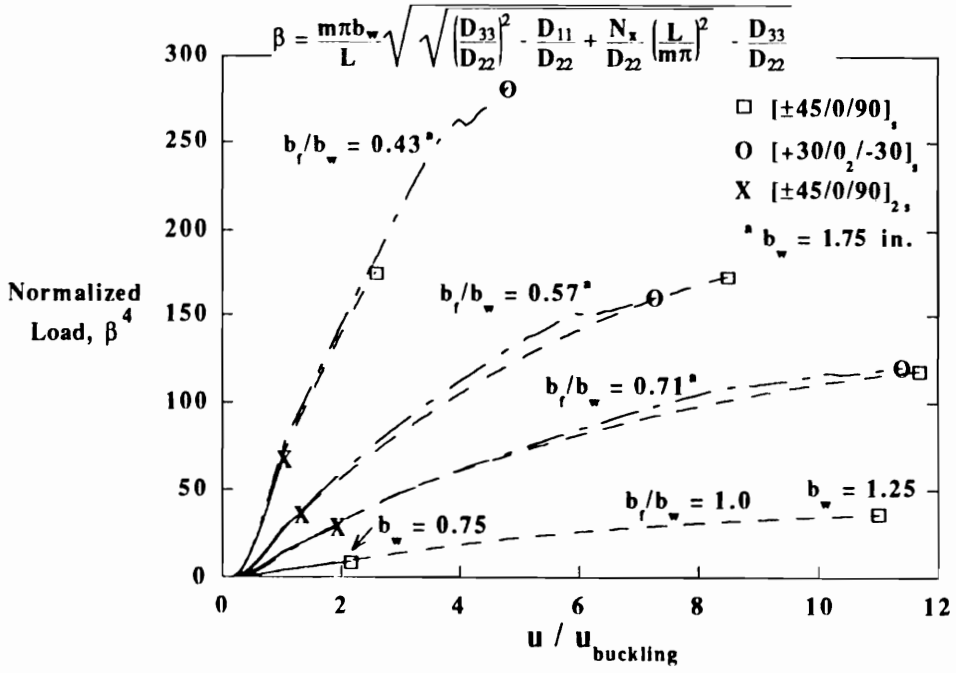

Figure 6-25. Normalization of postbuckling loads in terms of nondimensional parameter β. Parameter β normalizes postbuckling loads for the various stacking sequences for a given flange-to-web width ratio.

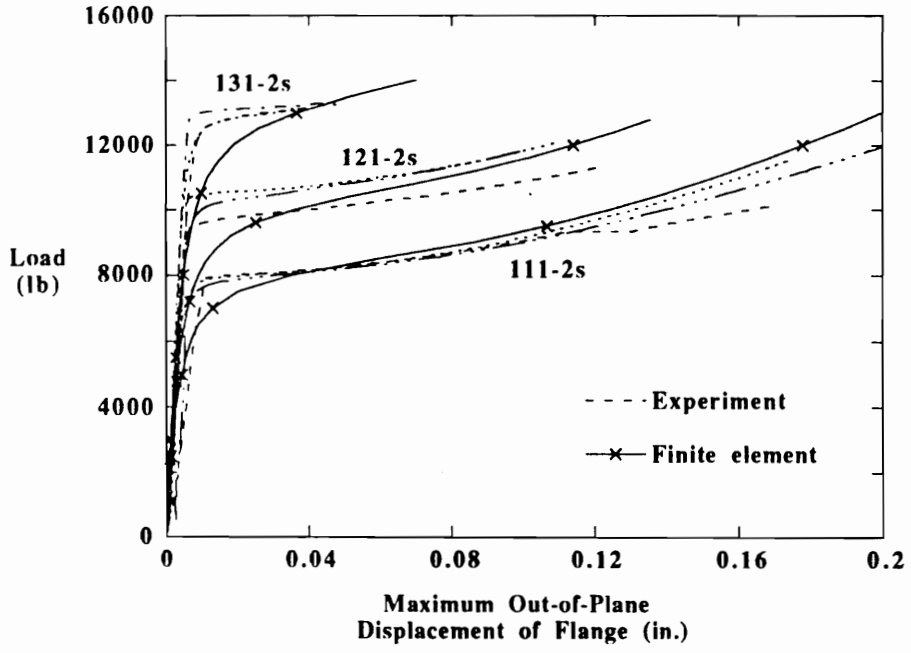

Figure 6-26. Comparison of DCDT and FEM out-of-plane deflections. Geometry: $b_w = 1.75$, $b_f = 1.25$, 1.0 and 0.75, $r = 0.125$ in. Stacking sequence: $[\pm 45/0/90]_{2s}$.

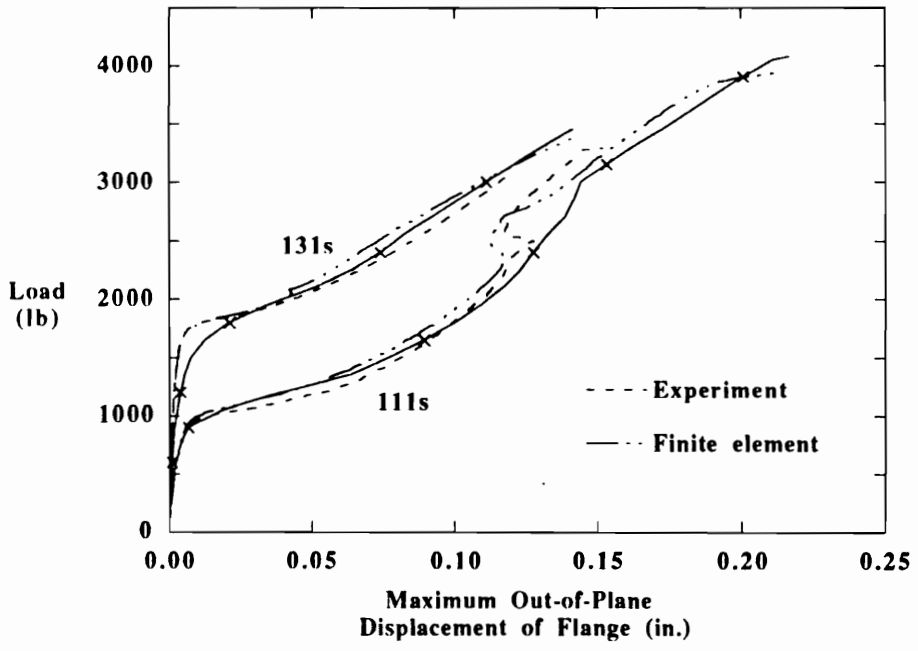

(a)

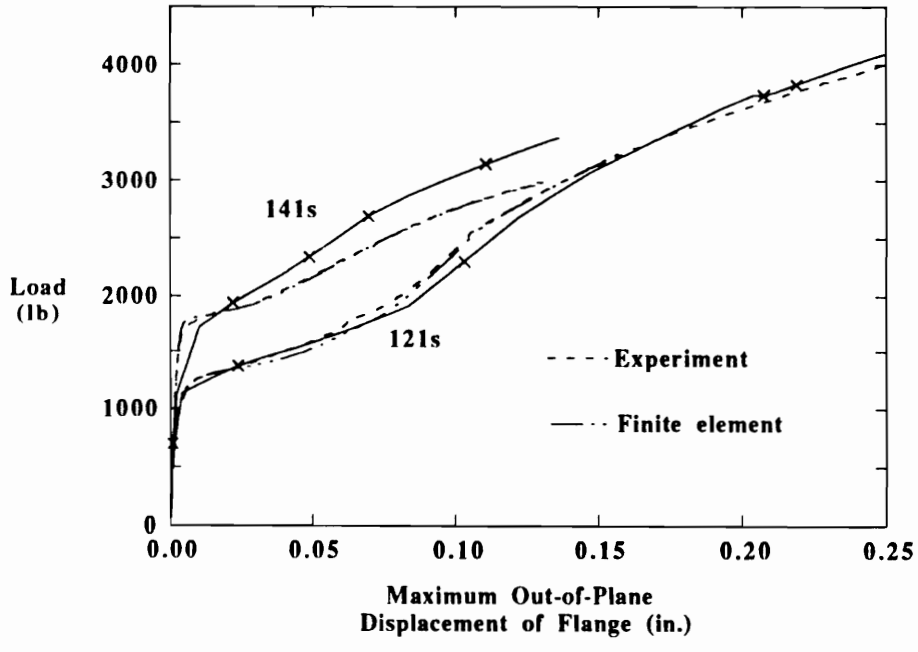

(b)

Figure 6-27. Comparison of DCDT and FEM out-of-plane deflections. Stacking sequence: $[\pm 45/0/90]_S$. Geometry: $b_w = 1.75$, $r = 0.125$, (a) $b_f = 1.25$ and 0.75, (b) $b_f = 1.0$ and 0.50 in.

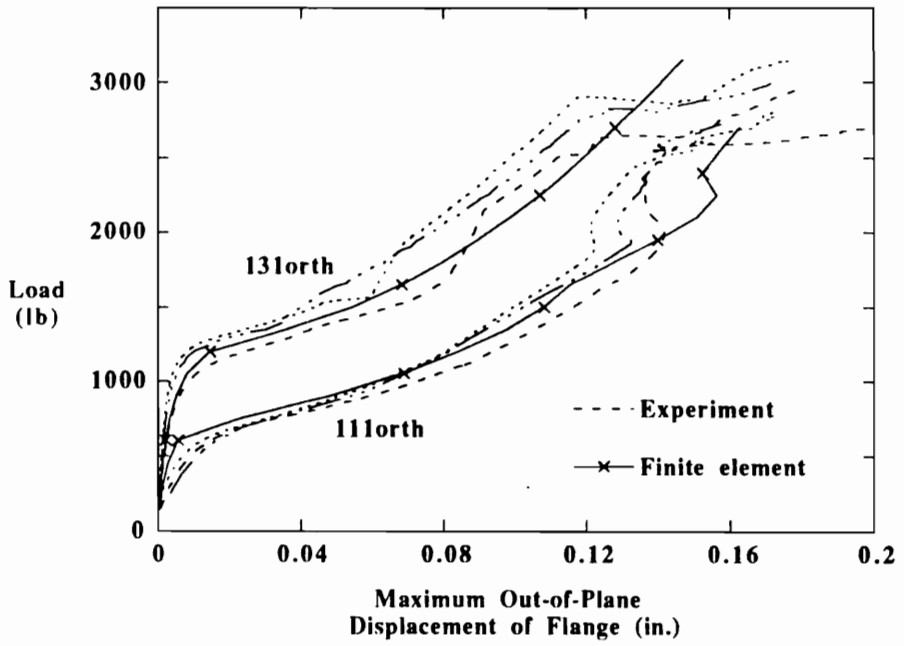

(a)

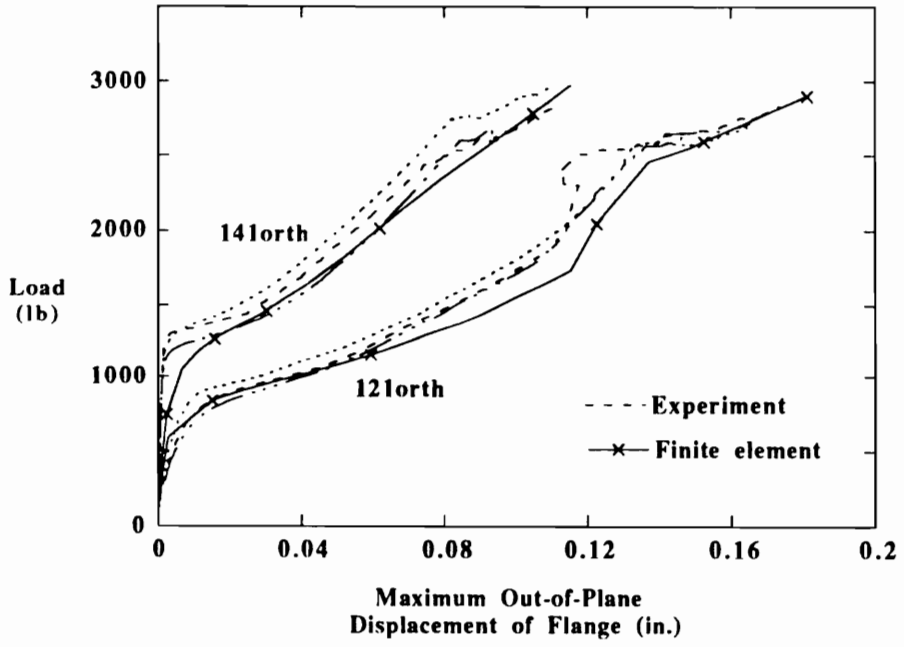

(b)

Figure 6-28. Comparison of DCDT and FEM of out-of-plane deflections. Stacking sequence: $[+30/0_2/-30]_s$. Geometry: $b_w = 1.75$, $r = 0.125$, (a) $b_f = 1.25$ and 0.75, (b) $b_f = 1.0$ and 0.50 in.

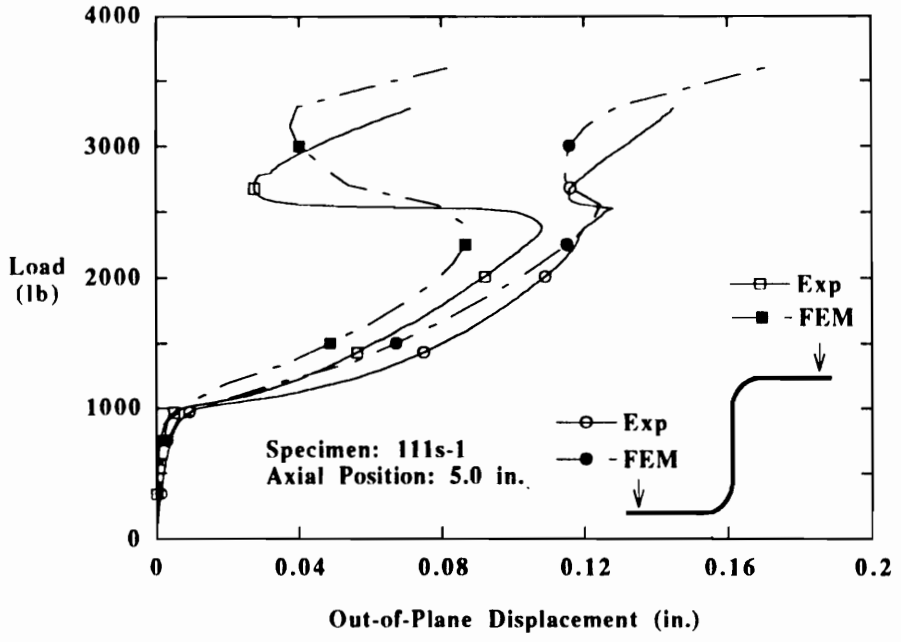

(a)

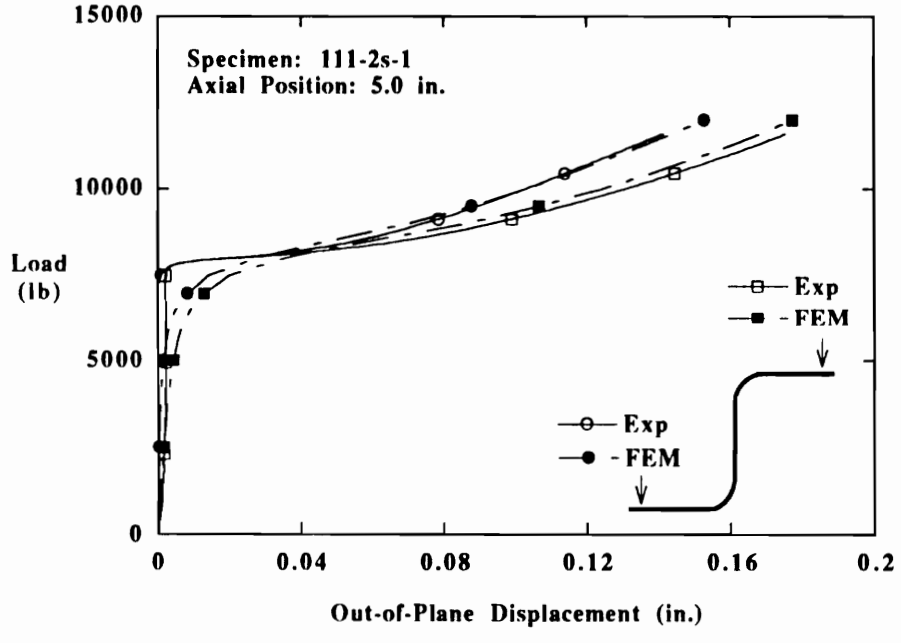

(b)

Figure 6-29. Comparison of DCDT and FEM out-of-plane deflections at mid-height axial location. Stacking sequences: (a) $[\pm 45/0/90]_S$ and (b) $[\pm 45/0/90]_{2S}$. Geometry: $b_w = 1.75$, $b_f = 1.25$, $r = 0.125$ in.

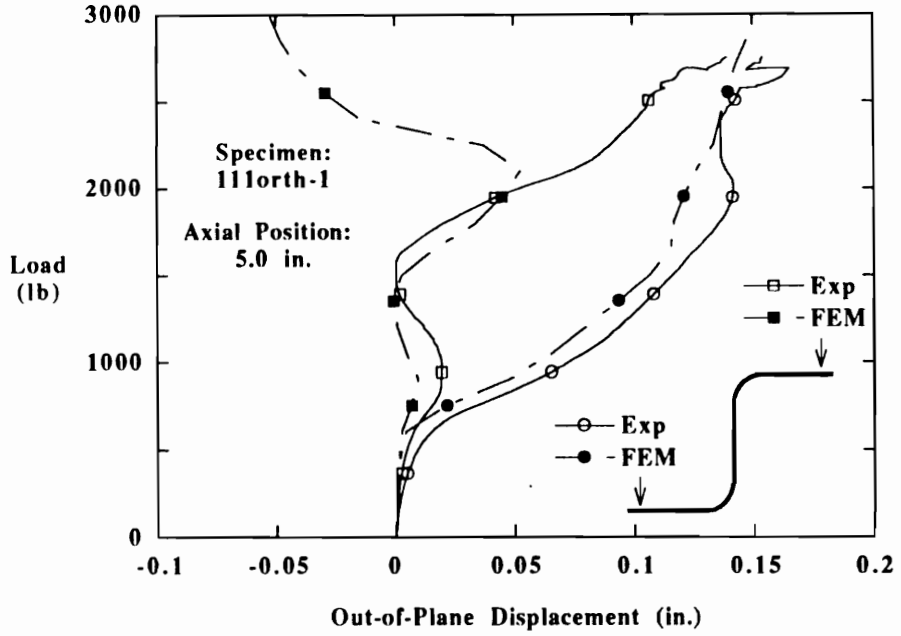

(a)

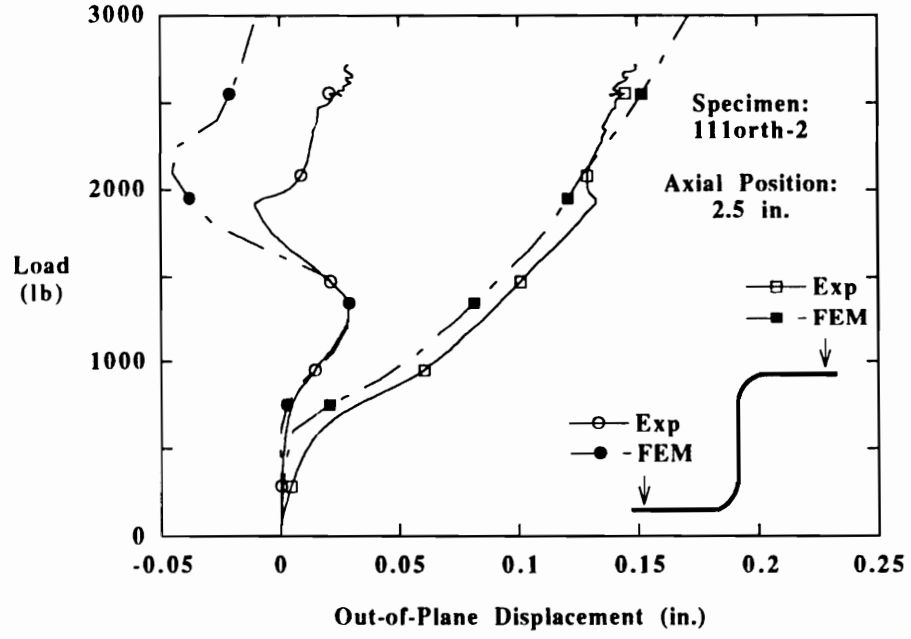

(b)

Figure 6-30. Comparison of DCDT and FEM out-of-plane deflections. Stacking sequence $[+30/0_2/-30]_S$. Geometry: $b_w = 1.75$, $b_f = 1.25$, $r = 0.125$ in. Axial location and experimental specimen: (a) 5.0 in., 111orth-1 and (b) 2.5 in., 111orth-2.

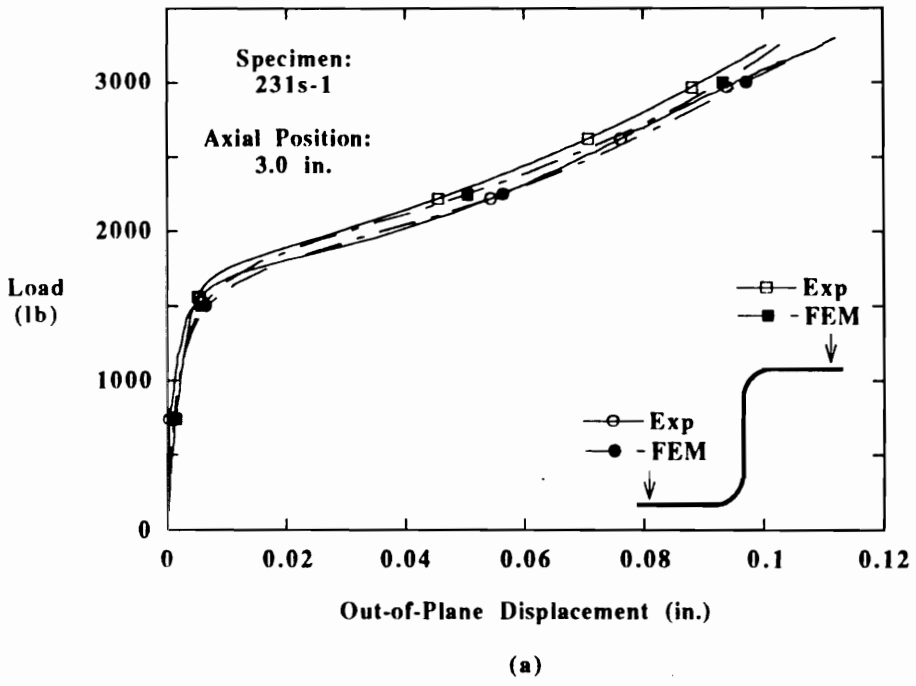

(a)

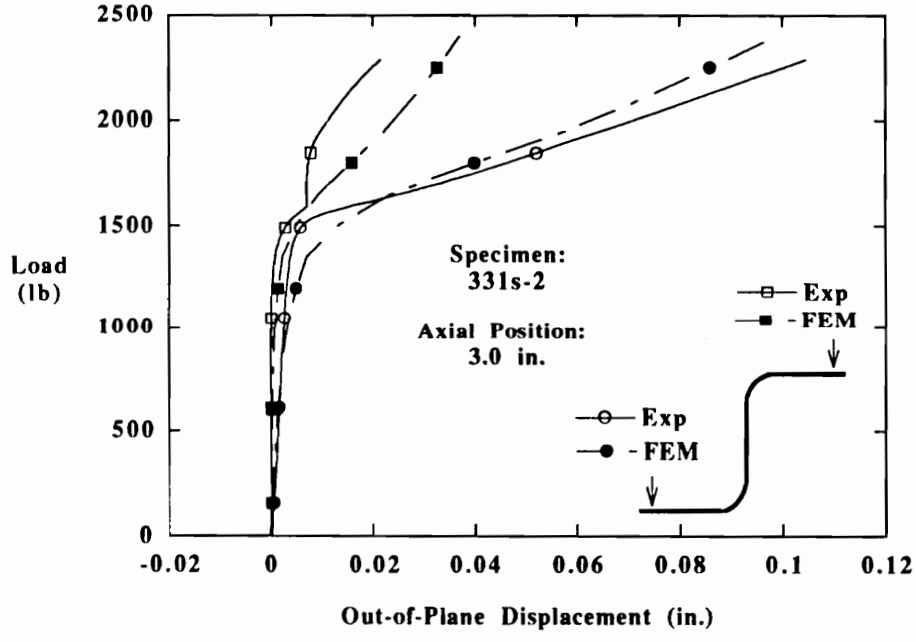

(b)

Figure 6-31. Comparison of DCDT and FEM out-of-plane deflections at mid-height axial location. Geometry: $b_f = 0.75$, $r = 0.125$, $b_w = 1.25$ (a) and 0.75 (b) in. Stacking sequence is $[\pm 45/0/90]_S$.

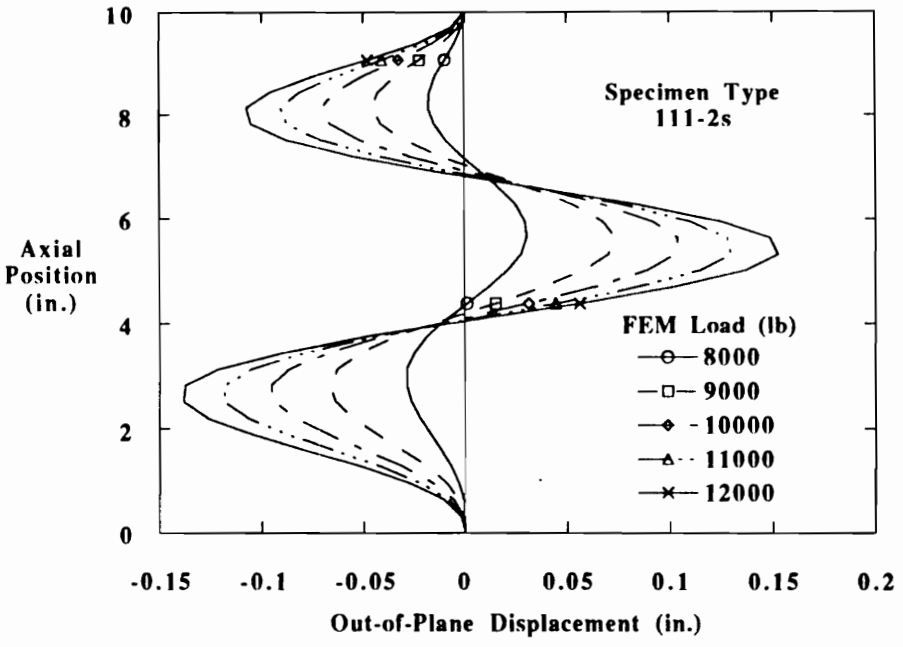

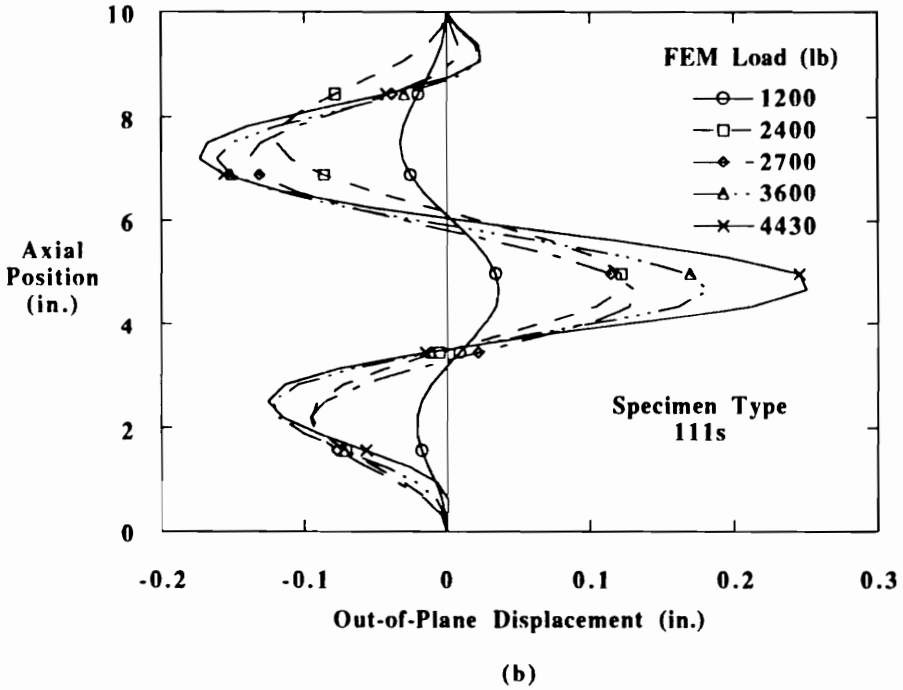

Figure 6-32. FEM distribution of out-of-plane deflection along the gage length at the flange free end. Stacking sequences: (a) $[\pm 45/0/90]_{2s}$ and (b) $[\pm 45/0/90]_{s}$. Geometry: $b_w = 1.75$, $b_f = 1.25$, $r = 0.125$ in.

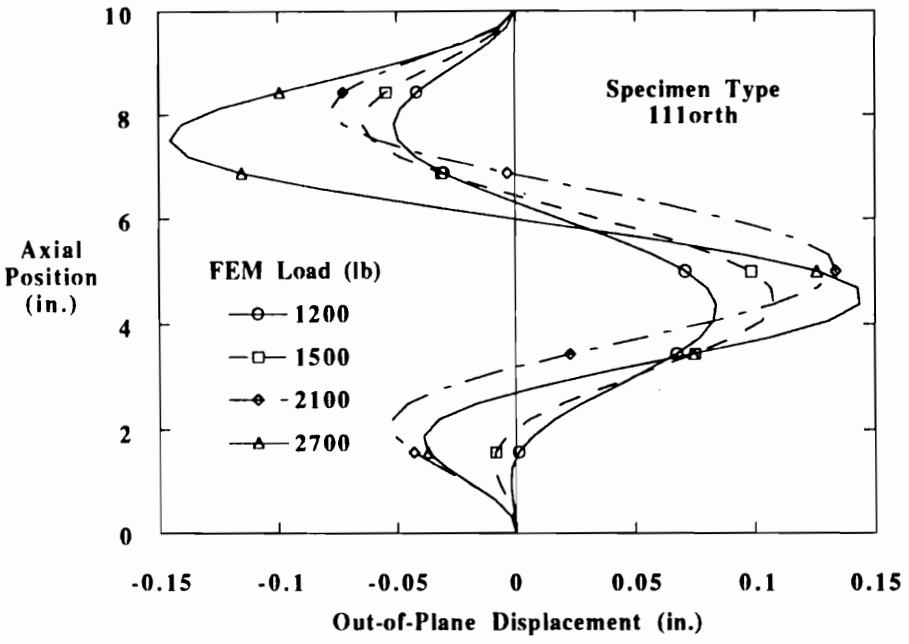

Figure 6-33. FEM distribution of out-of-plane deflection along the gage length at the flange free end. Stacking sequence: $[+30/0_2/-30]_S$. Geometry: $b_w = 1.75$, $b_f = 1.25$, $r = 0.125$ in.

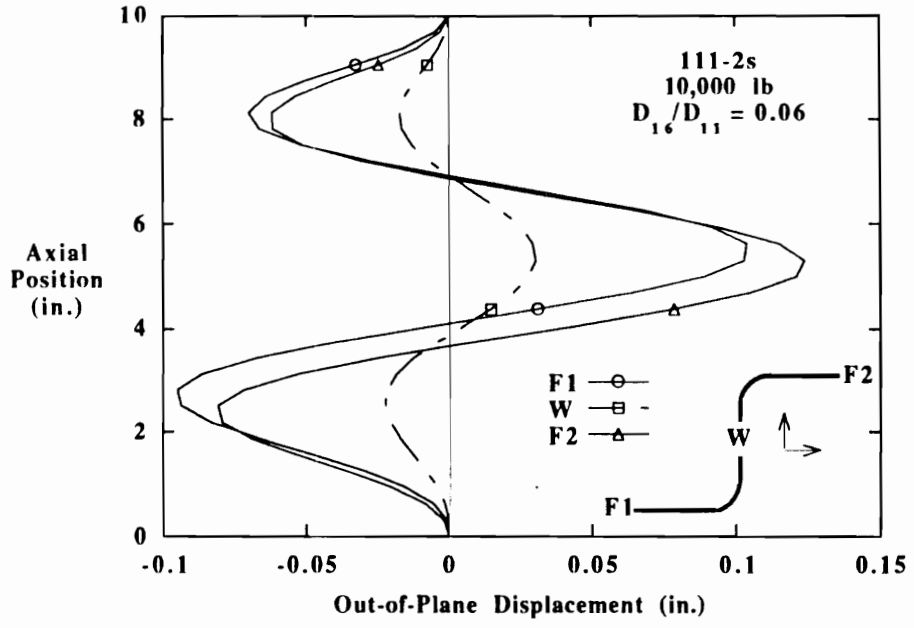

Figure 6-34. FEM mode shape for specimen type 111-2s and 10,000 lb load. Out-of-plane (a) and in-plane (b) displacements at the ends of both flanges and the center of the web. Stacking sequence: $[\pm 45/0/90]_{2s}$. Geometry: $b_w = 1.75$, $b_f = 1.25$, $r = 0.125$ in.

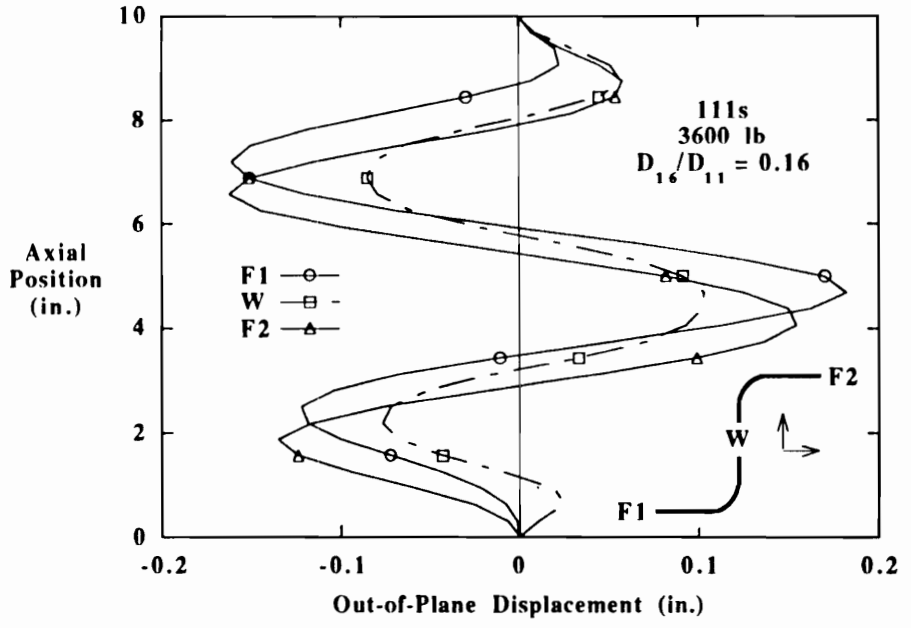

(a)

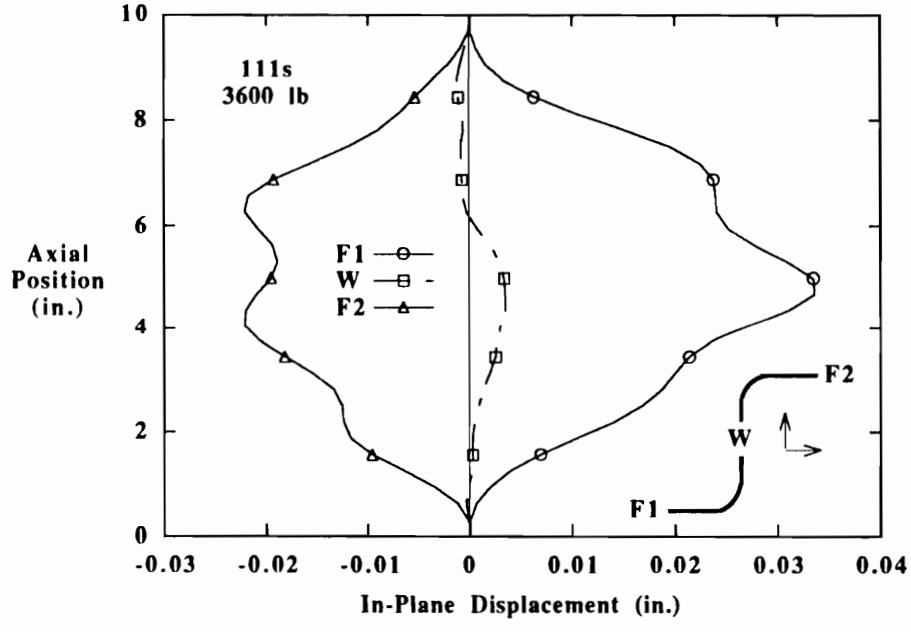

(b)

Figure 6-35. FEM mode shape for specimen type 111s and 3600 lb load. Out-of-plane (a) and in-plane (b) displacements at the ends of both flanges and the center of the web. Stacking sequence: $[\pm 45/0/90]_S$. Geometry: $b_w = 1.75$, $b_f = 1.25$, $r = 0.125$ in.

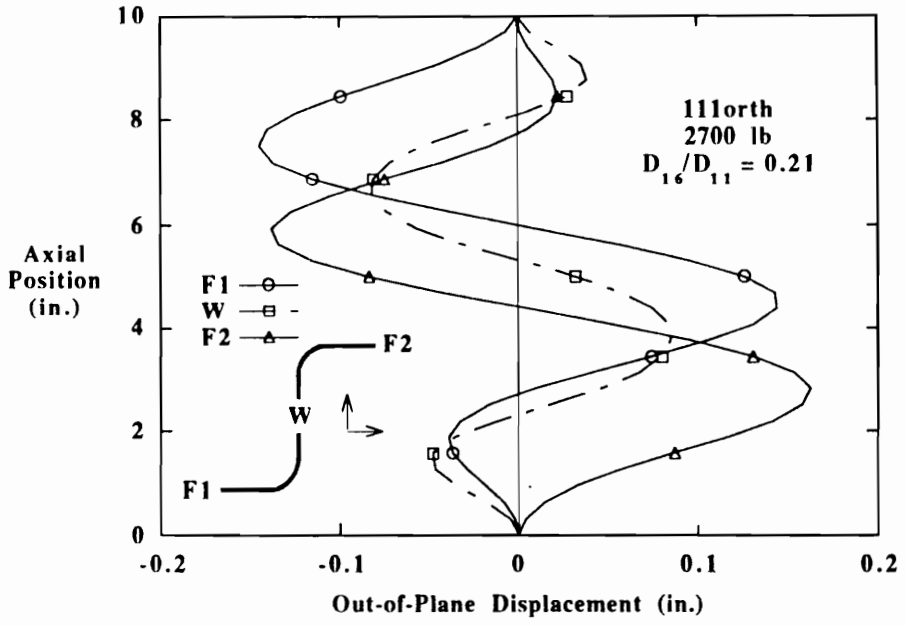

(a)

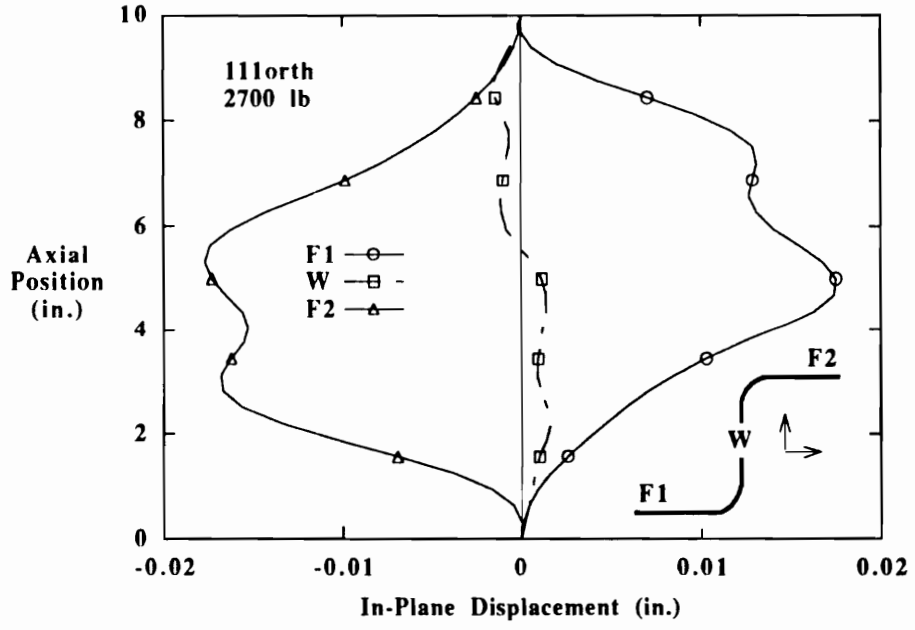

(b)

Figure 6-36. FEM mode shape for specimen type 111orth and 2700 lb load. Out-of-plane (a) and in-plane (b) displacements at the ends of both flanges and the center of the web. Stacking sequence: $[+30/0_2/-30]_S$. Geometry: b_w = 1.75, b_f = 1.25, r = 0.125 in.

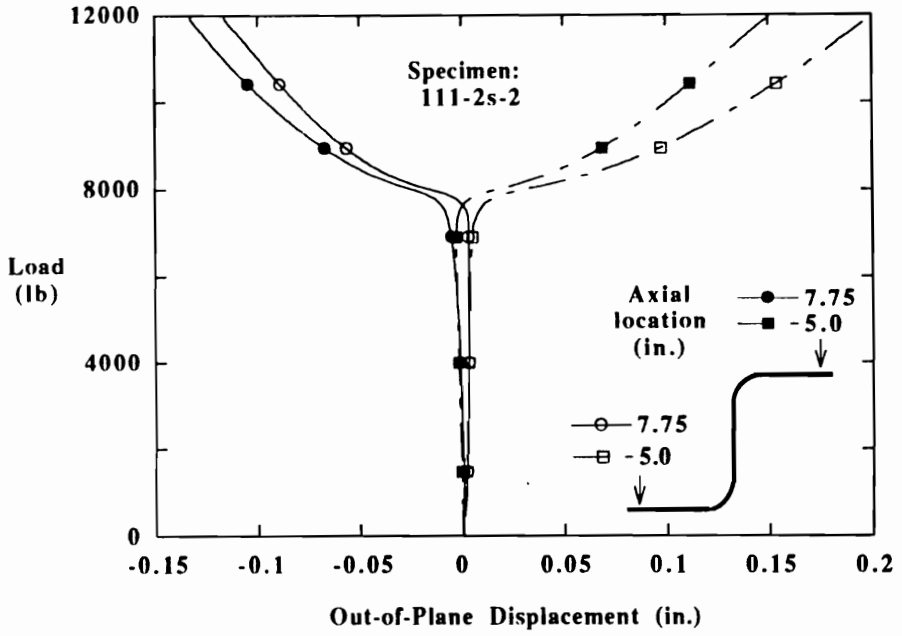

(a)

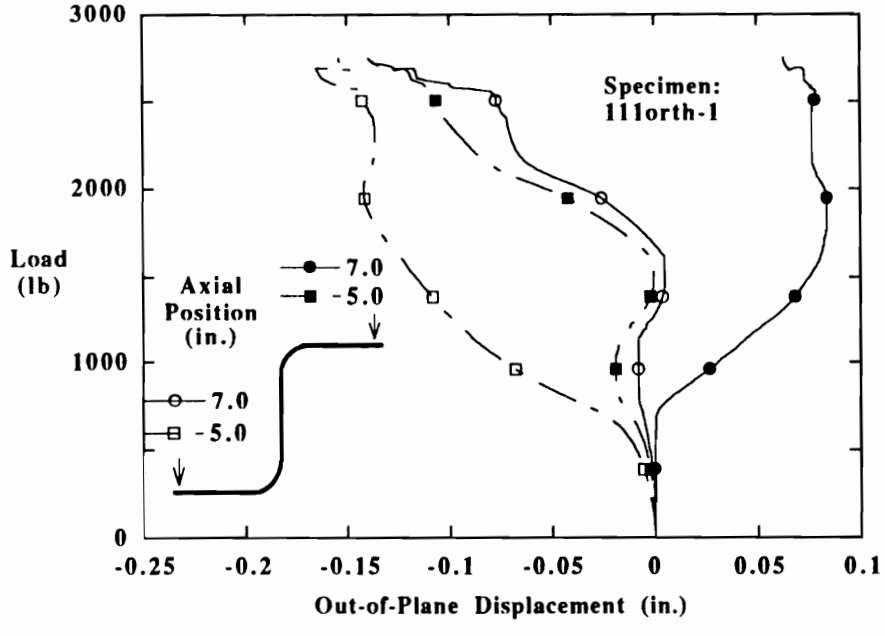

(b)

Figure 6-37. Symmetry of mode shape between the flanges as indicated by out-of-plane displacements for specimen 111-2s-2 (a) and 111orth-1 (b). Loss of symmetry caused by bending-twisting coupling.

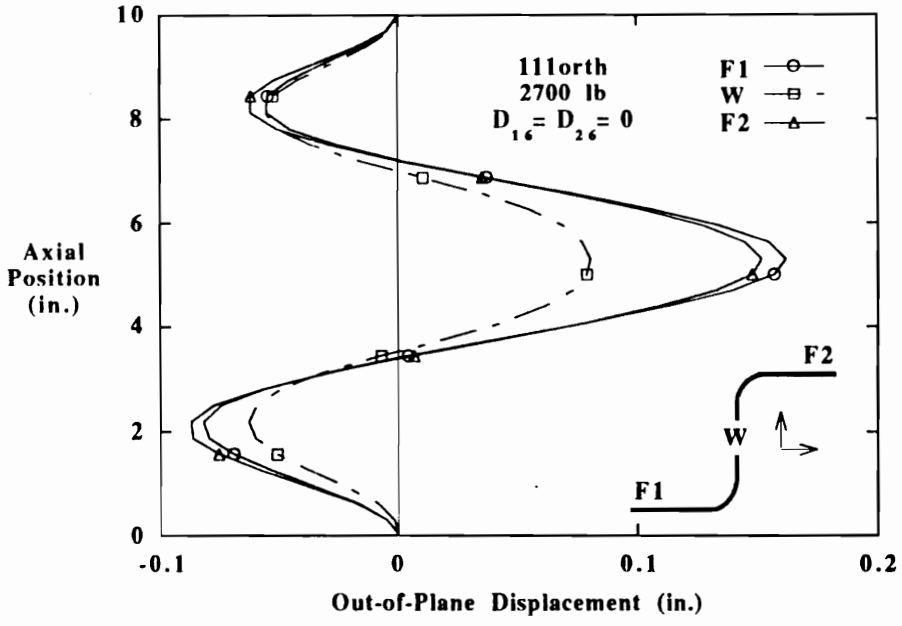

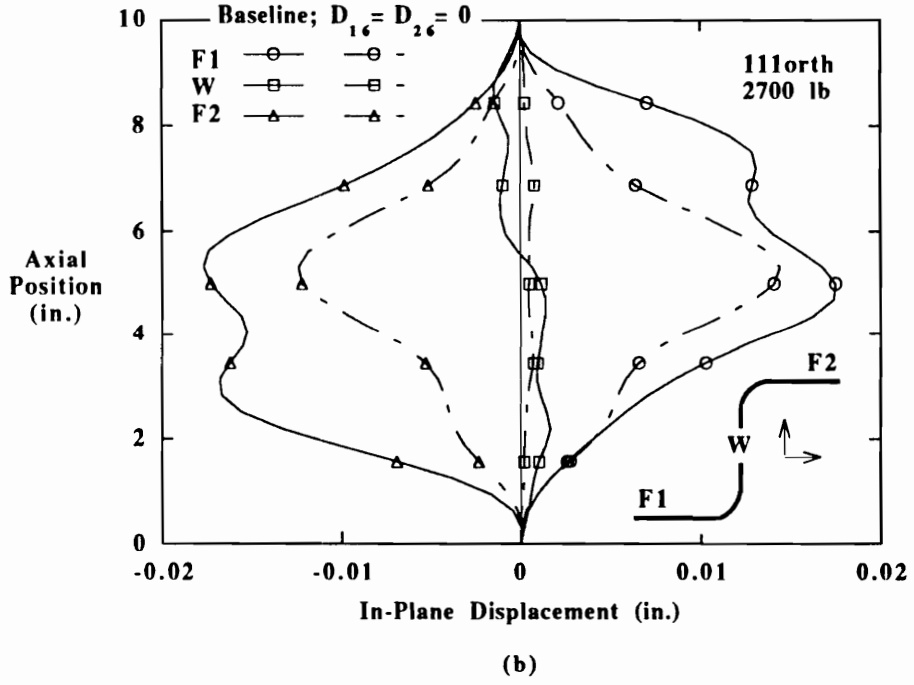

Figure 6-38. Effect of bending-twisting coupling stiffnesses D_{16} and D_{26} on mode shape of specimen type 111orth at 2700 lb load. Out-of-plane (a) and in-plane (b) displacements. Stacking sequence: $[+30/0_2/-30]_s$. Geometry: $b_w = 1.75$, $b_f = 1.25$, $r = 0.125$ in. Material coupling causes mode shape distortion, but structural mode interaction causes overall twisting of section.

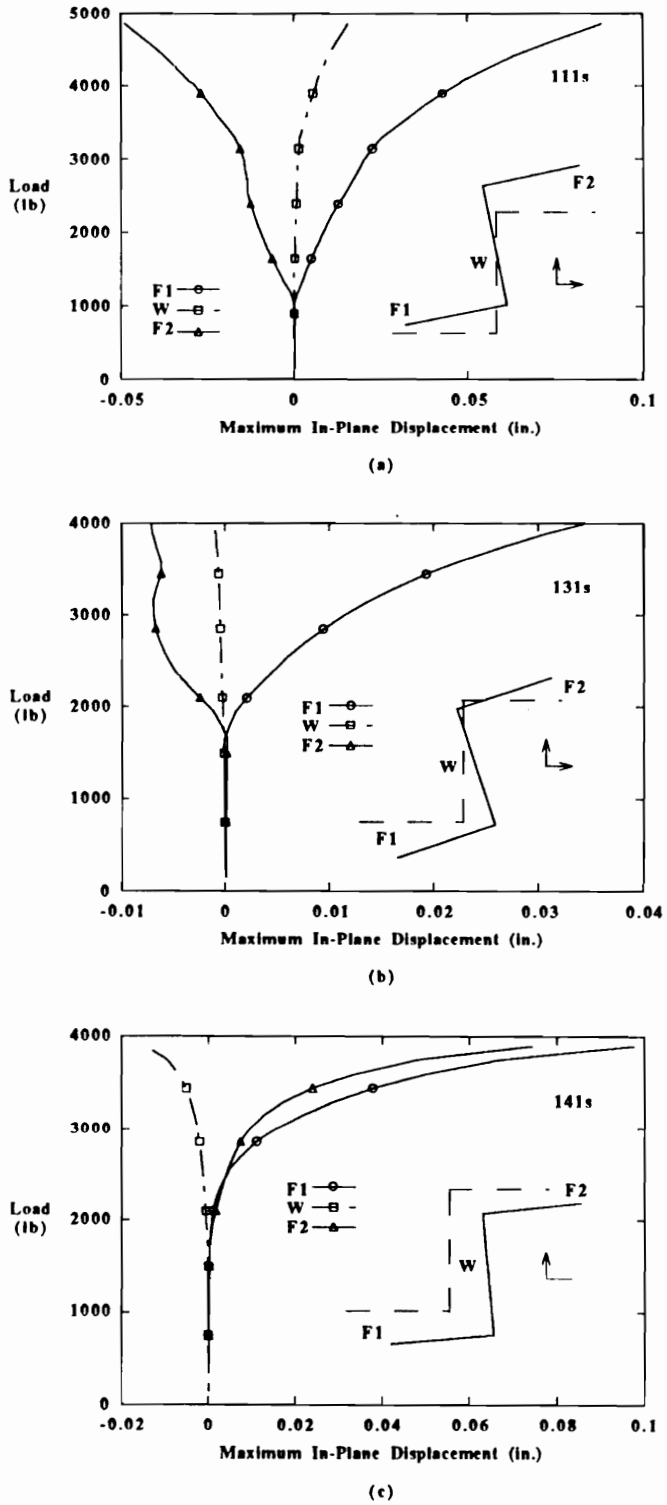

Figure 6-39. FEM transition from torsional to flexural mode interaction with decreasing flange width. Stacking sequence: $[\pm 45/0/90]_S$. Geometry: $b_w = 1.75$, $r = 0.125$, (a) $b_f = 1.25$, (b) $b_f = 0.75$ and (c) $b_f = 0.50$ in.

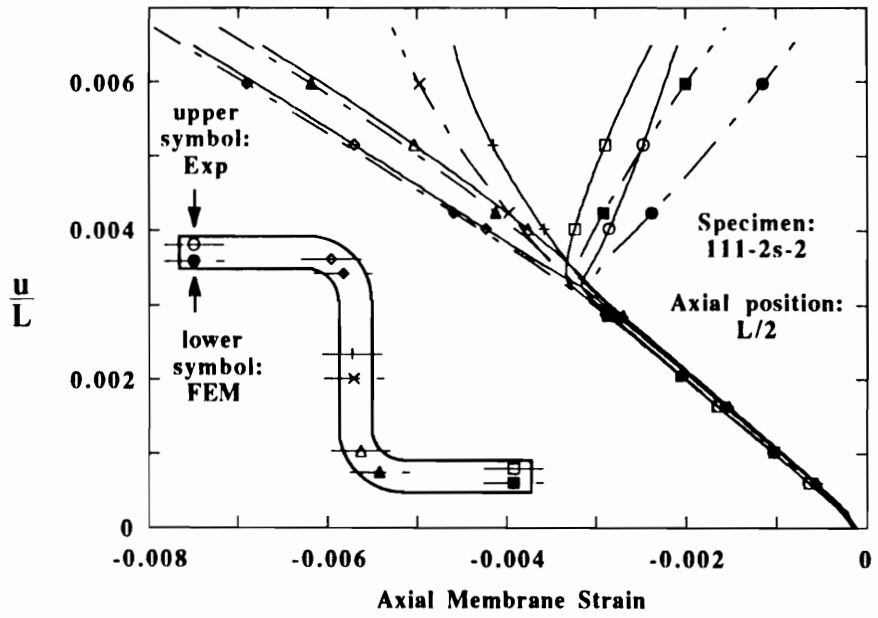

(a)

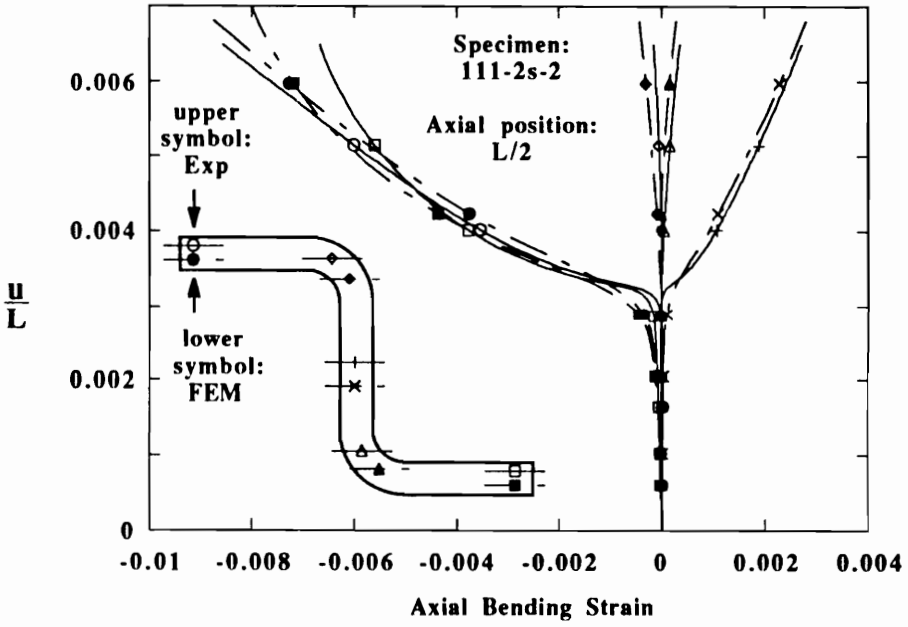

(b)

Figure 6-40. FEM and experimental (a) membrane and (b) bending strain data for specimen 111-2s-2. Stacking sequence: $[\pm 45/0/90]_{2s}$. Geometry: $b_w = 1.75$, $b_f = 1.25$, $r = 0.125$ in.

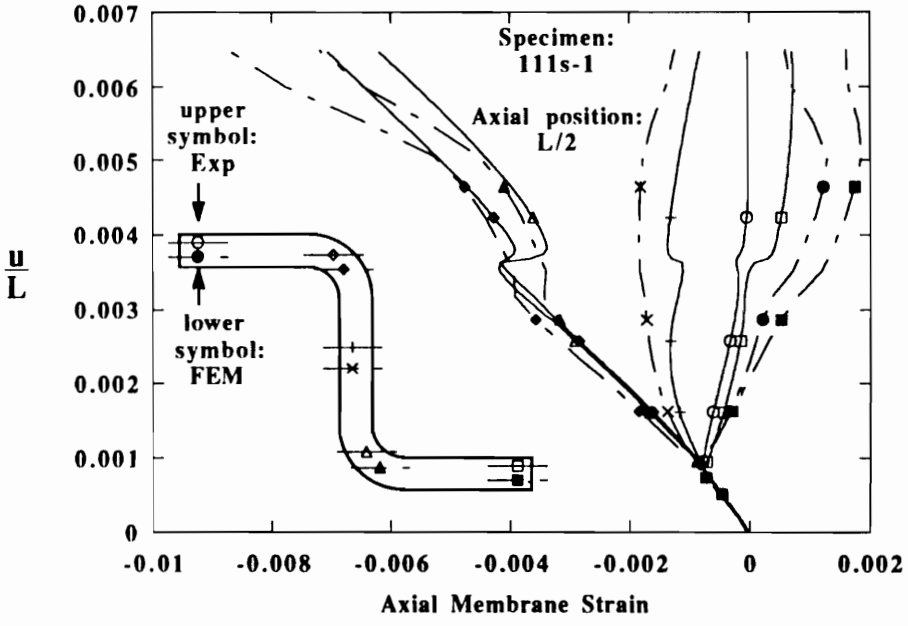

(a)

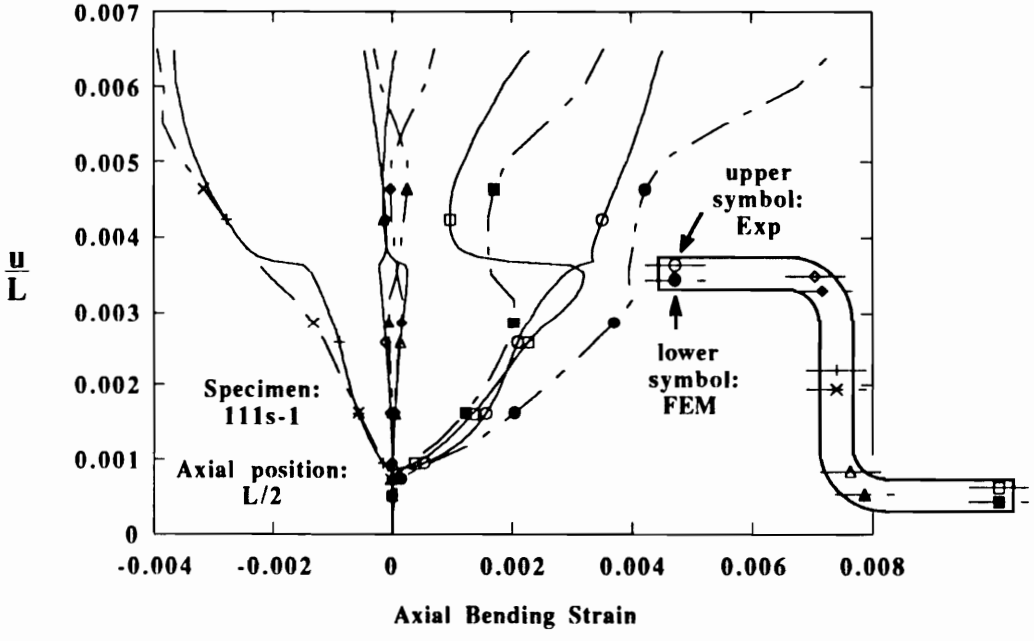

(b)

Figure 6-41. FEM and experimental (a) membrane and (b) bending strain data for specimen 111s-1. Stacking sequence: $[\pm 45/0/90]_S$. Geometry: $b_w = 1.75$, $b_f = 1.25$, $r = 0.125$ in.

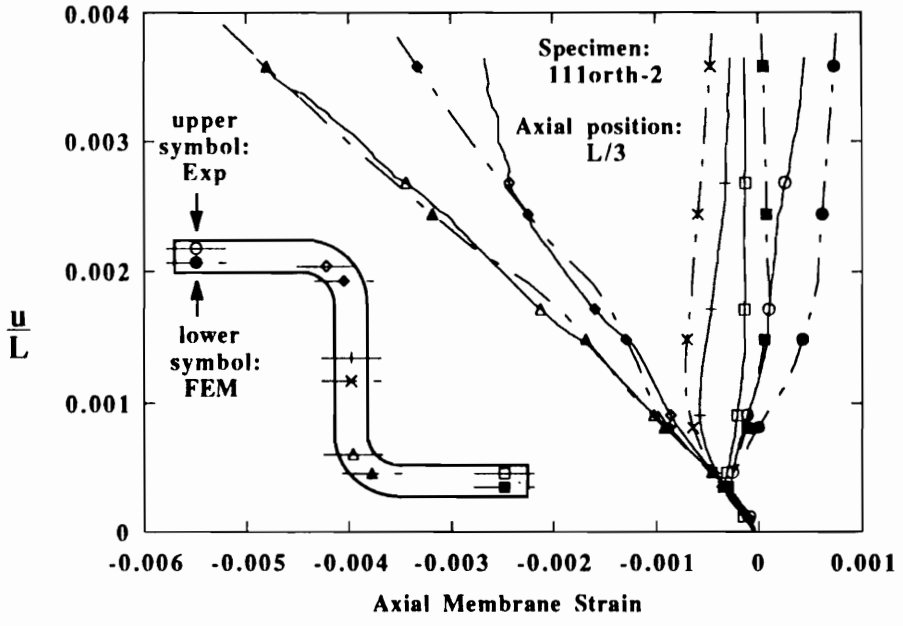

(a)

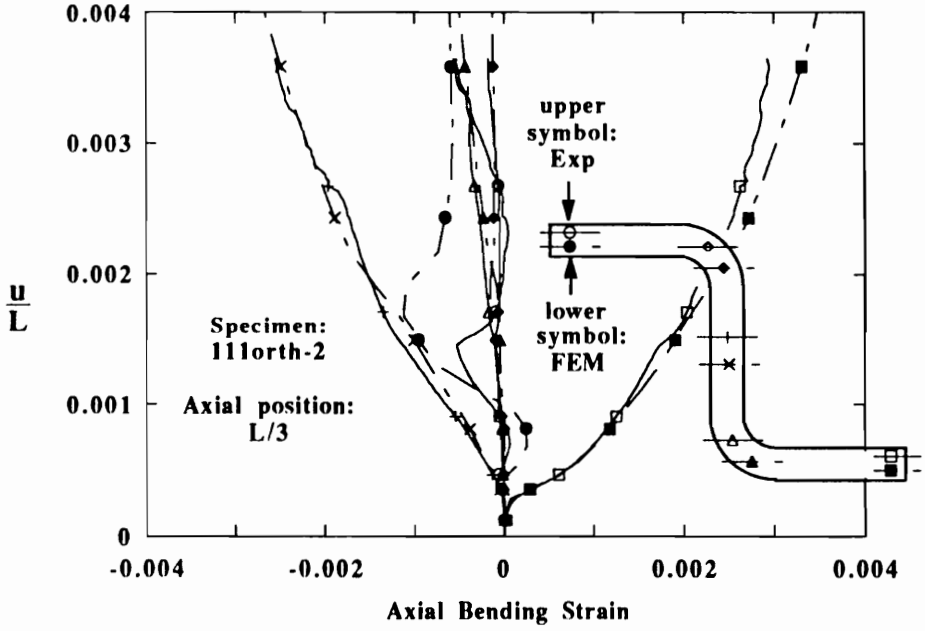

(b)

Figure 6-42. FEM and experimental (a) membrane and (b) bending strain data for specimen 111orth-2. Stacking sequence: $[+30/0_2/-30]_S$. Geometry: $b_w = 1.75$, $b_f = 1.25$, $r = 0.125$ in.

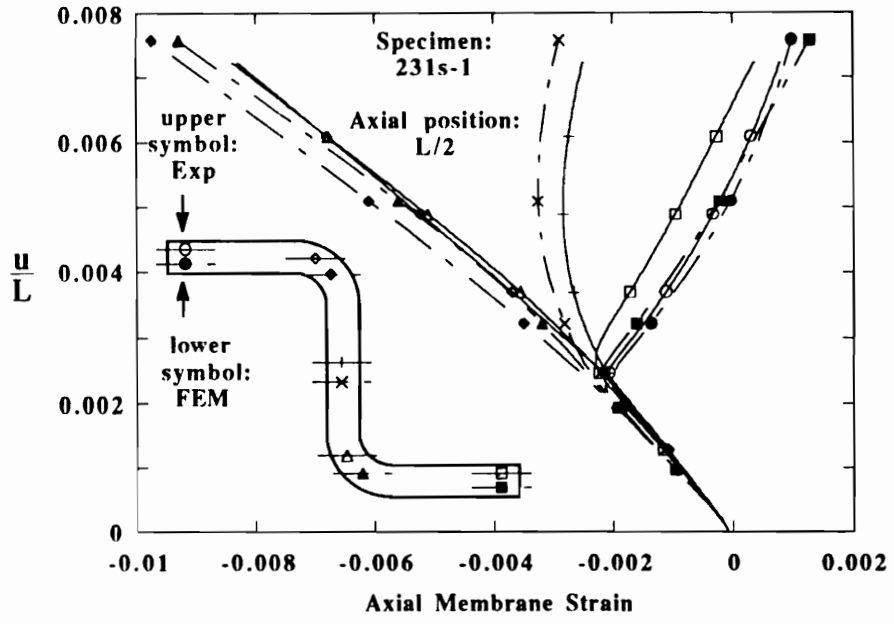

(a)

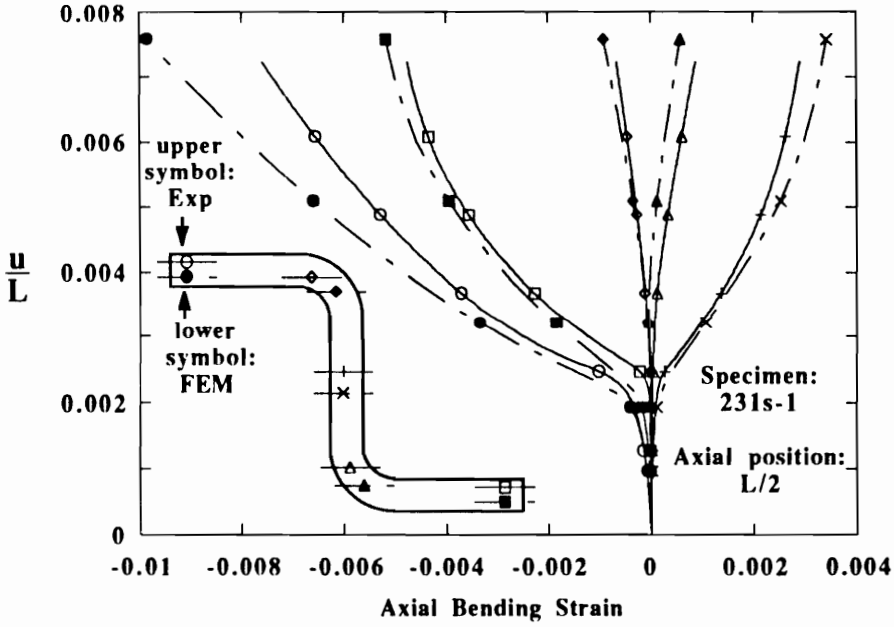

(b)

Figure 6-43. FEM and experimental (a) membrane and (b) bending strain data for specimen 231s-1. Stacking sequence: $[\pm 45/0/90]_S$. Geometry: $b_w = 1.25$, $b_f = 0.75$, $r = 0.125$ in.

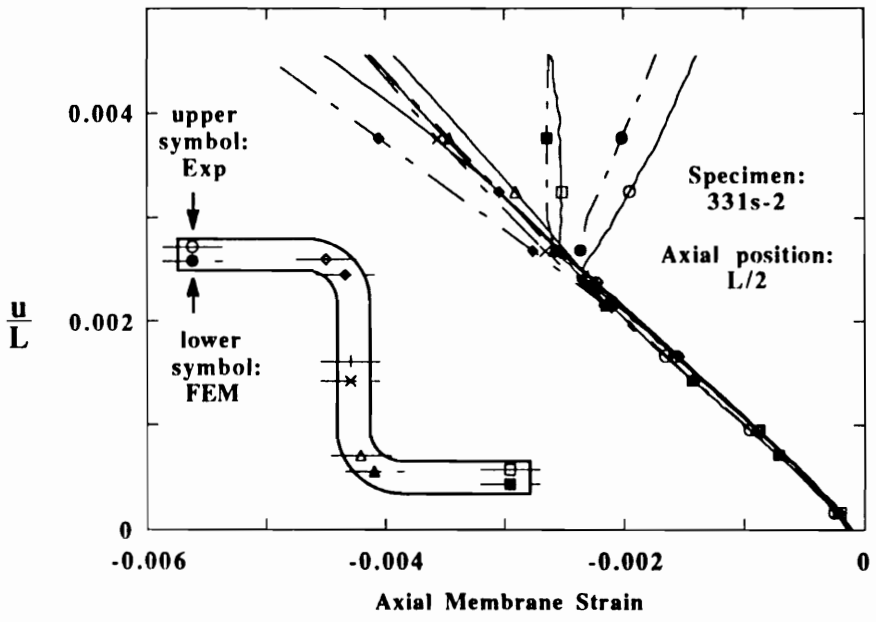

(a)

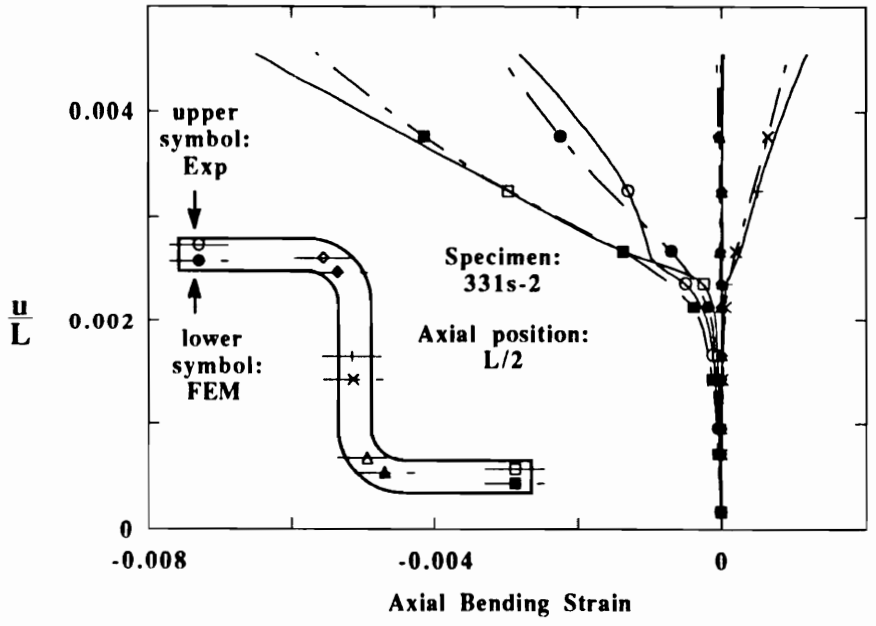

(b)

Figure 6-44. FEM and experimental (a) membrane and (b) bending strain data for specimen 331s-2. Stacking sequence: $[\pm 45/0/90]_S$. Geometry: $b_w = 0.75$, $b_f = 0.75$, $r = 0.125$ in.

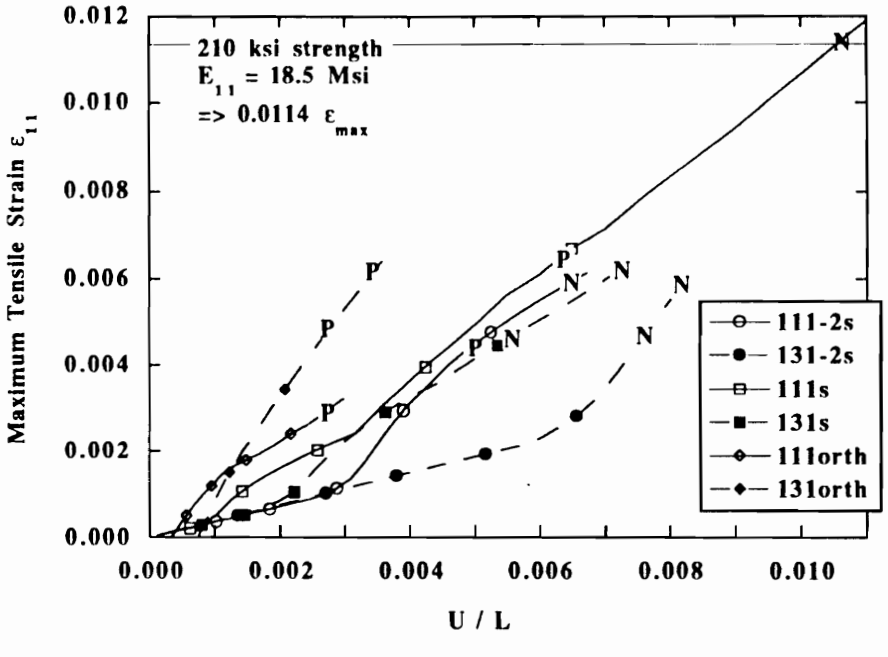

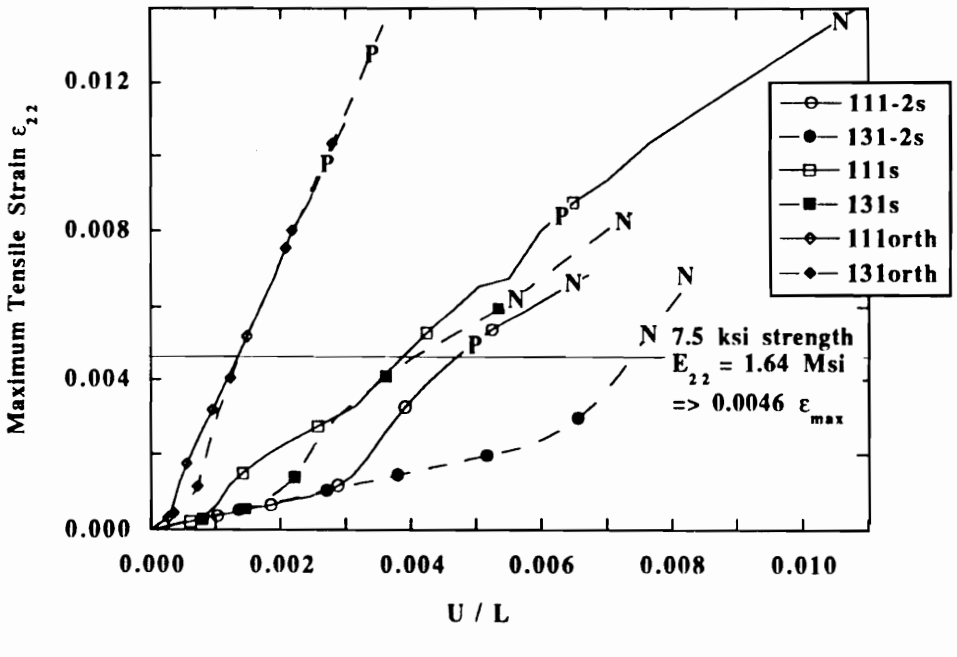

Figure 6-45. Maximum FEM tensile (a) fiber and (b) matrix strains as a function of flange size and stacking sequence. Symbols "N" and "P" denote experimental Nodal and Peak failure locations, respectively.

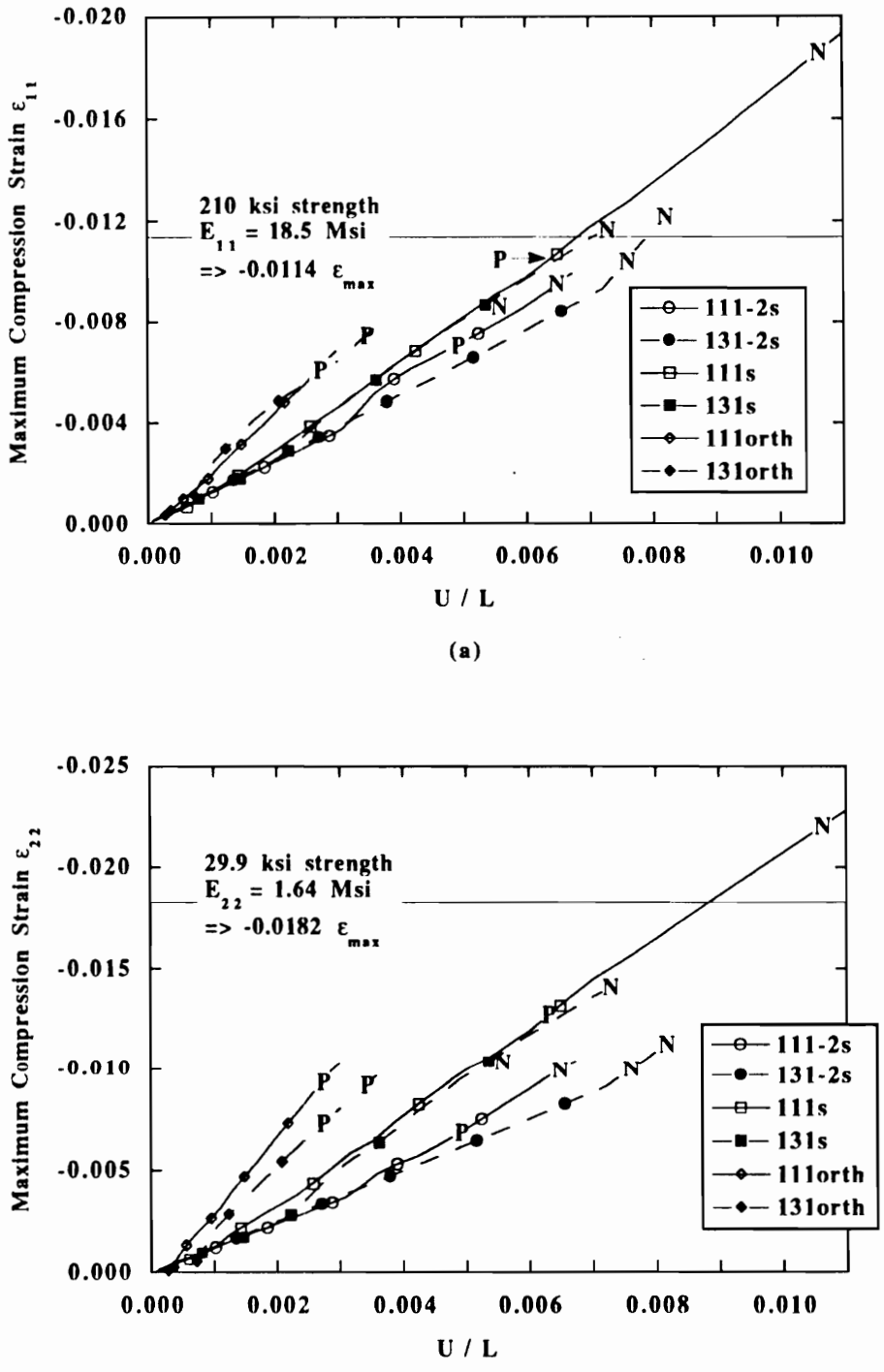

Figure 6-46. Maximum FEM compressive (a) fiber and (b) matrix strains as a function of flange size and stacking sequence. Symbols "N" and "P" denote experimental Nodal and Peak failure locations, respectively.

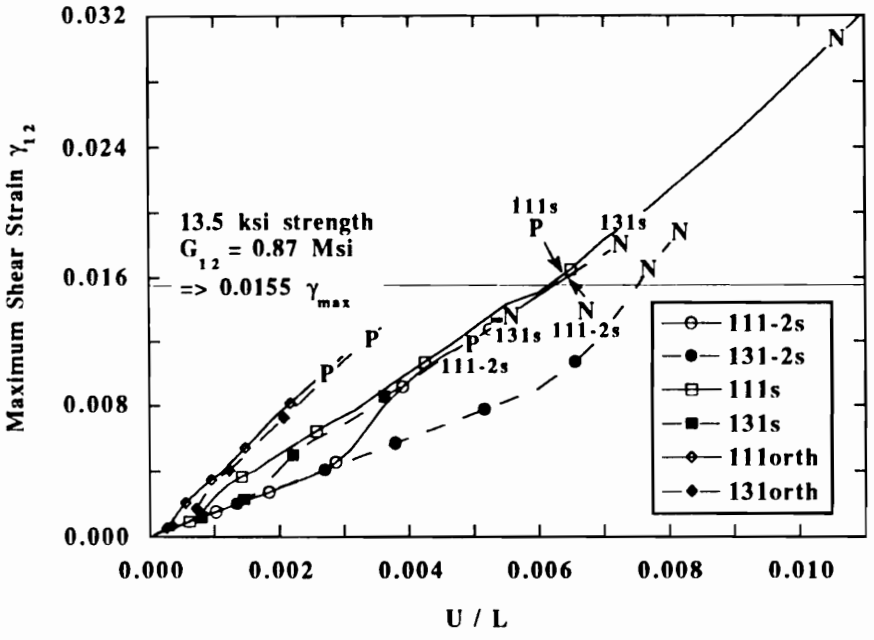

Figure 6-47. Maximum FEM in-plane shear strain as a function of flange size and stacking sequence. Symbols "N" and "P" denote experimental Nodal and Peak failure locations, respectively.

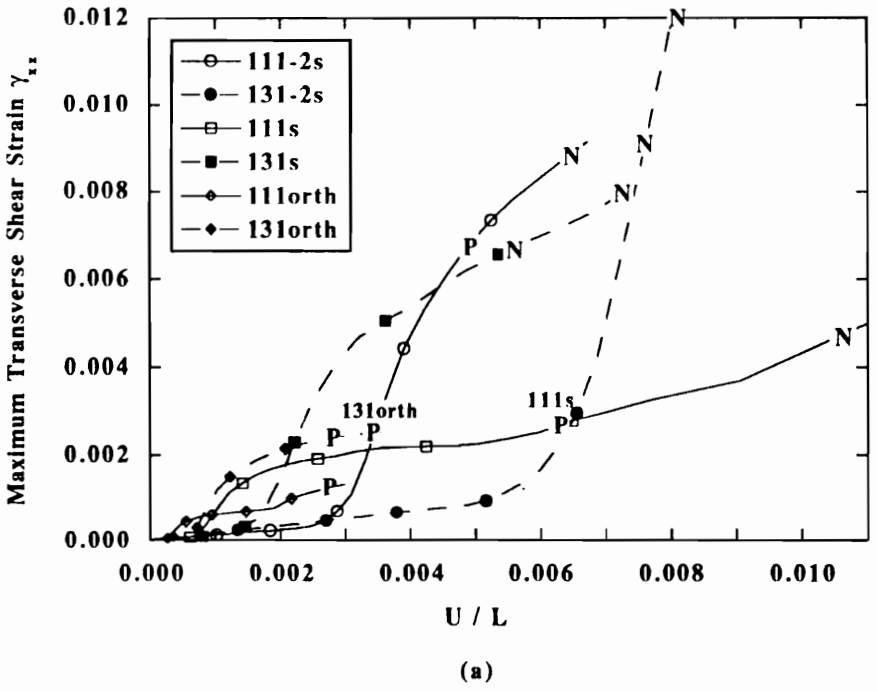

Figure 6-48. Maximum FEM transverse shear strains (a) γ_{xz} and (b) γ_{yz} as a function of flange size and stacking sequence. Symbols "N" and "P" denote experimental Nodal and Peak failure locations, respectively.

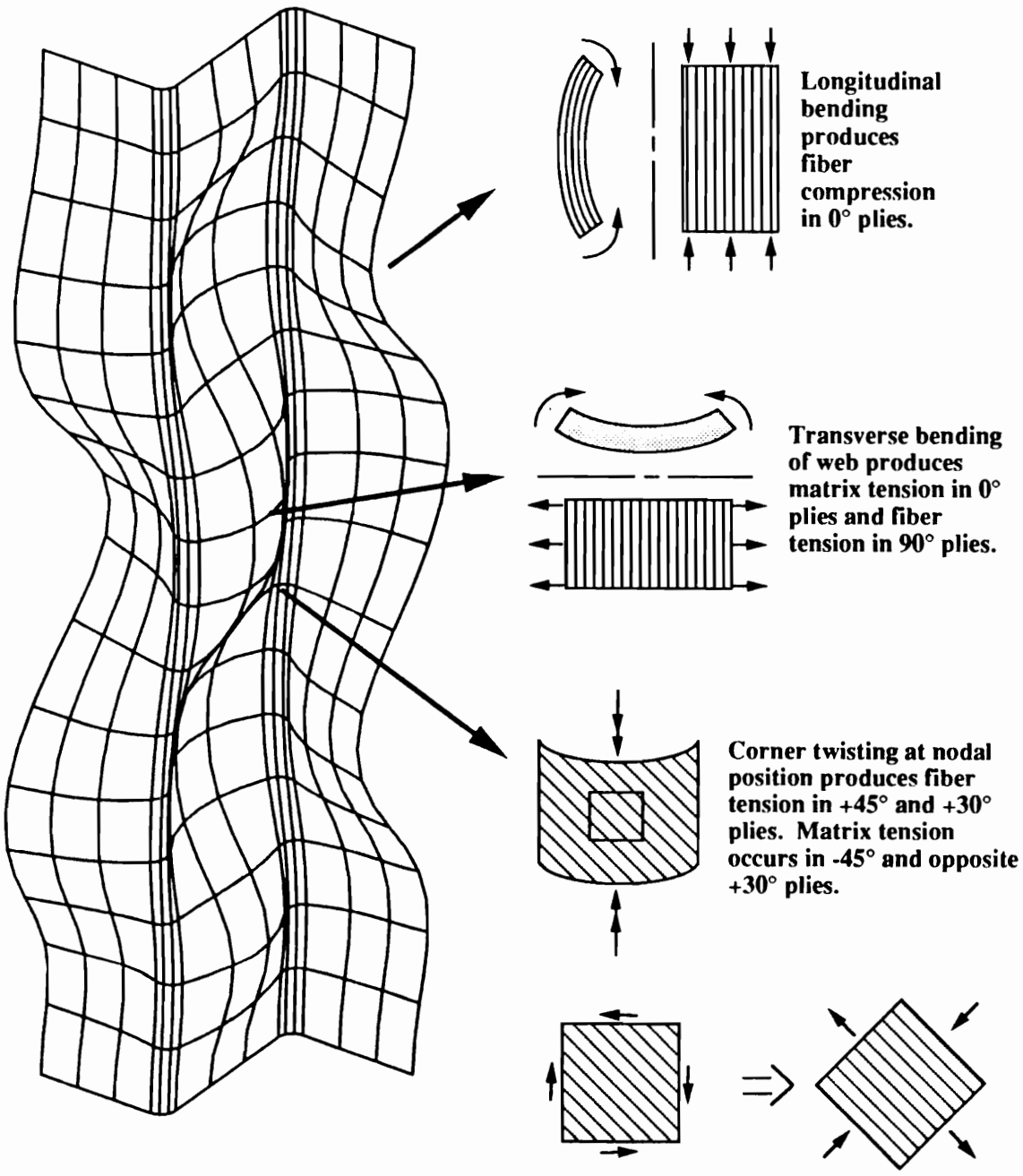

Figure 6-49. Predicted structural deformation associated with maximum extensional strains.

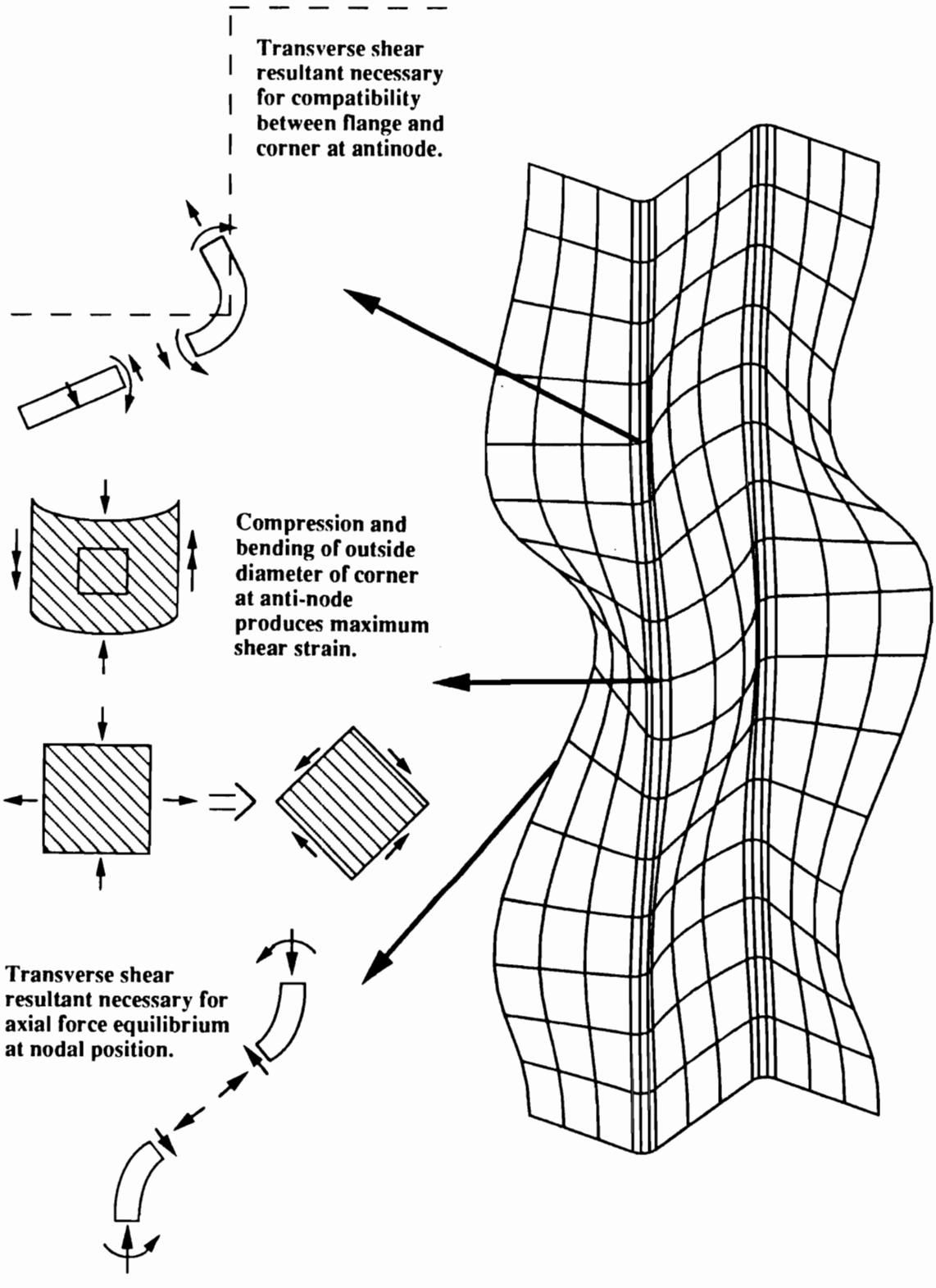

Figure 6-50. Predicted structural deformation associated with maximum shear strains.

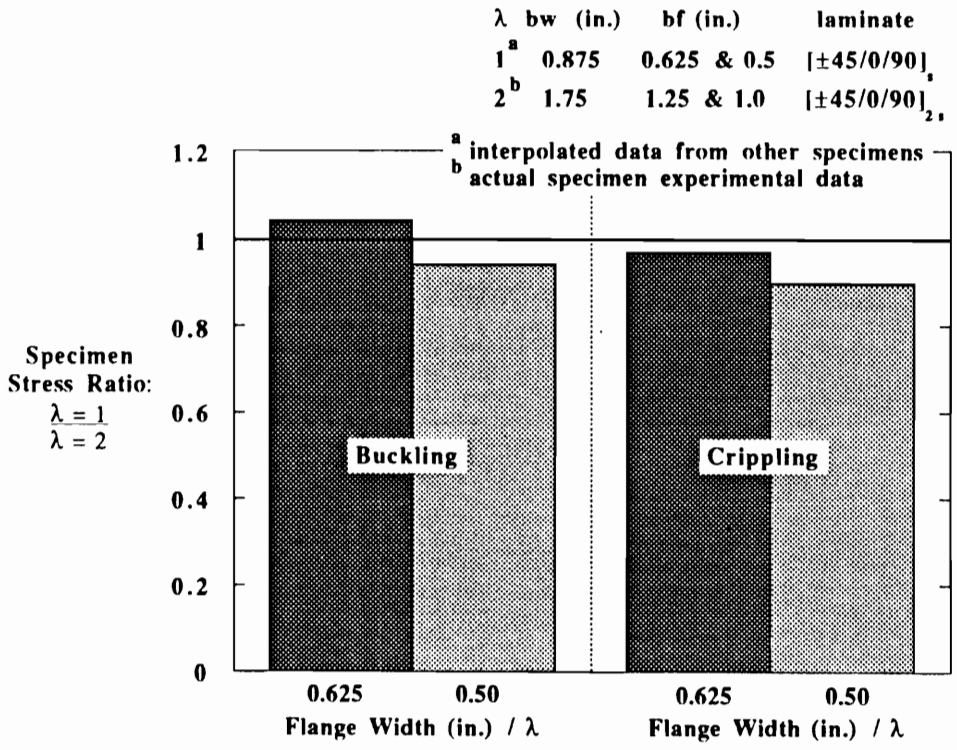

Figure 6-51. Normalized buckling and crippling stresses of small scale specimens. Significant scale effects are not observed.

APPENDIX. LINKED-PLATE MODEL FOR INITIAL LOCAL BUCKLING

1. The geometry and coordinate systems for the flange and web are given in Figure A-1.

2. The stability equations are:

$$D_{11}\frac{\partial^4 w}{\partial x^4} + 2(D_{12} + 2D_{66})\frac{\partial^4 w}{\partial x^2 \partial y_i^2} + D_{22}\frac{\partial^4 w}{\partial y_i^4} + N_x\frac{\partial^2 w}{\partial x^2} = 0 \qquad (A.1)$$

where i=1, 2 for the web and flange, respectively.

3. Displacement functions are assumed in the form:

$$w_i(x,y_i) = f_i(y_i)\sin\frac{m\pi x}{L} \qquad (A.2)$$

4. Displacement functions are substituted into the differential equations A.1, which then yield,

$$\left\{D_{11}\left(\frac{m\pi}{L}\right)^4 f_i - 2D_{33}\left(\frac{m\pi}{L}\right)^2 f_i'' + D_{22} f_i'''' - N_x\left(\frac{m\pi}{L}\right)^2 f_i\right\}\sin\frac{m\pi x}{L} = 0 \text{ or}$$

$$f_i'''' - 2\frac{D_{33}}{D_{22}}\left(\frac{m\pi}{L}\right)^2 f_i'' + \left(\frac{m\pi}{L}\right)^2\left\{\frac{D_{11}}{D_{22}}\left(\frac{m\pi}{L}\right)^2 - N_x\right\} f_i = 0 \qquad (A.3)$$

where $D_{33} = D_{12} + 2D_{66}$, and primes are used to denote differentiation with respect to y_i. Note that the two partial differential equations in w(x,y) have been transformed into two ordinary differential equations in $f_1(y_1)$ and $f_2(y_2)$.

5. Ordinary differential equations A.3 can be written in the following form, where D is the differential operator:

$$\left(D^2 - \lambda^2\right)\left(D^2 + \omega^2\right) f_i = 0 \qquad (A.4)$$

provided

$$\lambda, \omega = \frac{m\pi}{L}\sqrt{\sqrt{\left(\frac{D_{33}}{D_{22}}\right)^2 - \frac{D_{11}}{D_{22}} + \frac{N_x}{D_{22}}\left(\frac{L}{m\pi}\right)^2} \pm \frac{D_{33}}{D_{22}}} \; .$$

6. General solutions to equations A.4 are of the form:

web:

$$f_1(y_1) = A_1 \cosh \lambda y_1 + A_2 \sinh \lambda y_1 + A_3 \cos \omega y_1 + A_4 \sin \omega y_1 \qquad \text{(A.5a)}$$

flange:

$$f_2(y_2) = B_1 \cosh \lambda y_2 + B_2 \sinh \lambda y_2 + B_3 \cos \omega y_2 + B_4 \sin \omega y_2 \qquad \text{(A.5b)}$$

where the A_i, B_i (i=1,4) are undetermined coefficients.

7. A total of eight boundary and/or transition conditions are required to solve the two equations. Note that the origin of the coordinate systems for both the flange and web is at the corner. The following definitions are made for convenience:

$shw = \sinh(\lambda b_w/2)$, $\quad chw = \cosh(\lambda b_w/2)$,
$shf = \sinh(\lambda b_f)$, $\quad chf = \cosh(\lambda b_f)$,
$sw = \sin(\lambda b_w/2)$, $\quad cw = \cos(\lambda b_w/2)$,
$sf = \sin(\lambda b_f)$, $\quad cf = \cos(\lambda b_f)$,

$M = m\pi/L$,
$\gamma^2 = \lambda^2 D_{22} - M^2 D_{12}$, $\quad \delta^2 = \omega^2 D_{22} + M^2 D_{12}$,
$\eta^3 = \lambda M^2 D_{33} - \lambda^3 D_{22}$, $\quad \zeta^3 = \omega M^2 D_{33} + \omega^3 D_{22}$,

$p = \lambda b$, $\quad q = \omega b$,
$r^2 = \gamma^2 b^2$, $\quad s^2 = \delta^2 b^2$,
$u^3 = \eta^3 b^3$, $\quad v^3 = \zeta^3 b^3$,

where b = the width of plate 1 (b_w) or plate 2 (b_f) as indicated.

The boundary and transition conditions are identified below. Also identified are the equations resulting from the application of these conditions to the general form of the solution.

a. The position $y_1 = b_w/2$ corresponds to a plane of symmetry along the web centerline. Here, the transverse slope of the out-of-plane displacement and the transverse shear force are zero. These conditions require:

1). $$\frac{\partial w(x,b_w/2)}{\partial y_1} = 0 \Rightarrow A_1 \lambda \, shw + A_2 \lambda \, chw - A_3 \omega \, sw + A_4 \omega \, cw = 0$$

$$\Rightarrow [A_1 \, p \, shw + A_2 \, p \, chw - A_3 \, q \, sw + A_4 \, q \, cw]_1 = 0$$

2). $$Q_{y_1} = \left[\frac{\partial M_{xy}}{\partial x} + \frac{\partial M_y}{\partial y_1} \right]_{y_1 = b_w/2}$$

$$= \left[\frac{\partial}{\partial x} \left\{ -2D_{66} \frac{\partial^2 w}{\partial x \partial y_1} \right\} + \frac{\partial}{\partial y_1} \left\{ -D_{12} \frac{\partial^2 w}{\partial x^2} - D_{22} \frac{\partial^2 w}{\partial y_1^2} \right\} \right]_{y_1 = b_w/2}$$

$$= \left[-D_{33} \frac{\partial^3 w}{\partial x^2 \partial y_1} - D_{22} \frac{\partial^3 w}{\partial y_1^3} \right]_{y_1 = b_w/2}$$

$$\Rightarrow A_1 \eta^3 \, shw + A_2 \eta^3 \, chw - A_3 \zeta^3 \, sw + A_4 \zeta^3 \, cw = 0$$

$$\Rightarrow [A_1 \, u^3 \, shw + A_2 \, u^3 \, chw - A_3 \, v^3 \, sw + A_4 \, v^3 \, cw]_1 = 0$$

b. The positions $y_1 = 0$ and $y_2 = 0$ correspond to the flange-to-web corner. The conditions imposed here are that the corners remain straight, equilibrium of the bending moments is enforced and the angle of the corner is preserved. These conditions result in the following equations:

3). $w(x,y_1=0) = 0 \Rightarrow A_1 + A_3 = 0$

4). $[M_y(x,y_1=0)]_{web} + [M_y(x,y_2=0)]_{flange} = 0$

$$= \left[D_{12} \frac{\partial^2 w}{\partial x^2} + D_{22} \frac{\partial^2 w}{\partial y_1^2} \right]_{web} + \left[D_{12} \frac{\partial^2 w}{\partial x^2} + D_{22} \frac{\partial^2 w}{\partial y_2^2} \right]_{flange} = 0$$

$$\Rightarrow A_1 \gamma^2 - A_3 \delta^2 + B_1 \gamma^2 - B_3 \delta^2 = 0$$

5). $$\left[\frac{\partial w(x,y_1=0)}{\partial y_1} \right]_{web} - \left[\frac{\partial w(x,y_2=0)}{\partial y_2} \right]_{flange} = 0$$

$$\Rightarrow A_2 \lambda + A_4 \omega - B_2 \lambda - B_4 \omega = 0$$

6). $w(x,y_2=0) = 0 \Rightarrow B_1 + B_3 = 0$

c. The position $y_2 = b_f$ corresponds to the free end of the flange. Here, the Kirchoff shear force and the bending moment are zero. This requires:

7). $$V(x,y_2=b_f) = \left[Q_y + \frac{\partial M_{xy}}{\partial x} \right]_{y_2 = b_f} = 0$$

$$= - \left[(D_{12}+4D_{66}) \frac{\partial^3 w}{\partial x^2 \partial y_2} + D_{22} \frac{\partial^3 w}{\partial y_2^3} \right]_{y_2 = b_f} = 0$$

$$\Rightarrow B_1 \lambda \delta^2 \, shf + B_2 \lambda \delta^2 \, chf + B_3 \omega \gamma^2 \, sf - B_4 \omega \gamma^2 \, cf = 0$$

$$\Rightarrow [B_1 p s^2 \, shf + B_2 p s^2 \, chf + B_3 q r^2 \, sf - B_4 q r^2 \, cf]_2 = 0$$

8). $$My(x,y_2=b_f) = \left[D_{12} \frac{\partial^2 w}{\partial x^2} + D_{22} \frac{\partial^2 w}{\partial y_2^2} \right]_{y_2 = b_f} = 0$$

$$\Rightarrow B_1 \gamma^2 \, chf + B_2 \gamma^2 \, shf - B_3 \delta^2 \, cf - B_4 \delta^2 \, sf = 0$$

$$\Rightarrow [B_1 r^2 \, chf + B_2 r^2 \, shf - B_3 s^2 \, cf - B_4 s^2 \, sf]_2 = 0$$

8. The system of equations resulting from the imposition of the boundary and transition conditions on the general form of the solution can be represented as:

$$[K]\begin{Bmatrix}\{A\}\\ \{B\}\end{Bmatrix} = \{0\} \qquad (A.6)$$

where the coefficient matrix [K] is:

$$\begin{bmatrix}
[p\ shw & p\ chw & -q\ sw & q\ cw]_1 & 0 & 0 & 0 & 0 \\
[u^3\ shw & u^3\ chw & -v^3\ sw & v^3\ cw]_1 & 0 & 0 & 0 & 0 \\
1 & 0 & 1 & 0 & 0 & 0 & 0 & 0 \\
\gamma^2 & 0 & -\delta^2 & 0 & \gamma^2 & 0 & -\delta^2 & 0 \\
0 & \lambda & 0 & \omega & 0 & -\lambda & 0 & -\omega \\
0 & 0 & 0 & 0 & 1 & 0 & 1 & 0 \\
0 & 0 & 0 & 0 & [p\ s^2\ shf & p\ s^2\ chf & q\ r^2\ cf & -q\ r^2\ sf]_2 \\
0 & 0 & 0 & 0 & [r^2\ chf & r^2\ shf & -s^2\ cf & -s^2\ sf]_2
\end{bmatrix}$$

A nontrivial solution of equation A.6 requires that the coefficient matrix be singular. Therefore, the buckling condition is obtained by setting the determinant of the coefficient matrix [K] equal to zero.

9. A digression is now made to consider single plates analogous to the web and flange with a variety of boundary conditions along the unloaded, longitudinal edges. The various cases will be identified by the respective boundary conditions along the edge y=0, and at either y = b/2 (for the case of a plane of symmetry) or y=b (for the case of a free edge). The same general form of the solution (equation A.5) still applies.

a. (Simply-supported; Plane of symmetry)

1). $\dfrac{\partial w(x,b/2)}{\partial y} = 0 \Rightarrow A_1\, p\ shw + A_2\, p\ chw - A_3\, q\ sw + A_4\, q\ cw = 0$

2). $Q_y(x,b/2) = 0 \Rightarrow A_1\, u^3\ shw + A_2\, u^3\ chw - A_3\, v^3\ sw + A_4\, v^3\ cw = 0$

3). $w(x,0) = 0 \Rightarrow A_1 + A_3 = 0$

4). $M_y(x,0) = 0 \Rightarrow A_1 r^2 - A_3 s^2 = 0$

The determinant of the coefficient matrix is shown below:

$$\begin{vmatrix} p\,shw & p\,chw & -q\,sw & q\,cw \\ u^3\,shw & u^3\,chw & -v^3\,sw & v^3\,cw \\ 1 & 0 & 1 & 0 \\ r^2 & 0 & -s^2 & 0 \end{vmatrix}$$

The expanded determinant can be represented in the form: F(SS-sym).

b. (Clamped; Plane of symmetry)

1). $\dfrac{\partial w(x,b/2)}{\partial y} = 0 \Rightarrow A_1\,p\,shw + A_2\,p\,chw - A_3\,q\,sw + A_4\,q\,cw = 0$

2). $Q_y(x,b/2) = 0 \Rightarrow A_1\,u^3\,shw + A_2\,u^3\,chw - A_3\,v^3\,sw + A_4\,v^3\,cw = 0$

3). $w(x,0) = 0 \Rightarrow A_1 + A_3 = 0$

4). $\dfrac{\partial w(x,0)}{\partial y} = 0 \Rightarrow A_2\,p + A_4\,q = 0$

The determinant of the coefficient matrix is shown below:

$$\begin{vmatrix} p\,shw & p\,chw & -q\,sw & q\,cw \\ u^3\,shw & u^3\,chw & -v^3\,sw & v^3\,cw \\ 1 & 0 & 1 & 0 \\ 0 & p & 0 & q \end{vmatrix}$$

The expanded determinant can be represented in the form: F(Cl-sym).

c. (Simply-supported; Free)

1). $M_y(x,0) = 0 \Rightarrow B_1 r^2 - B_3 s^2 = 0$

2). $w(x,0) = 0 \Rightarrow B_1 + B_3 = 0$

3). $$V(x,b) = -\left[(D_{12}+4D_{66})\frac{\partial^3 w}{\partial x^2 \partial y} + D_{22}\frac{\partial^3 w}{\partial y^3}\right]_{y=b} = 0$$

$$\Rightarrow B_1 p s^2 shf + B_2 p s^2 chf + B_3 q r^2 sf - B_4 q r^2 cf = 0$$

4). $$My(x,b) = \left[D_{12}\frac{\partial^2 w}{\partial x^2} + D_{22}\frac{\partial^2 w}{\partial y^2}\right]_{y=b} = 0$$

$$\Rightarrow B_1 r^2 chf + B_2 r^2 shf - B_3 s^2 cf - B_4 s^2 sf = 0$$

The determinant of the coefficient matrix is shown below:

$$\begin{vmatrix} r^2 & 0 & -s^2 & 0 \\ 1 & 0 & 1 & 0 \\ p\,s^2\,shf & p\,s^2\,chf & q\,r^2\,sf & -q\,r^2\,cf \\ r^2\,chf & r^2\,shf & -s^2\,cf & -s^2\,sf \end{vmatrix}$$

The expanded determinant can be represented in the form: F(SS-free).

d. (Clamped; Free)

1). $$\frac{\partial w(x,0)}{\partial y} = 0 \Rightarrow B_2 p + B_4 q = 0$$

2). $w(x,0) = 0 \Rightarrow B_1 + B_3 = 0$

3). $V(x,b) = -\left[(D_{12}+4D_{66}) \frac{\partial^3 w}{\partial x^2 \partial y} + D_{22} \frac{\partial^3 w}{\partial y^3} \right]_{y=b} = 0$

$$\Rightarrow B_1\, p\, s^2\, shf + B_2\, p\, s^2\, chf + B_3\, q\, r^2\, sf - B_4\, q\, r^2\, cf = 0$$

4). $M_y(x,b) = \left[D_{12} \frac{\partial^2 w}{\partial x^2} + D_{22} \frac{\partial^2 w}{\partial y^2} \right]_{y=b} = 0$

$$\Rightarrow B_1\, r^2\, chf + B_2\, r^2\, shf - B_3\, s^2\, cf - B_4\, s^2\, sf = 0$$

The determinant of the coefficient matrix is shown below:

$$\begin{vmatrix} 0 & p & 0 & q \\ 1 & 0 & 1 & 0 \\ p\, s^2\, shf & p\, s^2\, chf & q\, r^2\, sf & -q\, r^2\, cf \\ r^2\, chf & r^2\, shf & -s^2\, cf & -s^2\, sf \end{vmatrix}$$

The expanded determinant can be represented in the form: F(Cl-free).

10. The determinant of the coefficient matrix in equation A.6 can be expanded using fourth order minors. Consider the first four columns. The only nonzero minors whose complements are also nonzero are those composed of rows 1,2,3,4 and 1,2,3,5. The associated complements from the last four columns are composed of rows 5,6,7,8 and 4,6,7,8, respectively. Comparison of the results from parts 8 and 9 indicates that the first minor, M_1, is equal to F(SS-sym)/b_w^2, (recalling that $r^2 = \gamma^2 b^2$ and $s^2 = \delta^2 b^2$), and the second minor, M_2, is equal to F(Cl-sym)/b_w, (recalling that $p = \lambda b$ and $q = \omega b$). Similarly, the first and second complements, C_1 and C_2, are equal to F(SS-free)/b_f^2 and -F(Cl-free)/b_f, respectively. Therefore, the expanded determinant can be represented in the form:

$$M_1\, C_1\, (-1)^{\mu} + M_2\, C_2\, (-1)^{\nu} = 0$$

$$= M_1\, C_1\, (-1)^{20} + M_2\, C_2\, (-1)^{21} = 0 \qquad \text{(A.7)}$$

where μ and ν are the sums of the numbers of the rows and columns contained in minors M_1 and M_2, respectively. Upon substitution of the minors and complements into equation A.7, the buckling condition becomes:

$$\left[\frac{F(SS\text{-}sym)}{b_w^2}\right]\left[\frac{-F(Cl\text{-}free)}{b_f}\right] - \left[\frac{F(Cl\text{-}sym)}{b_w}\right]\left[\frac{F(SS\text{-}free)}{b_f^2}\right] = 0$$

$$\Rightarrow \left[\frac{F(SS\text{-}sym)}{F(Cl\text{-}sym)}\right]_{web} + \frac{b_w}{b_f}\left[\frac{F(SS\text{-}free)}{F(Cl\text{-}free)}\right]_{flange} = 0 \qquad (A.8)$$

11. The solution of equation A.8 was obtained iteratively, using an incremental search and interval halving routine.

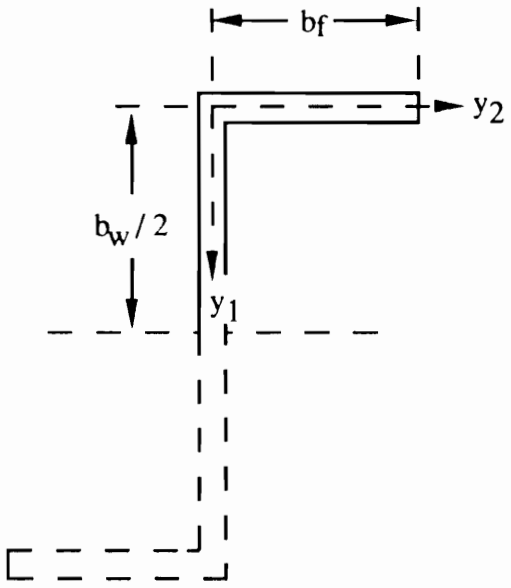

Figure A-1. Geometry and coordinate system for linked plate analysis of initial local buckling.

VITA

Todd Michael Wieland was born on March 5, 1962 in Grand Rapids, Michigan. In May 1984, he received a Bachelor of Science degree in Metallurgical Engineering from Michigan Technological University, Houghton, Michigan. He then entered the United States Navy and served as a Nuclear Power Research Officer in the Reactor Plant Materials Division of the Naval Nuclear Propulsion Directorate, achieving the rank of lieutenant. He entered the Ph.D. Program in the Department of Engineering Science and Mechanics at Virginia Polytechnic Institute and State University in August, 1988.